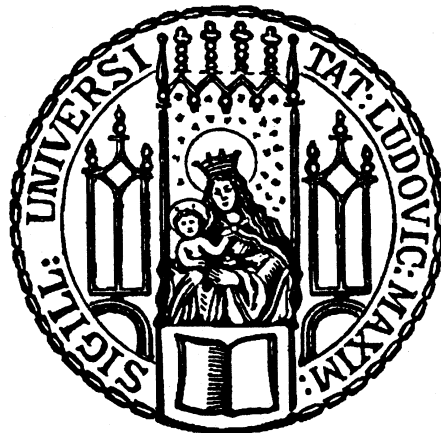

Negative Absolute Temperature and the Dynamics of Quantum Phase Transitions

Simon Braun



Dissertation
an der Fakultät für Physik
der Ludwig-Maximilians-Universität München

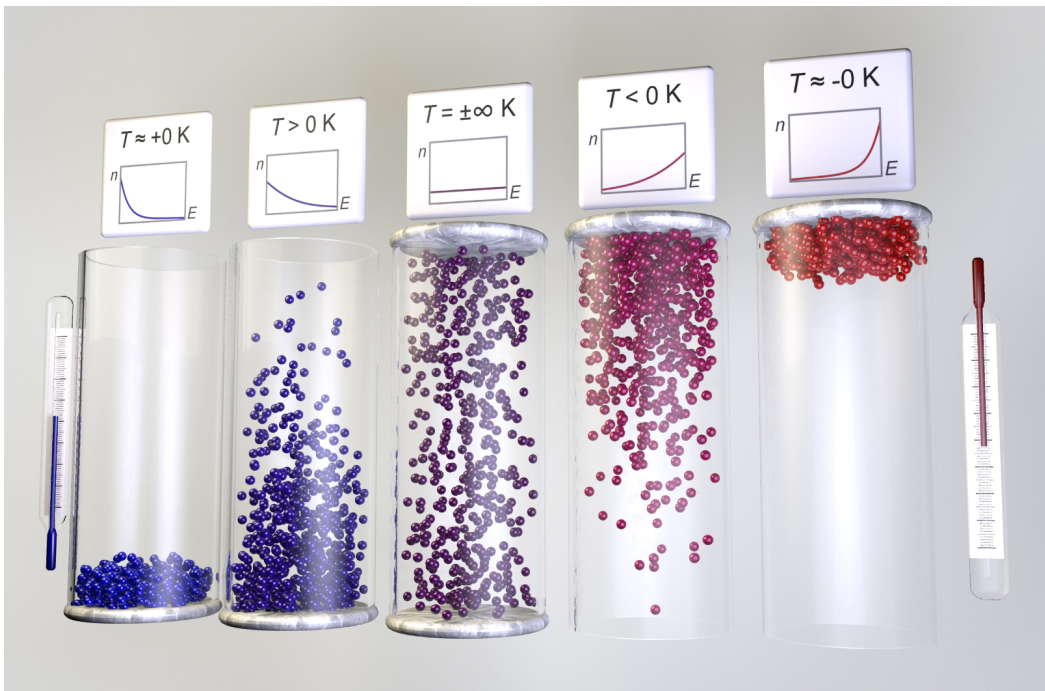
vorgelegt von
Simon Braun
aus München

München, Oktober 2014

meinen Eltern

Negative Absolute Temperature and the Dynamics of Quantum Phase Transitions

Simon Braun



München 2014

Erstgutachter: Prof. Dr. Immanuel Bloch

Zweitgutachter: Prof. Dr. Ulrich Schollwöck

Tag der mündlichen Prüfung: 11.12.2014

Zusammenfassung

In dieser Promotionsarbeit präsentiere ich die erstmalige Realisierung eines Zustands negativer absoluter Temperatur für bewegliche Teilchen, sowie zusätzlich die detaillierte Untersuchung der Dynamik eines Quantenphasenübergangs. Als Grundlage für die Experimente dienten uns ultrakalte Atome in optischen Gittern, die durch den Bose-Hubbard Hamilton-Operator beschrieben werden können.

Das Charakteristikum negativer Temperaturen ist eine invertierte Besetzungsverteilung, bei der Zustände hoher Energien stärker besetzt sind als niederenergetische Zustände. Daraus folgt die experimentelle Herausforderung, dass die möglichen Energien des Systems nach oben beschränkt sein müssen. Zum ersten Mal wurden negative Temperaturen in den 1950er Jahren in Bezug auf den Spinfreiheitsgrad von Atomkernen erreicht, welcher ein endliches Spektrum bildet. In dieser Arbeit stelle ich die erstmalige Realisierung von negativen Temperaturen auch für kinetische Freiheitsgrade vor. Dafür beschränkten wir die kinetische Energie auf ein einzelnes Band des Gitterpotenzials und nutzten die volle Flexibilität unseres Experiments, bestehend aus rotverstimmten Dipolfallen, blauverstimmten Gitterpotenzialen und einer Feshbach-Resonanz, um die Gesamtenergie des Systems zu limitieren. Durch die Messung der Impulsverteilung konnten wir nachweisen, dass die Atome vor allem Zustände höchster kinetischer Energie besetzen. Das Experiment ermöglicht in Zukunft unter anderem die Untersuchung von Systemen, bei denen der oberste Energiezustand besonders interessante Eigenschaften aufweist.

In einem weiteren Experiment untersuchten wir das komplexe dynamische Verhalten an einem Quantenphasenübergang, das auch in der modernen Physik noch nicht vollständig verstanden ist. Quantenphasenübergänge zeichnen sich durch eine fundamentale Änderung von Grundzustandseigenschaften bei Variation eines Parameters aus; Beispiele sind das Auftreten von magnetischer Ordnung oder von Supraleitung als Funktion der Dotierung in Cupraten. In diesem Projekt untersuchten wir den Phasenübergang von Mott-Isolator zu Suprafluid, einen paradigmatischen Vertreter der Quantenphasenübergänge, und dabei insbesondere, wie sich Kohärenz beim Übergang vom inkohärenten Mott-Isolator zum phasenkohärenten Suprafluid dynamisch aufbaut. Das komplexe Verhalten, das wir beobachten konnten, geht über die Vorhersagen existierender analytischer Modelle wie des Kibble-Zurek-Mechanismus' hinaus. Numerische Simulationen eindimensionaler Systeme unserer Kollegen von der FU Berlin stimmen hervorragend mit unseren experimentellen Daten überein und bestätigen unsere Messungen als zertifizierte Quantensimulation. Unsere umfangreichen Ergebnisse für unterschiedliche repulsive und attraktive Wechselwirkungen sowie Dimensionalitäten sind ein entscheidender Baustein, um in Zukunft ein tiefergehendes Verständnis des komplizierten dynamischen Verhaltens an Quantenphasenübergängen zu erreichen.

Abstract

In this thesis, I present the first realization of negative absolute temperatures for mobile particles as well as a detailed study of the complex dynamics of a quantum phase transition, namely from the Mott insulator to the superfluid. The experiments are carried out with ultracold bosons loaded into an optical lattice, which can be described by the Bose-Hubbard Hamiltonian. The measurements presented in this thesis were only possible due to the extraordinary control over quantum states that can nowadays be achieved in modern ultracold atoms setups.

Negative temperature states are characterized by an inverted occupation distribution, where high-energy states are populated more than low-energy states. This requires, as an experimental challenge, an upper bound on the possible energies of the system. Negative temperatures have been realized for the first time in the 1950s for the spin degree of freedom of nuclei, where the spectrum is finite. In this thesis, I present the first realization of negative temperatures for motional degrees of freedom. We limited the kinetic energy to a single band of the optical lattice potential and fully employed the tunability of our setup, including the combination of dipole potentials at blue- and red-detuned wavelengths and a Feshbach resonance, to create an upper bound on the total energy of the system. We identified the negative temperature state via its momentum distribution, which shows very strong occupation of the highest kinetic energy states. Amongst others, negative temperature states in optical lattices allow future research on systems where the highest energy state is of particular interest.

In a separate set of experiments, we investigated the complex dynamical behavior when a quantum phase transition is crossed, which poses still an open and challenging question for many-body theory. Quantum phase transitions are characterized by a dramatic change of ground state properties, for example the appearance of magnetic order or superconductivity as a function of doping in cuprates. In this project, we investigated the Mott insulator to superfluid transition, a paradigmatic example of a quantum phase transition. We performed a detailed study on how coherence emerges when the quantum phase transition from the incoherent Mott insulator to the phase-coherent superfluid state is crossed and found a rich behavior beyond the scope of any existing analytical model such as the Kibble-Zurek mechanism. We obtained excellent agreement with the numerical simulations of one-dimensional systems of our collaborators, supporting that our measurements can be considered a valid quantum simulation. Our extensive results for various repulsive and attractive interactions as well as dimensionalities contribute an essential piece for a future comprehensive understanding of the intricate dynamics of quantum phase transitions.

Contents

1	Introduction	15
2	Theory and Experimental Realization of Degenerate Bose Gases	21
2.1	Theory of Interacting Ultracold Bosons	21
2.1.1	Bose-Einstein Condensates	21
2.1.2	Weakly Interacting Bose Gas	22
2.1.3	Feshbach Resonances	23
2.2	Atom-Light Interactions and Optical Dipole Trap	26
2.2.1	Optical Dipole Potentials	26
2.2.2	Crossed Dipole Trap	27
2.2.3	Trap Frequencies	29
2.3	Experimental sequence	30
2.3.1	Initial Cooling Sequence	31
2.3.2	Evaporative Cooling	32
3	Ultracold Bosons in Optical Lattices	35
3.1	Experimental Realization of Optical Lattice Potentials	35
3.1.1	Laser Beam Setup	35
3.1.2	Anti-Trapping Potential	36
3.2	Single Particle in an Optical Lattice Potential	38
3.2.1	Bloch Bands	38
3.2.2	Wannier Functions	40
3.2.3	Tight-Binding Limit	41
3.2.4	Lattice Depth Calibration	42
3.2.5	Light-Assisted Collisions	44
3.3	Many Particles in an Optical Lattice Potential	46
3.3.1	Wavefunction of a BEC in an Optical Lattice	47
3.3.2	Bose-Hubbard Model	49
3.3.3	Superfluid and Mott Insulator Phase	50
3.4	Absorption Imaging	52
3.4.1	In Situ Imaging	53
3.4.2	Time-of-Flight Absorption Imaging	54

3.4.3	Measuring the Momentum Distribution	54
3.4.4	Measuring the Quasimomentum Distribution	56
3.5	Feshbach-Induced Mott Insulator	56
4	Theory of Negative Absolute Temperatures	59
4.1	What are Negative Absolute Temperatures?	59
4.1.1	Occupation Inversion	59
4.1.2	Definition of Temperature	60
4.2	Thermodynamic Equilibrium and Thermalization	61
4.2.1	Classical Thermalization	63
4.2.2	Quantum Thermalization	64
4.3	Experimental Realizations of Negative Absolute Temperatures	67
4.3.1	Realization of Upper Energy Bound	67
4.3.2	Negative Temperature for Nuclear Spin Systems	68
4.3.3	Effective Negative Temperature for Atomic Spin System	69
4.3.4	Are Lasers at Negative Temperature?	69
4.3.5	Negative Temperature for Motional Degrees of Freedom in an Optical Lattice	70
4.4	Implications of Negative Absolute Temperatures	73
4.4.1	Validity of the Laws of Thermodynamics	73
4.4.2	Carnot Efficiency	75
4.4.3	Negative Pressure	78
4.4.4	A Possible Relation between Negative Temperature and Dark Energy?	80
4.5	Definition of Entropy	82
4.5.1	Alternative Entropy Definition	83
4.5.2	Problems of the Alternative Entropy Definition	85
5	Realization of Negative Absolute Temperatures	89
5.1	Experimental Sequence and Images	89
5.1.1	Experimental Sequence	89
5.1.2	Inversion of the External Potential	91
5.1.3	Resulting TOF Images	92
5.2	Stability of the Negative Absolute Temperature State	94
5.2.1	Stability versus Trap Frequency	94
5.2.2	Stability versus Interaction	97
5.3	Extraction of Energy Distribution and of Absolute Temperature	99
5.3.1	Determination of Energy Distribution	99
5.3.2	Fitting a Bose-Einstein Distribution	101
5.3.3	Critical Temperatures	104
5.4	Extraction of Coherence Length	105
5.5	Negative Temperature in Other Dimensionalities	105
5.5.1	1D	106

5.5.2	3D	107
6	Emergence of Coherence and the Dynamics of Quantum Phase Transitions	111
6.1	Classical and Quantum Phase Transitions	111
6.1.1	Sudden and Adiabatic Approximations	113
6.1.2	Kibble-Zurek Mechanism	114
6.2	Experimental and Numerical Methods	117
6.2.1	Experimental Sequence for 1D	117
6.2.2	Experimental Sequence for Higher Dimensions and Attractive Interactions	119
6.2.3	Extraction of Coherence Length	120
6.2.4	Obtaining the In Situ Width	120
6.2.5	DMRG Calculations	124
6.2.6	Exact Diagonalization Calculations	125
6.2.7	Doublon-Holon Fermionic Model	126
6.2.8	Determination of Power-Law Exponents	128
6.3	Results in 1D	133
6.3.1	Power-Law Emergence of Coherence and the Kibble-Zurek Prediction	134
6.3.2	Applicability of the Kibble-Zurek Mechanism	137
6.3.3	Influence of the Trap	140
6.4	Emergence of Coherence in Higher Dimensions and for Attractive Interactions	144
6.4.1	Emergence of Coherence in 2D and 3D	145
6.4.2	Emergence of Coherence for Attractive Interactions	146
6.5	Dynamics after and during the Quench	149
6.5.1	Dynamics of the Cloud Size after the Quench	149
6.5.2	Dynamics of the Cloud Size during the Quench	150
6.5.3	Emergence of Coherence after the Quench	151
7	Conclusions and Outlook	155

1 Introduction

Nothing can be colder than absolute zero, as at zero Kelvin, the particles cease to move. This popular statement of thermodynamics is taught in high school and, in a classical picture, it is correct. In quantum mechanics, due to the zero point energy, the particles still show some motion even at absolute zero; the general statement that absolute zero is the coldest possible temperature, however, remains true. Yet, according to the definition of temperature, it is possible to create systems at negative absolute temperature. These are characterized by an inverted population distribution that is in thermal equilibrium and therefore stable. Due to the large occupation of high-energy states, however, a system at negative temperature is *hotter* than at any positive temperature; i.e. in thermal contact, heat would flow from the negative temperature to the positive temperature system.

In everyday life, we do not encounter negative temperatures. Due to the exponentially increasing occupation distribution at negative temperatures, an upper bound on the energy of the particles is required to keep the distribution normalizable. In the case of free particles, however, kinetic energy with its parabolic dispersion is unbounded from above. Therefore free particles can never be at negative temperature. The key challenge to realize negative temperatures lies in the implementation of such an upper energy bound. Negative temperatures were realized experimentally for the first time in 1951 by E. M. Purcell and R. V. Pound [1]. In their experiment, Purcell and Pound created a population inversion of the two Zeeman states of the nuclear spins of ^7Li in a homogeneous magnetic field. The inversion was in thermal equilibrium due to spin-spin relaxation processes and was found to be stable, limited only by the very slow spin-lattice relaxation. As the position of the nuclei was locked to the lattice sites in a crystal, kinetic energy of the ions was effectively excluded from the system. The resulting pure two-level system of the Zeeman states naturally provides an upper bound for the energy of the particles. The temperature that was realized in this experiment is therefore more precisely characterized by the term *negative spin temperature*. In 1956, Norman Ramsey published a first account on the thermodynamics and statistical mechanics at negative temperature [2].

Following this pioneering breakthrough, various experiments [3, 4] later realized negative spin temperatures for nuclear spin systems in a similar manner. In 2011, P. Medley and coworkers [5] created an effective negative spin temperature for ultracold ^{87}Rb atoms in an optical lattice, i.e. a standing wave pattern of laser beams. They implemented a sequence in which the atoms are locked to their lattice sites and, by reversing a magnetic field gradient,

the population of two hyperfine states is inverted and stable.

In this thesis, I present how we realized a negative temperature state that, for the first time, also includes kinetic energy, i.e. motional degrees of freedom. The experiment was recently suggested theoretically [6, 7] and became possible due to the great tunability of ultracold atoms in an optical lattice. The key feature of such a lattice system lies in the band structure that divides kinetic energy into several distinct bands and therefore provides an effective upper bound for the kinetic energy of atoms that are confined to the lowest band. To realize the negative temperature state for motional degrees of freedom, additional techniques are necessary, such as Feshbach resonances to control interatomic interactions. The blue-detuned optical lattice constitutes a special feature of our experimental apparatus that allows us to tune lattice depth and external confinement independently and is a crucial ingredient for our negative temperature experiment.

A major achievement in the development of the field of ultracold atoms was the first realization of a Bose-Einstein condensate (BEC) in 1995 [8–10]. The experiments in the following years focused on weakly interacting BECs that can be described by a macroscopic matter wave [11, 12] and are consistent with Bogoliubov’s mean-field theory [13, 14]. The superfluid property of these systems could be proven by the observation of the characteristic vortices [15–17]. In 1999, also the first ultracold cloud of fermions was achieved [18].

The introduction of Feshbach resonances into the research field [19] allowed the interatomic interactions to be tuned over a wide range via external magnetic fields and to enter the regime of strong correlations where interactions become so strong that they cannot be treated in a mean-field picture anymore. In the case of two-component fermionic systems, strong correlations enabled the study of the transition from molecular BECs [20–23] on the repulsive side of the Feshbach resonance to the formation of Bardeen-Cooper-Schrieffer (BCS) pairing [24, 25] on the attractive side. The superfluidity of the BCS state was again proven by the observation of vortices [26]. For bosonic systems, Feshbach resonances permitted, e.g., the measurement of the collapse of a Bose-Einstein condensate [27] and the observation of the long-predicted Efimov state [28–30].

In 1998, D. Jaksch and coworkers proposed the aforementioned optical lattices as an alternative route to strongly correlated systems [31]. Loading ultracold bosons into such a periodic potential allows the realization of the Bose-Hubbard Hamiltonian, a model system which was only known from condensed matter physics [32]. The atoms are trapped in such an array like the electrons in the ion crystal of a solid [33]. This similarity between the systems allows solid state physics to be simulated with ultracold atoms experiments. An experimental breakthrough was achieved in 2002, when M. Greiner and colleagues realized the superfluid to Mott insulator transition with ultracold atoms in a three-dimensional lattice [34].

Since then, the field of ultracold atoms in optical lattices grew rapidly, leading to the creation of Mott insulators in lower dimensions [35, 36] as well as for two-component fermionic gases [37, 38]. The great control and flexibility of optical lattice setups allowed the realization of ever more intriguing quantum mechanical systems, such as the Tonks-Girardeau

gas [39, 40], and more complex lattice geometries such as superlattices [41–43] and triangular and hexagonal lattice geometries [44, 45]. Recent progress in detection techniques now allows the imaging and addressing of single atoms on individual lattice sites [46–48]. This adds to the multitude of detection techniques of standard absorption imaging, phase-contrast imaging [49], noise correlation measurement [50, 51], and spectroscopic techniques [35, 52, 53].

The extraordinary control in optical lattice experiments already achieved nowadays brings us closer to the realization of a fundamental idea of Richard Feynman from 1982 [54]: As the Hilbert space of a quantum many-body system grows exponentially with system size, it is impossible to calculate and solve these systems on a classical computer as soon as the particle number exceeds some small number of order 20-30. Instead, Feynman suggested using a well-controlled quantum system to model the quantum system of interest via a quantum simulation. Indeed, some of the experiments conducted in recent years, where particular desired Hamiltonians have been precisely implemented, can already be interpreted as quantum simulations, and there is even more to come in the near future [55, 56].

In particular, quantum simulations can help to understand dynamical properties of quantum many-body systems. While the static properties of the Mott insulating and superfluid states are well understood, the dynamics of the transition between the two states is still an open problem. This particular transition is a prime example of a quantum phase transition [57] that is characterized by a drastic change of the nature of the ground state upon changing a parameter of the Hamiltonian, and belongs to the most exciting aspects of quantum many-body and condensed matter physics. There has been a considerable amount of research on quantum phase transitions in recent years; however, this research topic is still rather young.

Whereas the superfluid in an optical lattice is characterized by a well-defined phase relation across the system, in the Mott insulating regime, the local phases at each lattice site have obtained maximum uncertainty. Thus, during the quantum phase transition from the Mott insulator to the superfluid, phase coherence between distant lattice sites emerges. In this thesis, I describe a thorough study on the dynamical emergence of coherence at the Mott to superfluid phase transition. We measured the dynamics of the spreading of correlations in the system by varying the quench velocity across the transition. We find very good agreement of our one-dimensional results with density matrix renormalization group calculations, supporting our measurements as being a valid quantum simulation. For intermediate quench velocities, we find a power-law increase of the coherence length in the system, which is reminiscent of the behavior predicted by the popular Kibble-Zurek mechanism. However, we observe that the dynamics are more involved than suggested by the original Kibble-Zurek picture. We used our quantum simulator to measure the dynamics also in higher dimensions, where numerical simulations are categorically unfeasible, and for repulsive and attractive interactions.

Outline

- The second chapter is a brief overview of the theory of interacting ultracold bosons as well as of the experimental sequence that we use to create ultracold clouds of atoms. Also optical dipole potentials as a fundamental ingredient for the experiments are introduced.
- In the third chapter, the experimental implementation of optical lattices is described with an emphasis on the peculiarity of blue-detuned lattice potentials. The theory of both a single particle and many particles in a periodic potential is outlined and the Bose-Hubbard Hamiltonian is introduced. The experimental part illustrates how we calibrate the lattice depth and minimize light-assisted collisions. The various imaging techniques that are utilized for the experiments in this thesis are introduced. The measurement of a Feshbach-induced Mott insulator state is shown.
- The fourth chapter deals with the theory of negative temperatures and of thermalization processes. Negative temperatures are introduced and illustrated in an intuitive way. The theoretical foundations of thermodynamic equilibrium in both classical and quantum systems are outlined. The requirements for the creation of negative temperature states are introduced and previous experimental realizations are presented. The implications of negative temperature states such as the validity of the laws of thermodynamics at negative temperature and the efficiency of Carnot cycles are discussed. A recent discussion about the correct definition of entropy is recapitulated, which was triggered by our publication about negative temperatures.
- The fifth chapter presents our experimental implementation of negative temperatures for motional degrees of freedom. The experimental sequence for a two-dimensional system is given with emphasis on the inversion of the external potential. Lifetime measurements prove the stability of the negative temperature state and show the dependence on trap frequency and interactions. The method to extract the characteristic inverted occupation distribution is detailed, together with a Bose-Einstein fit from which the temperature can be estimated. The coherence length of the final state is analyzed. Finally, the realization of a negative temperature state in 1D is presented as well as the limitations of our experimental apparatus for an implementation in 3D.
- The sixth chapter contains theory and experiments on the second project of this thesis, the emergence of coherence at the Mott to superfluid quantum phase transition. Quantum phase transitions in general are introduced together with common approximations for the description of their dynamics including the Kibble-Zurek mechanism. The experimental sequence for the measurement as well as the experimental methods for the extraction of the coherence length are given. The determination of the power-law exponents for the emergence of coherence versus quench time is outlined, leading to more complex dynamics than expected from the original Kibble-Zurek picture. The results of theoretical calculations in 1D are compared with the experimental data and a quasiparticle explanation for the spreading of correlations for short quench times is presented. The applicability of the Kibble-Zurek approxima-

tion is investigated and the influence of the external trap in the experimental setup is discussed. Measurements of the emergence of coherence in higher dimensions are presented, showing the irrelevance of the dimensionality on the dynamics for high and intermediate quench velocities. Measurements for attractive interactions prove that the timescale for the emergence of coherence is a genuine property of the Mott to superfluid transition. Additional measurements about the time-resolved dynamics of the cloud size during and after the quench as well the emergence of coherence after the quench are presented.

Publications

The main results of this thesis are published in the following two papers:

- *Emergence of coherence and the dynamics of quantum phase transitions*
S. Braun, M. Friesdorf, S. S. Hodgman, M. Schreiber, J. P. Ronzheimer, A. Riera, M. del Rey, I. Bloch, J. Eisert, and U. Schneider
[arXiv 1403.7199 \(2014\)](https://arxiv.org/abs/1403.7199)
- *Negative absolute temperature for motional degrees of freedom*
S. Braun, J. P. Ronzheimer, M. Schreiber, S. S. Hodgman, T. Rom, I. Bloch, and U. Schneider
[Science 339, 52 \(2013\)](https://science.sciencemag.org/content/339/6117/52)

Additional publications to which I contributed during the course of my PhD:

- *Experimental evidence for the emergence of a coherent matter wave in the non-equilibrium dynamics of a strongly interacting gas of bosons*
J. P. Ronzheimer, M. Schreiber, S. Braun, S. S. Hodgman, L. Vidmar, S. Langer, F. Heidrich-Meisner, I. Bloch, and U. Schneider
in preparation
- *Comment on “Consistent thermostatistics forbids negative absolute temperatures”*
U. Schneider, S. Mandt, A. Rapp, S. Braun, H. Weimer, I. Bloch, and A. Rosch
[arXiv 1407.4127 \(2014\)](https://arxiv.org/abs/1407.4127)
- *Expansion dynamics of interacting bosons in homogeneous lattices in one and two dimensions*
J. P. Ronzheimer, M. Schreiber, S. Braun, S. S. Hodgman, S. Langer, I. P. McCulloch, F. Heidrich-Meisner, I. Bloch, and U. Schneider
[Phys. Rev. Lett. 110, 205301 \(2013\)](https://journals.aps.org/prl/abstract/10.1103/PhysRevLett.110.205301)
- *Fermionic transport and out-of-equilibrium dynamics in a homogeneous Hubbard model with ultracold atoms*
U. Schneider, L. Hackermüller, J. P. Ronzheimer, S. Will, S. Braun, T. Best, I. Bloch, E. Demler, S. Mandt, D. Rasch, and A. Rosch
[Nat. Phys. 8, 213 \(2012\)](https://journals.aps.org/nphys/abstract/10.1038/nphys2833)

1 Introduction

- *Coherent interaction of a single fermion with a small bosonic field*

S. Will, T. Best, S. Braun, U. Schneider, and I. Bloch

[Phys. Rev. Lett. 106, 115305 \(2011\)](#)

Earlier work in which I was involved:

- *Tunable external cavity diode laser using a micromachined silicon flexure and a volume holographic reflection grating for applications in atomic optics*

H.-C. Chuang, R. Jiménez-Martínez, S. Braun, D. Z. Anderson, and V. M. Bright

[J. Micro-Nanolith. MEM 7, 021010 \(2008\)](#)

2 Theory and Experimental Realization of Degenerate Bose Gases

In the first section of this chapter, I introduce the theoretical background of an interacting ultracold gas of bosonic atoms. In the second section I describe how atoms can be trapped in an optical dipole trap and how this trap is implemented for the experiments in this thesis. In the third section I give an overview of the experimental cycle with which a Bose-Einstein-condensate is created.

2.1 Theory of Interacting Ultracold Bosons

In this section, I present the theoretical foundations of ultracold bosonic gases. Feshbach resonances are introduced as a tool to tune interactions between particles, which is essential for the experiments in this thesis.

2.1.1 Bose-Einstein Condensates

In 1925, S. N. Bose [58] and A. Einstein [59] predicted Bose-Einstein-condensation as a phase transition for an ideal gas of indistinguishable bosonic particles. This phenomenon also exists for interacting particles, and was first realized in dilute gases of rubidium [8] and sodium [9] in 1995. At a critical phase space density, the wavefunctions of the individual particles start to overlap and a Bose-Einstein condensate (BEC) is formed. Here, a macroscopic number of particles occupy the same single-particle eigenstate, forming a macroscopic matter wave. In an ideal gas, the occupation of single-particle eigenstates with energy ϵ at temperature T is given by the Bose distribution function [60]

$$N(\epsilon) = \frac{1}{e^{\frac{\epsilon-\mu}{k_B T}} - 1}, \quad (2.1)$$

where k_B denotes Boltzmann's constant and the chemical potential μ is smaller than or equal to the energy ϵ_0 of the lowest energy state, $\mu \leq \epsilon_0$ ¹. Below a critical temperature T_c , the occupation N_0 of the single-particle ground state becomes macroscopic. In our

¹In the case of negative temperatures, $T \leq 0$, μ is greater or equal than the maximum single-particle energy ϵ_{\max} , $\mu \geq \epsilon_{\max}$.

experiment, the atoms are trapped in a three-dimensional harmonic trap for which the condensate fraction N_0/N is given by

$$\frac{N_0(T)}{N} = 1 - \left(\frac{T}{T_c}\right)^3. \quad (2.2)$$

At zero temperature, the gas is completely condensed and all particles occupy the lowest energy state. The many-body wavefunction is then described by a product of identical single-particle wavefunctions $\phi(\mathbf{r}_i)$,

$$\Psi_N(\mathbf{r}_1, \dots, \mathbf{r}_N) = \prod_{i=1}^N \phi(\mathbf{r}_i). \quad (2.3)$$

The condensate can also be described by a macroscopic wavefunction or order parameter [61]

$$\psi(\mathbf{r}) = \sqrt{N} \phi(\mathbf{r}), \quad (2.4)$$

which is identical to the single-particle wavefunction of the state in which the condensate develops, up to normalization. The particle density is $n(\mathbf{r}) = |\psi(\mathbf{r})|^2$. In the case of a harmonic trap, the single-particle ground state wavefunction $\phi(\mathbf{r})$ corresponds to a Gaussian, whereas in a homogeneous optical lattice, it corresponds to a Bloch wave at quasimomentum $\hbar q = 0$.

2.1.2 Weakly Interacting Bose Gas

In an ultracold dilute Bose gas, the mean particle distance is typically on the order of $\langle r \rangle \approx 100 \text{ nm}$ [62]. At these large distances, the electronic clouds of the atoms are well separated and the neutral atoms interact with each other via the van der Waals force [63–65], which originates from the interaction of induced electric dipole moments. The van der Waals potential scales as $V_{\text{vdW}} \propto -r^{-6}$, and has a range on the order of a few nm [62]. While elastic collisions, in which the internal states of the interacting particles remain unchanged, are able to redistribute momentum between particles and are therefore crucial for thermalization processes, inelastic collisions usually lead to atom losses, as the internal energies usually greatly exceed the depth of the external trapping potential. Both processes are described by quantum-mechanical scattering theory. In the following, I will introduce the theoretical description of elastic collisions.

At ultra-low temperatures, only s -wave scattering processes are relevant, as the kinetic energy of the colliding atoms is insufficient to overcome the centrifugal barrier for $l \neq 0$, where l is the orbital quantum number. As both the de Broglie wavelength of the atoms as well as the average atomic distance are much larger than the range of interactions, the actual inter-particle potential plays a minor role. Instead, the potential can be replaced by a simplified version leading to identical scattering properties, the point-like contact interaction

$$V_{\text{int}}(\mathbf{r}) = \frac{4\pi\hbar^2 a_s}{m} \cdot \delta^3(\mathbf{r}) = g \cdot \delta^3(\mathbf{r}). \quad (2.5)$$

Here, $\hbar = h/2\pi$ is Planck's constant, a_s the s -wave scattering length, m the atomic mass, and $g = 4\pi\hbar^2 a_s/m$ the coupling constant. The interaction in an ultracold, dilute atomic gas is described by only a single parameter, a_s . Whether a gas of average particle density \bar{n} can be considered as dilute is determined by the parameter $\bar{n}|a_s|^3$, which is usually smaller than 10^{-3} . In such a case, it is sufficient to consider only binary collisions and the system can be described by a mean-field description that was first introduced by Bogoliubov [66]. In second quantization, the boson field operator $\hat{\psi}(\mathbf{r})$ annihilates a particle at position \mathbf{r} . In the mean-field description, the field operator is split into its expectation value $\psi(\mathbf{r}, t) = \langle \hat{\psi}(\mathbf{r}, t) \rangle$, and a fluctuating field operator $\delta\hat{\psi}(\mathbf{r}, t)$,

$$\hat{\psi}(\mathbf{r}, t) = \psi(\mathbf{r}, t) + \delta\hat{\psi}(\mathbf{r}, t). \quad (2.6)$$

The complex function $\psi(\mathbf{r}, t)$ describes the BEC, while the operator $\delta\hat{\psi}(\mathbf{r}, t)$ describes quantum-mechanical and thermal fluctuations and thereby reflects non-condensed particles. The introduction of the function $\psi(\mathbf{r}, t)$ implicitly assumes spontaneous symmetry breaking in the system, as the wavefunction $\psi(\mathbf{r}, t)$ contains a well-defined phase, whereas the underlying Hamiltonian is invariant under a $U(1)$ gauge transformation.

When the fluctuations are neglected, in second quantization the Gross-Pitaevskii equation (GPE) [67, 68] follows,

$$i\hbar \frac{\partial}{\partial t} \psi(\mathbf{r}, t) = \left(-\frac{\hbar^2 \nabla^2}{2m} + V_{\text{ext}}(\mathbf{r}, t) + g|\psi(\mathbf{r}, t)|^2 \right) \psi(\mathbf{r}, t). \quad (2.7)$$

This has the form of a non-linear Schrödinger equation, where the interatomic interactions are described by a mean-field potential that is proportional to the atomic density $n(\mathbf{r}) = |\psi(\mathbf{r})|^2$. Also for the weakly interacting, dilute Bose gas, the many-body ground state wavefunction is still a product of identical single-particle states as in Eq. 2.3. In contrast to the noninteracting case, however, the weakly interacting gas does not condense into the single-particle ground state, but into a state which is a solution of the GPE.

By neglecting the fluctuations $\delta\hat{\psi}$, one implicitly assumes that all particles occupy the condensate, $N_0 = N$. In the weakly interacting regime $\bar{n}|a_s|^3 \ll 1$, a better description can be found by including the fluctuations to first order. This so-called Bogoliubov theory allows a description of elementary excitations of the condensate via quasi-particles. In this description, interactions lead to a depletion of the condensate mode as also excited modes are populated. This depletion is of order $\sqrt{\bar{n}|a_s|^3}$ and is rather small in typical experiments, about 1 %.

2.1.3 Feshbach Resonances

One great advantage of ultracold atom experiments lies in the tunability of interatomic interactions via Feshbach resonances. These can be understood via the interatomic potentials of the two colliding atoms, where the scattering process leads to an overall phase shift between the incoming and outgoing wave. This phase shift in turn determines the scattering length a_s , which is the only parameter required to describe the properties of

s-wave collisions. In principle, for a typical interatomic potential, a_s can assume any real value, corresponding to repulsive ($a_s > 0$) and attractive ($a_s < 0$) interactions. A Feshbach resonance allows a_s to be tuned by changing a homogeneous magnetic field B .

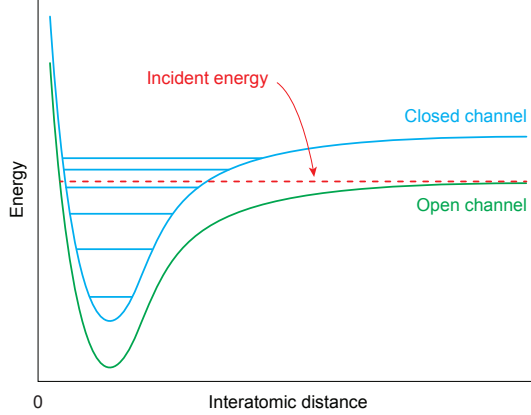


Figure 2.1: Sketch of molecular potential curves contributing to a Feshbach resonance. The energy of the molecular potential curves is plotted versus distance between two atoms. In the closed channel, also the bound states of the molecular potential are indicated as horizontal lines. The incident kinetic energy of the two atoms lies just above the asymptote of the open channel for large distances. When the energy of a bound state of the closed channel matches the incident energy, a Feshbach resonance occurs.

Figure 2.1 illustrates the principle of a Feshbach resonance. A scattering channel is defined by a set of quantum numbers which describe the internal state of the incoming and outgoing particles in the scattering process. Those channels for which the asymptotic energy at large interatomic distances lies below the energy of the two interacting atoms are called open channels. If the atoms are initially prepared in the energetically lowest state all other channels lie above this open channel and are energetically inaccessible; they are therefore called closed channels. In ultracold gases, the kinetic energy is very low, so the kinetic energy lies just above the asymptotic value of the open channel potential curve for large distances.

When a magnetic field B is applied during a scattering process, the total projection $M = m_1 + m_2$ of the spins onto the magnetic field axis is preserved. Although the other channels are energetically inaccessible at large atomic distances, the different atomic states are coupled if they have identical projection numbers M [69]. This coupling is the key for the manipulation of the scattering length via the magnetic field: The various combinations of atomic states with identical quantum number M have different magnetic moments. The relative offset between the different combinations can be shifted by changing the magnetic field because the different magnetic moments lead to different Zeeman shifts. This tuning can be employed to shift the energy of a bound molecular state of a closed channel in resonance with the kinetic energy of the particles. Here, a Feshbach resonance appears where the resulting resonant coupling to the molecular state greatly enhances the scattering length. At the position of the resonance, the scattering length diverges [70–73]. It can be

approximated by [74]

$$a_s(B) = a_{\text{bg}} \left(1 - \frac{w}{B - B_0} \right), \quad (2.8)$$

where a_{bg} is the background scattering length far away from the resonance at $B = B_0$ and w is the width of the resonance.

Feshbach resonances were first observed in ultracold gas experiments in 1998 [19]. Figure 2.2A shows the Feshbach resonance between two ^{39}K atoms in the lowest hyperfine state $|F, m_F\rangle = |1, +1\rangle$ [30]. This resonance was used for the experiments throughout this work to tune the interatomic interactions over a wide range of attractive and repulsive interactions. Figure 2.2B shows the Feshbach resonance between a ^{39}K atom and a ^{87}Rb atom both in their ground state $|1, +1\rangle$ [75]. This resonance was employed during evaporative cooling to enhance thermalization between the two species (Section 2.3.2).

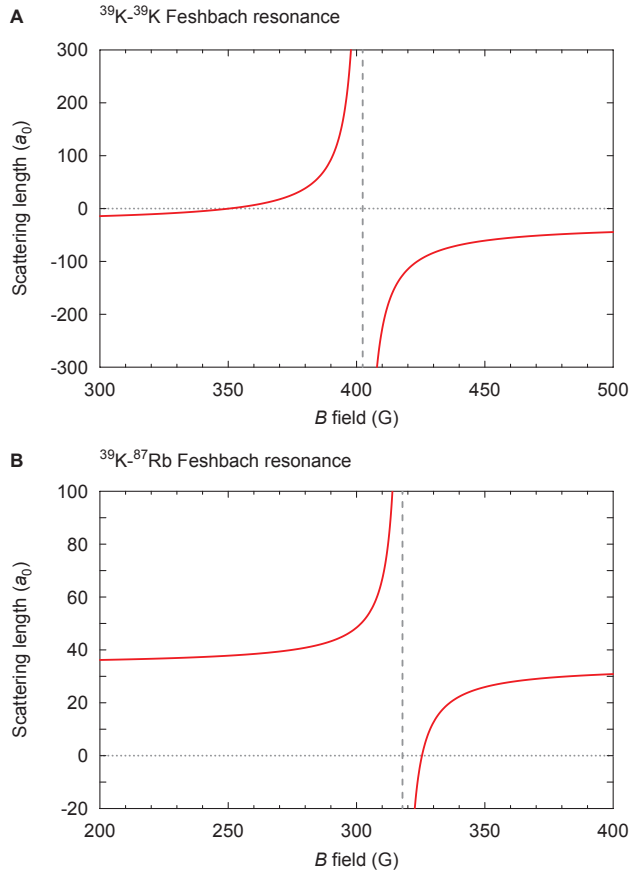


Figure 2.2: Feshbach resonances of alkali atoms that are employed in the experiments described in this work. Plotted is the calculated scattering length versus magnetic field B . The vertical dashed line indicates the position of the resonance, the dotted horizontal line zero scattering length. **A**, Intraspecies Feshbach resonance of two ^{39}K atoms both in the ground state $|F, m_F\rangle = |1, +1\rangle$ with parameters taken from [30]. **B**, Interspecies Feshbach resonance between a ^{39}K and a ^{87}Rb atom both in their ground state $|1, +1\rangle$ with parameters from [75].

2.2 Atom-Light Interactions and Optical Dipole Trap

Lasers are the workhorse in ultracold atoms experiments, for preparation, manipulation, as well as detection of the ultracold samples. The reason lies in the great tunability of the forces and potentials arising from atom-light interactions. Additionally, using dipole traps instead of magnetic traps releases the magnetic field as a degree of freedom which can be used to tune interactions via Feshbach resonances. Interaction of neutral atoms with a light field takes place in two ways – via dissipative and conservative interactions. The relevance of the two types depends on the detuning $\delta = \omega - \omega_0$ of the laser frequency ω from the transition frequency ω_0 of the atom [76].

2.2.1 Optical Dipole Potentials

For optical dipole potentials, the conservative part of the atom-light interaction is employed. In a semiclassical model, it can be described by the interaction of a non-resonant light field with the light-induced dipole moment $\mathbf{d} = \alpha(\omega)\mathbf{E}$ [77] of the atom, where $\alpha(\omega)$ is the complex polarizability of the atom and \mathbf{E} the electric field. This causes a shift in the energy levels of the atom, called the AC Stark shift. The dipole potential results from time-averaging as

$$V_{\text{dip}} = -\frac{1}{2}\langle \mathbf{d} \cdot \mathbf{E} \rangle \propto \text{Re}(\alpha)I, \quad (2.9)$$

which is proportional to the real part of the polarizability and the intensity I of the laser field. For not too large detunings $\delta \ll \omega$, one obtains the dipole potential [77]

$$V_{\text{dip}}(\mathbf{r}) = \frac{3\pi c^2}{2\omega_0^3} \frac{\Gamma}{\delta} I(\mathbf{r}), \quad (2.10)$$

with the speed of light c and the natural linewidth Γ of the atomic transition. In a particle picture, this conservative part of the interaction can also be viewed as a Raman process where an atom virtually absorbs a photon from the laser mode and re-emits it into the laser mode by stimulated emission. This process induces a phase shift on the light and an energy shift in the energy levels of the atom, just as in the semiclassical picture [76].

Scattering of photons by absorption from the laser mode and subsequent spontaneous emission into another mode is described by the scattering rate, which is proportional to the imaginary part of the polarizability, $\Gamma_{\text{sc}} \propto \text{Im}(\alpha)I$. For $\delta \ll \omega$ but not too small detunings $\delta \gg \Gamma$, saturation effects can be neglected and the scattering rate is calculated as

$$\Gamma_{\text{sc}}(\mathbf{r}) = \frac{3\pi c^2}{2\hbar\omega_0^3} \left(\frac{\Gamma}{\delta} \right)^2 I(\mathbf{r}). \quad (2.11)$$

This dissipative part of interactions is used for the initial laser cooling step (Section 2.3.1) and in absorption imaging [49] (Section 3.4). In the case of a conservative dipole potential, however, it is an adverse effect, as the momentum transfer associated with the photon scattering process leads to heating of the atomic cloud.

As the scattering rate scales as I/δ^2 and the dipole potential as I/δ , the ratio of the two scales as

$$\Gamma_{\text{sc}}/V_{\text{dip}} \propto \frac{1}{\delta}. \quad (2.12)$$

To minimize the scattering rate for the required potential depth, it is therefore common to use large detunings and high intensities.

By choosing appropriate intensity distributions $I(\mathbf{r})$, one can engineer a wealth of dipole potentials V_{dip} . The sign of the potential is given by the detuning δ : For a red-detuned light field ($\delta < 0$), the potential is attractive and ground state atoms experience a force towards the region of highest intensity (Fig. 2.3). A blue-detuned laser ($\delta > 0$), on the other hand, creates a repulsive potential where the atoms are pushed away from the high-intensity region. In the experiments of this work, the dipole trap is red-detuned at a wavelength of $\lambda_{\text{dip}} = 1064 \text{ nm}$, while the optical lattice is blue-detuned at a wavelength of $\lambda_{\text{lat}} = 736.65 \text{ nm}$.

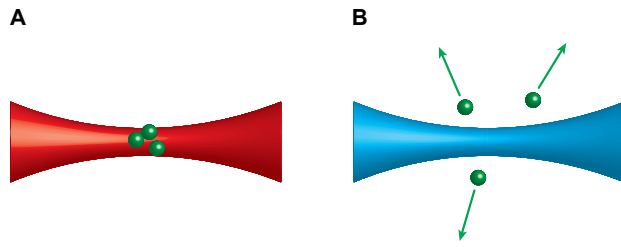


Figure 2.3: Illustration of the effect of optical dipole potentials. **A**, For red-detuned light ($\delta < 0$), the atoms are pulled to the position of highest intensity. **B**, For blue-detuned light ($\delta < 0$), the atoms are pushed away from the region of high intensity.

In case of the lattice laser which is relatively close to the D_1 and D_2 lines of ^{39}K at $\lambda_{D_1} = 770.1 \text{ nm}$ and $\lambda_{D_2} = 766.7 \text{ nm}$ [78], respectively, the fine structure splitting of the excited state needs to be considered. On the other hand, the dipole laser is rather far-detuned from the atomic transitions such that the rotating-wave approximation $\delta \ll \omega$ creates a substantial error. Considering these two corrections leads to a more precise expression for the dipole potential of [77]

$$V_{\text{dip}}(\mathbf{r}) = \frac{\pi c^2}{2\omega_0^3} \Gamma \left(\frac{1}{\omega - \omega_{D_1}} + \frac{1}{\omega + \omega_{D_1}} + \frac{2}{\omega - \omega_{D_2}} + \frac{2}{\omega + \omega_{D_2}} \right) I, \quad (2.13)$$

where ω_{D_1} and ω_{D_2} are the transition frequencies of the two lines over which Γ and ω are averaged.

2.2.2 Crossed Dipole Trap

In the experiment, the dipole trap consists of three Gaussian laser beams which intersect at approximately right angles at the point of their foci². The beam geometry forms an

²The light is created by two single-frequency, diode-pumped Nd:YAG solid-state lasers (Mephisto Mopa by InnoLight, now associated with Coherent) with total powers of 18 W and 28 W, respectively, at a wavelength of $\lambda_{\text{dip}} = 1064 \text{ nm}$.

oblate trap and is shown in Fig. 2.4. While the two beams in the horizontal (xy) plane are strongly elliptical with waists of $w_{1,y} = 280 \mu\text{m}$, $w_{1,z} = 33 \mu\text{m}$, $w_{2,x} = 340 \mu\text{m}$, and $w_{2,z} = 33 \mu\text{m}$, the vertical beam is circular with waists of $w_{3,x} = w_{3,y} = 150 \mu\text{m}$. The waist of the vertical beam is identical to the waists of the optical lattice beams, which allows the overall external potential to be appropriately tuned (Section 3.1.2). To avoid interferences between the beams, the polarizations are mutually orthogonal and the laser frequencies are detuned relative to each other by more than 100 MHz.

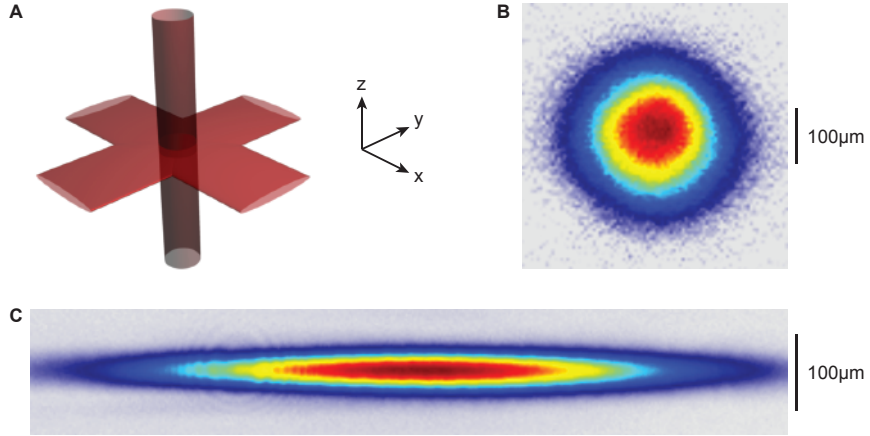


Figure 2.4: Configuration of the crossed dipole trap in the experimental setup. **A**, Illustration of the beam geometry. Two strongly elliptical beams cross in the horizontal plane, providing strong confinement against gravity. A spherical vertical beam allows the trap frequency to be tuned in the horizontal plane, independently of the intensity in the horizontal beams. For clarity, the increase of the waist along the longitudinal direction of the beams is not shown. **B**, Profile of the vertical beam, recorded with a CCD camera. **C**, Profile of the horizontal beam along the x -direction. The colors are scaled differently for the two images.

The trapping potential is given by the sum of all three trapping beams and gravity and is shown in Fig. 2.5A. While the potential is not isotropic for large distances away from the intersection, the small ultracold clouds mainly sample the central region, which can be approximated by a harmonic trapping potential and is in general elliptic. For all measurements presented in this thesis, we circularized the trapping potential by adjusting the relative laser powers of the two horizontal beams. The circular vertical beam also provides a circularly symmetric confinement and can be used as an additional degree of freedom to adjust the horizontal confinement.

The minimum position of the trap in the vertical direction is shifted by gravity (Fig. 2.5B); this shift is called gravitational sag. The magnitude of the sag is smallest for strong dipole potentials. For very weak dipole traps, below the so-called trap bottom, the dipole potential cannot hold the atoms against gravity anymore. The slope of the gravitational gradient and therefore also the gravitational sag depend on the mass of the particles (Fig. 2.5C). This is especially important in the evaporative cooling stage of our experiment (Section 2.3.2), where a good overlap between the ^{39}K and ^{87}Rb clouds in the dipole trap

is required for efficient thermalization between the species. Because of the large detuning of the dipole trap laser and the similar linewidths, the dipole potentials are almost equal for the two species; the atomic masses, on the other hand, differ by more than a factor of two. The large ellipticity of the two horizontal beams in the experiment provides a strong vertical confinement and therefore minimizes the sag for both species, ensuring good overlap and thermalization.

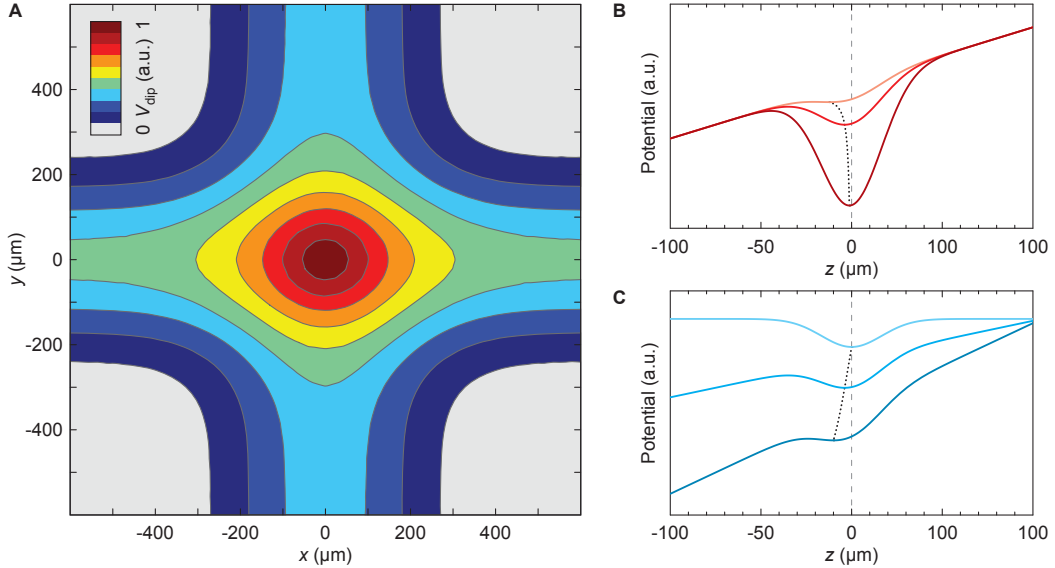


Figure 2.5: Trapping potential of an idealized version of the crossed dipole beam trap. **A**, Isopotential lines in the horizontal plane that crosses the focus of the beam in the vertical direction. In the central area, the potential can be approximated by a harmonic trap. **B**, The trapping potential along the vertical direction for a fixed gravitational potential, for increasing powers of the horizontal dipole beams (from light to dark). The absolute value of the sag, indicated by the dotted curve, can be reduced by increasing the trapping potential in the vertical direction. The vertical dashed line gives the minimum position without sag. **C**, The trapping potential along the vertical direction is plotted for increasing strengths of the gravitational potential gradient (from light to dark), occurring for heavier atomic species. For increasing gravitational potentials, the minimum position of the trap, shown by the dotted curve, shifts to lower positions. The vertical dashed line indicates the minimum position without sag.

2.2.3 Trap Frequencies

The central part of the dipole potential can be approximated by a harmonic trap,

$$V_{\text{dip}} = \frac{m}{2} (\omega_x^2 x^2 + \omega_y^2 y^2 + \omega_z^2 z^2), \quad (2.14)$$

where the three trap frequencies ω_x , ω_y , and ω_z fully parametrize the trap. We measure the trap frequencies by recording oscillations of the center of mass of the atomic cloud (*sloshing*) in the trap via time-of-flight imaging (Section 3.4.2): The real space oscillations are accompanied by oscillations in momentum space, which are translated into large amplitude oscillations of the cloud position after long time-of-flight. We excite the oscillations

by suddenly changing the vertical confinement and thus the gravitational sag. The oscillation along the vertical direction quickly couples to the horizontal directions, leading to harmonic oscillations along all three directions. Figure 2.6 shows sample trap frequency measurements along the x - and z -direction.

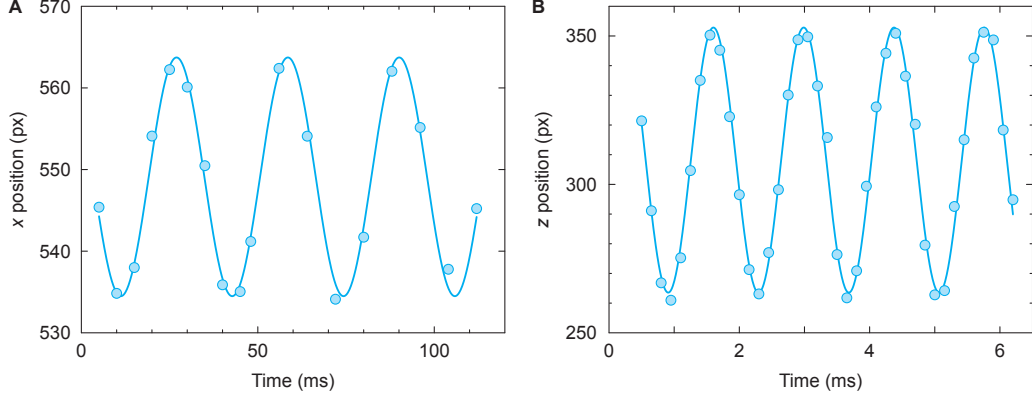


Figure 2.6: Trap frequency measurement. The data points are the center of mass position of the atomic cloud, determined by Gaussian fits after time-of-flight, versus hold time after exciting oscillations. The solid curves are sinusoidal fits, yielding trapping frequencies of **A**, $\omega_x = 2\pi \cdot 31.70(3)$ Hz along the horizontal x -direction and **B**, $\omega_z = 2\pi \cdot 721(3)$ Hz along the vertical z -direction with much stronger confinement.

Figure 2.7 shows the horizontal and vertical trap frequencies for various settings of powers of the dipole trap beams. A power-law fit to both curves yields an exponent of 0.48(2) (horizontal) and 0.46(1) (vertical). As the dipole potential V_{dip} scales linearly with power P (Eq. 2.10), we expect the trap frequencies to scale like $\omega_i \propto \sqrt{P}$ to which the fitted exponents are close. The vertical trap frequency reaches zero already at a non-vanishing dipole beam power P_{bottom} . This offset corresponds to the trap bottom. The trap bottom can be measured directly as the beam power at which the atoms fall out of the trap; such a measurement is more precise than the extrapolation shown in Fig. 2.7B.

From the measurements, we can parametrize the trap frequencies in our experimental setup depending on the dipole beam powers along the horizontal (P_{hor}) and vertical (P_{vert}) directions as

$$\omega_x = \omega_y = \sqrt{\gamma_{\text{hor}} P_{\text{hor}} + \gamma_{\text{vert}} P_{\text{vert}}} \quad (2.15)$$

$$\omega_z = \sqrt{\delta(P_{\text{hor}} - P_{\text{bottom}})}. \quad (2.16)$$

We always fix the ratio of the powers in the two horizontal dipole beams such that the two horizontal trap frequencies are approximately identical.

2.3 Experimental sequence

In this section, I give a short overview of the experimental sequence. The employed cooling techniques are nowadays standard in ultracold atoms experiments and treated in detail in

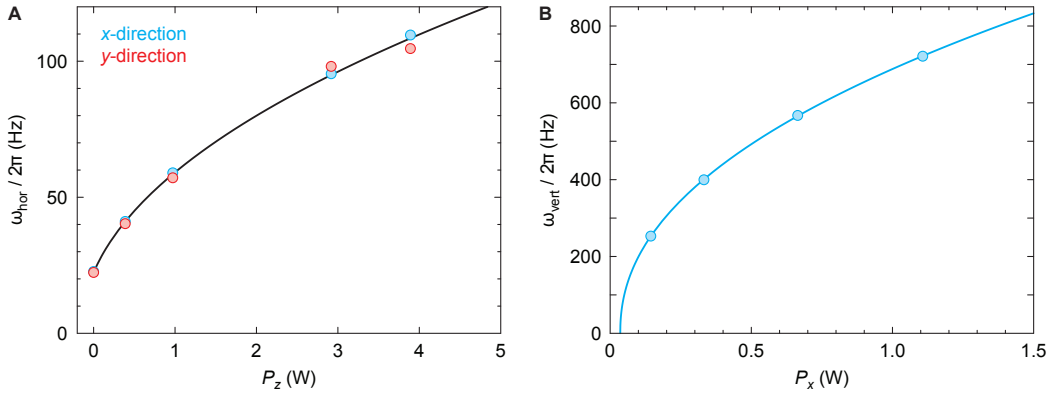


Figure 2.7: Trap frequency versus power in the dipole trap beams. The data points are trap frequencies extracted from sinusoidal fits to oscillation measurements. The solid lines are power-law fits. **A**, Horizontal trap frequencies $\omega_{\text{hor}}/2\pi$ versus power P_z in the vertical dipole beam. The power-law fit $\omega_{\text{hor}}/2\pi = (c + a P_z)^b$ yields an exponent of $b = 0.48(2)$ in agreement with the expected square-root behavior $b = 0.5$. The constant c accounts for the confinement of the horizontal dipole beams. **B**, Vertical trap frequency $\omega_{\text{vert}}/2\pi$ versus power P_x in the dipole beam along the x -direction. The power of the beam along the y -direction is changed proportionally (see main text). The power law fit $\omega_{\text{vert}}/2\pi = a(P_x - P_{\text{bottom}})^b$ yields an exponent $b = 0.46(1)$ that is also close to $b = 0.5$. The offset P_{bottom} from the origin is an extrapolation of the trap bottom (see main text).

books [76] and previous PhD theses of this experimental setup for the case of ^{87}Rb and ^{40}K atoms [79–82], and also for the case of ^{87}Rb and ^{39}K atoms [83]. I will mainly focus on peculiarities of the cycle that are connected to the cooling of bosonic ^{39}K instead of fermionic ^{40}K atoms.

2.3.1 Initial Cooling Sequence

At the beginning of each experimental cycle, we heat one dispenser for each species by running a current through them to increase the respective background pressures in the MOT chamber of the vacuum setup. Additionally, applying ultraviolet light at a wavelength of 365nm to the windows of the vacuum chamber turned out to be helpful in providing atoms by light-induced desorption [84]. A magneto-optical trap (MOT), consisting of one cooling and one repumping beam close to the D2 transition of ^{39}K , cools and loads ^{39}K atoms for around 10 seconds at the center of a quadrupole magnetic field. For the last 1 to 2 seconds of the ^{39}K MOT, a cooling and a repumping beam near the D2 transition of ^{87}Rb are applied additionally, creating a double-species MOT. Loading of the Rb MOT is more efficient than for K, probably because of the larger hyperfine splitting in the $5^P S_{3/2}$ manifold and the larger vapor pressure of Rb [78, 85]. After compressing the quadrupole trap, an optical molasses [76] yields additional cooling. At the end of the molasses phase, we polarize the spins into the $|5^2 S_{1/2}, F = 1, m_F = -1\rangle$ and $|4^2 S_{1/2}, F = 1, m_F = -1\rangle$ states in the case of ^{87}Rb and ^{39}K , respectively. A magnetic quadrupole trap is quickly established, trapping the atoms at the center [86]. The atoms are then transferred within

2 s over an L-shaped path of 40 cm length to the ultra-high vacuum (UHV) glass cell, by appropriately applying currents to a sequence of coil pairs [87]. During this transport, the atoms pass through a differential pumping tube that ensures a differential pressure between the two sections of the vacuum chamber. While effectively loading the MOT at rather high pressures between 10^{-9} and a few 10^{-8} mbar, the pressure in the glass cell can remain below 10^{-11} mbar. The transport scheme is also advantageous in that the MOT optics are separated from the dipole trap and optical lattice optics and therefore the optical access at the glass cell is improved.

2.3.2 Evaporative Cooling

In the glass cell, we perform forced evaporative cooling [88–90] on the Rubidium atoms in the quadrupole trap by driving microwave transitions to the untrapped $|F = 2, m_F = -2\rangle$ state. The potassium cloud is cooled sympathetically as it stays close to thermal equilibrium with the Rubidium cloud. We use Rubidium solely as a coolant for the Potassium atoms, as the experiments described in this thesis are performed with ^{39}K atoms only and as we are able to create much larger numbers of cold Rubidium than Potassium atoms in our experiment. In principle, forced evaporation of ^{87}Rb could also be achieved by driving radio-frequency (RF) transitions to the untrapped $m_F = 0, +1$ Zeeman states of the $F = 1$ manifold. However, as the Zeeman splitting for ^{39}K atoms in the $F = 1$ manifold is identical to that of ^{87}Rb atoms, the RF field would also drive transitions of ^{39}K atoms. These would therefore be evaporated and the final number of remaining Potassium atoms would be strongly reduced. To prevent Majorana losses at the magnetic field zero of the quadrupole trap, we apply a blue-detuned laser beam with a wavelength of $\lambda_p = 760\text{ nm}$ at the center of the trap in the vertical direction, commonly referred to as a plug beam [9, 49]. The small waist of $w_p \approx 30\text{ }\mu\text{m}$ in the horizontal directions provides a strong repulsive potential that prevents atoms from entering the region of low magnetic fields. At the end of the evaporative cooling stage in the quadrupole trap of a duration of 12 s, we typically obtain a few 10^6 ^{87}Rb and around 10^6 ^{39}K atoms at a temperature of around $2\text{ }\mu\text{K}$.

We then transfer the atomic clouds into the crossed dipole trap by increasing the powers in the dipole trap beams. By applying an additional homogeneous magnetic field, the zero point of the quadrupole field is moved along the vertical direction. At the same time, the strong dipole potential holds the atoms in place so that the quantization axis is adiabatically transformed and the atomic spins stay polarized. With the help of an intermediate horizontal homogeneous magnetic field, the field is finally adiabatically transformed into a vertical homogeneous field. In the dipole trap, we transfer both species into their absolute ground state $|F = 1, m_F = +1\rangle$ via a radio-frequency rapid adiabatic passage. Due to the identical Zeeman splitting of both species, the frequency sweep transfers both species simultaneously. We exponentially decrease the power in the dipole trap beams over 2.5 s and thereby further cool the atoms evaporatively. For weak dipole potentials, the high-energy atoms leave the trap in the vertical direction, following gravity. In this regime, predominantly Rubidium atoms are evaporated due to their larger mass. We optimize the

efficiency of sympathetic cooling of the Potassium atoms by increasing the interspecies *s*-wave scattering length during evaporation to $a_{\text{RbK}} \approx 70 a_0$ via the corresponding Feshbach resonance [91, 92] (Section 2.1.3). After all Rubidium atoms have been evaporated away, we directly cool the Potassium atoms for another 1.5 s by decreasing the dipole potential further. In this phase, we employ the intraspecies Feshbach resonance to increase the scattering length to $a_{\text{KK}} > 300 a_0$ (Section 2.1.3). At the end of the evaporation ramp, we typically obtain condensates between a few 10^4 and $1.2 \cdot 10^5$ ^{39}K atoms in the absolute ground state. The fraction of uncondensed atoms is below the detection threshold in time-of-flight images (Section 3.4.2). This condensate is the starting point for the experiments described in this thesis.

3 Ultracold Bosons in Optical Lattices

An optical lattice is a periodic potential in which ultracold atoms can be trapped. The system is a simple model for a crystal in solid state physics, where electrons move in a periodic structure created by immobile ions. It is precisely this similarity that allows to simulate phenomena from solid state physics with ultracold atoms, such as the Mott insulator to superfluid transition [34, 37, 38].

In the first section of this chapter I show how we experimentally realize optical lattice potentials and how the blue-detuned lattice creates a global anti-trapping potential for the atoms. In the second section I discuss single particle states in optical lattices, both in the Bloch basis as well as in the Wannier basis. I also show how we experimentally calibrate the lattice depth and minimize light-assisted collisions. In the third section the Bose-Hubbard model and the Mott to superfluid quantum phase transition as implications of many-body physics in optical lattices are introduced. In the fourth section I present the imaging techniques that we apply to extract information from the atomic clouds. In the fifth section I show our measurements on the Feshbach-induced superfluid to Mott insulator transition. Reviews of optical lattices and corresponding experiments can be found in Refs. [33, 93].

3.1 Experimental Realization of Optical Lattice Potentials

In this section, I describe the experimental implementation of the optical lattice potentials in our setup. Especially, I address the global anti-trapping potential that is created by the blue-detuned laser beams.

3.1.1 Laser Beam Setup

In our experiment, we create the optical lattice potential by superimposing two counter-propagating laser beams. To this end, an incoming laser beam is focused onto the center of

the dipole trap, collimated behind the atoms and retroreflected onto itself¹. The resulting one-dimensional standing wave pattern has a periodicity of $d_{\text{lat}} = \lambda_{\text{lat}}/2$ and creates a dipole potential (Section 2.2.1)

$$V(z) = V_{\text{lat}} \cdot \cos(k_{\text{lat}} z)^2 \quad (3.1)$$

for the atoms, where $k_{\text{lat}} = 2\pi/\lambda_{\text{lat}}$ is the wavenumber of the lattice. Due to interference, the lattice depth is given by $V_{\text{lat}} = 4V_{\text{in}}$, where the potential depth V_{in} of the incoming laser beam is proportional to its intensity. The lattice depth V_{lat} is usually given in units of the recoil energy

$$E_{\text{r}} = \frac{\hbar^2 k_{\text{lat}}^2}{2m}, \quad (3.2)$$

which indicates the change in kinetic energy of an initially resting atom after absorbing or emitting a photon from the laser field. In the experiment, we create standing wave potentials in all three directions by superimposing three pairs of laser beams. All beams are focused at the position of the atoms with waist of $w_0 \approx 150 \mu\text{m}$. We minimize interferences between the three beam pairs by choosing mutually orthogonal polarizations and detuning the frequencies by several tens of MHz [94]. As resulting potential we obtain a three-dimensional simple cubic lattice.

3.1.2 Anti-Trapping Potential

In the case of blue-detuned laser beams as in our experiment, the atoms are trapped at the nodes of the light field. The intensity and therefore also the lattice depth of a pair of Gaussian beams depends on the position within the beams. As the Rayleigh length for our lattice beams of several cm is very large, the lattice depth effectively only depends on the transverse, e.g., x -position in the Gaussian beam profile,

$$V_{\text{lat}}(x) = \tilde{V}_{\text{lat}} e^{-2x^2/w_0^2}, \quad (3.3)$$

where $\tilde{V}_{\text{lat}} > 0$ in the case of blue detuning. The lattice depth in turn influences the ground state energy of single particle states on individual lattice sites. In deep lattices, the on-site potential can be approximated by a harmonic potential, leading to a ground state energy of $E_{\text{gs}}(x) = \hbar\omega_{\text{site}}(x)/2$ with the on-site trap frequency

$$\omega_{\text{site}}(x) = \sqrt{\frac{2V_{\text{lat}}(x)k_{\text{lat}}^2}{m}}. \quad (3.4)$$

The Gaussian-shaped energy shift $E_{\text{gs}}(x)$ is equivalent to a global anti-trapping potential. In the harmonic approximation, the trap frequency of this potential scales as $\omega_{\text{lat}} \propto \sqrt{E_{\text{gs}}(0)} \propto \tilde{V}_{\text{lat}}^{1/4}$ and can be calculated as

$$\omega_{\text{lat}} = i \frac{\sqrt{2}\hbar}{mw_0\lambda_{\text{lat}}} \left(\frac{\tilde{V}_{\text{lat}}}{E_{\text{r}}} \right)^{1/4}. \quad (3.5)$$

¹We use a single-frequency Ti:Sa solid state laser (Coherent MBR) at a wavelength $\lambda_{\text{lat}} = 736.65 \text{ nm}$ with a power of up to 4 W. It is pumped by a diode-pumped, frequency-doubled ND:YVO₄ solid state laser (Coherent Verdi V18) at a wavelength $\lambda = 532 \text{ nm}$ with a power of 18 W.

An anti-trapping potential is formally given by an imaginary trap frequency.

A second, yet much smaller, contribution to the anti-trapping potential originates from the imbalance of the intensities of the two interfering laser beams. As the retroreflected laser beam suffers losses and imperfect reflections, its intensity at the position of the atoms is slightly lower than that of the incoming laser beam. The excess intensity of the incoming beam leads to a global repulsive dipole potential with a trap frequency that scales as $\omega_{\text{lat}2} \propto \sqrt{\tilde{V}_{\text{lat}}}$. Additionally, the intensity imbalance leads to an overall reduction of the lattice depth \tilde{V}_{lat} .

When both the anti-trapping lattice potential and the dipole trap potential are present simultaneously, in harmonic approximation, the dipole potential counteracts the global potential of the lattice. Depending on the strength of the dipole potential, the combined global potential can range from a trapping, over a flat to an anti-trapping potential. This combination therefore offers another degree of freedom in the experimental setup, by allowing to tune the external confinement and the lattice depth independently. We use this feature especially for the measurements of negative temperature states presented in this thesis.

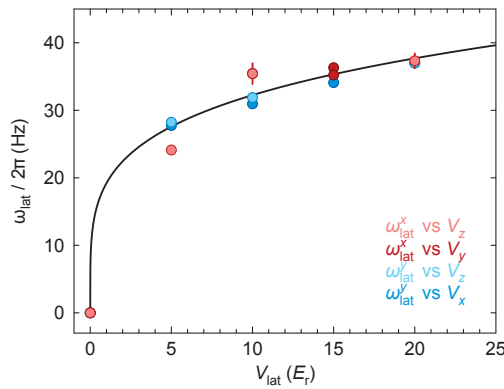


Figure 3.1: Anti-trapping frequencies ω_{lat} of lattice potential in the horizontal plane, extracted from ω_{tot} (see main text), versus lattice depth V_{lat} of orthogonal lattice beams. The solid line is a power-law fit $\omega_{\text{lat}}/2\pi = a V_{\text{lat}}^b$ to all data points simultaneously. The fitted exponent $b = 0.23(3)$ agrees with the theoretically expected exponent $b = 0.25$ (see main text).

By measuring the trap frequency ω_{tot} of the combined potential of dipole trap and one of the three optical lattice axes similarly to the pure dipole trap case (Section 2.2.3), we can extract the anti-trapping contribution of the lattice from

$$\omega_{\text{tot}} = \sqrt{\omega_{\text{dip}}^2 + \omega_{\text{lat}}^2}, \quad (3.6)$$

where ω_{dip} is the trap frequency of the pure dipole trap. From a power-law fit to the resulting anti-trapping frequencies (Fig. 3.1), we can extract an exponent of 0.23(3) which indeed agrees with the expected value of 0.25. The anti-trapping trap frequency ω_{lat}^x along one direction is given by the contributions of both transverse lattice beams, e.g.,

$$\omega_{\text{lat}}^x = \sqrt{\left(\beta_{xy} V_y^{1/4}\right)^2 + \left(\beta_{xz} V_z^{1/4}\right)^2}, \quad (3.7)$$

where V_i is the lattice depth in units of E_r of the lattice beams along the i -direction and where the parameters β_{ij} are determined from trap frequency measurements. In combination with the trap frequency calibration for the dipole trap potential (Section 2.2.3), we obtain a complete calibration of the trap frequencies in our setup in dependence of dipole trap powers and lattice depths.

3.2 Single Particle in an Optical Lattice Potential

In the noninteracting regime, the many-body state of ultracold atoms in an optical lattice can be given in terms of the single particle states when also considering the appropriate quantum statistics of the particles. In this section, I introduce the single particle states in the Bloch as well as the Wannier basis. I also show how we calibrate the lattice depth and minimize light-assisted collisions experimentally.

3.2.1 Bloch Bands

A single particle of mass m in a one-dimensional periodic potential $V_{\text{lat}}(x)$ as given by Eq. 3.1 is described by the Schrödinger equation

$$\hat{H}\phi_q^{(n)}(x) = E_q^{(n)}\phi_q^{(n)}(x) \text{ with } \hat{H} = -\frac{\hbar^2}{2m}\frac{\partial^2}{\partial x^2} + V_{\text{lat}}(x). \quad (3.8)$$

Here, the wavenumber q , corresponding to quasimomentum $\hbar q$, is a quantum number which lies within the first Brillouin zone ranging from $-\hbar k_{\text{lat}}$ to $\hbar k_{\text{lat}}$. The band index n as a second quantum number indicates that for each quasimomentum there is an infinite number of orthogonal solutions. The solutions of this equation are called Bloch waves and are delocalized eigenstates. According to the Bloch theorem, they can be written as a product of a plane wave e^{iqx} and a function $u_q^{(n)}(x)$ that has the same periodicity as the lattice [95],

$$\phi_q^{(n)}(x) = e^{iqx}u_q^{(n)}(x). \quad (3.9)$$

Due to the $2k_{\text{lat}}x$ periodicity, the functions $u_q^{(n)}$ can be written as a discrete Fourier sum

$$u_q^{(n)}(x) = \sum_l c_{q,l}^{(n)} e^{i2lk_{\text{lat}}x}. \quad (3.10)$$

The Bloch waves are then expressed as

$$\phi_q^{(n)}(x) = \sum_l c_{q,l}^{(n)} e^{i(q+2lk_{\text{lat}})x} \quad (3.11)$$

and are therefore given as a superposition of plane waves with wavevectors $q + 2lk_{\text{lat}}$. The $2lk_{\text{lat}}$ are called reciprocal lattice vectors [95]. By inserting the expansion (Eq. 3.11) into the Schrödinger equation (Eq. 3.8), truncating the index l and numerically diagonalizing the resulting matrix [94] one obtains the coefficients $c_{q,l}^{(n)}$ as well as the eigenenergies $E_q^{(n)}$. In Fig. 3.2, the band structure is plotted for various lattice depths.

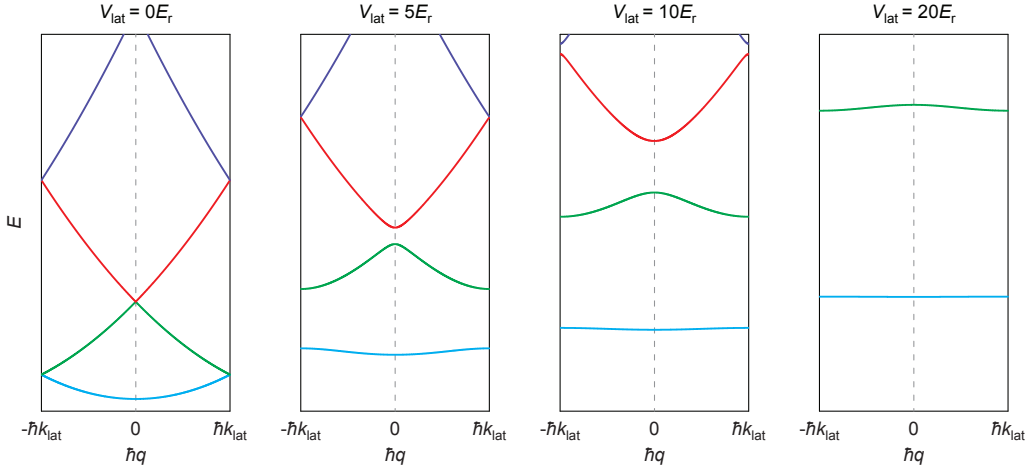


Figure 3.2: Band structure of a one-dimensional sinusoidal optical lattice for various lattice depths. The energy of the Bloch states is plotted versus quasimomentum $\hbar q$ in the reduced zone scheme.

For a vanishing lattice depth, the band structure is identical to the quadratic dispersion relation $E_q = \hbar^2 q^2 / 2m$ of a free particle. For finite lattice depths, band gaps open up, i.e. energy intervals that do not support any states. For larger lattice depths, these band gaps become larger while at the same time the widths of the individual bands decrease approximately exponentially, until the bands become flat in infinitely deep lattices. In this regime, the energies of the bands reach the limit $E^{(n)} = (n + 1/2)\hbar\omega_{\text{site}}$, corresponding to the harmonic approximation of Eq. 3.4. The strong decrease of the kinetic energy, given by the width of the bands, compared to the interaction energy allows to enter the strongly correlated regime even without the use of Feshbach resonances (Section 2.1.3).

In higher-dimensional simple cubic lattices, the dynamics along the individual dimensions are fully separable and the wavefunctions can be calculated separately for each axis. The total energy is given by the sum of the eigenenergies along the individual axes. In a three-dimensional lattice with equal lattice depths along all axes, the band gap between the lowest and the first excited band opens only above a finite lattice depth of $V_{\text{lat}} \approx 2.2 E_r$ [81].

As the relevant physics in the experiments described in this thesis happens in the lowest band, we put experimental emphasis on not populating higher bands. This especially includes, as a general condition for all lattice ramps in this thesis, that the lattice depth is varied only slowly compared to the characteristic timescale set by the band gap between the lowest and the first excited band. For the realization of negative temperature states for motional degrees of freedom, the band gap is a crucial requirement as it provides an upper limit of the kinetic energy, as long as the atoms are confined to the lowest band (Section 4.3.5).

Figure 3.3 shows the Bloch waves for two different quasimomenta in the lowest band. While the wavefunction at $\hbar q = 0$ has an identical phase factor $e^{iqx} = 1$ (cf. Eq. 3.9) at all lattice sites, the function at the edge of the Brillouin zone ($\hbar q = \hbar k_{\text{lat}}$) shows an

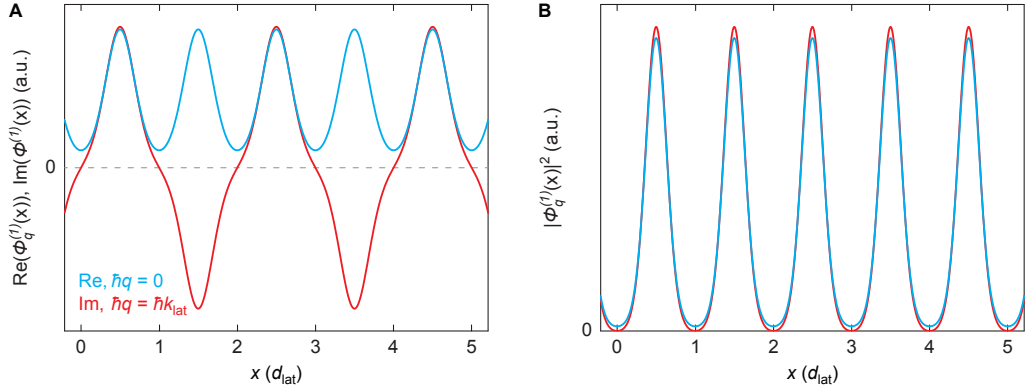


Figure 3.3: Wavefunction of Bloch states $\Phi_q^{(1)}(x)$ in the lowest band of an optical lattice of depth $V_{\text{lat}} = 8 E_r$ for two different quasimomenta at the center ($hq = 0$) and at the edge of the Brillouin zone ($hq = \hbar k_{\text{lat}}$). **A**, The real or imaginary, respectively, part of the wavefunctions illustrates the different phase factors of the two Bloch states. **B**, The probability densities are similar and involve the same lattice periodicity.

alternating phase factor $e^{iqx} = \pm 1$ from lattice site to lattice site. These two wavefunctions are relevant for our measurements of the emergence of coherence (Section 6.4.2).

3.2.2 Wannier Functions

Although the delocalized Bloch wavefunctions form a complete set of orthogonal wavefunctions, it is convenient to introduce an alternative basis, where particles are localized on individual lattice sites. These Wannier functions provide an orthonormal basis that is well-suited to describe short-range interactions between atoms. The Wannier function of a particle located at site i in the n th band is given as the Fourier transform of the Bloch waves

$$w_n(x - x_i) = \frac{1}{\sqrt{N}} \sum_q e^{iqx_i} \phi_q^{(n)}(x). \quad (3.12)$$

While the normalization N is given by the number of lattice sites in a finite system, in an infinite system, the sum is replaced by an integral. Figure 3.4 shows the Wannier functions in the lowest band for two different lattice depths. While for $V_{\text{lat}} = 2 E_r$ the Wannier function extends into neighboring lattice sites, for $V_{\text{lat}} = 10 E_r$ it is localized to a single lattice site. For deep lattices, the Wannier function approaches a Gaussian function, consistent with the harmonic approximation.

The side lobes of the Wannier function lead to a non-vanishing probability to find an atom on a neighboring lattice site. This effect is described by the tunneling matrix element between sites i and j ,

$$J_{ij} = - \int w_1(x - x_i) \left(-\frac{\hbar^2}{2m} \frac{\partial^2}{\partial x^2} + V_{\text{lat}}(x) \right) w_1(x - x_j) dx, \quad (3.13)$$

which only depends on the distances of the lattice sites $|i - j|$.

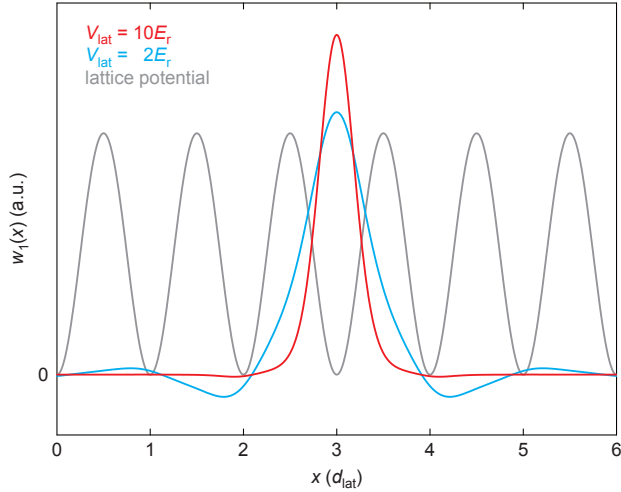


Figure 3.4: Wannier function $w_1(x)$ in the lowest band of an optical lattice for two different lattice depths. For deeper lattices, the Wannier function becomes more localized.

Also interactions between atoms on a single lattice site can be conveniently calculated via the Wannier functions. The interaction matrix element of two bosons in the same Wannier state on the same lattice site that interact via s -wave scattering (Section 2.1.2) in three dimensions is given by

$$U = \frac{4\pi\hbar^2 a}{m} \int |w_1(\mathbf{r})|^4 d\mathbf{r}^3, \quad (3.14)$$

with the scattering length a . As the single particle problem in an optical lattice is separable, the three-dimensional Wannier function is simply the product of the one-dimensional functions along the three lattice axes.

Conversely to the above construction of Wannier functions, every Bloch wave can be constructed from the set of Wannier functions as

$$\phi_q^{(n)}(x) = \frac{1}{\sqrt{N}} \sum_i e^{-iqx_i} w_n(x - x_i), \quad (3.15)$$

where the sum is performed over all lattice sites.

3.2.3 Tight-Binding Limit

For sufficiently deep lattices, the tunneling matrix element J_{ij} for tunneling in the lowest band over distances larger than one lattice can be neglected. This approximation is called tight-binding limit and is reached for lattice depths larger than approximately $5 E_r$ [31]. In this regime, only the tunneling matrix element between neighboring lattice sites $|i - j| = 1$ is relevant and is simply denoted as J . The bandwidth of the lowest band becomes $d \cdot 4J$, with the dimensionality d , and the dispersion relation of the lowest band is simply given by [33]

$$\epsilon_q = -2J \cos \left(\pi \frac{q}{k_{\text{lat}}} \right). \quad (3.16)$$

The decrease of the bandwidth for smaller values of J can also be understood in the framework of the effective mass m^* : For deeper lattices, the atoms become more localized on lattice sites, leading to a flattening of the dispersion. At the same time, a decreasing value of J leads to a reduced mobility of particles in the lattice. The mobility of the particles is governed by the effective mass of the particles, which is inversely proportional to the curvature of the band,

$$m^*(q) = \frac{\hbar^2}{\partial^2 \epsilon_q / \partial q^2}. \quad (3.17)$$

In the case of $q = 0$ in the tight-binding approximation, one obtains an effective mass that increases with decreasing tunnel coupling,

$$m^*(q = 0) = \frac{\hbar^2}{2Jd_{\text{lat}}^2}. \quad (3.18)$$

The tunneling time is defined as

$$\tau = \frac{\hbar}{J} \quad (3.19)$$

and is a measure for the timescale on which the atoms move in the lattice. The corresponding group velocity of the atoms is given by [93]

$$v_g = \frac{1}{\hbar} \frac{\partial \epsilon_q}{\partial q} = \frac{2d_{\text{lat}}}{\tau} \sin\left(\pi \frac{q}{k_{\text{lat}}}\right). \quad (3.20)$$

and is limited to the range of $-2d_{\text{lat}}/\tau \leq v_g \leq 2d_{\text{lat}}/\tau$. In contrast to free space, the group velocity does not monotonically increase with quasimomentum, but reaches its maximum values (in both directions) at wavenumbers $q = \pm k_{\text{lat}}/2$. At $q = 0$ as well as at the edges $q = \pm k_{\text{lat}}$ of the Brillouin zone, the group velocity vanishes.

3.2.4 Lattice Depth Calibration

The lattice depth can be calibrated by various methods that each have advantages and disadvantages in certain lattice depth regimes. In our experiment, we use two different procedures - lattice diffraction for shallow lattices and frequency modulation spectroscopy for deep lattices.

Lattice Diffraction

In this method, we extract the lattice depth from the diffraction of a coherent matter wave at the optical lattice potential. After preparing a condensate at zero momentum $|\psi(t=0)\rangle = |q_0 = 0\rangle$, we pulse the lattice for variable times τ on the order of tens of μs . Switching on the lattice potential suddenly leads to a projection of the plane wave of the condensate into the Bloch basis of the lattice. Because of the symmetry of the $|q_0 = 0\rangle$ state, only Bloch states $|n, q_0 = 0\rangle$ with odd band indices n contribute. While strong lattices allow transitions into several bands, for small lattice powers, the superposition

consists mainly of the Bloch states in the first and third band and higher bands can be neglected [79]:

$$|\psi(t=0)\rangle = c_1|n=1, q_0\rangle + c_3|n=3, q_0\rangle \quad (3.21)$$

Here, c_i are the corresponding coefficients. The time evolution of the state is given by the evolution of the phases of these two states according to their energies

$$|\psi(t)\rangle = c_1 e^{-i\epsilon_{q_0}^{(n=1)}t/\hbar}|n=1, q_0\rangle + c_3 e^{-i\epsilon_{q_0}^{(n=3)}t/\hbar}|n=3, q_0\rangle. \quad (3.22)$$

When the lattice is turned off after a time τ , the resulting state $|\psi(\tau)\rangle$ is projected back into the plane wave basis $|q_0 + 2k_{\text{lat}}\mu\rangle$, where μ is an integer. The amplitudes of the individual plane wave states are

$$\langle q_0 + 2k_{\text{lat}}\mu | \psi(\tau) \rangle = c_1^{(\mu)*} c_1 e^{-i\epsilon_{q_0}^{(n=1)}\tau/\hbar} + c_3^{(\mu)*} c_3 e^{-i\epsilon_{q_0}^{(n=3)}\tau/\hbar}. \quad (3.23)$$

Because of the weak lattice potential, only the components $\mu = 0$ and $\mu = \pm 1$ have significant contributions. Due to interference between the two terms, the probability $|\langle q_0 + 2k_{\text{lat}}\mu | \psi(\tau) \rangle|^2$ of finding an atom in any one of the plane wave states oscillates with the pulse time τ at a frequency $\nu = (\epsilon_3 - \epsilon_1)/\hbar$.

After the lattice pulse, we switch off all potentials and perform time-of-flight absorption imaging (Section 3.4.2). By counting the number of atoms in the different momentum states, we can observe this oscillation and measure the corresponding frequency (Fig. 3.5). By comparing the frequency to the results of a numerical band structure calculation, we can extract the lattice depth. For deeper lattices, also higher bands and plane wave states with higher momenta $|\mu| \geq 2$ contribute significantly. The probabilities therefore oscillate between several μ states and the resulting signal is more complicated than a pure sinusoidal signal as in the above case. While being more involved, one could in principle still extract the lattice depth from this signal. Instead, we apply a different method which is particularly suited to calibrate deep lattices.

Frequency Modulation Spectroscopy

In this method, we calibrate the lattice depth via a spectroscopic measurement of the transition frequency from the lowest band to the first excited band. We load a condensate of ^{39}K atoms into a one-dimensional optical lattice and parametrically excite [96] the atoms by modulating the frequency of the lattice beam with an amplitude of a few MHz and variable frequency. The frequency modulation translates into a modulation of the position of the potential minima. Under this lattice shaking, the parity of the wavefunction is not conserved anymore such that transitions between even and odd wavefunctions, such as between the lowest and the first excited band, are possible. When the modulation frequency ν_{mod} is resonant with the transition between the two bands, $h\nu_{\text{mod}} = E_q^2 - E_q^1$, atoms are excited. We measure the number of excited atoms by time-of-flight imaging including a band-mapping technique (Section 3.4.4). Figure 3.6 shows the measurement of a typical resulting peak, located at the transition frequency between the two bands. The peak is

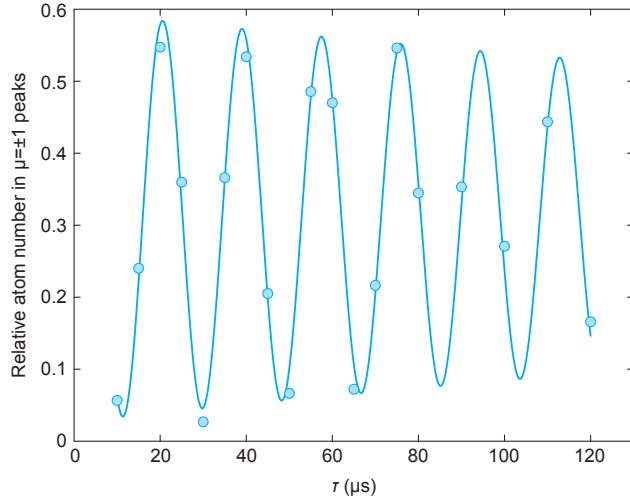


Figure 3.5: Lattice depth calibration measurement via lattice diffraction (see main text). The fraction of atoms in the $\mu = \pm 1$ peaks is determined via area sums in time-of-flight images and is plotted versus pulse time τ of the optical lattice pulse. The solid line shows a sinusoidal fit including exponential decay. Comparing the fitted frequency of $\nu = 54.2(2)$ kHz to a numerical calculation yields a lattice depth of $V_{\text{lat}} = 6.13(5) E_r$.

broadened by the finite bandwidths at the given lattice depth. As this effect is stronger for small lattice depths, this method is particularly suited for deep lattices. The extension of the cloud in the inhomogeneous lattice beam profile leads to an additional broadening. By comparing the extracted frequency with a numerical band structure calculation, we extract the depth of the optical lattice.

3.2.5 Light-Assisted Collisions

In the presence of a strong light field such as that of an optical lattice, atoms can scatter photons, leading to heating and losses of atoms from the trap. Additionally, when two or more atoms are located at the same lattice site, the atoms can undergo light-assisted collisions. In this process, two atoms on the same lattice site collide while one of the two atoms absorbs a photon during the collision. This process leads to the transfer of the atoms into an excited state molecular potential, as illustrated in Fig. 3.7. In the case of red-detuned laser light, an atom can only be excited if the photon energy is resonant with a bound state in an excited state potential. Such a bound state molecule decays over time and simultaneously releases a large amount of energy which ultimately leads to the loss of the two atoms from the trap. This loss channel can effectively be minimized by tuning the wavelength of the laser in between two bound states. For blue-detuned lasers, however, the atoms are excited above the atomic threshold where the molecular potentials are repulsive and provide unbound quantum states for any photon energy. The repulsive potential quickly accelerates the atoms away from each other before the excited atom decays into the ground state again via spontaneous emission of a photon. The increase in

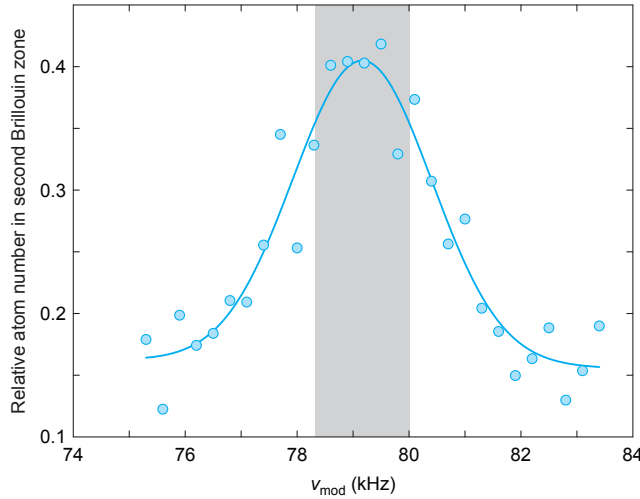


Figure 3.6: Lattice depth calibration measurement via frequency modulation spectroscopy (see main text). The relative atom number in the second Brillouin zone, determined via area sums in time-of-flight images using band-mapping, is plotted versus the frequency of the optical lattice frequency modulation. By comparing the fitted center frequency of $\nu_{\text{mod}} = 79.17(9)$ kHz to a numerical calculation, one obtains a lattice depth of $V_{\text{lat}} = 22.36(5) E_r$. The gray shaded area indicates the combined bandwidths of the lowest and the first excited band.

kinetic energy usually leads to the loss of the atom pair from the trap. In contrast to the red-detuned case, light-assisted collisions cannot effectively be suppressed for blue-detuned light because the unbound states form a continuum. Therefore, two or more atoms on a single lattice site always experience this additional loss channel.

By choosing the correct detuning, light-assisted collisions can still be minimized also for blue-detuned lattices. The probability for this process is determined by the Franck-Condon factor, which gives the overlap between the nuclear wavefunctions Ψ_g and Ψ_e of the ground state and the excited state, respectively:

$$FC = \left| \int \Psi_e^*(R) \Psi_g(R) dR \right|^2 \quad (3.24)$$

Here, R is the internuclear distance. The strongest contribution to the integral is typically located around the Condon point R_C , i.e. the distance at which the difference in potential energies matches the energy of a photon [97]. For different photon energies, different excited states are addressed with wavefunctions $\Psi_e(R)$ that are shifted relative to each other. As both wavefunctions $\Psi_g(R)$ and $\Psi_e(R)$ exhibit strong oscillations with distance R , the Franck-Condon factor strongly depends on the photon energy and, in fact, also oscillates. The atom losses in a blue-detuned light field therefore crucially depend on the precise laser wavelength.

To measure the losses, we load a BEC of ^{39}K atoms into a combined potential of dipole trap and a deep blue-detuned optical lattice with high filling. While the lattice light is present, two atoms on a single site can be lost due to light-assisted collisions. After

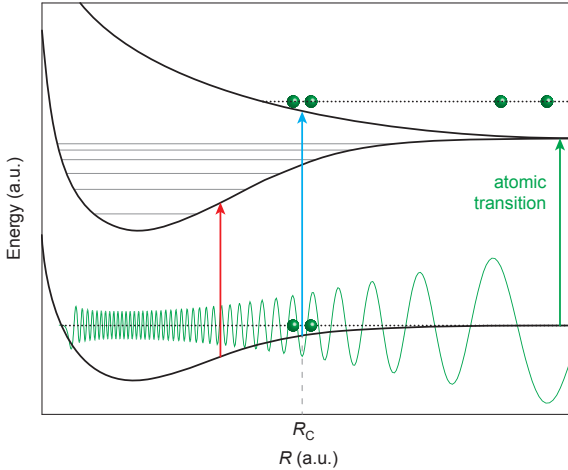


Figure 3.7: Illustration of light-assisted collisions. The energy of the diatomic molecular potential curves is plotted versus internuclear separation R . During a collision process, one atom can absorb a photon from a laser beam and thereby the pair of atoms is excited to an excited molecular potential curve. For red-detuned light with respect to the atomic transition, the photon energy has to match a bound molecular state, shown as horizontal gray lines. In contrast, for blue-detuned light, the excited scattering states form a continuum and thereby allow a transition for any laser frequency. The initial and final energies of the atom pair are indicated by the horizontal dotted lines. As the photon momentum is small compared to the momenta of the nuclei, the kinetic energy of the atoms does not change during the absorption process. The transition happens around the Condon point R_C (see main text). The green curve exemplifies the wavefunction of the ground state molecule.

this sequence, we count the number of remaining atoms in time-of-flight images (Section 3.4.2). We repeat this measurement for different lattice wavelengths λ_{lat} . The result (Fig. 3.8) shows a clear oscillation versus λ_{lat} . Additionally to this oscillatory behavior, the scattering rate Γ_{sc} scales with the detuning δ_{lat} as $\Gamma_{\text{sc}} \propto 1/\delta_{\text{lat}}^2$ (Section 2.2.1) and therefore the detuning should be as large as possible, given the available laser power. We choose a wavelength of $\lambda_{\text{lat}} = 736.65 \text{ nm}$ where both scattering and light-assisted collisions are minimized. More details about light-assisted collisions and the relevant molecular potential curves and wavefunctions, with emphasis on ^{40}K but with the same underlying principles, can be found in [81, 98, 99].

3.3 Many Particles in an Optical Lattice Potential

After discussing the single particle physics of individual atoms in a homogeneous lattice, this section deals with the many-body problem. I also incorporate the external trapping potential, thereby describing the realistic situation for the experiments in this thesis.

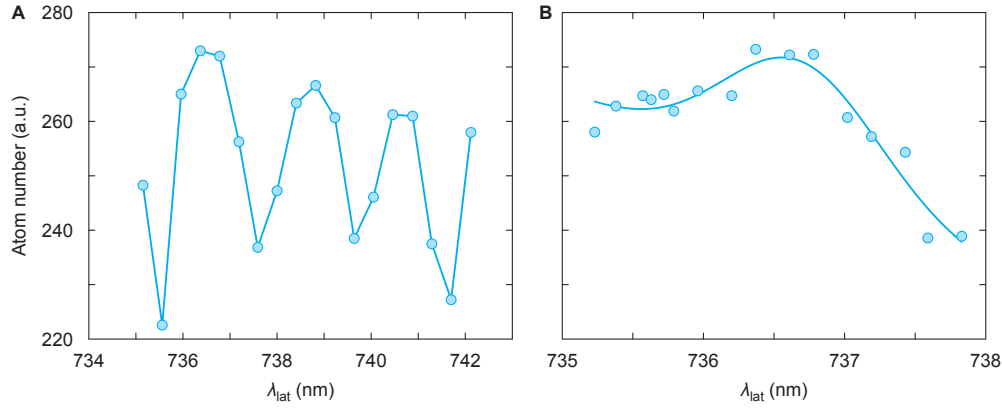


Figure 3.8: Minimizing light-assisted collisions. The total atom number, determined via area sums in time-of-flight images, after holding the atoms in an optical lattice is plotted versus lattice wavelength λ_{lat} . **A**, The oscillatory behavior is due to the Franck-Condon factor. The solid line guides the eye. **B**, A fine scan allows to determine the precise position of one of the minima of light-assisted collisions via a Gaussian fit (solid curve) at $\lambda_{\text{lat}} = 736.65(9)$ nm.

3.3.1 Wavefunction of a BEC in an Optical Lattice

If the tunnel coupling J is large compared to the interaction energy U of two atoms on the same site, the atoms are in the weakly interacting regime. Here, also in the presence of a three-dimensional lattice, the many-body ground state of bosons is a BEC. As outlined in Section 2.1.2, in the mean-field approximation, the macroscopic wavefunction of the condensate is described by the Gross-Pitaevskii equation. If the chemical potential μ is small compared to the lattice depth, the macroscopic wavefunction can be written as a sum of localized wavefunctions [100]

$$\psi(\mathbf{r}) = \sum_j \psi_j w(\mathbf{r} - \mathbf{r}_j) \text{ with } \psi_j = \sqrt{\bar{n}_j} e^{i\phi_j}. \quad (3.25)$$

The phases ϕ_j of the wavefunctions are well-defined in this regime, and the amplitude $\sqrt{\bar{n}_j}$ is given by the average particle number \bar{n}_j on the lattice site j , which here is assumed to be large, $\bar{n}_j \gg 1$. In higher dimensions, the index j is a vector. If the chemical potential does not exceed the lowest band gap, the localized wavefunctions $w(\mathbf{r} - \mathbf{r}_j)$ are given by the Wannier functions in the lowest band, $w_1(\mathbf{r} - \mathbf{r}_j)$. The system then follows a discretized version of the Gross-Pitaevskii equation with a Hamiltonian [100]

$$\hat{H} = -J \sum_{\langle i,j \rangle} \psi_i^* \psi_j + \sum_j V_j |\psi_j|^2 + \sum_j \frac{U}{2} |\psi_j|^4. \quad (3.26)$$

The first term corresponds to the kinetic energy with the tunneling matrix element from Eq. 3.13, where the summation includes all neighboring lattice sites $\langle i,j \rangle$. The second term gives the potential energy, where the energy offset V_j of a site is given by the slowly varying external harmonic potential $V_j = \int V_{\text{ext}}(\mathbf{r}) |w_1(\mathbf{r} - \mathbf{r}_i)|^2 d\mathbf{r}^3 \approx V_{\text{ext}}(\mathbf{r}_j)$. The third term describes the on-site interaction between atoms on the same lattice site with the

interaction matrix element from Eq. 3.14. This Hamiltonian is a special case of the more general Bose-Hubbard Hamiltonian (Eq. 3.35) for a macroscopic wavefunction.

The ground state wavefunction of a weakly interacting BEC in an optical lattice without external trap is given by the Bloch wave with quasimomentum $\hbar q = 0$. A comparison with the Bloch wave expression of Eq. 3.15 shows that the phases of the condensate wavefunctions on individual lattice sites are all equal, $\phi_j = 0$. Therefore, also in the inhomogeneous lattice, the ground state is characterized by a uniform phase. For a stationary state, the individual phases also have to evolve at the same rate. As the phase evolution is given by the term $e^{i\mu_j t/\hbar}$, this requires that the chemical potential μ_j is constant across the lattice.

Under the assumption that the interaction energy $\bar{n}_j U$ per atom is large compared to the tunnel coupling J , the kinetic energy term in the Hamiltonian can be neglected. In the case of shallow optical lattices, this so-called Thomas-Fermi approximation requires large occupation numbers \bar{n}_j on lattice sites. This approximation does not correspond to a transition into the Mott insulating regime, as J is still assumed to be large compared to the interaction U between two atoms. As the requirement of large occupation numbers is not always fulfilled experimentally, the results of this calculation should be considered rather qualitative for the real experimental situation. In the Thomas-Fermi approximation, the energy on a lattice site is given by

$$E_j \approx V_j |\psi_j|^2 + \frac{U}{2} |\psi_j|^4 = V_j \bar{n}_j + \frac{U}{2} \bar{n}_j^2 \quad (3.27)$$

and the chemical potential therefore reads

$$\mu_j = \frac{\partial E_j}{\partial \bar{n}_j} = V_j + U \bar{n}_j \equiv \mu = \text{const.} \quad (3.28)$$

An illustration of the chemical potential is shown in Fig. 3.9A.

In the case of a small lattice spacing d_{lat} compared to the extension of the cloud, the occupation numbers \bar{n}_j can be approximated by a continuous distribution $\bar{n}(\mathbf{r})$ with the particle density given by $\bar{n}(\mathbf{r})/d_{\text{lat}}^3$. For a harmonic confinement with an aspect ratio $\gamma = \omega_z/\omega_x = \omega_z/\omega_y$, one can define an effective distance [79]

$$\rho^2 = x_j^2 + y_j^2 + \gamma^2 z_j^2, \quad (3.29)$$

such that the potential is expressed as

$$V_{\text{ext}}(\rho) = \frac{m}{2} \omega_x^2 \rho^2. \quad (3.30)$$

The chemical potential μ is fixed by the total atom number

$$N = \int \frac{\bar{n}(\mathbf{r})}{d_{\text{lat}}^3} d\mathbf{r}^3. \quad (3.31)$$

The requirement of a constant chemical potential in Eq. 3.28 directly leads to the density distribution of the atoms

$$\bar{n}(\rho) = \max \left(\frac{\mu - \frac{m}{2} \omega_x^2 \rho^2}{U}, 0 \right) \quad (3.32)$$

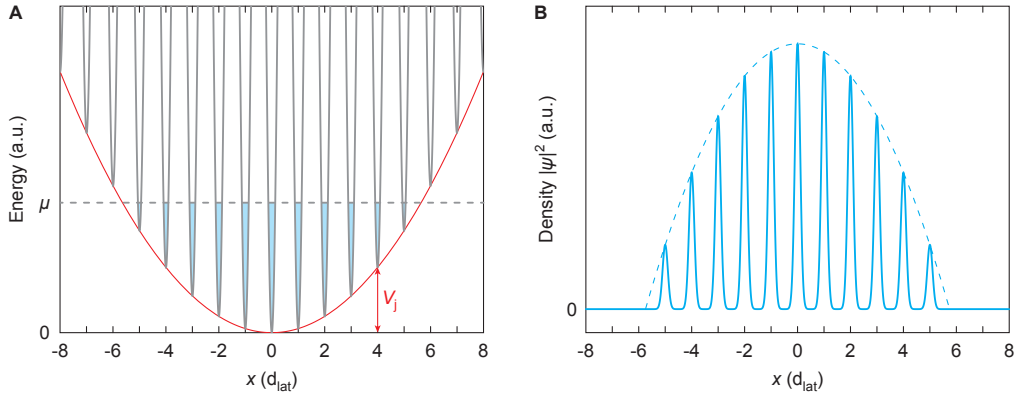


Figure 3.9: Macroscopic wavefunction in an inhomogeneous optical lattice. **A**, In the inhomogeneous case, the external trapping potential (red curve) creates an energy offset V_j for each lattice site. The chemical potential μ_j can be approximated as the sum of V_j and the interaction energy per atom. In the stationary state, it has to be constant across the lattice, $\mu_j = \mu$. **B**, The previous requirement results in an atomic density profile (solid curve) that is enveloped by a Thomas-Fermi parabola (dashed curve).

which exhibits the typical Thomas-Fermi parabola (Fig. 3.9B). The Thomas-Fermi radius is given by

$$\rho_{\text{TF}} = \sqrt{\frac{2\mu}{m\omega_x^2}} \quad (3.33)$$

and the chemical potential can be calculated as [94]

$$\mu = \left(\frac{15d_{\text{lat}}^3 m^{3/2} N U \gamma \omega_x^3}{16\sqrt{2}\pi} \right)^{2/5}. \quad (3.34)$$

3.3.2 Bose-Hubbard Model

The description of a BEC in an optical lattice as a macroscopic wavefunction like in the previous section is only valid for shallow lattices. For deeper lattices, correlations between atoms increase and may lead to a loss of the wave properties of the system. For large interactions U compared to the tunneling J , the particles undergo a quantum phase transition into a state of isolated localized particles, the Mott insulator [31, 32] which was first observed by M. Greiner et al. [34] for ultracold atoms.

In second quantization, the Hamiltonian of interacting bosons in the presence of a periodic potential is conveniently written in the Wannier basis. For small energies, it is sufficient to consider only Wannier functions in the lowest band. Additionally, one makes the approximation of the tight-binding limit (Section 3.2.3) as well as of a contact interaction potential (Section 2.1.2) for s -wave interactions where only interactions between atoms on the same lattice site are relevant. These assumptions lead to the Bose-Hubbard Hamiltonian:

$$\hat{H} = -J \sum_{\langle i,j \rangle} \hat{a}_i^\dagger \hat{a}_j + \frac{U}{2} \sum_i \hat{n}_i (\hat{n}_i - 1) + \sum_i (V_i - \mu) \hat{n}_i \quad (3.35)$$

The operators \hat{a}_i^\dagger and \hat{a}_i create and annihilate, respectively, a boson in a Wannier state on lattice site i , and $\hat{n}_i = \hat{a}_i^\dagger \hat{a}_i$ is the number operator for bosons on site i . The chemical potential μ is introduced to fix the atom number in a grand-canonical ensemble. The other parameters are identical to Eq. 3.26. The Hamiltonian consists of three terms, kinetic, interaction, and potential energy (cf. Eq. 3.26).

3.3.3 Superfluid and Mott Insulator Phase

The Bose-Hubbard model exhibits a prime example of a genuine quantum phase transition that is driven by quantum fluctuations. This transition connects the superfluid and the Mott insulating phases. The fundamental properties of these phases can already be understood in a homogeneous lattice system, where the energy offset between lattice sites vanishes, $V_i = 0$, and are outlined in the following.

If the tunnel coupling J is much larger than the interaction U , the many-body ground state ψ_{SF} is given by a condensate in the Bloch state $|n = 1, q = 0\rangle$ (Section 3.3.1) where each of N particles is delocalized over all M lattice sites,

$$|\psi_{\text{SF}}\rangle(U/J \approx 0) = \left(\frac{1}{\sqrt{M}} \sum_{j=1}^M \hat{a}_j^\dagger \right)^N |0\rangle. \quad (3.36)$$

In the limit of large N and M , the state can be approximated by a product of coherent states on individual lattice sites [33],

$$|\psi_{\text{SF}}\rangle \approx \prod_{j=1}^M |\alpha_j\rangle, \quad (3.37)$$

which are eigenstates of the annihilation operator,

$$\hat{a}_j |\alpha_j\rangle = \alpha_j |\alpha_j\rangle. \quad (3.38)$$

The amplitudes $\alpha_j = \sqrt{\bar{n}_j} e^{i\phi_j}$ are determined by the average occupation number $\bar{n}_j = \bar{n} = N/M$ and the phase ϕ_j and define the condensate wavefunction on the lattice sites (cf. Eq. 3.25). The phases ϕ_j are well-defined on each lattice site, establishing phase coherence in the ground state, and the system is superfluid. Expressed in the Fock basis, these coherent states are a superposition of the Fock states $|n\rangle_j$ [101],

$$|\alpha_j\rangle = e^{-|\alpha_j|^2/2} \sum_{n=0}^{\infty} \frac{\alpha_j^n}{\sqrt{n!}} |n\rangle_j. \quad (3.39)$$

The occupation of the individual Fock states follows a Poissonian statistics with variance $\sigma^2 = \bar{n}$.

In the case where U is much larger than J , atom number fluctuations on individual lattice sites are energetically costly and are strongly suppressed. Instead, if the filling in the homogeneous case is commensurate, $\bar{n} \in \mathbb{N}$, the atoms are localized to individual lattice

sites and the ground state is the Mott insulator. This state is described by a product of Fock states with exactly \bar{n} atoms per lattice site,

$$|\psi_{\text{MI}}\rangle(J/U \approx 0) = \prod_j \frac{1}{\bar{n}!} \left(\hat{a}_j^\dagger \right)^{\bar{n}} |0\rangle. \quad (3.40)$$

In this regime, the atom number per site is well-defined, but the phase of the matter wave is maximally uncertain. In contrast to the superfluid regime, the expectation value of the annihilation operator on individual lattice sites equals zero and phase coherence has vanished. In the homogeneous case where the filling is not commensurate, the ground state is a superfluid.

When the ratio U/J is increased, at a critical value $(U/J)_c$, the system will undergo a quantum phase transition from the superfluid to the Mott insulator state in the commensurate case. This phase transition is driven by quantum fluctuations [57] and therefore also occurs at zero temperature when thermal fluctuations are frozen out. The critical value depends on both dimensionality of the system as well as on the filling \bar{n} . In the case of $\bar{n} = 1$, quantum Monte-Carlo and density-matrix renormalization group calculations provided the values $(U/J)_c \approx 3.3$ [102–104] in 1D, $(U/J)_c = 16.7$ [105] in 2D, and 29.3 [106] in 3D.

The inhomogeneous system, if the external potential varies slowly enough, can be approximated by a series of homogeneous systems with locally varying chemical potential

$$\mu_i = \mu - V_i. \quad (3.41)$$

In this local density approximation, all local quantities such as filling n_i are approximated by the respective quantities of the homogeneous system,

$$n_i = n(\mu - V_i, T). \quad (3.42)$$

The chemical potential μ in the center of the trap is still adjusted to obtain the correct atom number in the grand canonical ensemble.

Figure 3.10A qualitatively shows the phase diagram of the 2D Bose-Hubbard model [107–109]. The ground state depends on both the value J/U as well as on the chemical potential μ_i . An inhomogeneous system samples a range of chemical potentials from a maximum value in the center of the trap to $\mu_i = 0$ at the border of the cloud, indicated by the vertical line. For large J/U values, the system is superfluid at every point in the trap. In contrast, for small J/U , the system alternates between Mott insulating and superfluid phases. The corresponding profile of the 2D cloud in Fig. 3.10B shows the characteristic structure of Mott insulating shells with superfluid shells in between. This wedding cake structure has also been observed in experiments [47, 110, 111].

When the critical point is crossed, the excitation spectrum in the system changes, which is an essential feature of a quantum phase transition. In the superfluid regime, the lowest excitations are Bogoliubov excitations which exhibit a gapless spectrum. These excitations correspond to phase differences between lattice sites and may have arbitrarily small

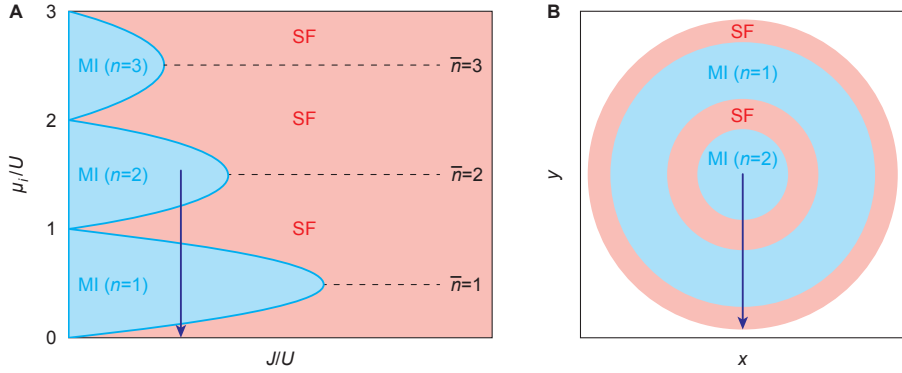


Figure 3.10: Mott insulator (MI) and superfluid (SF) phases in an inhomogeneous system. **A**, Schematic phase diagram of chemical potential μ_i versus J/U in 2D or 3D. Along the horizontal dashed lines, the density is integer-valued in the superfluid regime. The arrow exemplary indicates the range of μ_i that is present in a trapped system, with the largest μ_i at the center of the cloud and $\mu_i = 0$ at the border. **B**, Visualization of the corresponding shell structure in a 2D system.

energies. Additionally, there are also purely gapped excitations of a different kind in the superfluid regime. These originate from the Higgs amplitude mode and correspond to collective superfluid density variations in the system [112]. When the Mott insulating regime is entered, a gap Δ in the spectrum opens up which is responsible for the insulating properties of the state. In this regime, excitations correspond to the creation of particle-hole pairs, where a particle is an extra particle on a lattice site on top of the Mott insulator, and a hole a reduction of the Mott insulator by one particle. The gap depends on the value J/U and the filling n of the Mott insulator and can be extracted from the phase diagram. It is given by the difference of chemical potentials at the upper and lower edge of the corresponding Mott lobe. In the deep Mott insulating regime, $J/U \ll 1$, it simply equals the interaction energy, $\Delta = U$: For any n , creating a particle-hole pair requires a particle to hop on an already occupied lattice site, at the cost of the interaction energy U .

3.4 Absorption Imaging

To extract information about the atomic ensembles in the experiments described in this thesis, we always use standard absorption imaging. This can be applied either to *in situ* clouds, or alternatively to clouds that have expanded after some time-of-flight (TOF).

In absorption imaging, a near-resonant laser beam is directed onto the atoms which absorb a fraction of the intensity. The resulting intensity profile $I(x, y)$ of the beam is imaged onto a CCD camera. Additionally, an image of the reference intensity distribution $I_0(x, y)$ without atoms is taken. Combining both images, the optical density $D(x, y)$ of the atomic cloud can be determined from the Lambert-Beer absorption law,

$$I(x, y) = I_0(x, y)e^{-D(x, y)} \text{ with } D(x, y) = \frac{\sigma_0}{1 + 4\delta^2/\Gamma^2} n_{\text{col}}(x, y). \quad (3.43)$$

This expression assumes the thin lens approximation and a low intensity of the imaging beam compared to the saturation intensity of the atomic transition. The parameter δ is the detuning of the imaging beam, Γ the linewidth of the atomic transition, and $n_{\text{col}}(x, y) = \int n(x, y, z) dz$ the integrated density along the beam direction. The resonant cross section $\sigma_0 = 3\lambda^2/2\pi$ is valid for a two-level atom that is imaged with polarized light of wavelength λ . In the case of linearly polarized light and a vanishing magnetic field, several degenerate Zeeman levels can be occupied such that the atom does not constitute a two-level system anymore. In the case of ^{39}K , the cross section then has to be corrected by a factor of $7/15 \approx 0.47$. In our experiment, the imaging light in our standard imaging axis along the z -direction is not perfectly linearly polarized and the correction factor was measured for ^{87}Rb as 0.40(5) [113]; due to the identical hyperfine structure of the two atomic species, we assume the same correction factor for ^{39}K . On the CCD chip, we measure the integrated intensity over the area of an individual pixel, corresponding to a column density that is averaged over an area A in the focal plane, determined by the magnification of the imaging system. Therefore, by multiplying the measured column density with the area A , we obtain the corresponding atom number. The resolution of our imaging system is approximately $3 \mu\text{m}$, which we deduced from measurements of very small atom clouds and which is consistent with the expectation from diffraction theory.

3.4.1 In Situ Imaging

We use absorption imaging to directly measure the in situ distribution of the cloud. This is especially relevant for the experiments concerning the emergence of coherence when crossing the Mott to superfluid phase transition, where the in situ cloud size is required for a determination of the coherence length (Section 6.2.4). However, according to Eq. 3.43, clouds with very high optical densities such as Bose-Einstein condensates lead to an exponentially small amount of transmitted light which cannot be distinguished from noise in the images. In these regions of high optical densities, the images do not provide any information about the column density. To circumvent this problem, phase-contrast imaging [49] could be used which extracts information from the phase shift that the atomic cloud induces in a detuned imaging beam rather than from the absorption of a near-resonant beam. For the purposes of the experiments described in this thesis, however, absorption in situ imaging is sufficient, as the broad wings of the atomic clouds in our oblate dipole trap geometry allow to estimate the optical density of the cloud center.

In the experiments about the emergence of coherence, to image the in situ distribution in a shallow optical lattice at $V_{\text{latt}} = 6 E_r$, we quickly ramp up all three lattices to the deepest possible value of $V_{\text{latt}} = 33 E_r$ to freeze out the atomic distribution. During a hold time of several ms in the deep lattice, we switch off the magnetic field and perform absorption imaging on the in situ cloud. Absorption imaging at high magnetic fields is problematic due to the various Zeeman levels that are populated during the imaging process, which provide transitions that are not resonant with the imaging light. These detuned transitions do not contribute to the absorption signal but mainly provide phase shifts to the imaging light,

distorting the absorption signal of the resonant transition.

3.4.2 Time-of-Flight Absorption Imaging

The momentum distribution of the atomic cloud can be measured via time-of-flight (TOF) absorption imaging. At the end of an experimental sequence, all trapping potentials are switched off and the atomic cloud evolves in free space for a certain time t_{TOF} . At the end of this period, a standard absorption image is taken.

During time-of-flight, the atoms are accelerated by gravity. Additionally, if interactions between the atoms can be neglected, the atoms will evolve according to their initial velocities. For very long t_{TOF} , the *in situ* distribution of the cloud can be neglected, and the spatial distribution of the cloud is given by the initial momentum distribution. For short and intermediate t_{TOF} , the *in situ* distribution has to be taken into account when analyzing TOF images.

3.4.3 Measuring the Momentum Distribution

If the lattices are instantaneously switched off at the beginning of the TOF period, the quasimomentum states $|\hbar q\rangle$ in the lattice are projected into the basis of plane waves $|p\rangle$ (cf. Section 3.2.4). These plane wave states then determine the momentum at which the atoms evolve during TOF. A BEC at $|\hbar q = 0\rangle$ therefore shows up as an array of peaks, spaced by $2\hbar k_{\text{lat}}$, corresponding to the superposition state in the plane wave basis and reflecting the phase coherence of the superfluid state. In contrast, a Mott insulating state of localized atoms at unity filling is given by a superposition of all $|\hbar q\rangle$ states in the lowest band. The projection leads to a broad distribution of the plane wave states and the TOF image shows only a broad peak, determined by the on-site Wannier function, without any obvious additional features, reflecting the absence of phase coherence between lattice sites [34, 114].

Modeling the interference pattern

The interference pattern contains information about the phase coherence between lattice sites. We extract this information by calculating the interference pattern in a simple model and comparing the calculated patterns to the experimentally measured one by a fit.

The momentum distribution of the atoms in the optical lattice is [115]

$$\langle \hat{n}(\mathbf{k}) \rangle = \frac{1}{\mathcal{N}} |\tilde{w}(\mathbf{k})|^2 S(\mathbf{k}), \quad (3.44)$$

where the Fourier transform of the on-site Wannier function $\tilde{w}(\mathbf{k})$ determines the overall envelope of the interference pattern, and \mathcal{N} is a normalization factor. The interference term $S(\mathbf{k})$ is given by a sum over all lattice sites at positions \mathbf{r}_μ ,

$$S(\mathbf{k}) = \sum_{\mathbf{r}_\mu, \mathbf{r}_\nu} \exp(i\mathbf{k}(\mathbf{r}_\mu - \mathbf{r}_\nu)) \langle \hat{a}_\mu^\dagger \hat{a}_\nu \rangle. \quad (3.45)$$

In the experimental sequence, we record the momentum distribution via absorption imaging after *finite* time-of-flight t_{TOF} . In the images, we attribute to each position \mathbf{r} in real space a momentum $\hbar\mathbf{k} = m\mathbf{r}/t_{\text{TOF}}$. Since after finite t_{TOF} , the initial positions \mathbf{r}_μ of the atoms still influence the measured distribution, the interference pattern is generalized to [115]

$$\tilde{S}(\mathbf{k}) = \sum_{\mathbf{r}_\mu, \mathbf{r}_\nu} \exp \left(i\mathbf{k}(\mathbf{r}_\mu - \mathbf{r}_\nu) - i \frac{m}{2\hbar t_{\text{TOF}}} (\mathbf{r}_\mu^2 - \mathbf{r}_\nu^2) \right) \langle \hat{a}_\mu^\dagger \hat{a}_\nu \rangle. \quad (3.46)$$

The second term in the exponential provides a correction of a pure Fourier transform of the in situ distribution for finite TOF [115]. It is equivalent to the quadratic term in the Fresnel approximation of near-field optics. We model the correlator by assuming a Gaussian in situ density distribution and exponentially decaying correlations between lattice sites,

$$\langle \hat{a}_\mu^\dagger \hat{a}_\nu \rangle_{(T>0)} = \sqrt{n_\mu} \sqrt{n_\nu} \cdot \exp \left(-\frac{|\mathbf{r}_\mu - \mathbf{r}_\nu|}{\xi} \right) \quad (3.47)$$

$$= \exp \left(-\frac{\mathbf{r}_\mu^2 + \mathbf{r}_\nu^2}{4R^2} - \frac{|\mathbf{r}_\mu - \mathbf{r}_\nu|}{\xi} \right), \quad (3.48)$$

where ξ is the correlation length and n_μ the density at site μ . In the case of negative temperature, where we expect condensation at $\hbar q_i = \pm \hbar k_{\text{lat}}$, with q_i indicating the components of \mathbf{q} , this correlator contains an additional phase term,

$$\langle \hat{a}_\mu^\dagger \hat{a}_\nu \rangle_{(T<0)} = \langle \hat{a}_\mu^\dagger \hat{a}_\nu \rangle_{(T>0)} \cdot e^{i\mathbf{k}_{\text{lat}}(\mathbf{r}_\mu - \mathbf{r}_\nu)}, \quad (3.49)$$

where $\mathbf{k}_{\text{lat}} = (k_{\text{lat}}, k_{\text{lat}}, k_{\text{lat}})$ in the 3D case. While $\hbar q = 0$ at positive temperature corresponds to a constant phase between lattice sites, $\hbar q_i = \pm \hbar k_{\text{lat}}$ features an alternating phase (cf. Fig. 3.3).

To fit a measured interference pattern, we integrate the image along one axis of a region of interest (ROI) and thus obtain 1D data which we normalize (Fig. 3.11). For the comparison, we calculate the expected interference patterns for a 1D system. Results for both exemplary integrated data and calculated interference curves are shown in Fig. 3.12. For very small coherence lengths $\xi \ll d_{\text{lat}}$, only the Fourier transform of the Wannier function as envelope function is visible. For larger ξ , the interference peaks become more pronounced and their width decreases. For large ξ , the peak widths saturate at a minimum value which is given by the in situ width R of the atomic cloud. Yet, also the region between the peaks contains valuable information that we use for the extraction of the coherence length.

We minimize the sum of absolute residuals of the calculated interference curves with respect to the averaged experimental curve and thus obtain ξ . This fitted ξ value, however, can only be an approximation to the real coherence length in the system: The imaged cloud is an average over several 2D layers with different radii R . Also, the assumption of a Gaussian in situ density distribution is only an approximation to the real distribution. However, the optimal calculated curve in Fig. 3.12 shows very good agreement with the experimental data, indicating that our assumptions of a Gaussian in situ density distribution and exponentially decaying correlations between lattice sites allow a good description of the experimental situation.

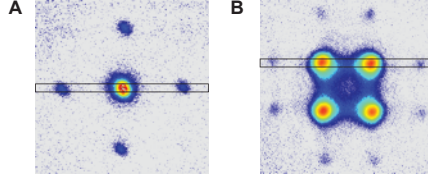


Figure 3.11: Obtaining 1D data from TOF images. The experimental data is integrated along the short axis of a thin ROI that includes potential interference peaks (black boxes). Images from, **A**, a positive temperature, and, **B**, a negative temperature experiment in 2D.

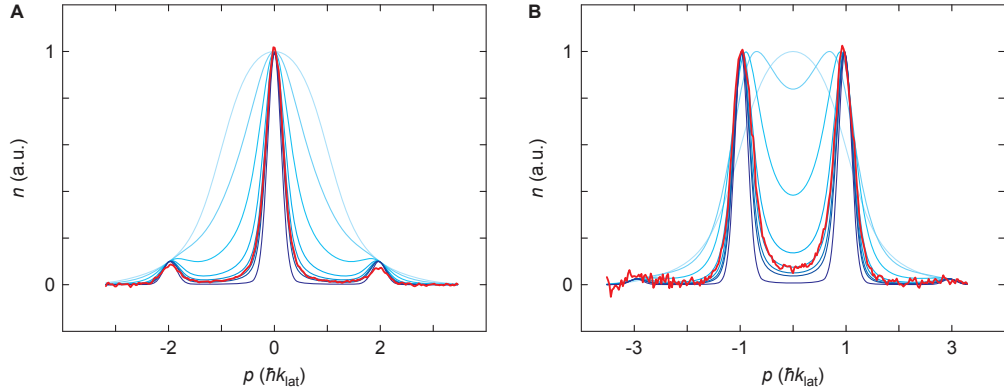


Figure 3.12: Extracting the coherence length by comparing experimental data (red curve) with calculated interference patterns for coherence lengths $\xi = (0.1, 0.5, 1, 2, 3, 4, 5, 20) d_{\text{lat}}$ (blue curves, from light to dark). Both experimental data and theory curves are normalized to a maximum value of 1. **A**, Data from a positive temperature experiment in a 2D system. Theory curves are calculated for a Gaussian width $R = 32 d_{\text{lat}}$. **B**, Data from a negative temperature experiment (Section 5) in 2D. Compared to the positive temperature case, the peaks are shifted by half the Brillouin zone. Theory curves are calculated for a Gaussian width $R = 31 d_{\text{lat}}$.

3.4.4 Measuring the Quasimomentum Distribution

A related time-of-flight imaging technique is the so-called band mapping. Here, the lattice potential is not switched off instantaneously, but on a timescale which is fast compared to the tunneling dynamics in the lowest band, but adiabatic with respect to transitions into other bands [116, 117]. During this ramp, a Bloch wave $|\hbar q\rangle$ is adiabatically transferred into the plane wave state $|p = \hbar q\rangle$. The momentum distribution therefore directly reflects the quasimomentum in the lattice. With this method, also atoms in higher bands can be clearly identified as they are transferred to higher plane waves, corresponding to higher Brillouin zones.

3.5 Feshbach-Induced Mott Insulator

As outlined in Section 3.3.3, the transition from the superfluid to the Mott insulating regime is determined by the fraction U/J . Typically, this fraction is tuned by changing the depth

of the optical lattice. Alternatively, the transition can also be achieved by only changing the interaction $U \propto a$ via the scattering length a [118]. The species ^{39}K is predestined for this route due to its broad Feshbach resonance in the absolute ground state (Section 2.1.3). We mapped out the phase transition for various interactions by preparing an ultracold cloud of ^{39}K atoms at various scattering lengths and then ramping a 3D optical lattice to variable lattice depth. The TOF images in Fig. 3.13 show the loss of phase coherence at the phase transition via the typical disappearance of the interference pattern. Although the atoms in our experiment are trapped in an external harmonic potential leading to an inhomogeneous filling, we obtain a qualitatively good agreement with the theoretical prediction of $(U/J)_c = 29.3$ from quantum Monte-Carlo calculations for a 3D system at $n = 1$ [106].

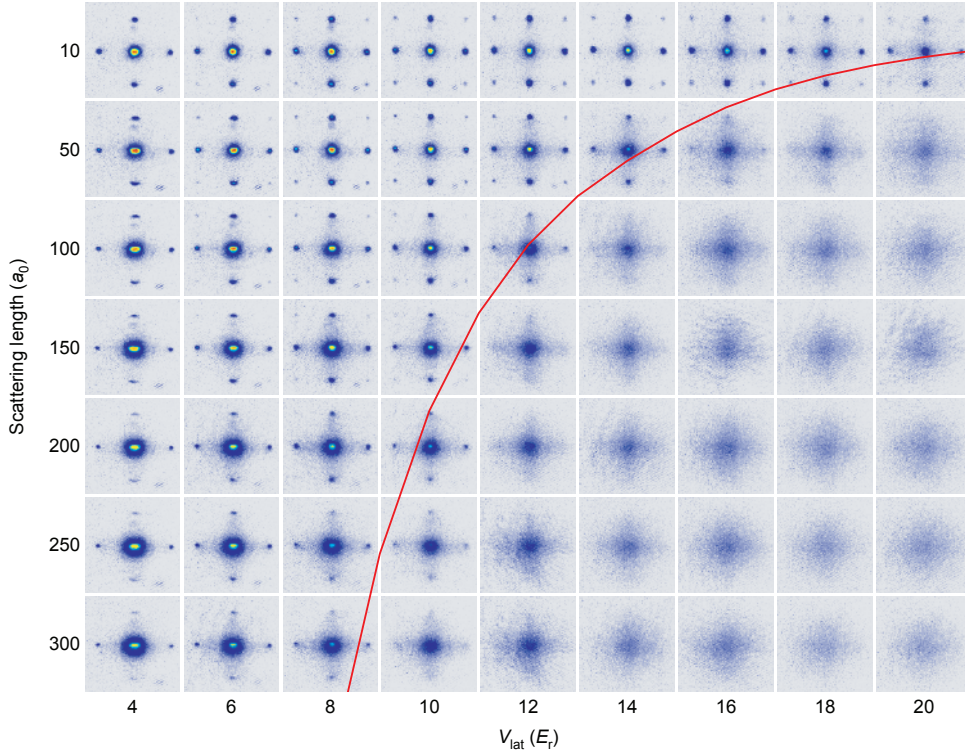


Figure 3.13: Feshbach-induced Mott insulator. Time-of-flight images are plotted for various lattice depths and scattering lengths. The strength of the interference pattern is a measure for the superfluidity of the system. The red solid line is the theoretical value of the Mott transition of $(U/J)_c = 29.3$ from quantum Monte-Carlo calculations for a 3D system at $n = 1$ [106].

4 Theory of Negative Absolute Temperatures

In this chapter I lay out the theoretical background for negative absolute temperatures. In the first section I present how negative temperatures are defined and what they mean physically. In the second section the concept of thermodynamic equilibrium and the approach to it, i.e. thermalization, are introduced, both for classical and quantum systems. In the third section I show how negative temperatures can be realized in experiments and how this has been done previously. In the fourth section I discuss some of the implications of negative temperatures. I also address some of the confusion that is connected with the concept of negative temperatures. In the fifth section, I lay out a recent discussion about the correct definition of entropy which also affects the concept of negative temperature. This chapter is strongly connected with our publication *Negative Absolute Temperature for Motional Degrees of Freedom* [119].

4.1 What are Negative Absolute Temperatures?

Here I describe the fundamental concepts of negative absolute temperatures - how they are defined and what they mean physically.

4.1.1 Occupation Inversion

Absolute temperature T is usually bound to be strictly positive. However, under special conditions, also negative absolute temperatures are possible. An intuitive understanding of negative temperatures can be obtained in the canonical ensemble via the Boltzmann distribution

$$P_i = \frac{1}{Z(T)} e^{-E_i/k_B T}, \quad (4.1)$$

which is normalized by the partition function $Z(T) = \sum_i e^{-E_i/k_B T}$. This distribution gives the probability P_i for a canonical ensemble in thermal equilibrium with a heat bath to occupy a quantum state i with energy E_i . In Fig. 4.1, an illustration of the Boltzmann distribution for several temperatures is given. In the case of a very small positive temperature, most particles will occupy states with very low energy. The Boltzmann distribution

is strongly peaked near the lowest possible energy – the ground state. This lower energy bound is necessary to obtain a normalizable distribution: Otherwise the probabilities P_i would diverge for $E_i \rightarrow -\infty$ and thus also $Z(T)$. For increasing temperatures, more particles will also occupy higher energy states, leading to a broader Boltzmann distribution. In the case of an infinite temperature, the occupation of individual states becomes independent of energy; therefore the Boltzmann distribution is flat. To realize such a state, however, both a lower and an upper bound in the energy spectrum is required for a normalizable distribution P_i . Inserting a temperature of negative infinity leads to the same distribution as positive infinity. In fact, these two extreme values describe the same quantum state. By inserting a finite negative temperature into the Boltzmann formula (Eq. 4.1), the exponentially decreasing function turns into an exponentially increasing one. In this case, states with high energies are more strongly occupied than states with low energies. To realize such a state, an upper energy bound is required such that the distribution of the particles does not diverge for infinite energies. If the numerical value of the negative temperature is increased close to $T = -0\text{ K}$, most atoms will occupy states near the upper energy bound and the Boltzmann distribution will be strongly peaked here. The strong symmetry between positive and negative temperature states is similar to the symmetric spectrum of systems with both lower and upper energy bounds, such as spin systems where only two spin states are available.

4.1.2 Definition of Temperature

The formal thermodynamic definition of temperature is given via entropy,

$$\frac{1}{T} = \left. \frac{\partial S}{\partial E} \right|_V. \quad (4.2)$$

Figure 4.2 shows an idealized curve $S(E)$ for a system with both lower and upper energy bounds. The internal energy E is given by the total energy of all particles in the system. Therefore, the limiting energies E_{\min} and E_{\max} in the graph correspond to the minimum and maximum energy of the total system. At minimum energy, only the ground state would be populated and the entropy would reach its minimum value, which would be zero in the case of a non-degenerate ground state, and the temperature would be zero. For increasing energies, also higher energy states are populated and the entropy increases. At the average energy E_0 of all microstates, the occupation distribution becomes flat, corresponding to a maximized number of microstates leading to the same macrostate and therefore to maximum entropy S_{\max} . If the energy in the system is increased even further, high-energy states are occupied more strongly than low-energy states. This narrower occupation distribution leads to a reduced entropy in the system. In the extreme case of maximum energy, the number of available microstates is minimized, in the case of non-degeneracy to one, leading to vanishing entropy. According to Eq. 4.2, the inverse absolute temperature is given by the slope of this curve. In the blue area, temperature is therefore positive, and in the red area negative. The temperature axis is thus monotonically increasing over the

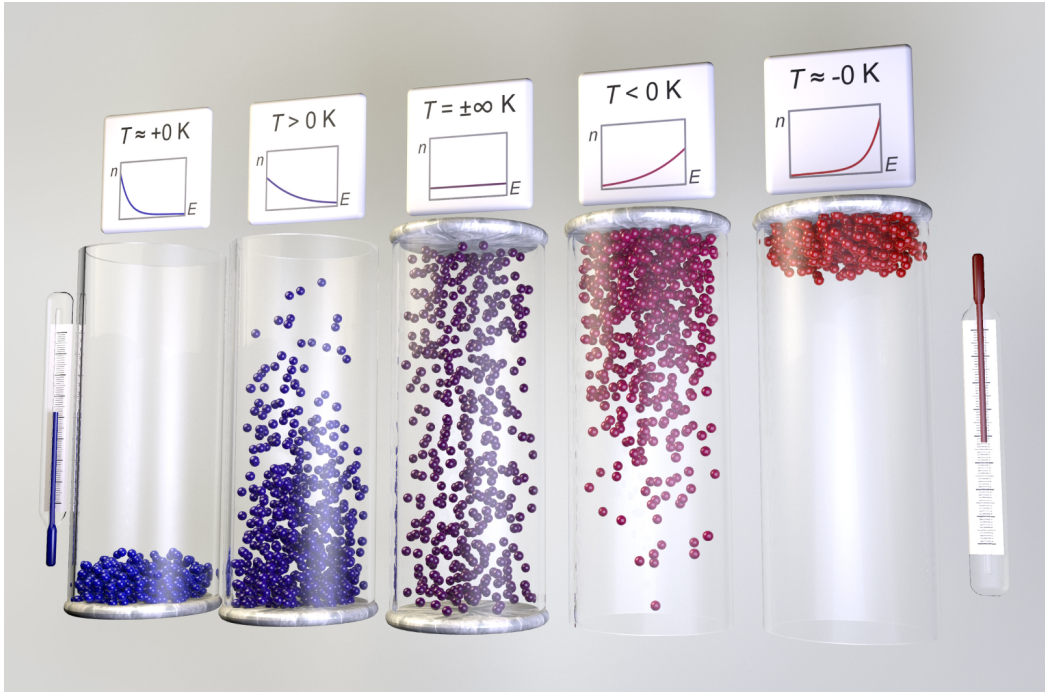


Figure 4.1: Visualization of the Boltzmann distribution for various temperatures T . The spheres indicate particles that are distributed in, e.g., a gravitational potential. In this illustration, however, the vertical axis indicates total energy of the particles, which also includes kinetic energy. The marble disks symbolize energy bounds in the system: While for positive temperatures, a lower energy bound is required, for negative temperatures an upper bound is necessary, and for positive or negative infinite temperature, both lower and upper bounds are required. The corresponding Boltzmann distributions are sketched in the graphs at the top. For details, see main text.

whole energy range, but contains a discontinuous jump from positive to negative infinity. This counterintuitive behavior of the temperature scale is a consequence of the historical definition of temperature. An alternative definition of temperature such as $-\beta = -1/k_B T$ would be monotonically increasing throughout the entire range. This temperature scale would also emphasize the fact that negative temperatures are actually hotter than positive temperatures: In thermal contact, heat flows from a negative temperature system to a system at positive temperature [2].

4.2 Thermodynamic Equilibrium and Thermalization

To be able to assign a temperature to a system, it is necessary that the system is in thermal equilibrium, otherwise temperature is not defined. In thermodynamics, an isolated system is said to be in thermal equilibrium if it can be described by a few macroscopic parameters and if these parameters do not change over time. Two systems are said to be in thermal equilibrium if they do not transfer heat between each other even though they are able

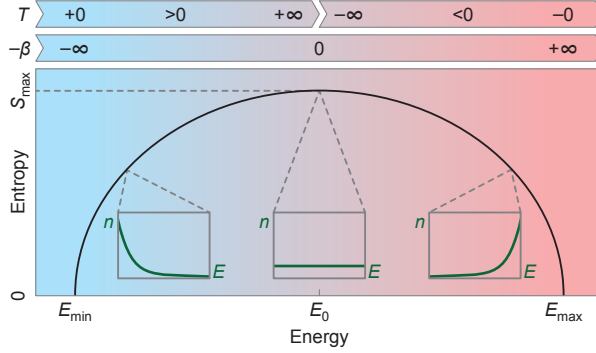


Figure 4.2: Sketch of entropy versus internal energy in a canonical ensemble with both lower (E_{\min}) and upper bounds (E_{\max}) for the total internal energy. In the blue area temperature is positive and in the red area negative. At infinite temperature the entropy reaches its maximum value S_{\max} . An alternative temperature definition $-\beta$ does not involve a discontinuous jump like the well-established definition T does. The insets show sample occupation distributions of single-particle states for positive, infinite, and negative temperatures, assuming weak interactions.

to. If they are unable to exchange heat, they are said to be in thermal equilibrium if they would not do so if they were able to. In thermal equilibrium, the temperature of the two systems is equal. In the case of open systems that can additionally exchange work and matter, thermodynamic equilibrium also requires, in addition to the above thermal equilibrium, also mechanical equilibrium (i.e. identical pressures in both systems) and chemical equilibrium (i.e. identical chemical potentials) [120].

In statistical mechanics, a widespread definition of thermodynamic equilibrium is based on the fundamental postulate of statistical mechanics: A macroscopic system in thermodynamic equilibrium can be found with equal probability in any of the microstates that are consistent with the macroscopic parameters of the system. For an isolated system with fixed particle number, volume, and energy, this corresponds to the microcanonical ensemble. If the system can exchange heat, work, or matter with the surroundings, this leads to other statistical ensembles such as the canonical or the grand-canonical ensemble. Following this widespread ensemplist view [121], in classical mechanics a system is said to be in thermodynamic equilibrium if its probability distribution ρ over phase space is close to the distribution ρ_{ens} of the corresponding ensemble,

$$\rho \approx \rho_{\text{ens}}. \quad (4.3)$$

As the statistical ensembles correspond to those macrostates with maximum entropy under given external conditions, an equivalent definition can be given via entropy: A system is in thermal equilibrium if the entropy is maximized under the given external conditions.

As an alternative to applying statistical ensembles to a system as a whole, one may also split the system into several subsystems that are weakly coupled with each other and may exchange heat, work and matter. The surroundings of a small subsystem can then be considered as an external bath. The above definition of thermodynamic equilibrium

corresponds to global thermodynamic equilibrium, where all subsystems are in thermal equilibrium by themselves and with each other. In this framework, alternatively, a system may also be in partial or local thermodynamic equilibrium [60]: As the relaxation time increases with system size, individual small subsystems may already be in thermodynamic equilibrium, while the subsystems have not yet equilibrated between each other. Partial thermodynamic equilibrium may also refer to different processes that appear on different timescales. For example, a mixture of substances undergoing a chemical reaction may quickly reach equilibrium with respect to the motion of the molecules, whereas equilibrium with respect to the slow chemical reaction is not yet established [60].

Equilibrium states are distinct states of a system and most systems are found at non-equilibrium. The challenging questions are: Under what circumstances does a non-equilibrium system reach thermal equilibrium and how long does it take? In the following section I introduce some of the established concepts of thermalization.

4.2.1 Classical Thermalization

The ability of a classical system to thermalize is contained in the concept of ergodicity. It states that an isolated system, for almost every initial condition $X(0)$, uniformly covers the accessible hypersurface of phase space when it evolves over time to become $X(t)$. *Almost every* means that the set of exceptions is of measure zero [122]. Ergodicity therefore ensures that all microstates will be reached with equal probability during time evolution. After some time, the probabilities of an ergodic system in a particular macroscopic state are thus equally distributed among the microstates, consistent with the fundamental postulate of statistical mechanics.

The time average of a function $f(t)$ can be defined as

$$\overline{f(t)} = \lim_{T \rightarrow \infty} \frac{1}{T} \int_0^T dt f(t). \quad (4.4)$$

Classical ergodicity can be formulated via the trajectory $X(t)$ of an isolated system in phase space, with initial condition $X(0)$ at fixed energy E [122],

$$\overline{\delta(X - X(t))} \equiv \lim_{T \rightarrow \infty} \frac{1}{T} \int_0^T dt \delta(X - X(t)) = \rho_{mc}(E). \quad (4.5)$$

Here, δ indicates the delta distribution, X an arbitrary point in phase space, and $\rho_{mc}(E)$ the classical microcanonical density with energy E .

The timescale over which a macroscopic system explores the entire phase space, however, can be very large so that the thermodynamic equilibrium state exhibits a special form of ergodicity breaking. For example, below the Curie temperature, a ferromagnetic system should explore all states with a time-averaged magnetization of zero. However, the spontaneous magnetization of the system, an example of spontaneous symmetry breaking, does not change its direction anymore and therefore breaks ergodicity.

The notion of ergodicity is closely related to integrability: If a classical system with s degrees of freedom and, thus, a $2s$ -dimensional phase space, contains s conservation

laws (i.e. integrals of motion) it is called integrable. In this case, the restrictions due to the integrals of motion restrict the system to a subspace of the total phase space and the system is therefore non-ergodic and does not thermalize. Such integrals of motion (in addition to total energy and momentum) could be, e.g., the absolute value of the velocity of non-interacting particles. As another example of a non-ergodic system, in the solar system, if interactions between planets are neglected, conservation of energy and angular momentum leads to regular orbits of the planets around the sun. The concept of ergodicity is also linked to chaotic behavior: If a system exhibits full dynamical chaos, its motion in phase space is ergodic [123]. On the other hand, the pure presence of a nonlinearity in a system is not sufficient for ergodic behavior to emerge [124–128]. In general, it is challenging to prove ergodicity for a given system, yet most interacting many-body systems behave ergodically. A detailed account of integrability can be found in [83].

4.2.2 Quantum Thermalization

The most direct transfer of classical ergodicity into the quantum case would be to require that the long time average of the density matrix of a system equals the density matrix $\hat{\rho}_{\text{mc}}$ of the corresponding, e.g. microcanonical, ensemble. This formulation, however, is almost never fulfilled [122]: A quantum-mechanical system is initially prepared in an arbitrary superposition $|\psi(0)\rangle = \sum_{\alpha} C_{\alpha} |\Psi_{\alpha}\rangle$ of energy eigenstates $|\Psi_{\alpha}\rangle$, with $\hat{H}|\Psi_{\alpha}\rangle = E_{\alpha}|\Psi_{\alpha}\rangle$. The time evolution is given by

$$|\psi(t)\rangle = e^{-i\hat{H}t}|\psi(0)\rangle = \sum_{\alpha} C_{\alpha} e^{-iE_{\alpha}t}|\psi_{\alpha}\rangle. \quad (4.6)$$

The long time average of the density matrix

$$\overline{|\psi(t)\rangle\langle\psi(t)|} = \sum_{\alpha} |C_{\alpha}|^2 |\psi_{\alpha}\rangle\langle\psi_{\alpha}| = \hat{\rho}_{\text{diag}} \quad (4.7)$$

is given by the so-called diagonal ensemble [122]. As the prefactors C_{α} of the initial state do not change during unitary evolution, this long time average is in general different from the microcanonical ensemble

$$\hat{\rho}_{\text{mc}} = \sum_{\alpha} \frac{1}{N} |\psi_{\alpha}\rangle\langle\psi_{\alpha}|, \quad (4.8)$$

where N is the number of energy eigenstates in the energy interval $I \equiv [E_0 - \Delta E, E_0 + \Delta E]$ around the energy expectation value E_0 . With this definition, a generic quantum system would almost never be ergodic.

Instead, the quantum version of ergodicity is meaningfully expressed with the help of natural observables, i.e. observables that can be directly measured in a given experimental situation, such as local observables like densities or short-range correlation functions or macroscopic observables derived from local observables [122, 129, 130]. The expectation value of any observable \hat{O} is given by

$$\langle \hat{O}(t) \rangle \equiv \langle \psi(t) | \hat{O} | \psi(t) \rangle = \sum_{\alpha, \beta} C_{\alpha}^* C_{\beta} e^{i(E_{\alpha} - E_{\beta})t} O_{\alpha\beta}, \quad (4.9)$$

with the matrix elements $O_{\alpha\beta} = \langle \Psi_\alpha | \hat{O} | \Psi_\beta \rangle$. As the oscillating terms average out, the long-time average of this expectation value is then

$$\overline{\langle \hat{O} \rangle} = \sum_{\alpha} |C_{\alpha}|^2 O_{\alpha\alpha}, \quad (4.10)$$

which may also be called, similar to Eq. 4.7, a diagonal ensemble [130]. If a system does relax, it has to relax to this value.

If the expectation value of an observable behaves thermally, it has to approach the value predicted by the appropriate statistical ensemble [130],

$$\overline{\langle \hat{O} \rangle} = \langle \hat{O} \rangle_{\text{ens}}. \quad (4.11)$$

In the following, I present the ramifications for the case of the microcanonical ensemble $\hat{\rho}_{\text{ens}} = \hat{\rho}_{\text{mc}}$ which implies the following ensemble average of the observable:

$$\langle \hat{O} \rangle_{\text{mc}}(E_0) \equiv \text{Tr}(\hat{O}\hat{\rho}_{\text{mc}}) = \frac{1}{N} \sum_{\alpha, E_{\alpha} \in I} O_{\alpha\alpha} \quad (4.12)$$

Equation 4.11 therefore implies

$$\sum_{\alpha} |C_{\alpha}|^2 O_{\alpha\alpha} = \frac{1}{N} \sum_{\alpha, E_{\alpha} \in I} O_{\alpha\alpha}. \quad (4.13)$$

This statement embodies thermodynamic universality: While the left-hand side depends on the coefficients C_{α} and therefore on the initial state of the system, the right-hand side only depends on total energy. There are in general three options as to how this equality can be fulfilled, depending on the fluctuations of either the eigenstate occupation numbers (EONs) $|C_{\alpha}|^2$ or of the eigenstate expectation values (EEVs) $O_{\alpha\alpha}$: First, if both EEVs and EONs fluctuate strongly but in an uncorrelated way, a state with given EONs samples the EEVs without any bias. Second, if the EONs fluctuate very little, $|C_{\alpha}|^2 \approx 1/N \forall \alpha$, the initial state has similar weight of all eigenstates in the interval. Both these scenarios, however, impose constraints on the initial state of the system and have therefore only very limited applicability. In the third case, the EEVs fluctuate only very little between eigenstates close in energy.

This last option is called the eigenstate thermalization hypothesis [130–132], and it does not put constraints on the initial state of the system. It assumes that the expectation value of a natural observable with respect to any energy eigenstate $|\psi_{\alpha}\rangle$ in the interval I equals the ensemble average,

$$\langle \psi_{\alpha} | \hat{O} | \psi_{\alpha} \rangle = \langle \hat{O} \rangle_{\text{ens}}(E_{\alpha}). \quad (4.14)$$

There is no proof that the eigenstate thermalization hypothesis is the correct mechanism for thermalization in isolated quantum systems. However, several theoretical simulations provide strong evidence that the hypothesis is indeed the underlying process [130].

In addition to the above ergodicity statement, there is an even stronger statement via observables, called normal typicality [121]. It is stronger in the sense that it not only

makes a statement about time averages, but about the properties of a quantum state for most times during its evolution. This property of the quantum state investigated here is the joint probability distribution of the outcome when measuring a commuting family of macroscopic observables (such as temperature or pressure). In a nutshell, a system in an initial state $|\psi(0)\rangle$ is called *normal* if this state develops such that, for most times, this joint probability distribution is close to the ensemble probability distribution [121]. The ensemble probability distribution itself is very strongly dominated by those values of the macroscopic observables that correspond to thermal equilibrium [121]. In other words, a system that is normal for an initial state $|\psi(0)\rangle$ is in thermal equilibrium for most times of the evolution. *Normal typicality* states that *typical* macroscopic systems, consisting of a Hilbert space and a set of commuting macroscopic observables, are normal for *every* initial state $|\psi(0)\rangle$ [121]. This is a statement about the vast majority of systems and thus is not a proof for a particular given system. However, the statement gives reason to believe that, in practice, macroscopic systems are normal [121].

Quantum ergodicity, as in the classical case, is closely related to the concept of quantum integrability. A straightforward extension of the classical definition of integrability to the quantum case is not meaningful, as one can easily find a set of s_H conserved quantities, where s_H is the dimensionality of the Hilbert space, such as the projection operators to the energy eigenstates. An alternative definition of quantum integrability would be to require that a system is exactly solvable and, thus, all eigenstates can explicitly be constructed [133]. To date, however, there are several definitions of quantum integrability and not a single unique established one [133]. For the experiments presented in this thesis, it is important to know that free models are in general integrable, such as noninteracting bosons or fermions in optical lattices in any dimension. Also hard-core bosons in a 1D system constitute an integrable system as they can be mapped to free fermions [134]. In a 1D lattice, this mapping is achieved via a Jordan-Wigner transformation [135, 136]. A compelling example of an integrable system of strongly interacting bosons in 1D without a lattice was given with a quantum version of Newton's cradle [137]. The Bose-Hubbard model at intermediate interactions, as is mostly investigated in this thesis, is in general non-integrable [33] and atoms are therefore expected to thermalize. For example, a numerical simulation convincingly showed that bosons released into a 2D lattice thermalize to the microcanonical ensemble [130]. An experimental study of the relaxation of an initially prepared density wave in a 1D optical lattice for intermediate interactions also suggests thermalization [138]. A detailed study of non-equilibrium dynamics in ultracold atoms and the connection to integrability can be found in the thesis of Philipp Ronzheimer [83].

Also integrable systems relax during time evolution, but to states that cannot be described by the ensemble average, i.e. thermodynamic equilibrium. The so-called generalized Gibbs ensemble has proven to be successful in describing the asymptotic states of integrable systems, taking into account the constraints of the system [122, 139–141]. The timescale for relaxation and thermalization processes is yet another question. In the case of integrable quantum systems, a phenomenon called prethermalization has been suggested and mea-

sured, where the system rapidly establishes a quasi-stationary state that already contains some properties of equilibrium [142–147]. Full thermalization, if it happens at all, then occurs on a much longer timescale. These prethermalized states can be described via the generalized Gibbs ensemble [122].

There are, however, also non-integrable systems that do not thermalize, a prominent example being systems exhibiting many-body localization [148]: In such systems, particles can be localized by a sufficiently strong disorder potential and do not thermalize despite interactions; this may even happen in the case of highly excited states [148]. In this case, the particles do not even relax to a modified ensemble such as the generalized Gibbs ensemble [148]. The latter is also true in the analogous noninteracting case, where Anderson localization [149] prevents relaxation of the system [148].

4.3 Experimental Realizations of Negative Absolute Temperatures

In this section I discuss how negative temperatures can be realized experimentally. The key challenge is to create an upper bound in the energy spectrum. I discuss how negative temperature states have been realized previously, for localized nuclear spin as well as atomic spin systems, and establish why lasers with population inversion cannot be considered systems at negative temperature. Finally, I show how negative temperatures can be realized with ultracold atoms in optical lattices.

4.3.1 Realization of Upper Energy Bound

As already introduced, an upper bound in the energy spectrum is the crucial feature necessary for the realization of negative temperatures. This upper bound has to be established with respect to all degrees of freedom that take part in the occupation inversion at negative temperature. One could separate some degrees of freedom from the rest and create a thermalized negative temperature state only for these isolated degrees of freedom. In the case where no degrees of freedom are isolated, an upper bound has to be created for the total energy of the system.

This is precisely the reason why we never encounter negative temperature states in daily life: Kinetic energy E_{kin} of free particles is related to momentum p by the quadratic dispersion $E_{\text{kin}} \propto p^2$ and therefore is unbounded from above. Instead, kinetic energy for free particles is only bounded from below, and therefore all systems in daily life are at positive temperature. This asymmetry is in contrast to the picture given in Fig. 4.1, where positive and negative temperatures together with lower and upper energy bounds constitute a very symmetric situation. It is a fundamental question why the world mostly exists at positive and not at negative temperature.

To realize an upper energy bound in the lab, the system in addition has to be isolated from the environment which is in general at positive temperatures. If the system is coupled

to an arbitrarily small system that does not possess an upper energy bound, the negative temperature state is not stable [150].

4.3.2 Negative Temperature for Nuclear Spin Systems

E. M. Purcell and R. V. Pound [1] were the first to experimentally create negative absolute temperatures. In their experiment, they applied the recently developed NMR techniques for solid materials [151] to ^7Li nuclear spins with $I = 1/2$ [4] arranged in a LiF crystal: In a thermalized ensemble of these spins in a strong homogeneous magnetic field B along the z direction, the two energy levels corresponding to the two Zeeman states $I_z = \pm 1/2$ are occupied according to the Boltzmann distribution $p \propto \exp(-E_Z/k_B T)$. Here, $E_Z = -\hbar\gamma IB$ is the Zeeman energy, with the gyromagnetic ratio γ . The occupation difference is usually very small, due to the small energy difference of the Zeeman levels, but can be increased by increasing the ratio B/T . By applying an oscillating magnetic field with a frequency that is resonant with the energy difference of the two Zeeman states, some of the spins can be excited to the upper energy level, and therefore energy is transferred into the nuclear spin system. This energy transfer depends on the initial population imbalance and increases the resistance of the resonant circuit, including a radio-frequency (RF) coil that creates the oscillating field. The resistance is measured by the regulation electronics that keeps the amplitude of the oscillating magnetic field constant [152], and is a measure for the relative population imbalance of the two states.

To create negative temperatures, Purcell and Pound reversed a homogeneous B field of 100 G in a timescale of $0.2\ \mu\text{s}$ which is too fast for the nuclear spins to follow adiabatically [1]: The timescale of the spins in this system to follow changes in the magnetic field adiabatically is set by the spin-spin relaxation time τ_2 [4] at roughly $\tau_2 \approx 20\ \mu\text{s}$ [1]. The resulting population inversion of the two energy levels turned out to be stable so that the sample could be inserted into the strong homogeneous magnetic field of 6376 G for the NMR measurement. The measured signal was negative, indicating a net energy transfer from the nuclear spin system to the RF coil. The RF field therefore induces radiation of the nuclear spins. By repeating the NMR measurement over time, the negative signal was found to decay, crossing zero and finally reaching the original positive strength corresponding to the positive temperature of the lattice. The spin system therefore slowly relaxes to the positive temperature state, by crossing $T = \pm\infty$ at which equal populations in both Zeeman states lead to a vanishing NMR signal. The timescale for this relaxation process is determined by the spin-lattice relaxation time τ_1 [4] and was found to be about 5 minutes [1]. The negative temperature state is therefore metastable. The spins attain a thermal distribution on a timescale of the spin-spin relaxation time τ_2 [3]. Therefore, during the relaxation process, the spin system can indeed be assigned a meaningful temperature. As only the Zeeman levels are taking part in the population inversion and not, e.g., the motional degrees of freedom of the nuclei in the lattice structure, the negative temperature is more precisely termed *negative spin temperature*.

After this initial creation of negative spin temperatures, various similar experiments

have been performed with nuclear spins [3, 4] where negative spin temperatures could be achieved.

4.3.3 Effective Negative Temperature for Atomic Spin System

P. Medley et al. [5] created an effective negative spin temperature for ultracold atoms in an optical lattice. For this purpose, a mixture of two hyperfine states of ^{87}Rb was created in a magnetic field gradient. The gradient is chosen such that two clouds with different hyperfine states are displaced from each other but still overlap in some region. The width w of the region is proportional to the temperature T and inversely proportional to the magnetic field gradient $\nabla|\mathbf{B}|$, $w \propto T/\nabla|\mathbf{B}|$. The temperature can be obtained from the width of the region via spin gradient thermometry [153]. For the creation of effective negative spin temperatures, an optical lattice was ramped up slowly such that the atom clouds entered the Mott insulating regime. In this regime, the timescale for the exchange of two spins (i.e. hyperfine states) is very long, on the order of 1 s. The atoms can therefore be considered as isolated from each other, and the spin distribution is frozen. The magnetic field gradient was then reversed on a timescale much faster than 1 s. As the temperature scales according to $T \propto w \cdot \nabla|\mathbf{B}|$, this leads to an effective negative temperature. During the quench of the gradient, the ensemble remains in thermal equilibrium, because the spin distribution corresponds (for any choice of $\nabla|\mathbf{B}|$) to a thermal distribution and is stable. As the kinetic degree of freedom of the atoms is frozen, however, the negative temperature is an effective spin temperature. By choosing a small magnitude for the reversed gradient, negative spin temperatures with very small absolute values of $T = -(50 \pm 20) \text{ pK}$ could be realized, where the measured value was limited by the optical resolution of the imaging system. A hold time measurement showed heating of the prepared samples only after a hold time of 3 s, indicating the good stability of the effective negative spin temperature state.

4.3.4 Are Lasers at Negative Temperature?

A stationary population inversion of the energy levels also exists in the gain medium of lasers, reminiscent of a negative temperature state. However, a population inversion alone, even in a steady state as in a laser, is not sufficient for the system to be in a thermal equilibrium state. The latter is required for temperature to be a meaningful notion and to assign a temperature to a system. Thermal equilibrium implies that the system stays in its state when it is isolated from the environment. This is the case for the implementations of negative temperatures for nuclear and atomic spins. In a gain medium of a laser, however, the population inversion is created by the laser pump. As soon as the gain medium is isolated from the pump, the population inversion immediately decays until an equilibrium distribution at positive temperature is reached. Therefore, when the pump is activated, the gain medium is in a steady state, but not in thermal equilibrium. Thus one cannot assign the gain medium in a laser a temperature at all [4].

4.3.5 Negative Temperature for Motional Degrees of Freedom in an Optical Lattice

So far, negative temperatures have only been created for spin degrees of freedom. In these systems, the discrete and finite spectrum of the Zeeman states naturally provides both lower and upper energy bounds. The upper energy bound is the key challenge for the realization of negative temperatures for motional degrees of freedom, i.e. where the occupation of the kinetic energy levels is described by an inverted thermal distribution.

Ultracold atoms in optical lattices have been theoretically suggested as a possible implementation scheme for negative temperatures for motional degrees of freedom [6, 7]. A great advantage of such systems lies in the very good isolation from the environment which is at positive temperature and would immediately destroy the negative temperature state upon thermal contact. As a key feature, optical lattices provide an elegant way of creating an upper bound on kinetic energy: If the thermal energy of the atoms trapped in an optical lattice potential is much smaller than the band gap between the lowest and the first excited band, the atoms will be confined to the lowest band. The kinetic energy for ultracold atoms in an optical lattice is therefore effectively limited to the lowest band, providing both a lower and an upper limit. In the case of negative temperatures, the atoms will predominantly occupy the kinetic energy states close to the upper band edge. At this upper limit, the spectrum of the available states is identical but inverted compared to the lower band edge; only are the quasimomenta shifted by half the Brillouin zone. This strong symmetry between the lower and the upper band edge is another advantage of the Hubbard Hamiltonian: It directly follows that thermalization at the upper band edge is just as efficient as at the lower limit and a thermalized state with population inversion is actually realizable experimentally.

To create a negative temperature state, however, not only kinetic energy but all relevant degrees of freedom have to be limited from above. This prevents the realization of negative temperatures for motional degrees of freedom in solids: Here, the electrons also experience a band structure like in an optical lattice but couple to phonons that provide a spectrum with only a lower bound.

Negative temperature in the Bose-Hubbard Hamiltonian

Ultracold bosons in the tight-binding limit and confined to the lowest band are described by the Bose-Hubbard Hamiltonian (Section 3.3.2),

$$H = -J \sum_{\langle i,j \rangle} \hat{a}_i^\dagger \hat{a}_j + \frac{U}{2} \sum_i \hat{n}_i (\hat{n}_i - 1) + V \sum_i \mathbf{r}_i^2 \hat{n}_i, \quad (4.15)$$

containing interaction and potential energy in addition to kinetic energy. Thus, to realize a negative temperature state for bosons in this system, also interaction and potential energy need to be limited from above. Figure 4.3 illustrates the energy bounds of the three terms in the Bose-Hubbard model and shows how lower and upper bounds can be realized. As

already outlined, kinetic energy E_{kin} is restricted to the lowest band of width $4dJ$, where d is the dimensionality (Section 3.2.3).

The energy bound of the on-site interaction term depends on the sign of the interaction U . Bose-Einstein condensates are initially prepared at repulsive interactions with $U > 0$ in ultracold atom experiments to prevent collapse [27]. In principle, all atoms could occupy the same lattice site in an optical lattice. In the thermodynamic limit, this would lead to a diverging interaction energy per particle. For repulsive interactions, interaction energy therefore contains a lower bound at zero energy, in the case when all atoms occupy different lattice sites, but not an upper bound. The situation is inverted in the case of attractive interactions with $U < 0$ where zero interaction energy indeed constitutes an upper bound.

The energy bound of the potential term analogously depends on the sign of the external potential V , where ultracold atoms in experiments are initially trapped in a trapping potential with $V > 0$. In such a potential, a minimum in potential energy is reached when all atoms gather at the trap center, while potential energy can be increased to arbitrarily high values by atoms occupying remote sites. When the external confinement is instead converted to an anti-trapping potential with $V < 0$, the trap center instead constitutes an upper limit for potential energy. As a conclusion, an upper bound for the total energy of the Bose-Hubbard model can be realized with attractive interactions and an anti-trapping potential.

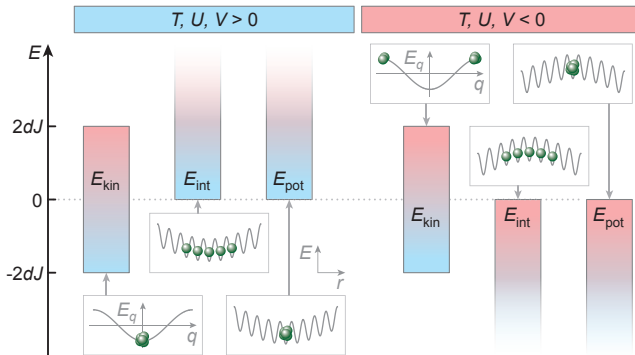


Figure 4.3: Energy bounds of the kinetic (E_{kin}), interaction (E_{int}) and potential energy term (E_{pot}) of the two-dimensional Bose-Hubbard Hamiltonian. The insets illustrate the bounds either in quasimomentum or real space. In a sufficiently deep optical lattice, if the atoms are confined to the lowest band, kinetic energy is limited both from below and above. At positive U and V , interaction and potential energy are limited from below. For attractive interactions ($U < 0$) and an anti-trapping potential ($V < 0$), they provide an upper bound such that all three terms are limited from above.

When realizing the Bose-Hubbard model with attractive interactions and negative temperature, an important question arises: How does the phase diagram in this regime look like, e.g. does the superfluid to Mott insulator phase transition happen at the same absolute values of $|U|/J$ as for the repulsive Bose-Hubbard model at positive temperature (cf. Fig. 3.10)?

Any thermal state of a system with Hamiltonian \hat{H} and therefore also the phase diagram of this system is determined by the equilibrium density matrix [7]

$$\hat{\rho} = e^{-\frac{\hat{H}}{k_B T}}. \quad (4.16)$$

Apparently, if a system is prepared with an inverted Hamiltonian $\hat{H}' = -\hat{H}$ and at negative temperature $T' = -T$, the resulting density matrix will be identical, $\hat{\rho}' = \hat{\rho}$. In our experiment, the Bose-Hubbard Hamiltonian (Eq. 4.15) consists of three terms, i.e. inverting the total Hamiltonian corresponds to inverting each of the three terms. In the experimental sequence (Section 5.1), however, we only invert the interaction $U \rightarrow -U$ and the external potential $V \rightarrow -V$, as required for the upper energy bound, but the tunneling parameter J is unchanged. However, the tight-binding dispersion relation of the lowest band (Eq. 3.16)

$$E_{\text{kin}} = -2J \cos\left(\pi \frac{q}{k_{\text{lat}}}\right) \quad (4.17)$$

shows that the sign of J can effectively be changed if the quasimomentum $\hbar q$ is shifted by half the width of the Brillouin zone, $\hbar q \rightarrow \hbar q + \hbar k_{\text{lat}}$ [7]:

$$E_{\text{kin}} \rightarrow -2J \cos\left(\pi \frac{q + k_{\text{lat}}}{k_{\text{lat}}}\right) = 2J \cos\left(\pi \frac{q}{k_{\text{lat}}}\right) \quad (4.18)$$

This is precisely what happens in the experiment (cf. Section 5.1.3): The strongest occupation shifts from the $\hbar q = 0$ state to the edge of the Brillouin zone at $\hbar q = \pm \hbar k_{\text{lat}}$ and, thus, the quasimomenta are shifted by $\hbar k_{\text{lat}}$. Therefore, the phase diagram of the attractive Bose-Hubbard model at negative temperature is indeed the same as the phase diagram of the repulsive Bose-Hubbard model at positive temperature under the condition that all quasimomenta are shifted by half the Brillouin zone [7]. Therefore, also the superfluid to Mott insulator transition is expected at the same $|U|/J$ values in both cases [154].

Negative temperature in the Fermi-Hubbard Hamiltonian

In contrast, fermionic atoms are described by the Fermi-Hubbard Hamiltonian,

$$H = -J \sum_{\langle i,j \rangle, \sigma} \hat{c}_{i,\sigma}^\dagger \hat{c}_{j,\sigma} + U \sum_i \hat{n}_{i,\downarrow} \hat{n}_{i,\uparrow} + V \sum_i \mathbf{r}_i^2 (\hat{n}_{i,\downarrow} + \hat{n}_{i,\uparrow}), \quad (4.19)$$

where the index $\sigma \in \{\downarrow, \uparrow\}$ denotes two different hyperfine states of the atoms, $\hat{c}_{i,\sigma}$ and $\hat{c}_{i,\sigma}^\dagger$ are the annihilation and creation operators for a fermion, respectively, and $\hat{n}_{i,\sigma} = \hat{c}_{i,\sigma}^\dagger \hat{c}_{i,\sigma}$ is the atom number operator.

The crucial difference compared to the Bose-Hubbard Hamiltonian lies in the Pauli exclusion principle that limits the occupation numbers to $\hat{n}_{i,\sigma} \in \{0, 1\}$. The on-site interaction therefore, in addition to the lower bound of 0, also possesses an upper bound of $U/2$ per particle. Negative temperatures are therefore possible for both attractive and repulsive interactions [155]. They have been realized, at least for local thermal equilibrium, in expansion experiments of fermionic band insulators in a homogeneous lattice [156] in

our group. The experimental sequence of this experiment was similar to the one employed in the experiment described in this thesis (Section 5.1). By adiabatically ramping up an optical lattice, instead of a Mott insulator a band insulator of non-interacting fermions was created. In the deep lattice, the interactions were rapidly switched to repulsive or attractive interactions, creating a state at maximum or minimum interaction energy, respectively. Then, the trapping potential was rapidly turned off instead of being converted into an anti-trapping potential. The lattice depth was suddenly decreased, and thereby expansion of the atomic cloud and also thermalization between atoms was initiated.

During expansion, interaction energy was converted into kinetic energy as the density and the number of doublons decreased. The formation of the negative temperature state was indirectly deduced from the observed identical expansion for repulsive and attractive interactions: The symmetry of the lowest band leads to the same group velocity at the center of the Brillouin zone as at the edge, although the kinetic energies are different (Eq. 3.20). In the case of attractive interactions, a conversion of interaction into kinetic energy should lower the mean kinetic energy and thus states with low kinetic energies are expected to be occupied more strongly, described by a positive temperature. For repulsive interactions, on the other hand, high kinetic energies should prevail, leading to an inverted distribution consistent with negative temperature.

From a more general viewpoint, the identical expansion for repulsive and attractive interactions can be understood from the symmetry of the Hubbard Hamiltonian presented above for the bosonic version: Both the initial band insulator state in the experiment presented here and the density operator are invariant, up to a global phase, with respect to shifting quasimomenta by half the Brillouin zone. Changing the sign of the interaction U and effectively shifting quasimomenta by half the Brillouin zone is, in the absence of a global trapping potential, equivalent to an inversion of the Hamiltonian. Because the latter is equivalent to time reversal under which both the initial state and the density operator are invariant, the dynamics are identical [156].

4.4 Implications of Negative Absolute Temperatures

In this section, I describe some of the implications of negative temperatures such as the validity of the laws of thermodynamics at negative temperature. I show how Carnot efficiencies above unity could be realized and how this is not in contradiction with energy conservation. Finally, I show that negative temperatures necessarily entail negative pressure and vice versa, and comment on a possible relation between negative temperature and dark energy in cosmology.

4.4.1 Validity of the Laws of Thermodynamics

To discuss whether the fundamental laws of thermodynamics also apply for negative temperatures, some quantities have to be clarified. The temperature definition $T = (\partial S / \partial E)^{-1}$ applies for both positive and negative temperatures, i.e. for all thermal ensembles with

any energy between the lower and upper energy bounds, if existing. The zeroth law of thermodynamics is therefore unaltered: Temperature is equal for all systems in thermal equilibrium. The definitions of work δW and heat δQ can also be the same for positive and negative temperatures [2]. The first law, indicating energy conservation as $dU = \delta Q - \delta W$, is valid for negative temperatures as well.

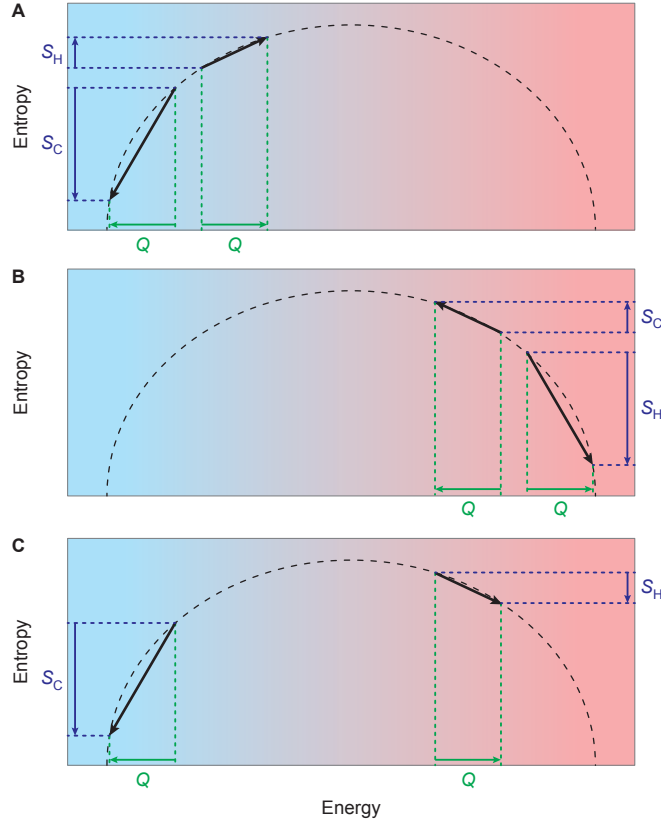


Figure 4.4: Clausius statement of the second law of thermodynamics. A heat transfer Q from a cold system to a hot system always leads to a decrease of the total entropy $S = S_C + S_H$ of the combined system. The Clausius statement is therefore consistent with the entropy statement of the second law. **A**, Both systems at positive temperature. **B**, Both systems at negative temperature. **C**, The cold system at positive temperature and the hot system at negative temperature.

For the second law, a clarification has to be made about the terms *hot* and *cold*. The temperature axis, ordered in terms of energy contained in a system, starts at $+0\text{ K}$, increases to $+\infty$, jumps to $-\infty$, and increases to -0 K . This ordering of temperatures is also consistent with the heat flow from hot to cold, when two systems are brought into thermal contact: Heat flows from the hotter to the colder system. Therefore, in contrast to the numerical temperature value, the above ordering is taken as ordering for the terms *hot* and *cold*. The coldest possible system is at $T = +0\text{ K}$, the hottest possible at $T = -0\text{ K}$. With this definition, the various statements of the second law can be investigated. The

entropy formulation of the second law also applies to negative temperatures: The entropy of a system is a variable of its state and the entropy of an isolated system can never decrease [2]. The Clausius statement is also unaltered: It is impossible to build a machine operating in a closed cycle that will produce no other effect than the transfer of heat from a cooler to a hotter body [2]. Figure 4.4 illustrates how this formulation is consistent with the entropy formulation: A heat transfer from cold to hot always leads to a decrease of the total entropy of both systems, irrespective of whether the systems are at positive or negative temperature.

The Kelvin-Planck formulation, on the other hand, poses some subtleties. While extracting heat from a positive reservoir and performing an equivalent amount of work is clearly reducing the total entropy, the total entropy for such a process even increases for a negative temperature reservoir. In fact, the latter process is indeed possible [2]: It is possible to construct a closed-cycle engine that only extracts heat from a negative temperature reservoir and performs an equivalent amount of work. For example, in the first negative temperature experiment, the RF signal was amplified as it passed through the negative temperature sample (Section 4.3.2). In contrast, dumping heat into a negative temperature reservoir by performing work on an engine reduces the total entropy. Therefore, this reversed process which is easily feasible on the positive temperature side, is not possible for negative temperatures. Thus, the Kelvin-Planck formulation has to be altered to the following: It is not possible to build an engine that will operate in a closed cycle and produce no other effect than (a) the extraction of heat from a positive temperature reservoir with the performance of an equivalent amount of work or (b) the rejection of heat into a negative temperature reservoir with the corresponding work being done on the engine [2].

The third law of thermodynamics is also unchanged if a temperature of absolute zero is understood as both positive zero and negative zero: It is not possible by any procedure, in a finite number of operations, to reduce any system to the absolute zero of positive temperature or to raise any system to the absolute zero of negative temperature [2]. This discussion about the laws of thermodynamics emphasizes the symmetry between positive and negative temperatures: The difficulty of heating a hot system at negative temperatures is analogous to the challenge of cooling a cold system at positive temperatures.

4.4.2 Carnot Efficiency

The Carnot efficiency indicates the largest efficiency achievable in a closed cycle of a working body operating between a hot and a cold reservoir at temperatures T_H and T_C , respectively. Such a cycle operating at the Carnot limit is characterized by zero entropy production. The efficiency η of a heat engine is given by the ratio of work W performed during one cycle over the heat Q_H that is extracted from the hot reservoir,

$$\eta = \frac{W}{Q_H} = \frac{Q_H - Q_C}{Q_H} = 1 - \frac{Q_C}{Q_H} = 1 - \frac{T_C}{T_H}, \quad (4.20)$$

where Q_C is the heat dumped into the cold reservoir. In the last step, the relation $\delta Q = T dS$ for reversible processes was used where dS is the entropy change. Equation 4.20 is also applicable to negative temperatures. The results, however, may sound counterintuitive at first sight and have to be clarified.

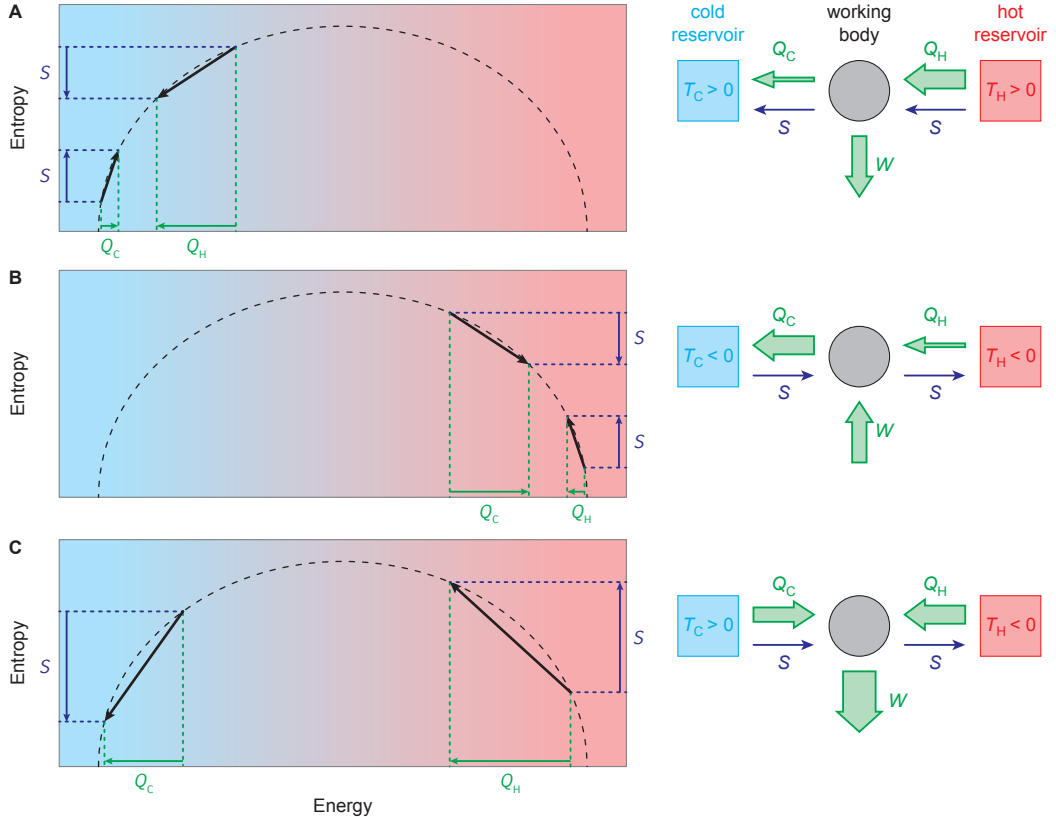


Figure 4.5: Illustration of constant entropy machines. Heat (Q_H , Q_C), work (W) and entropy flows (S) are indicated by arrows, where the length of the arrows in the entropy versus energy graphs on the left is exaggerated. In an ideal Carnot cycle, the reservoirs are infinitely large such that the temperatures T_H and T_C are constant throughout the cycle and the arrows in the diagram are infinitesimal. In the schematic diagrams of the cycles on the right, the width of the arrows qualitatively indicates the amount of heat or work. **A**, The usual Carnot cycle operating between two positive temperature reservoirs leads to an efficiency between 0 and 1. **B**, If both reservoirs are at negative temperature, the efficiency is negative and therefore work must be supplied to maintain the cycle. This cycle is the mirror image of the case with positive temperatures. **C** If the hot reservoir is at negative temperature and the cold reservoir at positive temperature, the efficiency is larger than 1. In this case, heat can be extracted from both reservoirs simultaneously.

In the case of both temperatures T_H and T_C being positive (Fig. 4.5A), the resulting efficiency is always between 0 and 1, i.e. some fraction of the extracted heat from the hot reservoir is converted into work, and the remainder is dumped into the cold reservoir such that the increase in entropy S of the cold reservoir precisely balances the decrease in

entropy of the hot reservoir and the net entropy production during the cycle is zero. If the heat engine is reversed, work must be supplied to maintain the cycle. The cycle then operates as a heat pump.

If both reservoirs are at negative temperatures (Fig. 4.5B), then $T_C/T_H = |T_C|/|T_H| > 1$. Therefore, the efficiency is negative, $\eta < 0$, and its absolute value can be very large. Thus, work must be performed to transfer heat from the hotter to the colder reservoir, in contrast to positive temperatures. In this case, entropy flows from the cold to the hot reservoir, also in contrast to the positive temperature case. If the engine is reversed, it delivers work by transporting heat from the cold to the hot reservoir [2], which is not possible in the case of positive temperatures. The roles of engine and heat pumps are thus reversed compared to the case with positive temperatures above: The cycle between negative temperatures is the mirror image of the cycle between positive temperatures.

A peculiar case is given if the hot reservoir is at negative temperature and the cold reservoir at positive temperature. The ratio of the temperatures is negative in this case, $T_C/T_H < 0$, leading to a Carnot efficiency above unity, $\eta > 1$. Thus, the work delivered by the engine is larger than the heat extracted from the *hot* reservoir. At first sight, this may seem like a contradiction to energy conservation. However, the key for an understanding of this seemingly unphysical result lies in the slope of the entropy curve (Fig. 4.5C). In contrast to positive temperatures, at negative temperatures entropy increases when heat is extracted from a reservoir. Thus, heat can be extracted from both reservoirs at the same time, while the increase of entropy of the negative temperature reservoir is precisely compensated by a decrease of entropy of the positive temperature reservoir. The work produced by the cycle is therefore, instead of the difference as in the usual case, the sum of both heat quanta, $W = Q_H + Q_C$. Also in this case, entropy flows from the cold to the hot reservoir, in contrast to the usual heat engine at positive temperatures. If this engine is reversed, work must be supplied to increase the energy in both reservoirs simultaneously.

To realize such an engine, however, one would need to find a way to couple these two reservoirs. It turns out that the regions of opposite temperature are not adiabatically connected at $\beta = 0$, i.e. it is not possible to drive a system across the plane $\beta = 0$ without producing entropy [157]. Therefore a Carnot engine that operates between a positive and a negative temperature reservoir through $\beta = 0$ is impossible. Still, it is in principle possible to build an engine that operates between a positive and a negative temperature reservoir where the efficiency, due to the entropy production when crossing $\beta = 0$, is below the Carnot limit but still above unity. Alternatively, the ideal Carnot efficiency can be reached if $\beta = 0$ is not crossed quasi-statically but if a process connects the eigenstates at positive and negative temperature exactly such that no entropy is produced. For example, an ideal π -pulse inverts the population of a two-level system without producing entropy.

Figure 4.6 shows a possible realization of an engine with efficiency above unity in the Carnot sense. It consists of three stable two-level systems as heat reservoirs and working body, e.g. hyperfine states of atoms with negligible spontaneous emission that thermalize via collisions. The working body is initially at very low temperature $T_{W,i} \approx 0$ where

the ground state is predominantly occupied. When the working body is coupled to the cold reservoir at positive temperature $T_C > T_{W,i}$, heat and entropy are transferred to the working body until $T_W = T_C$, i.e. the occupation of the excited state of the working body increases. After decoupling, the working body is coupled to the hot reservoir at temperature $T_H \approx -0$. Again, heat flows into the working body until $T_W = T_H$, corresponding to a strong occupation of the excited state. This heat flow is accompanied by a reverse entropy flow into the hot reservoir. During both couplings, also some entropy is created as these couplings are nonadiabatic processes. After decoupling, a coherent external electromagnetic field is applied to extract the energy from the working body. A π -pulse of the field leads to a de-population of the excited state until $T_W \approx 0$, similarly to the initial state; simultaneously the field is amplified. Thus, work is extracted from the working body which was previously gained from both the cold and the hot reservoirs, leading to an efficiency $\eta > 1$.

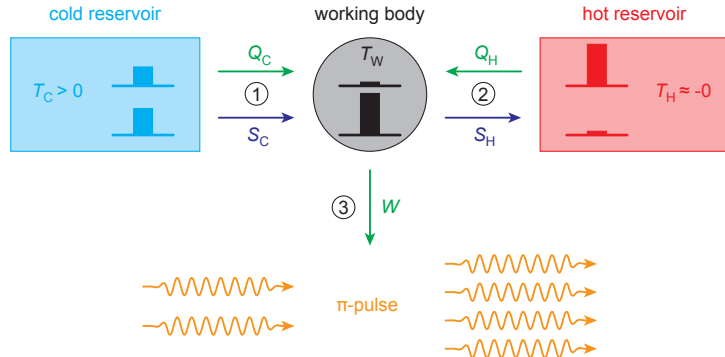


Figure 4.6: Possible realization of a heat engine with efficiency $\eta > 1$. A working body operates between a cold reservoir at positive temperature T_C and a hot reservoir at negative temperature T_H , where all three systems consist of stable two-level systems. The height of the bars schematically indicates the occupation probabilities of the ground and the excited state of the reservoirs and of the initial state of the working body. In steps 1 and 2, the working body is consecutively brought into thermal contact with the two reservoirs and the heat Q_C and Q_H flows during the subsequent thermalization. The corresponding entropy flows are indicated by S_C and S_H . In step 3, work is performed by the working body on an external electromagnetic field, which is applied as a π -pulse. For details, see main text.

4.4.3 Negative Pressure

A thermal gas at attractive interactions and in an anti-trapping potential, such as in our realization of negative temperature, turns out to be at negative pressure. This can be derived via the local density approximation, which assigns an effective chemical potential to each position x in the trapping potential $V(x)$ [33],

$$\mu(x) = \mu_0 - V(x), \quad (4.21)$$

where μ_0 is the chemical potential at the center of the trap. In an inhomogeneous system, also the pressure $P(x)$ depends on the position. Far away from the center, at $x = x_{\text{remote}}$

where the density $n(x)$ of the gas approaches zero, also the pressure vanishes, $P(x_{\text{remote}}) = 0$. The pressure at the center $P_0 = P(x_0)$ can trivially be expressed via an integration along the axis of the trap (Fig. 4.7),

$$P_0 = \int_{P(x_{\text{remote}})}^{P_0} dP. \quad (4.22)$$

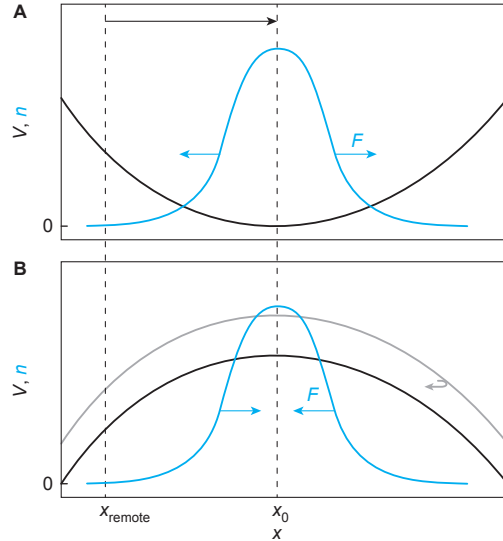


Figure 4.7: Determination of the pressure at the cloud center. The external potential is sketched in black, and the density distribution in blue. The arrow indicates the integration path from a remote position x_{remote} to the cloud center x_0 (see main text). **A**, In the case of a trapping potential, the atomic cloud exerts an outward-pointing force on the external trapping potential. **B**, In the anti-trapping case, the force of the atomic cloud is directed towards the center. The gray curve indicates the upper band edge in the case of an optical lattice at which the atoms are Bragg reflected (gray arrow). For details, see main text.

The pressure differential can be expressed via the Gibbs-Duhem equation $N d\mu = -S dT + \tilde{V} dP$, which relates the intensive properties of a thermodynamical system. Under the assumption of thermodynamic equilibrium, $T = \text{const}$, the pressure differential can be expressed as $dP = n d\mu$, where the density $n = N/\tilde{V}$ is given by particle number N and volume \tilde{V} . Inserting this differential into Eq. 4.22 gives

$$P_0 = \int_{\mu(x_{\text{remote}})}^{\mu_0} n(\mu) d\mu = \int_{x_{\text{remote}}}^{x_0} n(x) \frac{\partial \mu}{\partial x} dx. \quad (4.23)$$

The local density approximation 4.21 allows us to express the chemical potential via the trapping potential, $\partial \mu / \partial x = -\partial V / \partial x$, which yields

$$P_0 = - \int_{x_{\text{remote}}}^{x_0} n(x) \frac{\partial V}{\partial x} dx. \quad (4.24)$$

The density is always greater than zero, $n(x) \geq 0$. The partial derivative of the trapping potential, however, is negative in the case of a trapping potential (Fig. 4.7A) and positive

in the case of an anti-trapping potential (Fig. 4.7B). Therefore, the pressure at the center of the cloud is positive in the case of a trapping potential and negative in the case of a stable gas in thermodynamic equilibrium in an anti-trapping potential. In the former case, the atomic cloud exerts a force onto the trapping potential that is directed from inside to the outside, as usual for a gas at positive pressure that is trapped in a finite volume. In the latter case, however, the cloud exerts an inward-pointing force onto the anti-trapping potential. The origin of this force in our experiment is rooted in the band structure of the optical lattice potential: After transferring momentum onto the anti-trapping potential, corresponding to the lower band edge of the lowest band, the atoms leave the central region of the potential and travel outwards. When reaching the upper band edge, on the other hand, the atoms are Bragg reflected [158] and return towards the trap center (Fig. 4.7B). Attractive interactions between the particles as in our experiment provide an additional contribution of an inward-pointing force.

In the following, I will derive a generalized stability condition for a gas which is applicable to both positive and negative pressures, following the derivation given in our publication [119]. To reach thermal equilibrium, a gas with fixed total energy E that is trapped in a box of volume \tilde{V}_{box} will maximize its entropy S under the given constraints. The volume of the gas \tilde{V} can adopt any value, with the upper limit of \tilde{V}_{box} . Usually, this leads to the condition of a positive pressure P where the gas fills the whole box, $\tilde{V} = \tilde{V}_{\text{box}}$ [60]. In a more general treatment, however, the maximum entropy principle only requires

$$\left. \frac{\partial S}{\partial \tilde{V}} \right|_E \geq 0. \quad (4.25)$$

If the derivate was negative, the gas would spontaneously contract and thereby increase its entropy. Thus, there would not exist an equilibrium solution with $\tilde{V} = \tilde{V}_{\text{box}}$, but instead the gas would be unstable against collapse. The partial derivative can be extracted from the energy differential $dE = T dS - P d\tilde{V}$ as

$$\left. \frac{\partial S}{\partial \tilde{V}} \right|_E = \frac{P}{T}. \quad (4.26)$$

Therefore, in thermal equilibrium, pressure and temperature necessarily have the same sign, $P/T \geq 0$. Negative pressures therefore imply negative temperatures and vice versa.

Usually, a gas with attractive interactions is expected to contract and, in the case of a sufficiently large Bose-Einstein condensate at attractive interactions, even to collapse – it is unstable [27]. In our experiment, however, the gas at attractive interactions and negative pressure in an anti-trapping potential is stabilized against collapse by the negative temperature.

4.4.4 A Possible Relation between Negative Temperature and Dark Energy?

As outlined in the previous paragraph, a gas with attractive interactions and negative pressure is stabilized against collapse by a negative temperature. There is a similarity to

the universe as a whole: All mass and energy contained in the universe exerts a mutual attraction, resulting in an overall force that is directed towards a contraction of the universe. Observations, however, indicate that the universe in contrast expands at an accelerating rate, and is therefore stabilized against collapse [159, 160]. Dark energy is postulated as the driving force for the accelerating expansion and is contained in the cosmological constant Λ in the corresponding equations of general relativity.

By inserting the Friedman-Lemaître-Robertson-Walker metric into the Einstein field equations, one obtains the two Friedman equations [161]:

$$\left(\frac{\dot{a}}{a}\right)^2 = \frac{8\pi G}{3}\rho - \frac{kc^2}{a^2} \quad (4.27)$$

$$\frac{\ddot{a}}{a} = -\frac{4\pi G}{3c^2}(\rho c^2 + 3p) \quad (4.28)$$

Here, $a = a(t)$ is the scale factor, a relative measure for the size of the universe, G the gravitational constant, k the curvature of spacetime which, according to the latest measurements [162], is probably flat ($k = 0$), and c the speed of light. The total energy density ρ contains the contributions from matter ρ_{mat} (both baryonic and dark), radiation ρ_{rad} , and dark energy ρ_Λ , thus $\rho = \rho_{\text{mat}} + \rho_{\text{rad}} + \rho_\Lambda$. Similarly, also the total pressure p is the sum of all three contributions, $p = p_{\text{mat}} + p_{\text{rad}} + p_\Lambda$. The second equation, sometimes also called Friedman acceleration equation, expresses the acceleration of the scale factor in terms of mass and pressure and is therefore fundamental for the future expansion of the universe.

As the movement of particles on a cosmological scale is collisionless at non-relativistic velocities, the pressure of matter can be assumed to be zero, $p_{\text{mat}} = 0$. The pressure of radiation, on the other hand, is related to the energy density via $p_{\text{rad}} = c^2\rho_{\text{rad}}/3$. The pressure of dark energy, finally, is negative and can be expressed via the energy density as $p_\Lambda = -c^2\rho_\Lambda$. Inserting these expressions into the right hand side of Eq. 4.28, one obtains

$$\frac{\ddot{a}}{a} = -\frac{4\pi G}{3}(\rho_{\text{mat}} + 2\rho_{\text{rad}} - 2\rho_\Lambda). \quad (4.29)$$

Today, in contrast to the very early stage of the universe, the energy density of radiation is negligible, $\rho_{\text{rad}} \ll \rho_{\text{mat}}, \rho_\Lambda$. According to the latest research results from the Planck collaboration on the cosmic microwave background, only $\rho_{\text{mat}} = 31.7\%$ of the total energy in the universe consists of dark matter and baryonic matter, while $\rho_\Lambda = 68.3\%$ is made out of dark energy [162]. Therefore, the second derivative of the scale factor is positive and the expansion of the universe accelerates.

Thus, despite attractive interactions between the constituent particles, the universe does not collapse, just like in our experimental realization of negative temperature. In both cases, the pressure of the system is negative. In the case of cosmology, the negative pressure originates from dark energy. As shown in Eqs. 4.25 and 4.26, in a stable system at thermal equilibrium, negative pressure implies negative temperature and vice versa. However, whether there is a connection between negative temperature and dark energy and

whether negative temperature plays a role for the accelerated expansion of the universe is both unclear and rather speculative, as well as being beyond the scope of this work.

4.5 Definition of Entropy

Formally, in the formula introduced above (Eq. 4.2),

$$\frac{1}{T} = \left. \frac{\partial S}{\partial E} \right|_V, \quad (4.30)$$

temperature is defined with the help of entropy S . In this work, I use the standard definition of von Neumann entropy

$$S(\hat{\rho}) = -k_B \text{Tr}(\hat{\rho} \ln \hat{\rho}), \quad (4.31)$$

where $\hat{\rho}$ is the density matrix of the system. In the microcanonical ensemble in thermal equilibrium, this definition is equivalent to the Boltzmann entropy

$$S_B = k_B \ln \Omega(E, V, N) \quad (4.32)$$

that is common in most physics textbooks [163] and established in the great majority of the physics community. For clarity, I denote the Boltzmann entropy here as S_B . In the definition, $\Omega(E, V, N)$ is the number of accessible microstates for a system in a well-defined macrostate, e.g. in the microcanonical ensemble for fixed energy E , volume V , and particle number N . Usually, one counts the number of states in a small interval between E and $E + \delta E$, where δE is chosen arbitrarily. Therefore, entropy is not uniquely defined but only up to an additive quantity. $\Omega(E, V, N)$ is, up to a constant ϵ , given by the density of states $g(E, V, N)$,

$$\Omega(E, V, N) = \epsilon g(E, V, N). \quad (4.33)$$

Temperature can thus be expressed as [164]

$$T_B = \left(\frac{\partial S_B}{\partial E} \right)^{-1} = \frac{1}{k_B} \frac{g}{g'}, \quad (4.34)$$

which I denote for clarity as Boltzmann temperature T_B ; g' indicates the derivative, $g' = \partial g / \partial E$. The Boltzmann temperature is therefore negative when $g' < 0$, i.e. when the density of states is decreasing with energy as on the right-hand side of Fig. 4.2.

While this section is mostly about the microcanonical definition of entropy, it is not clear that our experimental system, with which we create the negative temperature state, is correctly described by the microcanonical ensemble: At the end of the evaporation sequence (Section 2.3.2), the energy E of the system is not clearly defined, as individual realizations of the same sequence may result in different values of E . Thus, the system may be in a mixture of different energies E . Although after evaporation, the system is isolated from the environment, parameter changes (e.g. ramps of the lattice depth or the trap frequency) are still performed externally and may still change the energy E . For example, in the case of ideal adiabatic parameter changes, entropy rather than energy

will be conserved in the system. These deviations from an ideal microcanonical ensemble, however, do not handicap the thermodynamic description of our experimental setup, as in the thermodynamic limit the various ensembles are equivalent if the Boltzmann entropy is concave with respect to energy [165] (cf. Section 4.5.2).

4.5.1 Alternative Entropy Definition

In a recent publication [164], a different definition of entropy S_V was advocated, defined via the integrated density of states $G(E, V, N) = \int_{E_0}^E g(E', V, N) dE'$, with E_0 the ground state energy,

$$S_V = k_B \ln G(E, V, N). \quad (4.35)$$

In this definition, not only all accessible states in a small interval around E are considered, but all energy states from the ground state up to energy E . This definition of entropy was discussed by Gibbs in 1902 [166] and also used by Paul Hertz in 1910 [167], and therefore the authors call it the Gibbs entropy. It should not, however, be confused with the well-known Gibbs entropy formula

$$S_G = -k_B \sum_i p_i \ln p_i, \quad (4.36)$$

where p_i is the probability that the eigenstate i occurs during the fluctuations of the system and which is the classical analog of the von Neumann entropy (Eq. 4.31). The Boltzmann entropy (Eq. 4.32) is a special case of the Gibbs entropy formula where the probabilities of all Ω accessible microstates are equal, $p_i = 1/\Omega$. To avoid confusion, I will therefore call the alternative entropy definition (Eq. 4.35) *volume entropy* S_V , as it takes into account all microstates in a phase-space volume up to a maximum energy. Analogously, the Boltzmann entropy could also be called surface entropy. I will call the temperature following from the volume entropy definition *volume temperature* T_V , which is given by

$$T_V = \left(\frac{\partial S_V}{\partial E} \right)^{-1} = \frac{1}{k_B} \frac{G}{g}. \quad (4.37)$$

Because the density of states g as well as the integrated density of states G are always positive, the volume temperature can never be negative.

Following the definition of volume temperature, all realizations of negative temperatures including the one presented in this work would have to be named differently. Nonetheless, the physical innovation of creating stable systems with population inversion in thermal equilibrium would remain unaffected. It remains to be clarified which statistical entropy definition is correct, i.e. which temperature corresponds to the thermodynamic temperature T , and whether the claim from Ref. [164] is substantiated. The authors in Ref. [164] argue that a consistent thermostatistical model, consisting of a pair (ρ, S) of a density operator

ρ and an entropy potential S , must satisfy the differential structure of thermodynamics,

$$dS = \left(\frac{\partial S}{\partial E} \right) dE + \left(\frac{\partial S}{\partial V} \right) dV + \sum_i \left(\frac{\partial S}{\partial A_i} \right) dA_i \quad (4.38)$$

$$\equiv \frac{1}{T} dE + \frac{P}{T} dV + \sum_i \frac{a_i}{T} dA_i, \quad (4.39)$$

where A_i denotes potential additional external parameters such as magnetic field. To fulfill this equation, the equalities [164]

$$T \left(\frac{\partial S}{\partial A_\mu} \right)_E = - \left(\frac{\partial E}{\partial A_\mu} \right)_S = - \left\langle \frac{\partial \hat{H}}{\partial A_\mu} \right\rangle \quad (4.40)$$

have to be satisfied for any $A_\mu \in \{V, A_i\}$. Here, the second equation requires that thermodynamic quantities are correctly identified with statistical expectation values [164]. The authors show that the microcanonical density operator

$$\hat{\rho}_{mc} = \frac{\delta(E - \hat{H})}{g} \quad (4.41)$$

together with the volume entropy S_V indeed fulfills this equation for any system size, in contrast to the combination $(\hat{\rho}_{mc}, S_B)$ for small systems, and conclude that S_B cannot define a thermodynamic entropy [164]. Additionally, the authors argue that, for classical systems with confined trajectories and finite ground state energy, only T_V fulfills the equipartition theorem for all canonical coordinates, whereas T_B does not [164], at least for small systems.

For typical large systems with unbounded spectra, the differences between the two definitions become negligible, and also the width δE of the energy band in the Boltzmann definition does not play a role: For these large systems, the number of states grows so fast with increasing energy E that almost all states in the energy volume up to E are concentrated around E [168]. For small systems, however, the differences are significant. The authors give several examples of small systems of one or few particles where S_V , in contrast to S_B , produces meaningful results for the heat capacity. For a system with a bounded energy spectrum with lower limit $E_0 = 0$ and upper limit E_+ , however, the two definitions yield different results even in the case of many particles. The authors calculated the entropies and temperatures for a system of N weakly interacting bosonic oscillators [164]. The result (Fig. 4.8) shows that for any energy close to or above half the maximum energy of the system, $E \gtrsim E_+/2$, the two definitions yield fundamentally different temperatures, in particular that the negative (Boltzmann) temperature experiments described in this work are assigned a positive volume temperature.

The temperature that we extract in our experiment by fitting a canonical Bose-Einstein distribution to the one-particle energy distribution, however, yields a negative value (Section 5.3.2). The authors show that the one-particle distribution yields the Boltzmann temperature T_B [164]. They provide a formula that allows the volume temperature T_V to be calculated from T_B [164],

$$T_B = \frac{T_V}{1 - k_B/C}, \quad (4.42)$$

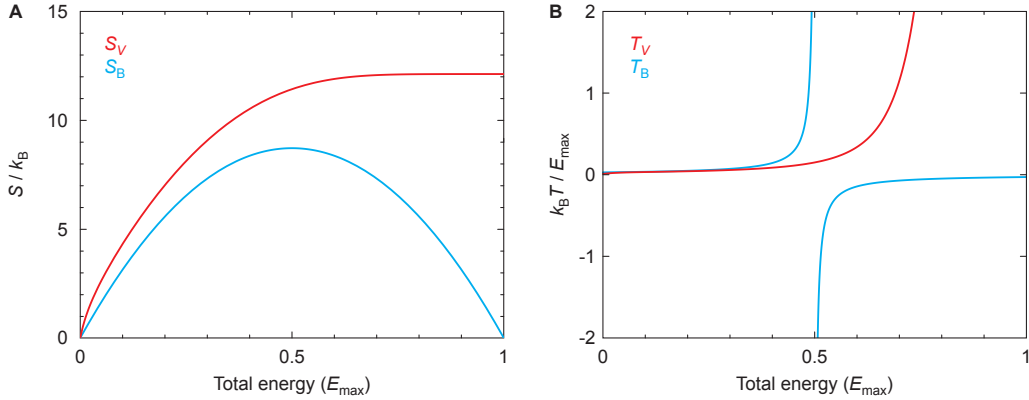


Figure 4.8: Comparison of Boltzmann and volume entropy and the corresponding temperatures. The curves are calculated for a system of 10 weakly interacting bosonic oscillators [164], providing both a lower ($E_{\min} = 0$) and an upper bound E_{\max} for the total energy. **A**, While the Boltzmann entropy S_B decreases again for energies $E > E_{\max}/2$, the volume entropy S_V is monotonically increasing throughout the whole energy range. **B**, The corresponding Boltzmann temperature T_B diverges at $E = E_{\max}/2$ and features a discontinuous jump from positive to negative infinity. For $E > E_{\max}/2$, it is always negative. In contrast, the volume temperature T_V is always positive and increases monotonically up to a finite maximum value T_V^{\max} at $E = E_{\max}$ which depends on the system size. In this case, $k_B T_V^{\max}/E_{\max} \approx 1800$.

which would be positive instead. Here, $C = (\partial T_V / \partial E)^{-1}$ is the total heat capacity associated with T_V .

As described in Section 4.4.2, combining a positive and a negative (Boltzmann) temperature reservoir in an engine leads to Carnot efficiencies above unity. As the volume temperature is always positive, inserting the corresponding volume temperatures into the formula for the Carnot efficiency

$$\eta = 1 - \frac{T_C}{T_H} \quad (4.43)$$

leads to efficiencies that cannot exceed one. The authors argue that an efficiency exceeding one would be impossible [164]. However, as outlined in Section 4.4.2, an efficiency above unity is not at all a physical mystery or in contradiction to energy conservation but simply a consequence of the definition of the Carnot efficiency as the ratio of work performed over the heat that is extracted from the hot reservoir alone.

4.5.2 Problems of the Alternative Entropy Definition

Although a detailed discussion of the correct definition of entropy is outside the scope of this thesis, in this section, I briefly comment on some of the implications of volume entropy. Some of the arguments below can also be found in recent publications [169], including one from our group [170]. The discussion is ongoing [171, 172] and will certainly continue.

Temperature as an ordering relation and the zeroth law of thermodynamics

Temperature as an intensive quantity defines an ordering relation for physical systems: Systems can be arranged in a row, from the coldest to the hottest systems. If two systems are brought into contact, heat will always flow from the hotter to the colder system. This is consistent with the Clausius formulation of the second law of thermodynamics, stating that no process can exist whose only effect is the transfer of heat from a colder to a hotter reservoir. The Boltzmann entropy and temperature definition is consistent with such an ordering relation, if one takes into account that systems at negative Boltzmann temperature are hotter than any system at positive Boltzmann temperature: Heat will always flow from the system with the larger numerical value of Boltzmann temperature to the one with the smaller value of the same sign; if two systems with different sign of Boltzmann temperature are brought into contact, heat will flow from the negative temperature system to the positive temperature one. The parameter $-\beta_B = -1/k_B T_B$ orders the systems from coldest to hottest, also including negative temperatures.

Figure 4.9 shows an example, where a small isolated system with an upper energy bound, consisting of a few particles and described by the microcanonical ensemble, may be prepared at negative Boltzmann temperature $T_B^s < 0$ ($-\beta_B^s > 0$), i.e. with a stable population inversion. Additionally, a large system, i.e. a thermal bath, may be prepared at large positive temperature, $T_B^b \rightarrow \infty$ ($-\beta_B^b \approx 0$). If these two systems are brought into weak thermal contact, heat will flow from the small system to the bath. In equilibrium, the small system, which is then described by the canonical ensemble, will have attained the positive temperature T_V^b of the bath and the population inversion will have vanished. This heat flow, as stated above, is correctly predicted via Boltzmann temperature.

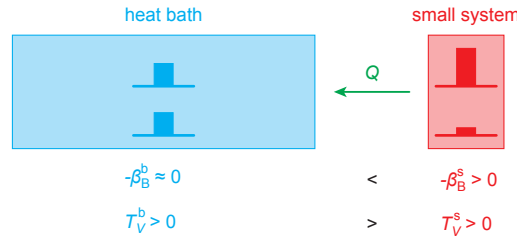


Figure 4.9: Temperature as an ordering relation. When a small system at negative Boltzmann temperature is coupled to a large bath close to infinite Boltzmann temperature, heat Q flows from the small system to the bath. This is consistent with the ordering of the systems via Boltzmann temperature, but not via volume temperature. For details, see main text. The filled rectangles illustrate the occupation of the energy levels in the systems.

Following the definition of volume entropy, however, the same small system is initially at a positive, finite volume temperature T_V^s . In finite systems, the value of the volume temperature reaches a finite, positive value T_V^{\max} in the limit of maximum energy [164]. This finite value and also the overall $T_V(E)$ curve in Fig. 4.8B depend on the specific system, especially on system size. For a large bath, the bath temperature in the above example will be at a volume temperature that is larger than the one of the small system

with population inversion, $T_V^b > T_V^s$. The observed heat flow in this case therefore happens from the system at lower volume temperature to the system at higher volume temperature. Volume temperature therefore does not constitute an ordering relation for physical systems, in contrast to Boltzmann temperature.

Just knowing the value of volume temperature of two systems is therefore not sufficient in determining which system is actually hotter. As a consequence, two systems that are in thermal equilibrium with each other may have different volume temperatures, violating the zeroth law of thermodynamics. This also becomes evident from Eq. 4.42: Two systems in thermal equilibrium possess the same Boltzmann temperature, and one may calculate the corresponding volume temperatures from this equation. As this equation, however, includes the total heat capacity C , the volume temperatures depend on system size and are, in general, not equal.

Consistency with other ensembles

An isolated system, where particle and heat exchange with the environment may be neglected, is well-described by the microcanonical ensemble. It is, however, also possible to describe a large system with weak couplings between its constituents approximately within the framework of the canonical or grand-canonical ensemble: A small subsystem, for example a single atom in the final stage of our experiment where interactions are weak, is coupled to the rest of the system, e.g. 10^5 atoms, which may be considered as a heat bath. The subsystem is in thermodynamic equilibrium with the bath and can therefore approximately be described by the canonical ensemble. The one-particle energy distribution is in the classical limit described by the famous Boltzmann distribution Eq. 4.1. The canonical temperature $T = T_{\text{can}}$ in the Boltzmann formula is negative for a thermal state with population inversion. This temperature turns out to be identical to the Boltzmann temperature, $T_{\text{can}} = T_B$, of the microcanonical ensemble [164].

The suggestion for the alternative volume entropy definition applies to the microcanonical ensemble [164]. The definition of temperature T_{can} in the canonical ensemble remains unaffected. The authors provide Eq. 4.42 which allows the measured canonical temperature $T_{\text{can}} = T_B$ to be converted into volume temperature T_V , which is in general different. Hence, following the definition of volume entropy, the temperature of the system as a whole is different from the individual temperature of any subsystem. The temperature of an isolated system would thus have lost its role as the parameter that controls equilibrium of one part of the system with another [163]. The definition of volume entropy also renders the equivalence of ensembles impossible. In contrast, the equivalence of ensembles is established in the thermodynamic limit in the case of Boltzmann entropy if it is concave with respect to energy as in Fig. 4.8A [165].

5 Realization of Negative Absolute Temperatures

This chapter is closely based on our publication *Negative Absolute Temperature for Motional Degrees of Freedom* [119]. In the first section of this chapter, I describe the experimental realization and observation of negative absolute temperatures in a two-dimensional system. In the second section I show results of stability measurements of the negative temperature state. In the third section I demonstrate how the energy distribution and the temperature of the final state can be approximately determined and compare this temperature to critical temperatures for both the superfluid and the Bose-Einstein condensation transition. In the fourth section I describe how we derive an approximate coherence length of the final phase-coherent state at negative temperature. Finally, the fifth section deals with the realization of negative temperature states in one and three dimensions.

5.1 Experimental Sequence and Images

In this section, I describe the experimental sequence for the creation of negative temperature states in a two-dimensional system where the vertical lattice is very deep, creating isolated two-dimensional layers of atoms. I also show an analogous sequence for a standard positive temperature state for comparison. Some emphasis in this chapter is put on details of the inversion of the external harmonic confinement. Resulting time-of-flight images are shown for both negative and positive temperatures.

5.1.1 Experimental Sequence

The initial state of ultracold atoms experiments is necessarily always at positive temperature. In order to realize negative temperatures, at some point the transition has to be made between the two. For the transition, we choose a state which is an eigenstate of the Hamiltonian in both the repulsive and attractive regime, such that the transition does not trigger any dynamics in the system and the final negative temperature state is stable. Such a state is given by an $n = 1$ Mott insulator close to the atomic limit, $|U|/J \rightarrow \infty$, which can be approximated by a product of Fock states, $|\Psi\rangle = \prod_i \hat{a}_i^\dagger |0\rangle$, where \hat{a}_i^\dagger is the creation operator for a boson on lattice site i . The general idea of the sequence (Fig. 5.1) is based

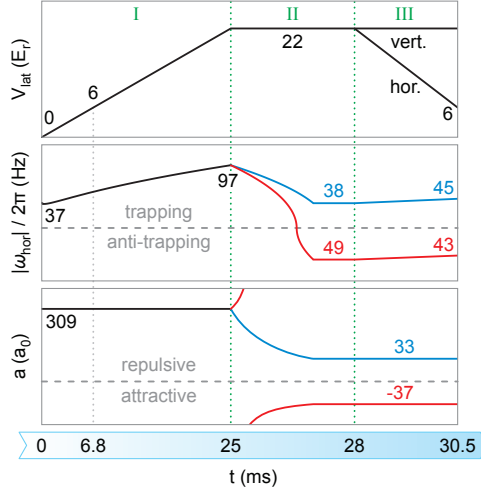


Figure 5.1: Experimental sequence for the creation of negative temperatures in 2D. The lattice depth V_{lat} , horizontal trap frequency ω_{hor} and scattering length a are plotted versus time t . The sequence for a final negative temperature state is red, and blue for a positive temperature state. In the negative temperature case, the magnetic field crosses a Feshbach resonance and thus the scattering length diverges.

on a proposal by A. Rapp et al. [7], building on earlier works by A. P. Mosk [6]. It consists of loading a repulsively interacting BEC into an optical lattice deep in the Mott insulating regime (region I), changing U and V to negative values (region II) and finally melting the Mott insulator by decreasing $|U|/J$ again via a lattice ramp (region III). For comparison, we also created a positive absolute temperature state with a corresponding sequence.

We initially prepared a condensate of $N = 1.1(2) \times 10^5$ ^{39}K at positive temperature in an oblate dipole trap with trapping frequencies of $\omega_{\text{hor}} = 2\pi \times 37(1)$ Hz and $\omega_{\text{vert}} = \omega_z = 2\pi \times 181(12)$ Hz along the horizontal and vertical directions, respectively. The horizontal trap frequency is given by the root mean square of the trapping frequencies along the two horizontal directions, $\omega_{\text{hor}} = \sqrt{(\omega_x^2 + \omega_y^2)/2}$. The condensate is essentially pure since in time-of-flight images the thermal cloud around the condensate is below the detection limit. We linearly ramped up a three-dimensional optical lattice (region I in Fig. 5.1) with simple cubic symmetry and of wavelength $\lambda_{\text{lat}} = 736.65$ nm within 25 ms to a lattice depth of $V_{\text{lat}} = 22(1)$ E_r . The scattering length during the lattice loading ramp was large at $a = 309(5)$ a_0 , giving a very large value $U/J > 800$ and minimizing doubly occupied sites in the Mott insulating state. When crossing the Feshbach resonance to the attractive side, these double occupancies would result in atoms excited to higher bands [173]. During the loading, we increased the trapping frequencies to $\omega_{\text{hor}} = 2\pi \times 97(4)$ Hz and $\omega_{\text{vert}} = 2\pi \times 215(13)$ Hz by changing the power of the dipole trap beams in order to increase the fraction of atoms within the Mott insulating core.

In the deep lattice (region II), the tunneling time is large at $\tau = h/2\pi J = 10(2)$ ms, and therefore tunneling is essentially negligible. Once in the deep lattice, we ramped the

magnetic field B within 2 ms to its final value. Due to a Feshbach resonance at $B = 402.50(3)$ G [30] this changes the scattering length to either a positive, repulsive value at $a = 33(1) a_0$ or a negative, attractive value at $a = -37(1) a_0$. In both cases, the system stays in the Mott insulating regime at $|U/J| > 80$. Simultaneously with the magnetic field ramp, we decreased the horizontal trap frequency to $\omega_{\text{hor}} = 2\pi \times 39(4)$ Hz in the repulsive case by decreasing the power of the dipole trap beams. In the attractive case we changed to the maximum possible anti-trapping potential with a formally imaginary trap frequency of $|\omega_{\text{hor}}| = 2\pi \times 49(1)$ Hz by reducing the power of the dipole trap beams to zero.

After a hold time of 1 ms, we linearly decreased the horizontal lattice depth (region III) within 2.5 ms to $V_{\text{hor}} = 6.1(1) E_r$, resulting in final values of $U/J = -2.1(1)$ in the attractive case and $U/J = +1.9(1)$ in the repulsive case. We kept the vertical lattice depth at $V_{\text{vert}} \approx 22(1) E_r$ to avoid adverse effects due to gravity and to enable strong anti-trapping potentials (Section 5.1.2). During this lattice ramp, we kept the dipole trap beams turned off, resulting in trapping frequencies that change only marginally.

For imaging, we instantly switch off all optical potentials and subsequently ramped down the homogeneous magnetic field within 2 ms to zero. After a total time-of-flight (TOF) of 7 ms, we recorded absorption images along the vertical direction. For a sufficient transformation of the imaged atomic distribution from real space into momentum space, one would ideally want to use longer TOF. However, since for longer TOF also the optical density (and therefore the signal-to-noise ratio in the images) decreases due to the expansion of the cloud, the chosen TOF is a compromise. The whole sequence was experimentally optimized to maximize the visibility of the final interference pattern at negative temperature.

5.1.2 Inversion of the External Potential

In principle, negative temperature states can also be created in three dimensions, by additionally inverting the vertical trapping potential. In the experiment, however, this inversion would also result in an inversion of the gravitational sag. The atoms would therefore experience a strong vertical gradient at their position, leading to Bloch oscillations and dephasing between lattice sites. This problem could be circumvented by additionally applying a vertical magnetic field gradient. However, in our experiment, we chose a different approach by keeping the vertical lattice strong, which provides an additional experimental advantage: As the anti-trapping potential is generated by the lattice beams, the more intense vertical lattice beam allows higher anti-trapping potentials of up to $|\omega_{\text{hor}}| = 2\pi \times 43(1)$ Hz in the final shallow lattice compared to the creation of negative temperature states in three dimensions. The challenges of the realization of negative temperatures in three dimensions with our setup are also detailed in Section 5.5.2.

In the chosen two-dimensional lattice setup, to exactly invert the potential energy term of the Hamiltonian, the horizontal confinement should have been precisely inverted, from the initial trap frequency of $\omega_{\text{hor},i} = 2\pi \times 97(4)$ Hz to the final value of $|\omega_{\text{hor},f}| = 2\pi \times 97$ Hz. In the case of the interaction energy term, the Feshbach ramp should have provided a final scattering length a_f which is precisely inverted compared to the initial one $a_i = 309 a_0$,

$a_f = -309 a_0$. The final sequence then should have precisely imaged the loading sequence. However, in the experiment, a precise inversion of the trapping potential would only be possible with the help of additional blue-detuned anti-trapping beams, which were not available during the measurements for this work but could be a future improvement of the experimental setup.

The available lower anti-trapping trap frequency of $|\omega_{\text{hor}}| = 2\pi \times 43(1)$ Hz would require a large amount of mass redistribution during ramp-down: During the ramp, the atomic distribution follows the change in U/J to realize the transition from the flat-top $n = 1$ distribution in the Mott insulating state to the parabolic Thomas-Fermi distribution in the superfluid regime. This redistribution guarantees that the chemical potential across the system stays flat during ramp-down. If the atoms were not able to achieve this change, the resulting inhomogeneous chemical potential would lead to dephasing between lattice sites, reducing the phase coherence of the final, ideally superfluid state. To prevent the adverse dephasing effect, we have optimized the visibility of the interference pattern and therefore the phase coherence of the final state by adjusting the scattering length a . The resulting reduced value of $a = -37(1) a_0$ partially compensates the reduced trap frequency and thereby minimizes the total amount of redistribution during ramp-down. A detailed analysis of the dynamics during lattice ramp-down in an external potential can be found in Chapter 6, and especially in Section 6.3.3.

Concerning the ramp time, ramping down the lattice within 25 ms as in the loading sequence is in principle possible and leads to a comparable final visibility that is only 4 % below the visibility for the chosen 2.5 ms ramp. The small reduction of the visibility originates from the minimized, yet inevitable dephasing that increases with longer ramp times. Only in the limit of an adiabatic lattice ramp, where the chemical potential is homogeneous throughout the entire ramp, would dephasing not be present. However, heating effects limit the final visibility in this regime (Section 6.3.3). Overall, in order to minimize dephasing, a ramp time of 2.5 ms turned out to be ideal experimentally. Despite the rather short ramp time, the obtained stability of the final state (Section 5.2) shows that the created states are sufficiently close to equilibrium.

5.1.3 Resulting TOF Images

Figure 5.2 shows TOF images for various times during the sequence, which are indicated in Fig. 5.1. Interference peaks of the initial superfluid during lattice ramp up, at $V_{\text{lat}} = 6.1(1) E_r$ ($t = 6.8$ ms, top image) are visible, indicating phase coherence across the system. The strong incoherent background, however, results from the strong repulsive interactions due to quantum depletion [174]. To obtain an image that is comparable to the final positive and negative temperature images, we also show an analogous image for identical dipole trap and lattice ramps, but at a scattering length of $a = 33(1) a_0$ ($t = 6.8$ ms, bottom image). As soon as the Mott insulating regime is entered, the interference peaks vanish ($t = 25$ ms). After changing the scattering length to weaker positive ($t = 28$ ms, top image) or negative (bottom image) values, only weak nearest-neighbor correlations are expected, resulting in

similar (but not identical) images for the two cases.

After reducing the depth of the horizontal lattices, and thereby entering the superfluid regime again, the coherence peaks reappear. For positive scattering length ($t = 30.5$ ms, top image), the image is comparable to the initial image during lattice loading for the same interaction ($t = 6.8$ ms, bottom image), although the peaks are somewhat broadened due to heating during the experimental sequence. The high central peak indicates strong occupation of the $\hbar q = 0$ state at minimum kinetic energy, with higher order peaks at $\hbar q = \pm 2\hbar k_{\text{lat}}$ in both directions. In the case of attractive interactions, however, the center of the Brillouin zone is only weakly populated, while sharp peaks show up in the corners of the Brillouin zone, again with higher order peaks. These peaks indicate a strong occupation of the $\hbar q = \pm \hbar k_{\text{lat}}$ state in both directions, which is at maximum kinetic energy. The spontaneous development of these sharp peaks is the smoking-gun signature for the formation of a negative temperature state for motional degrees of freedom: The highest total energy state, which in the case of a shallow optical lattice corresponds to the highest kinetic energy state, is occupied the strongest, thus constituting an inverted population distribution. There are in principle two possible routes to enter the negative temperature regime: Either the system stays close to thermal equilibrium throughout the entire lattice sequence, or alternatively the system relaxes towards a thermal negative temperature distribution during lattice ramp-down. Either of these options shows the thermodynamic stability of the negative temperature state.

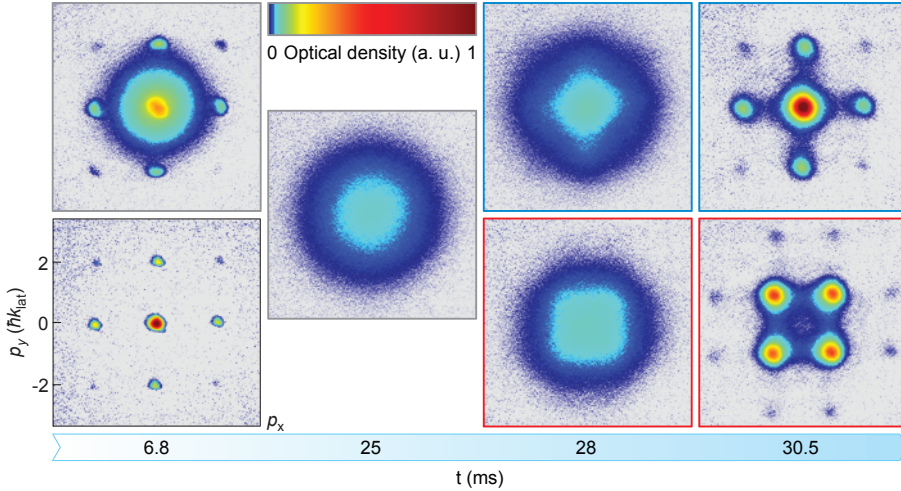


Figure 5.2: Time-of-flight images at various times during the sequence as indicated in Fig. 5.1. Blue borders indicate the sequence for the final positive temperature state, red for the negative temperature state. The initial picture at $t = 6.8$ ms is taken once for a scattering length of $a = 309(5) a_0$ as used in the sequence, and once for $a = 33(1) a_0$. The latter image, where the optical density is rescaled by a factor of 0.25, is comparable to the final images at $t = 30.5$ ms. All images are averages of approximately 20 individual shots.

5.2 Stability of the Negative Absolute Temperature State

In this section I describe the measurements of the stability of the negative temperature state, as well as the positive temperature state for comparison. The influence of trap frequency as well as the effect of interactions on the stability are discussed.

5.2.1 Stability versus Trap Frequency

To investigate the stability of the final negative and positive temperature states, we perform the sequence outlined in the previous section to create these states. Instead of immediately switching off all trapping potentials, however, we hold the cloud for variable times in the final shallow lattice at $V_{\text{hor}} = 6.1(1) E_r$ and $V_{\text{vert}} = 22(1) E_r$. After this hold time, we switch off all trapping potentials and the magnetic field and record images after 7 ms TOF, as described in the previous section.

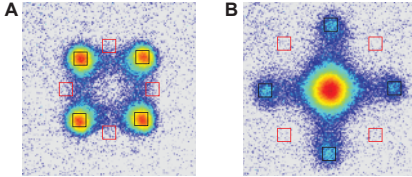


Figure 5.3: Extraction of visibility. The total atom number in the black (n_b) and in the red boxes (n_r) is determined via area sums. The visibility V is calculated according to Eq. 5.1. Due to the different symmetries of the **A**, negative and **B**, positive temperature states, the position of the boxes is different in the two cases.

As a quantitative measure for the quality of the states, we extract the visibility V of the interference pattern in the TOF images,

$$V = \frac{n_b - n_r}{n_b + n_r}, \quad (5.1)$$

where n_b and n_r count the total number of atoms in the black and red boxes, respectively. Since the negative and the positive temperature states have different symmetry, we define the visibility differently for the two cases (Fig. 5.3).

The resulting visibilities are plotted in Fig. 5.4 versus hold time along with exponential fits to the decay. The extracted lifetimes from the fits are shown in Fig. 5.5. For the optimal anti-trapping potential with a trap frequency of $\omega_{\text{hor}} = 2\pi \times 43(1) \text{ Hz}$, the lifetime of the negative temperature state exceeds 600 ms and is just as long as for the analogous positive temperature state. From the point of view of statistical mechanics, the high stability of the negative temperature state is rooted in the maximum entropy principle: The chosen experimental sequence has put the system into a state of high internal energy E , which, as the system is isolated, is conserved. For the given energy E , the negative temperature state is the state with maximum entropy which therefore has to be stable. The stability of

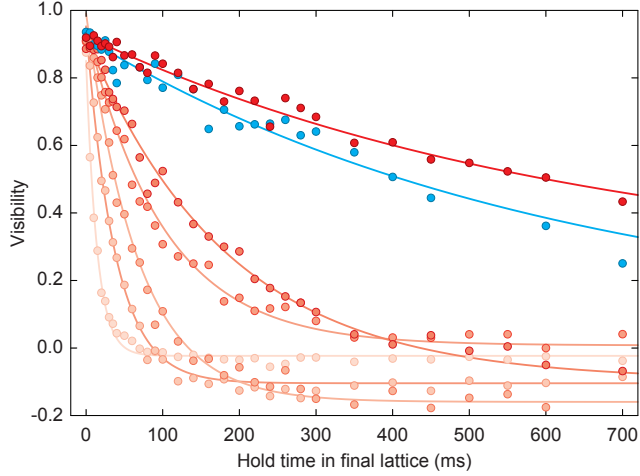


Figure 5.4: Stability of the final negative temperature state. Red data points are measurements for attractive, blue for repulsive interactions. For attractive interactions, we performed the measurement for various trap frequencies, from dark to light, $|\omega_{\text{hor}}|/2\pi = 43(1)$ Hz, $22(3)$ Hz and $6(8)$ Hz anti-trapping, $21(4)$ Hz, $42(3)$ Hz, $85(4)$ Hz trapping. The positive temperature data is taken at $45(3)$ Hz trapping. The solid lines are exponential fits. For the strongest anti-trapping potential, the lifetime of the negative temperature state is as long as that of the positive temperature state.

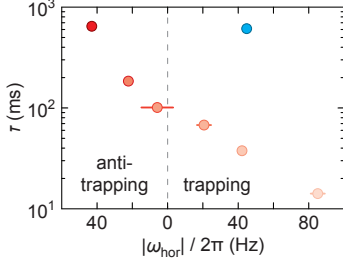


Figure 5.5: Coherence lifetimes. The lifetimes τ are obtained from the exponential fits in Fig. 5.4. Red data points are for attractive interactions, blue for repulsive. The color scale is the same as in Fig. 5.4. The lifetime for the strongest anti-trapping potential is similar to the lifetime of the positive temperature state.

the negative temperature state can also be explained in an intuitive picture by the energy bounds present in the system: Usually, one would expect the atoms at maximum potential energy to follow the potential gradient and thereby reduce their potential energy such as a ball on top of a hill. In the isolated system, potential energy can only be reduced by converting it into either interaction or kinetic energy. Because of the energy bounds in the system, both of these are limited from above. The many-body ground state at a negative temperature close to $T = -0$ K in the shallow lattice maximizes the sum of interaction and kinetic energy such that this sum cannot increase any further. Therefore, there is no channel available to absorb energy and the potential energy cannot be reduced. Thus, the

atoms stay at maximum potential energy; more generally, they remain at their maximum energy many-body state and are stable. Although it is intuitive that the ground state of the system is a stable state, the same argument can also be applied to the positive temperature case: In this case, the potential energy of the atoms is close to the minimum, and also the sum of interaction and kinetic energy of the many-body state is minimized. Therefore, also in this case, energy cannot be converted from one form to another, rendering the many-body state stable.

Figures 5.4 and 5.5 also show the same measurement for different trap frequencies. In the deep lattice, instead of realizing the optimal trap frequency, we ramped within 2 ms to various different intensities for the vertical dipole trap beam, resulting in different trapping frequencies. The measurement shows that in the case of non-optimal trapping frequencies, the lifetime drops quickly. In these cases, the required redistribution of atoms during lattice ramp-down when crossing the Mott to superfluid transition is not minimized, and thus cannot be achieved during the relatively short ramp time of 2.5 ms. Therefore, the chemical potential at the end of the lattice ramp is less homogeneous across the system, and dephasing between lattice sites is stronger. The dephasing is responsible for the decay of visibility when holding the final state in the shallow lattice, and becomes faster the more the trapping potential deviates from the optimal one.

For weak trapping potentials (i.e. small real trap frequencies) the visibility can even reach negative values after hold times of around 100 ms. In the case of a trapping potential – in contrast to an anti-trapping one – the system is no longer bounded from above and the negative temperature state is no longer stable. In this case, the atoms are able to partially convert kinetic energy into potential energy, leading to a stronger occupation of the $\hbar q = 0$ state. The corresponding TOF images then rather resemble a positive temperature state (e.g., Fig. 5.6 for a trapping potential of $\omega_{\text{hor}} = 2\pi \times 21$ Hz and $t_{\text{hold}} = 700$ ms). When evaluating the visibility as defined for the negative temperature state, this results in negative values.

Time-dependent Gutzwiller mean-field theory calculations [175] show that in the case of trapping potentials, the attractively interacting cloud is also allowed to expand by clustering, i.e. by creating higher occupation on individual lattice sites, and thereby reducing interaction energy and converting it into potential energy. This expansion is shown to be strongest in the case of small trapping frequencies, ultimately also leading to atoms completely leaving the trap [175]. Experimentally, we also observe a strong loss of atoms in the case of small absolute trapping frequencies for both trapping and anti-trapping potentials where the trapping potential is essentially flat (Fig. 5.6 for an anti-trapping potential of $|\omega_{\text{hor}}| = 2\pi \times 6$ Hz and $t_{\text{hold}} = 700$ ms). For small absolute trapping frequencies and long hold times, distortions are visible in the TOF images. These can be attributed to residual deviations of the trapping potential from the purely harmonic case, which are most severe far away from the trap center. The expanding clouds in the case of small absolute trapping frequencies probe these deviations and are thus distorted.

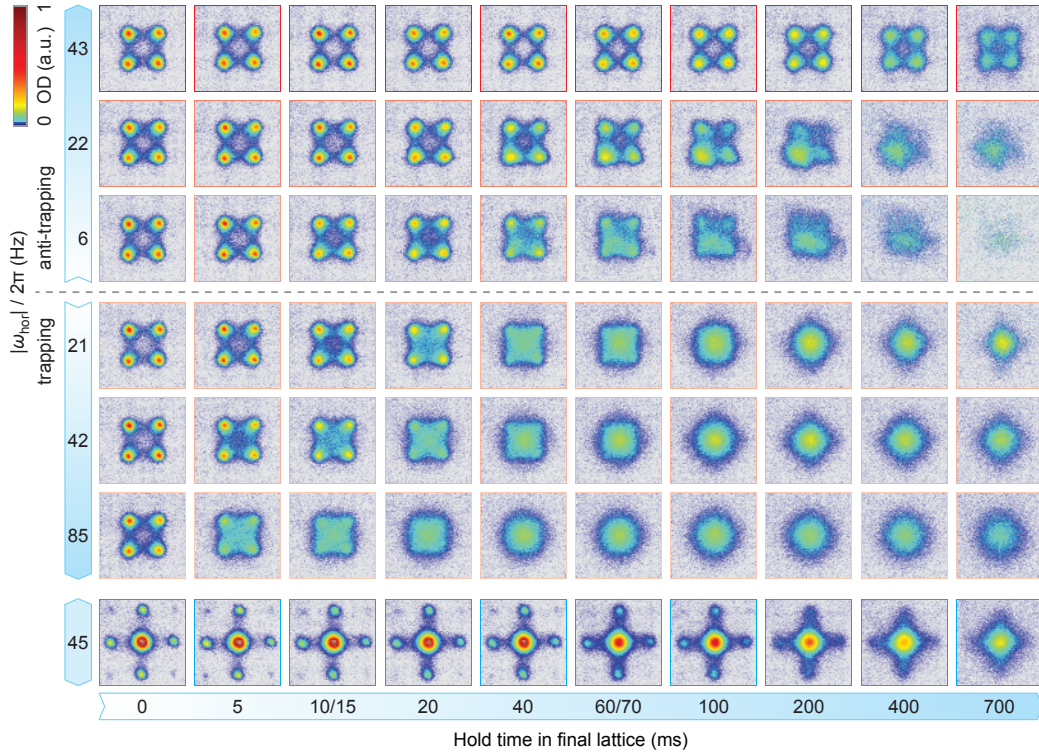


Figure 5.6: Sample time-of-flight images for the determination of visibility plotted in Fig. 5.4. Red frames indicate attractive, blue frames repulsive interactions. Qualitatively, the loss of coherence over time can be observed in these images. In the case of attractive interactions, this happens faster for less anti-trapping potentials. For long hold times, atom losses and distortions are visible mainly in the case of weak external potentials (see main text).

5.2.2 Stability versus Interaction

We also investigated how the lifetime of the final negative and positive temperature states changes for various interactions. For these measurements, we chose a final anti-trapping potential with trap frequency $|\omega_{\text{hor}}| = 2\pi \times 43(1)$ Hz but ramped the scattering length within 2 ms to different values than the previously optimized ones of $a = 33(1) a_0$ and $a = -37(1) a_0$. We then kept the scattering length fixed during lattice ramp-down. Despite the similarity in the protocol, there is an important difference in this measurement compared to the previous trap frequency measurement: As U/J is proportional to the scattering length a , choosing different a values results in different initial and final values of U/J for the lattice ramp. The Mott to superfluid quench induced by the lattice ramp therefore reaches differently deep into the superfluid regime.

We evaluated the data identically to the previous measurement, by extracting the visibility for various hold times. The results are plotted in Fig. 5.7, together with exponential fits. We find that the small scattering length of $a = -37 a_0$ is optimal, giving the largest lifetime of 890(50) ms (Fig. 5.8). Negative scattering lengths even closer to zero are technically

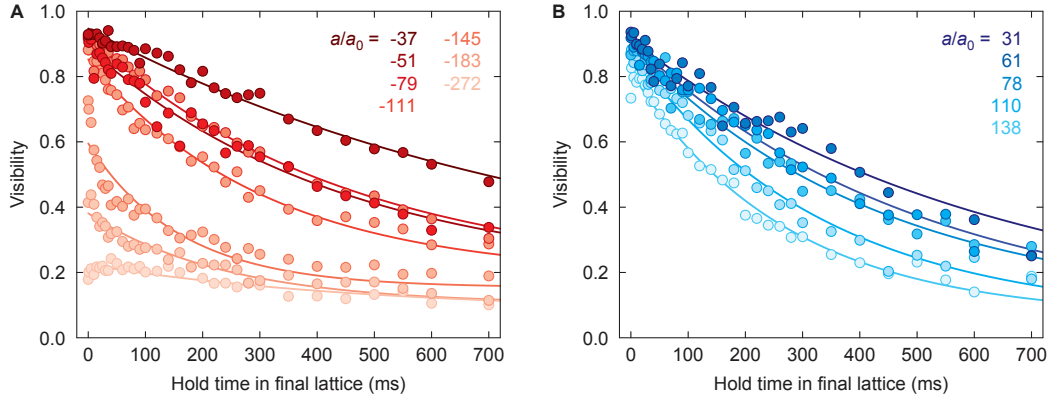


Figure 5.7: Visibility of the final negative (**A**) and positive (**B**) temperature states versus hold time for various scattering lengths. The visibility is evaluated as in Fig. 5.3. In both cases, the stability of the state is maximized for rather small scattering lengths. The reduced visibility at zero hold time for strong interactions is caused by the reduced coherence length of a system that is closer to the Mott insulating regime. Solid lines are exponential fits.

challenging to reach as they are located at small magnetic fields, due to the background scattering length $a_{\text{bg}} = -29.0(3) a_0$ [30] of the Feshbach resonance (cf. Section 2.1.3). For stronger attractive interactions, already the initial visibility decreases. This can be explained by the different final $(U/J)_f$ values, which can be as large as $(U/J)_f = -10$ in the case of $a = -183 a_0$. As the critical value for the Mott to superfluid transition is at $(U/J)_c = 16.7$ [105], this value is not very deep in the superfluid regime, reducing the observed visibility of the interference pattern. The reduced lifetime for scattering lengths which differ from the optimal one can again be understood via dephasing: The potential of the mean-field interaction of the atomic cloud effectively modifies the external potential experienced by the atoms. Therefore, for some interaction strength, the mean-field potential is optimal in terms of the mass redistribution which is required during the Mott to superfluid transition in order to obtain a homogeneous chemical potential. If the required redistribution is too large for the ramp duration, the cloud cannot follow the ramp adiabatically but instead will be excited, resulting in an inhomogeneous chemical potential across the cloud. The inhomogeneous chemical potential causes dephasing between lattice sites, which in turn reduces the visibility of the interference pattern over time (cf. Section 6.3.3).

We also performed analogous measurements in the case of a final positive temperature state. We observe the same behavior, with the longest lifetime of 610(50) ms for a relatively weak scattering length of $a = 31 a_0$. The lifetime also drops for stronger interactions. The similarity of the optimal scattering lengths for both cases is caused by the similar trapping frequencies of $|\omega_{\text{hor}}| = 2\pi \times 43(1)$ Hz for an anti-trapping potential in the negative temperature case and of $\omega_{\text{hor}} = 2\pi \times 45(3)$ Hz for a trapping potential in the positive temperature case which we chose intentionally. We therefore expect similar atomic distributions in both cases and therefore also similar optimal interaction strengths. This measurement also

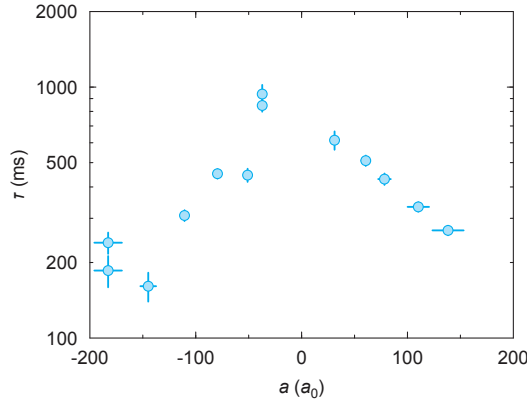


Figure 5.8: Coherence lifetimes of positive and negative temperature states for various scattering lengths a . The lifetimes τ , obtained from the exponential fits in Fig. 5.7, reveal that rather weak interactions are optimal in both cases. They also highlight the symmetry between positive and negative temperature states.

highlights the strong symmetry between negative and positive temperature distributions.

5.3 Extraction of Energy Distribution and of Absolute Temperature

In this section I present how we extracted the kinetic energy distribution from the measured quasimomentum distributions. I also show how we determined the temperature of the negative and positive temperature states, by fitting Bose-Einstein distribution functions to the measured quasimomentum distribution. We compared the measured temperatures to estimated critical temperatures for condensation and the superfluid transition in the two-dimensional system.

5.3.1 Determination of Energy Distribution

To measure the quasimomentum distribution experimentally, we applied band-mapping before imaging (Section 3.4.4). For both negative and positive temperature cases, we took about 20 individual images and averaged them. As the TOF of $t_{\text{TOF}} = 7 \text{ ms}$ is finite, the measured distributions do not represent the pure quasimomentum distributions, but are still convolved with the *in situ* density distribution. Since the lattice beams in the experimental setup are not perfectly orthogonal, the first Brillouin zone is not represented by a perfect square in the TOF images. We corrected this slight asymmetry in the negative temperature images by fitting the positions of the four peaks in an image and subsequently applying a shearing transformation to all images, thereby mapping the first Brillouin zone onto a square. In the case of the positive temperature images, we extracted the necessary shearing transformation from the fitted positions of the first order coherence peaks in a

TOF image without band mapping. Additionally, due to slight experimental asymmetries, the four peaks in the negative temperature images do not have the same amplitudes. As a correction, we multiplied the averaged image with a linearly interpolated normalization map. We did not apply an analogous normalization to the averaged image at positive temperature as there is only a single sharp peak present. The resulting averaged images are shown in Fig. 5.9.

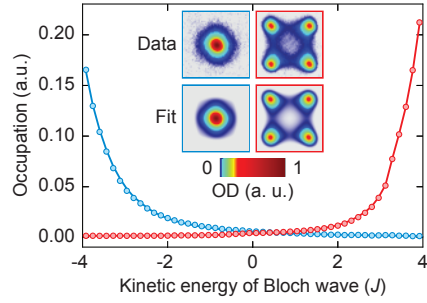


Figure 5.9: Occupation distributions. The data points show the measured occupation of kinetic energies within the first Brillouin zone for the final negative (red) and positive (blue) temperature state, highlighting the population inversion of the negative temperature state. These data points are extracted from time-of-flight images with band-mapping technique (top insets), showing the quasimomentum distribution. The originally recorded images were symmetrized and are still broadened by the in situ cloud size and the imaging system. The solid lines in the main graph show the occupation of the kinetic energies for the fitted distributions, showing very good agreement with the measured distributions. The kinetic energy distributions are derived from the fitted quasimomentum distributions (bottom insets) with a noninteracting Bose-Einstein distribution assuming a homogeneous system, and show qualitatively good agreement with the measured TOF distributions. The broadening of the experimental images has been included in the fitted distributions as well.

To extract the energy occupation we assign the corresponding quasimomentum ($\hbar q_x, \hbar q_y$) to each pixel in the two-dimensional image by employing the fitted peak positions used for the shearing transformation. This gives the quasimomentum distribution $n_{\text{exp}}(q_x, q_y)$ in the first Brillouin zone, where we neglect atoms imaged beyond the first Brillouin zone. This quasimomentum distribution, however, is still convolved with the in situ density distribution and therefore an approximation to the real distribution. By using the tight-binding dispersion relation at the given lattice depth (Eq. 3.16),

$$E_{\text{kin}}(q_x, q_y) = -2J \left[\cos\left(\pi \frac{q_x}{k_{\text{lat}}}\right) + \cos\left(\pi \frac{q_y}{k_{\text{lat}}}\right) \right], \quad (5.2)$$

we obtain the kinetic energy distribution $n_{\text{exp}}(E_{\text{kin}}(q_x, q_y))$, i.e. the number of atoms with a given kinetic energy. This model neglects interaction and potential energy. To obtain the occupation $\rho_{\text{exp}}(E_{\text{kin}})$ per Bloch wave, we normalized the kinetic energy distribution by the numerically calculated density of states in the two-dimensional optical lattice $D_2(E_{\text{kin}})$,

$$\rho_{\text{exp}}(E_{\text{kin}}) = n_{\text{exp}}(E_{\text{kin}}(q_x, q_y))/D_2(E_{\text{kin}}). \quad (5.3)$$

The result is shown as the data points in Fig. 5.9, demonstrating the expected exponentially increasing and decreasing occupation functions.

5.3.2 Fitting a Bose-Einstein Distribution

To obtain an estimate for the temperature of the negative and positive temperature states, we fitted the experimentally extracted quasimomentum distribution $n_{\text{exp}}(q_x, q_y)$ with a Bose-Einstein distribution function for the kinetic energy (neglecting interaction and potential energy),

$$n_{\text{fit}}(q_x, q_y) = \frac{1}{e^{(E_{\text{kin}}(q_x, q_y) - \mu)/k_B T} - 1} + o, \quad (5.4)$$

where independent fitting parameters are the chemical potential μ , the absolute temperature T , and a constant offset o . We convolved this distribution with an elliptical Gaussian function to take into account the convolution with the in situ distribution after finite TOF and the expansion of the cloud along the vertical direction during time-of-flight: Since the vertical lattice axis, along which the cloud expands, and the imaging axis are not perfectly parallel, the vertical expansion of the cloud is projected into the imaging plane and appears in the TOF images as a convolution of the cloud with an elliptical Gaussian.

In the case of the negative temperature image, we fixed both the aspect ratio and the rotation angle of the elliptical Gaussian by fitting the central peak in a positive temperature image. Thus, only the width σ_G of the elliptical Gaussian remains as free parameter for the fit. As an additional fitting parameter, we also included the length l_{BZ} of the first Brillouin zone after TOF. Since the distribution extends beyond the first Brillouin zone due to the Gaussian convolution, we also included pixels on the outside of the first Brillouin zone in the fit. Therefore, there are five free parameters in the negative temperature fit, μ , T , o , σ_G , and l_{BZ} . To obtain reliable values for each free parameter in the fit, it is necessary that the effects of the different parameters on the fit function are distinguishable. Both higher temperature T and larger width σ_G increase the width of the four peaks in the negative temperature fit. However, as the profiles of the unconvolved peaks in the corners of the Brillouin zone are shaped as quadrants instead of being circular, the effect of a larger width σ_G , which broadens the peaks in the convolved image in all directions simultaneously, is different from the effect of increasing temperature T , which broadens the peaks only towards the center of the Brillouin zone. Therefore, fitting both parameters simultaneously yields reliable results. Monitoring the residual sum of squares shows that this fit is stable, as there is only a single global minimum.

For the positive temperature image, it is not possible to use both σ_G and T as free parameters, because they are not independent when fitting only a single round peak. Instead, by assuming that the Gaussian convolution function is the same in the negative and positive temperature case, we fixed σ_G to the value obtained from the negative temperature fit. As also l_{BZ} cannot be extracted from a single peak, we fixed its value by fitting the first order coherence peaks in a positive temperature image without band-mapping. Thus, in the positive temperature case, the free parameters are reduced to μ , T , and o .

As Bose enhancement increases with filling in the lattice, the fitted temperature extracted from a measured quasimomentum distribution increases with assumed filling in the fit (cf. Fig. 5.11). The filling enters the fitting process through the chemical potential, which determines the overall atom number, and through the discretization of the first Brillouin zone: The discretization defines the number of available quasimomentum states, which in turn equals the number of contributing lattice sites. While the atom number can be determined from TOF images, the precise number of contributing lattice sites can only be roughly estimated due to the inherent integration in absorption images and the inhomogeneous, decreasing filling at the edge of the cloud. In an initial attempt to obtain an upper bound for the absolute value of temperature in both negative and positive temperature cases (see below), we normalized the experimental data to the number of quasimomentum states used in the fits, corresponding to unity filling in the optical lattice. The resulting fitted distributions are shown in Fig. 5.9 as the lower two insets. They include the convolution with an elliptical Gaussian and reproduce well the measured experimental data above. From these fitted distributions, we extract the occupation per Bloch wave $\rho_{\text{fit}}(E_{\text{kin}})$ analogously to the experimental data. The result is shown as the solid lines in Fig. 5.9 and is in excellent agreement with the experimental data. The temperatures that we extract from the fits are $T = -2.2 \text{ J}/k_{\text{B}}$ and $T = 2.7 \text{ J}/k_{\text{B}}$, where the errors are dominated by systematic uncertainties about the filling and discussed in the following. The very good agreement between data and a thermal Bose-Einstein distribution function, together with the great stability, indicate that the final negative and positive temperature states are indeed thermalized.

The fitting procedure neglects interaction as well as potential energy. By using a manageable, homogeneous model system and by assuming unity filling for this system, we overestimate the average filling of the real system: In the experiment, the atoms are trapped in a harmonic trap and we expect unity filling to be reached only in the center of the cloud, while the filling decreases at the edge of the cloud. The TOF images therefore average over many two-dimensional systems with different fillings each (Section 3.4). As the density distribution realized in the experiment is not precisely known, it is very challenging to perform the whole fitting procedure for this real distribution. Instead, we estimate a more realistic average filling of the in situ cloud. The final lattice ramp of 2.5 ms from the Mott insulating to the superfluid regime allows no more than 2 tunneling events (Section 6.2.1), limiting the overall mass transport possible during the ramp. Therefore it is an acceptable approximation to assume the same average filling \bar{n} at the end of the lattice ramp in the superfluid regime as at the beginning of the lattice ramp in the Mott insulating regime. The average filling in the Mott insulating regime depends on the average entropy per particle, S/N . In our experiment, we expect the entropy to lie somewhere between zero, which implies $\bar{n} = 1$, and an upper bound of $S/N \approx 1.5 k_{\text{B}}$, which gives $\bar{n} \approx 0.5$. An intermediate value of $S/N \approx 0.8 k_{\text{B}}$ corresponds to $\bar{n} \approx 0.7$.

In both negative and positive temperature cases we performed the fit to the same experimental data several times, fixing the filling each time to different values resulting in

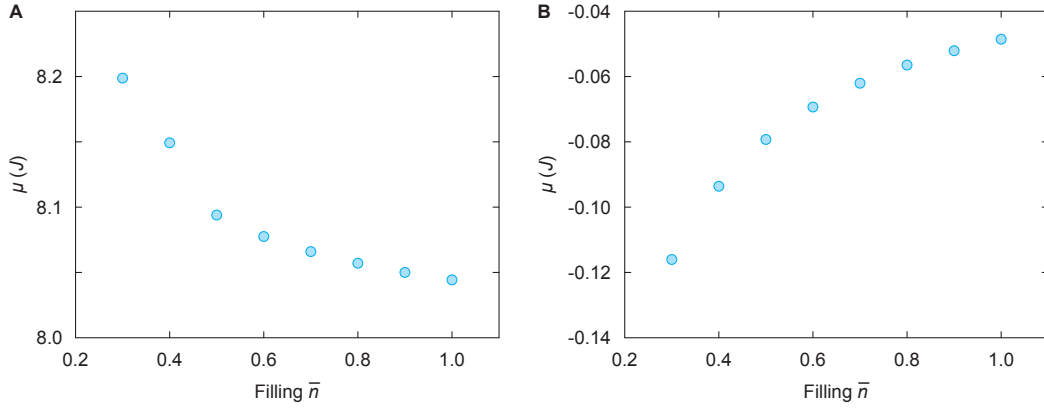


Figure 5.10: Chemical potential for various assumed fillings in the fit. The chemical potentials μ are adjusted in the Bose-Einstein fits and result in different fillings. The kinetic energies in the lowest band range from 0 to $8J$. **A**, Fit results for the negative temperature case. **B**, Positive temperature case.

different chemical potentials (Fig. 5.10). For these fillings, we extracted the temperatures and found an approximately linear scaling of temperature with filling in both cases (Fig. 5.11). From the linear fits, we extract that in the negative temperature case, a filling of $\bar{n} = 0.7$ results in a fitted temperature whose absolute value is 17(2) % lower than the one for $\bar{n} = 1$, and a filling of $\bar{n} = 0.5$ gives a temperature which is 29(2) % lower. In the positive temperature case, the temperatures are 23(1) % and 38(1) %, respectively, lower. Therefore, the fitted temperatures of $T = -2.2 J/k_B$ and $T = 2.7 J/k_B$ that assume $\bar{n} = 1$ are systematically too large (considering the absolute values) and represent only upper bounds for the real temperatures realized in the experiment.

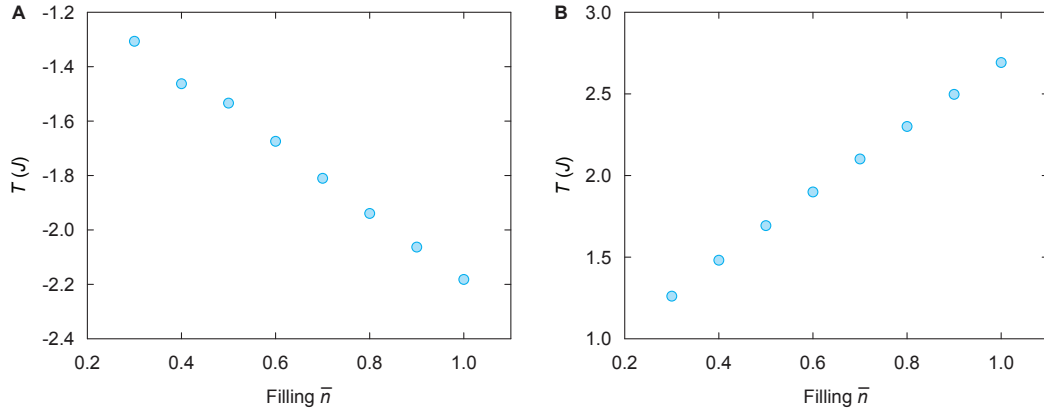


Figure 5.11: Fitted temperature for various assumed fillings in the fit. The temperatures T show an approximately linear dependence on the filling that is fixed for the fitting process via the chemical potential. A realistic average filling $\bar{n} < 1$ leads to a reduction of the absolute value of the absolute temperature, compared to $\bar{n} = 1$. The values obtained from the fits assuming $\bar{n} = 1$ are therefore upper bounds for the temperature. **A**, Negative temperature case. **B**, Positive temperature case.

5.3.3 Critical Temperatures

We compare our fitted temperatures with estimated critical temperatures for our system. In an infinitely large two-dimensional system in free space, condensation into a BEC at $\mathbf{p} = 0$ does not exist [176, 177]. But in the 2D trapped system, as realized in our experiment, condensation for non-interacting bosons is possible [178, 179]. In this case, the critical temperature is

$$T_c = \sqrt{\frac{6N_{2D}}{\pi^2}} \frac{\hbar\omega_{\text{hor}}}{k_B}, \quad (5.5)$$

with the atom number N_{2D} .

This expression can be adjusted for the case of a 2D optical lattice via the effective mass approximation for small quasimomenta [93],

$$-2J \left[\cos\left(\pi \frac{q_x}{k_{\text{lat}}}\right) + \cos\left(\pi \frac{q_y}{k_{\text{lat}}}\right) \right] \approx -2J + \frac{\hbar^2(q_x^2 + q_y^2)}{2m_{\text{eff}}}, \quad (5.6)$$

where the effective mass is given by

$$m_{\text{eff}} = \frac{\hbar^2}{2Jd_{\text{lat}}^2}. \quad (5.7)$$

In our case of a lattice depth of $V_{\text{lat}} = 6 E_r$, this yields $m_{\text{eff}}/m = 2.008 \approx 2$. Due to the effective mass, the trap frequency effectively changes to

$$\omega_{\text{hor}}^{\text{eff}} = \sqrt{\frac{m}{m_{\text{eff}}}} \omega_{\text{hor}}. \quad (5.8)$$

This effective trap frequency can be inserted into Eq. 5.5 for the bare trap frequency ω_{hor} .

We estimate the atom number in the central 2D layer by assuming that all atoms are part of a perfect $n = 1$ Mott insulator, without any surrounding shells. The shape of this Mott insulator is elliptical, where the trap frequencies $\omega_{\text{hor}} = 2\pi \times 97(4)$ Hz and $\omega_{\text{vert}} = 2\pi \times 215(13)$ Hz determine the aspect ratio $\gamma = \omega_{\text{vert}}/\omega_{\text{hor}} = 2.21(16)$. The radius R of the central layer in the horizontal direction can be calculated from the atom number $N = 105(14) \times 10^3$ via the volume of the ellipsoid, $V = \frac{4}{3}\pi R^3/\gamma = d_{\text{lat}}^3 N$. The area of the central layer is calculated as $A = \pi R^2 = \pi(3\gamma d_{\text{lat}}^3 N/4\pi)^{2/3} = d_{\text{lat}}^2 N_{2D}$ and leads to the number of atoms in the central layer,

$$N_{2D} = \pi \left(\frac{3\gamma N}{4\pi} \right)^{\frac{2}{3}} \approx 4.6(4) \times 10^3. \quad (5.9)$$

Substituting this into Eq. 5.5 gives an estimated critical temperature of $T_c = 3.4(2) J/k_B$. Below T_c , a quasicondensate with fluctuating phase is expected. Only well below T_c will the phase fluctuations decrease on length scales on the order of the Thomas Fermi radius [180], such that the quasicondensate will turn into a real condensate. This approximation, however, is not valid in the case of interacting bosons in the thermodynamic limit. In this case, the BEC transition is replaced by a Berezinskii-Kosterlitz-Thouless (BKT) transition to a superfluid [181]. From quantum Monte Carlo calculations, this transition is expected

at a critical temperature of $T_{\text{BKT}} \approx 1.8 J/k_B$ for the parameters used in our experiment [105]. However, quantum Monte Carlo calculations have also shown that even well above T_{BKT} , quasicondensate correlations appear [182].

As both the experimentally fitted temperatures as well as T_c are approximate estimates, we cannot conclusively decide whether our final negative and positive temperature states are in either the BEC or the superfluid regime.

5.4 Extraction of Coherence Length

We extract the coherence length of the final negative temperature state from the TOF images by the fitting procedure described in Section 3.4.3. To fit a measured interference pattern, we take a thin horizontal region of interest (ROI) in the TOF image, only containing two out of the four negative temperature peaks. We assume a Gaussian in situ density distribution with width $R = 30 d_{\text{lat}}$ (cf. Section 6.2.4). Performing the procedure for 20 different images of the same final negative temperature state, we obtain a coherence length of $\xi = 2.5(1) d_{\text{lat}}$. In Fig. 5.12, the optimal calculated curve for one of the experimental images is plotted together with the data. Details about the dynamics of the spreading of correlations during the final lattice ramp can be found in Chapter 6.

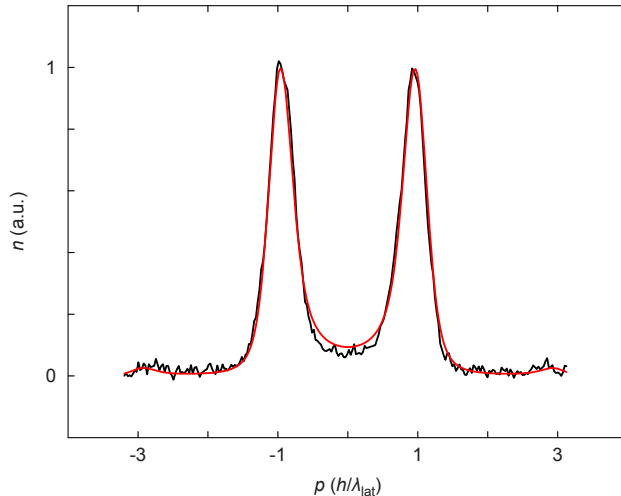


Figure 5.12: Extraction of coherence length. The experimental data (black) is obtained by averaging a time-of-flight image in a thin ROI that contains two of the four coherence peaks. The fitted calculated interference pattern (red) for an in situ width $R = 30 d_{\text{lat}}$ yields the coherence length of the system.

5.5 Negative Temperature in Other Dimensionalities

In this section, I present experimental results about the realization of negative temperature states in 1D and 3D. The major results have all been discussed in 2D which is, due to the

gravitational sag, favored over 3D for the realization of negative temperature states in our experimental setup (cf. Section 5.1.2).

5.5.1 1D

We are also able to realize a negative temperature state in 1D, by not ramping down the horizontal lattice along the y -direction in the final ramp. Coherence is still visible in the images along the y -direction in the case where the transverse lattices are kept at $V = 19 E_r$. As we are mainly interested in the coherence along the longitudinal x -direction, we suppress the transverse coherence by rapidly increasing the transverse lattices within 0.1 ms (negative temperature) or within 0.4 ms (positive temperature) to $V = 30 E_r$ as soon as the lattice loading to $V = 19 E_r$ has been finished. In principle, we could also ramp up the lattices to $V = 30 E_r$ at the same rate as the lattice ramp to $V = 19 E_r$. However, the Ti:Sa laser used for the creation of the optical lattice potential exhibits an amplitude noise resonance at 85 kHz, which coincides with the bandgap at a lattice depth of $V = 25.5 E_r$. For this reason, we observe strong heating of the atoms at this lattice depth. The full sequence is similar to the 2D case and is shown in Fig. 5.13.

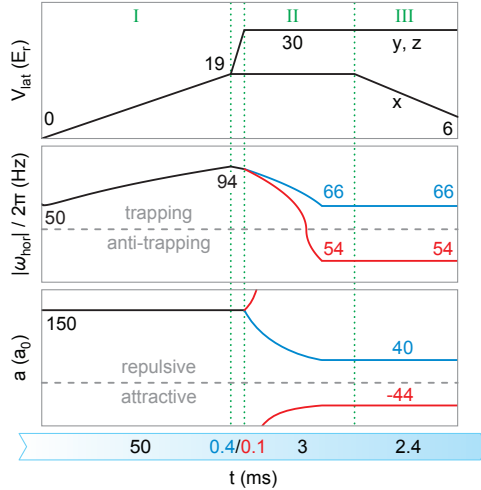


Figure 5.13: Experimental sequence for negative (red) and positive (blue) temperatures in 1D. The sequence is very similar to the one in the 2D case (Fig. 5.1). In contrast to the 2D sequence, only the x -lattice depth is ramped down in the end. After the loading sequence to $V_{\text{lat}} = 19 E_r$, both y - and z -lattice are quickly increased to $V_{\text{lat}} = 30 E_r$ to reduce the coherence along these directions (see main text). Trapping frequencies and scattering lengths were optimized specifically for the 1D case.

In Fig. 5.14 images are shown for the final positive and negative temperature state. As coherence is only established along the x -direction, a characteristic stripe pattern appears.

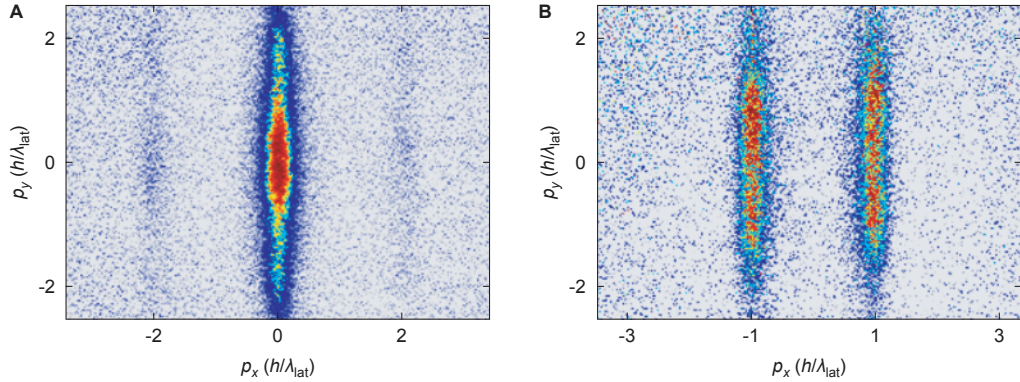


Figure 5.14: Time-of-flight images of the final positive (**A**) and negative temperature state (**B**) in 1D. Phase coherence is visible only along the x -direction. In both transverse directions, it is suppressed by the deep optical lattices. The colors in the two images are individually scaled.

5.5.2 3D

In the 3D case, the population inversion is also visible after an analogous sequence. The sequences for both negative and positive temperature states in 3D (Fig. 5.15) were experimentally optimized to maximize the lifetime of the final states. We performed a lifetime measurement analogous to that in Section 5.2, by holding for variable times in the final shallow lattice and by evaluating the visibility in the final TOF images. While the visibility in the negative temperature case (Fig. 5.16A) at the end of the lattice ramp is comparable to the 2D case (Fig. 5.4), the lifetime of the negative temperature state of $\tau = 2(1)$ ms is very short. In the case of such a short lifetime, the final state cannot be considered a thermal state at all and therefore also cannot be assigned a temperature. The atom number during the hold time is quite stable and is not responsible for the fast decrease of visibility (Fig. 5.16B). In contrast, the lifetime of the positive temperature state is much longer with $\tau = 1.2(4)$ s, where the atom number decreases on a similarly long timescale (Fig. 5.17).

The lifetime in the positive temperature case is very long, and comparable to the lifetimes in the 2D negative and positive temperature cases. The drastic decrease of the lifetime in the negative temperature case can be explained by the effect of the gravitational sag (Section 2.2.2). The equilibrium position is given by the minimum of the combined potential of both dipole trap and gravitational force, which is shifted downwards compared to the case without gravity (Fig. 5.18). This equilibrium position changes during the experimental sequence, depending on the trap frequency in the vertical direction. The clouds are initially prepared in a dipole trap with a high vertical trap frequency. During the initial lattice ramp, this vertical trap frequency changes only slightly and reaches $\omega_{\text{vert}} = 227$ Hz at the end of the ramp. At this point, the atoms are trapped in the deep lattice and locked to their respective lattice sites. In the positive temperature case, the vertical trap frequency and therefore also the gravitational sag remain approximately constant while the lattice

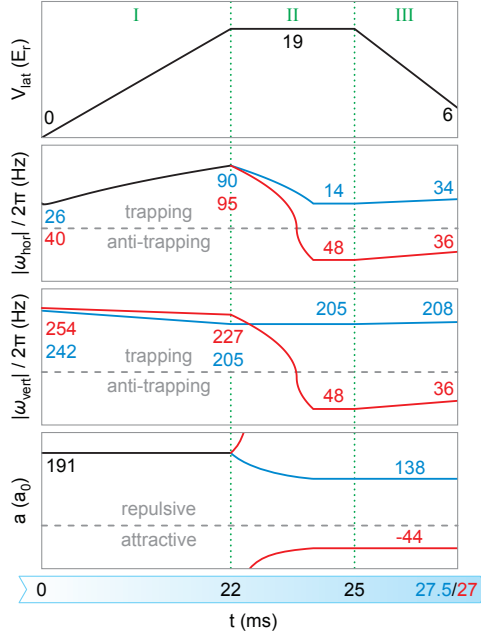


Figure 5.15: Optimized sequence for the creation of negative (red) and analogous positive temperatures (blue) in 3D, depicted schematically. In contrast to the sequence in 2D (Fig. 5.1), the depth of all three lattice beams is ramped down. Trap frequencies and scattering lengths are optimized to maximize the lifetimes of the final states. In the 3D case, also the vertical trap frequency ω_{vert} is relevant. Due to experimental constraints, the final ω_{vert} in the negative temperature case is limited to small absolute values.

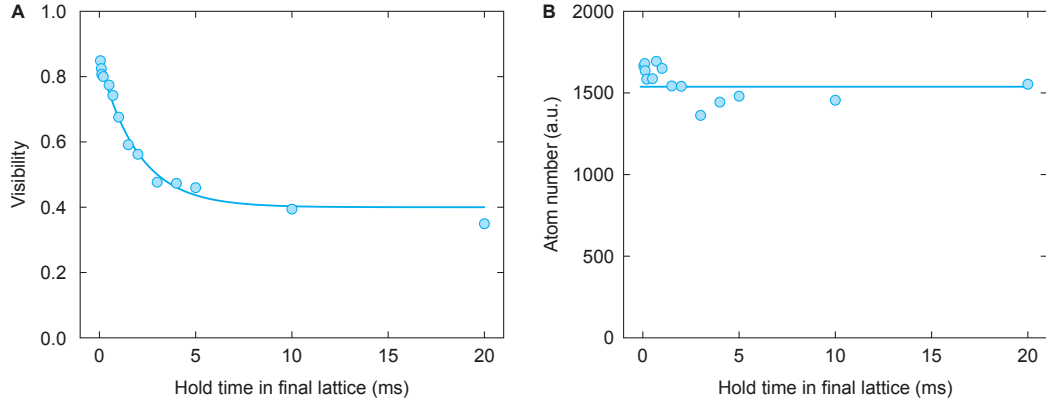


Figure 5.16: Lifetime measurement of the negative temperature state in 3D. **A**, The visibility is evaluated as in Fig. 5.3 from time-of-flight images versus hold time in the final shallow optical lattice. The solid line is an exponential fit. Despite the optimization of the sequence, the lifetime is only small ($\tau = 2(1)$ ms). **B**, The total atom number is measured via area sums. The horizontal line guides the eye. As the atom number is essentially constant over the entire range of hold times, atom losses can be excluded as a reason for the fast loss of coherence.

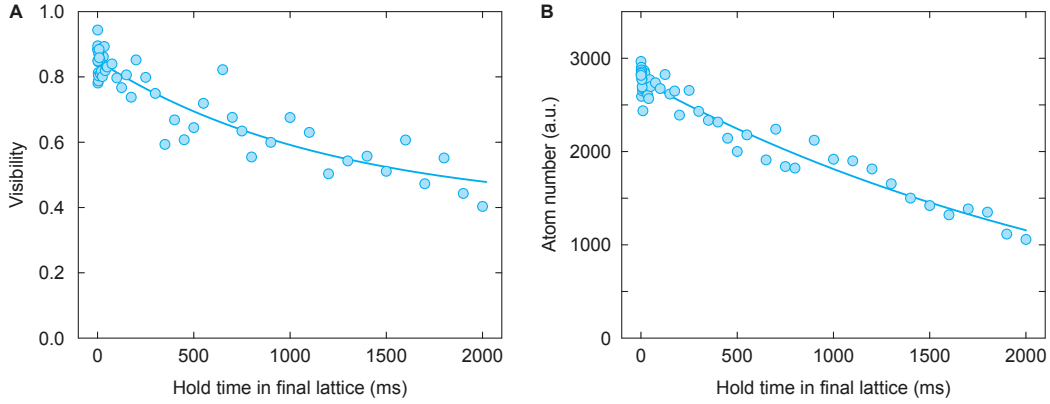


Figure 5.17: Analogous lifetime measurement as in Fig. 5.16 for the final positive temperature state. **A**, The lifetime $\tau = 1.2(4)$ s of coherence is much longer than for the negative temperature state, and comparable to the lifetimes in the 2D case. **B**, Atom losses become relevant on a similar timescale ($\tau = 2.6(1.0)$ s) as the loss of coherence.

is reduced from the Mott insulating to the superfluid regime (Fig. 5.15). In this case, the atoms in the cloud redistribute in order to keep the chemical potential homogeneous throughout the system (Section 5.1.2), leading to a long lifetime of the final state.

In contrast, in the negative temperature case, the external trapping potential is transformed into an anti-trapping potential in the deep lattice. In this case, the equilibrium position of the external potential and the gravitational potential, however, moves to a position above the location without gravity. As the atoms are locked to their lattice sites, they cannot reach this equilibrium position, but instead experience a strong gradient along the vertical direction (Fig. 5.18). As the distance to the equilibrium position is on the order of 300 lattice sites, it is also impossible for them to reach this position during lattice ramp-down. Therefore, once phase coherence between lattice sites starts to emerge, the strong gradient at the position of the atoms will lead to fast dephasing and destroy the visibility of the interference pattern in TOF images. We estimate the energy difference between two neighboring lattice sites for the case of a final anti-trapping potential with a trap frequency of $\omega_{\text{vert}} = 48$ Hz, and obtain $\Delta\nu \approx 370$ Hz. We therefore expect dephasing on a timescale of $(\Delta\nu)^{-1} = 2.7$ ms which explains our experimental result.

Stable negative temperatures could, however, also be created in 3D. The obvious solution would be to compensate the gravitational potential with a magnetic field gradient. In the course of this work, we have not implemented this solution, but it may constitute a future improvement for the setup. But since the magnetic field degree of freedom is required for the homogeneous magnetic field around the Feshbach resonance, one has to be careful with the magnetic field inhomogeneity across the cloud. The required magnetic field gradient B' can be calculated from the Zeeman shift $\delta\nu_Z = -g_F m_F \mu_B B' z / h = mgz/h$ with the gravity of earth $g = 9.81$ m/s² as $B' = 0.5$ mG/d_{lat}. Estimating the extension of the cloud along the vertical direction from an $n = 1$ ellipsoid, as described in Section 5.3.3, gives a diameter of around $2R_{\text{vert}} = 34 d_{\text{lat}}$. The maximum required difference of the magnetic field across

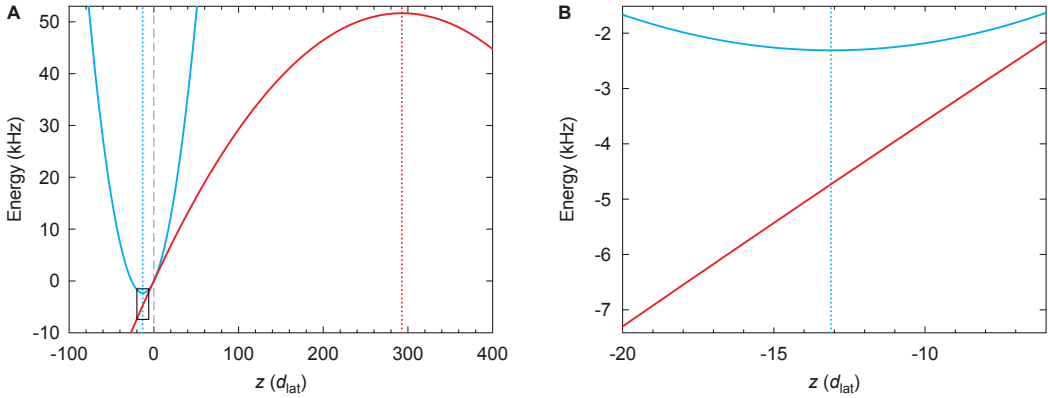


Figure 5.18: Potential energy along the vertical direction in the 3D case. **A**, Coarse plot, **B**, Zoom, area indicated by the small black rectangle in **A**. The blue curve is the combined potential of a harmonic trapping potential with trap frequency $\omega_{\text{vert}}/2\pi = 227 \text{ Hz}$ and gravity for ^{39}K atoms. The gravitational sag is $z_{\text{sag}} \approx -13 d_{\text{lat}}$ (blue dotted line). The red curve is the combined potential for the case of a harmonic anti-trapping potential with trap frequency $|\omega_{\text{vert}}|/2\pi = 48 \text{ Hz}$. In this case the gravitational sag is positive, $z_{\text{sag}} \approx 300 d_{\text{lat}}$ (red dotted line). In the deep lattice, however, the atoms are trapped at their positions around $z \approx -13 d_{\text{lat}}$. The anti-trapping potential leads to an approximately linear potential at the position of the atoms that causes dephasing (see main text). The gray dashed line indicates the trap minimum without gravity.

the cloud is therefore $B' \cdot 34 d_{\text{lat}} = 8.6 \text{ mG}$. When for example using a magnetic field of $B = 397.9 \text{ G}$ near the Feshbach resonance at $B_0 = 402.50(3) \text{ G}$ [30] to realize a scattering length of $a = 300 a_0$, the magnetic field inhomogeneity would result in a variation of the scattering length across the cloud of $\Delta a/a = 0.2\%$. This effect is therefore very small and the compensation scheme should be feasible.

For the 3D implementation of negative temperatures, there is another limitation of our experimental setup: The maximum achievable anti-trapping potentials in the vertical direction are limited due to the laser beam geometry. As the anti-trapping potential is created by the intensity profiles of the lattice beams itself, and the lattice beam profiles are circular, the anti-trapping trap frequency along the vertical direction can only be as strong as in the horizontal directions. As our dipole beams are elliptical, creating a rather high trap frequency along the vertical direction to have good confinement against gravity, we cannot precisely invert the trapping potential along the vertical direction in the deep lattice. This limitation is similar to the imperfect inversion of the horizontal trapping potential in the 2D case (Section 5.1.2) and leads to additional dephasing in the final state. It could be resolved by additional blue-detuned anti-trapping beams.

6 Emergence of Coherence and the Dynamics of Quantum Phase Transitions

This chapter is based on our publication *Emergence of coherence and the dynamics of quantum phase transitions* [183]. In the first section, I give an introduction to classical and quantum phase transitions (QPTs) and how the dynamics across QPTs can be described within the Kibble-Zurek framework. In the second section, I describe the experimental sequence, data evaluation and numerical methods that we, as a collaboration, used to investigate the emergence of coherence across a QPT. In the third section, I discuss the experimental and numerical results for the emergence of coherence in a quench in 1D and compare them to the predictions of the Kibble-Zurek mechanism. In the fourth section, I present the results for the emergence of coherence in higher dimensions as well as for attractive interactions, along with the conclusions that can be drawn from these measurements. In the fifth section, I show unpublished data about the emergence of coherence *after* a quench as well as additional in situ data, emphasizing the different timescales for the local emergence of coherence and global thermalization.

6.1 Classical and Quantum Phase Transitions

Phase transitions are ubiquitous phenomena, describing the transition of a thermodynamic system from one state of matter to another. Many times, these states of matter, or phases, differ by their symmetry. For example, the spins aligned in the same direction in a ferromagnet constitute a phase of low symmetry where rotational and time reversal symmetry are spontaneously broken due to the choice of a particular direction, while randomly oriented spins in the paramagnetic phase above the Curie temperature represent a more symmetric phase [184]. Following Landau's mean-field theory of phase transitions, one may define a quantity that characterizes the symmetry that is broken at the phase transition, called order parameter η [60]. In the above example of ferromagnetism, the order parameter is the magnetization; it is zero in the paramagnetic phase and at the phase transition, and acquires a finite value in the ferromagnetic phase. Following Landau, the thermodynamic

potential of the system can be expanded in the vicinity of the phase transition in powers of the order parameter η [60]. In thermodynamic equilibrium, this thermodynamic potential, e.g. Helmholtz free energy in the canonical ensemble, adopts its minimum value. From this condition, one can obtain the value of the order parameter and also other quantities of the system such as entropy and specific heat in the vicinity of the phase transition. In general, the theory of phase transitions is intricate even in the case of classical phase transitions and therefore was not developed until the late 19th century. Nowadays, phase transitions are classified into two broad categories, first order and continuous phase transitions [185].

First order phase transitions are characterized by a discontinuity in the order parameter as well as in the first derivatives of the thermodynamic potential (e.g. free energy), such as density or entropy. This discontinuity involves latent heat at the phase transition, thus the system absorbs or releases an additional amount of heat during the phase transition while the temperature stays constant. In this regime, the system is in a mixed state of two phases simultaneously. Familiar examples for first order phase transitions are the melting of ice and boiling of water below the critical point: While boiling, water absorbs a large amount of heat which increases the entropy of the system and leads to a jump in entropy and pressure at the phase transition. Also the order parameter, the density difference between the liquid and gas phase, exhibits a discontinuity [186]. During this process, water is in a mixed-phase regime, where some part has completed the phase transition and the rest has not.

Continuous phase transitions are characterized by continuous first derivatives of the thermodynamic free energy, including the order parameter, but discontinuous second or higher order derivatives. Consequently, continuous phase transitions do not involve latent heat. For example, in the paramagnet to ferromagnet phase transition, the magnetization continuously changes from zero to a finite value, but the magnetic susceptibility, a second-order derivative, exhibits a jump. The correlation length ξ , i.e. the length scale on which fluctuations in a system appear, diverges at the transition point of a continuous phase transition, and can often¹ be described by a power-law behavior [188]

$$\xi \propto |\epsilon|^{-\nu}, \quad (6.1)$$

where $\epsilon = (T - T_c)/T_c$ is the relative distance of the temperature T from the critical point T_c . The exponent ν is an example of the critical exponents that allow to categorize continuous phase transitions into distinct classes. Universality states that very different physical systems may possess the same set of critical exponents and thus belong to the same universality class [184]. As fluctuations at the transition point appear on all length scales, the diverging correlation length indicates scale invariance of these critical fluctuations [184], and can be observed in the liquid water to vapor transition that turns into a continuous phase transition right at the critical point: The densities of the two phases become identical, and the latent heat vanishes. The diverging correlation length, in this case the length

¹An important exception is the Kosterlitz-Thouless transition [187], where the correlation length near the critical point shows an exponential scaling. This transition is also relevant for the measurements presented in this thesis (Section 6.3.1).

scale of density fluctuations, manifests itself in the critical opalescence where long-range fluctuations scatter light of all wavelengths [189]. This critical point, which is a special point of a first order phase transition curve, is not to be confused with multicritical points. The latter are special points within a critical manifold (e.g. a phase transition curve) of continuous phase transitions that belong to a different universality class than the usual one of this manifold. Multicritical points are borders of a critical manifold, or the points on intersection and branch lines of critical manifolds [190].

Classical phase transitions describe changes of thermodynamic properties of a system and are based on the competition between energy and the entropy of thermal fluctuations. At $T = 0$, thermal fluctuations vanish and hence a phase transition cannot be classical anymore. Instead, at absolute zero, quantum fluctuations of the ground state (i.e. fluctuations of an observable around its expectation value due to the Heisenberg uncertainty principle in the case when the Hamiltonian contains non-commuting terms [57]) become relevant and may change the properties of the ground state substantially, leading to different quantum phases. By changing a parameter of the system at $T = 0$, one may enter a different quantum phase and thereby cross the quantum phase transition, which is defined as a phase transition driven by quantum fluctuations [191]. The classification into first order and continuous or second order phase transitions also applies to quantum phase transitions [192]. An example of a first order quantum phase transitions is the emergence of superconductivity in band ferromagnets [193]. Just as in continuous classical phase transitions, in continuous quantum phase transitions, the characteristic power-law behavior of Eq. 6.1 can often be found. In this case, however, $\epsilon = (\lambda - \lambda_c)/\lambda_c$ describes the relative distance of a non-thermal control parameter λ of the Hamiltonian from the quantum critical point λ_c . At finite temperature, thermal fluctuations of energy $k_B T$ compete with quantum fluctuations. As long as quantum fluctuations are still dominant, remnants of a quantum phase transition can also be observed at finite T [194]. One of the most famous continuous quantum phase transitions is the Mott insulator to superfluid transition, which we investigated in this project. While the critical curve of the Mott lobes (Fig. 3.10) belongs to one particular universality class, the tip of the Mott lobe constitutes a multicritical point and thus belongs to a different universality class with different critical exponents. While in this work, we examined the transition at the tip of the Mott lobe, the transition at the side of the Mott lobe was studied previously also with an ultracold atoms setup [195]. Other previous experiments on quantum phase transitions investigated the inverse superfluid to Mott insulator phase transition [111], the vacuum to superfluid transition [196], or spinor Bose-Einstein condensates entering a ferromagnetic state [197].

6.1.1 Sudden and Adiabatic Approximations

In general, it can be a very challenging task to describe the dynamics of quantum mechanical systems during a quench, i.e. when a parameter of the Hamiltonian H is changed over time t . Depending on the quench speed, however, two limiting cases apply which can be solved more easily.

Sudden approximation: During an instantaneous quench, $\partial H/\partial t \rightarrow \infty$ for a time period $\Delta t \rightarrow 0$. The initial state wavefunction $\langle r|\psi_0\rangle$ remains unchanged and is projected into a new basis, corresponding to the energy eigenstates of the final Hamiltonian. An initial pure state $|\psi_0\rangle$ is in general projected into a superposition of eigenstates of the final Hamiltonian and the initial quantum numbers are lost. The dynamics in the final Hamiltonian is determined by the phase evolution of the individual eigenstates.

Adiabatic approximation: We assume that the system is initially in a nondegenerate energy eigenstate $|\psi_0\rangle$ of the Hamiltonian which is separated throughout the quench by gaps Δ_i from the other energy eigenstates $|\psi_i\rangle$. For infinitely slow quenches, $\Delta t \rightarrow \infty$ and $\partial H/\partial t \rightarrow 0$, the system adiabatically follows the change of the eigenstate $|\psi_0(t)\rangle$ over time, i.e. it remains in this eigenstate, $|\psi(t)\rangle = |\psi_0(t)\rangle$. The spatial wavefunction $\langle r|\psi(t)\rangle$ adapts accordingly and gradually changes. The system retains all quantum numbers for which the corresponding operators commute with the Hamiltonian throughout the quench. The condition for adiabaticity is given by [198]

$$|\langle\psi_i|\partial H/\partial t|\psi_0\rangle| \ll \Delta_i^2/\hbar, \quad (6.2)$$

which needs to be fulfilled for all eigenstates $|\psi_i\rangle \neq |\psi_0\rangle$. It ensures a sufficiently large gap throughout the quench and prevents excitations of the system into nearby states.

The simplicity of these two limiting cases is appealing. However, the vast majority of real dynamical processes are neither sudden nor adiabatic.

6.1.2 Kibble-Zurek Mechanism

The Kibble-Zurek mechanism (KZM) [188, 199–202] provides an intuitive and calculable picture for the creation of defects and the resulting correlation length in a system when a continuous phase transition is crossed at a finite rate. Originally, the KZM was developed for classical phase transitions [199, 200], but it can also be applied to the case of quantum phase transitions [188], where a control parameter λ of the Hamiltonian is quenched over the critical point λ_c . Via the KZM, the size of domains and the corresponding correlation length of a system after a phase transition can be estimated. The basic statement of the KZM is that essential properties of the final state after the phase transition scale as a power-law with the quench rate, i.e. the velocity at which the phase transition is crossed, and that the exponent of this power-law depends only on the critical exponents of the model at equilibrium. One may therefore view the KZM as an extension of the universal equilibrium properties of a model to its dynamical behavior at the phase transition. The KZM has been successfully applied in many circumstances, both to experimental results and numerical simulations [201, 203–207].

The spectral gap Δ , i.e. the energy of the lowest excitation above the ground state, closes at the critical point of a continuous quantum phase transition [57]. Near the critical point, the functional behavior of the gap can be described via the critical exponents ν and z , where the latter is the dynamical exponent,

$$\Delta \propto |\epsilon|^{z\nu}. \quad (6.3)$$

Here, ϵ indicates the distance of the control parameter λ from the critical point λ_c in dimensionless units,

$$\epsilon = \frac{\lambda - \lambda_c}{\lambda_c}. \quad (6.4)$$

With the quench rate $\dot{\epsilon}$, one can define a characteristic timescale

$$\tau_\epsilon(t) = \left| \frac{\epsilon(t)}{\dot{\epsilon}(t)} \right| \quad (6.5)$$

for the instantaneous relative change of ϵ during the ramp. The inverse of the quench rate at the position $t = 0$ of the phase transition is a characteristic measure for the quench and is usually denoted [188]

$$\tau_Q = \left| \frac{1}{\dot{\epsilon}(0)} \right|. \quad (6.6)$$

The relaxation time τ of the system indicates how fast the system is able to react to external changes. It is given by the inverse of the gap Δ and therefore diverges at the critical point,

$$\tau \propto |\epsilon|^{-\nu z}. \quad (6.7)$$

This divergence of the relaxation time is also called critical slowing down [202]. The correlation length ξ diverges at the critical point and is expected to scale as in Eq. 6.1,

$$\xi \propto |\epsilon|^{-\nu}. \quad (6.8)$$

The basic idea of KZM is to split the evolution across the quantum phase transition into several regimes, which are called either adiabatic or frozen, combining the two limiting cases from Section 6.1.1 (Fig. 6.1). The initial state of the system, far away from the phase transition, is assumed to be the ground state. In this regime, the ground state is protected by a large gap Δ , and the dynamics are assumed to be adiabatic such that the system remains in the ground state. The correlation length ξ of the system therefore adapts continuously.

At some point $\hat{\epsilon}$, the freeze-out point, as the gap closes towards the critical point where the correlation length diverges, the timescale τ_ϵ for the external parameter change becomes shorter than the relaxation time τ of the system, and the system cannot follow the external parameter change anymore. The dynamics therefore cease to be adiabatic. Only if this happens sufficiently close to the phase transition, where the ground state properties can be described via the critical exponents, can one calculate this point $\hat{\epsilon}$ via the critical exponents [188]. In general, the quench can be linearized near the critical point, $|\dot{\epsilon}(t)| \approx |\dot{\epsilon}(0)| = 1/\tau_Q$, such that the above condition

$$\tau_\epsilon = \frac{|\epsilon|}{1/\tau_Q} \stackrel{!}{=} \tau \propto |\epsilon|^{-\nu z} \quad (6.9)$$

leads to

$$|\hat{\epsilon}| \propto \tau_Q^{-\frac{1}{1+\nu z}}. \quad (6.10)$$

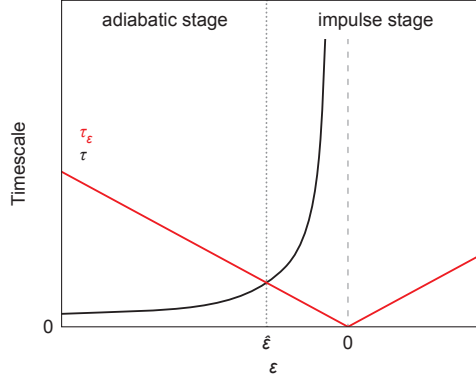


Figure 6.1: Illustration of the Kibble-Zurek mechanism. The relaxation timescale τ of a system and the timescale of a quench τ_ϵ are plotted versus the quench parameter ϵ . The crossing of the two at $\hat{\epsilon}$ divides the quench into an adiabatic and a frozen regime (dotted line). For details, see main text.

Closer to the critical point, the dynamics are considered frozen, i.e. the sudden approximation applies and the correlation length ξ of the system does not change anymore. Therefore, the final correlation length after crossing the phase transition is, according to this approximation, given by the value at $\hat{\epsilon}$,

$$\hat{\xi} \propto \tau_Q^{\frac{\nu}{1+\nu z}}. \quad (6.11)$$

This is the main statement of the KZM [202]. In an alternative derivation leading to the same result, the freeze-out point is sometimes derived via a sonic horizon picture, instead of the above strict sudden approximation [200, 208]: Within the freeze-out regime, from time T_1 to T_2 , correlations can spread maximally with the corresponding sound velocity $v_s(t)$, establishing a correlation length limited by the sonic horizon [208]

$$h = \int_{T_1}^{T_2} v_s(t) dt. \quad (6.12)$$

To determine the size of the freeze-out regime one needs to compare the ground state correlation length with this sonic horizon. At the point where the two are equal, the propagation of correlations in the freeze-out regime is identical to the correlation length already established in the adiabatic regime. The correlation length therefore does not increase further during the freeze-out regime.

The KZM prediction for slow quenches across continuous phase transitions has been checked in various integrable models. A phase transition in free (i.e. noninteracting) fermionic systems can be mapped to a set of Landau-Zener anti-crossings, where an actual crossing corresponds to the excitation of a quasiparticle in the system. The quasiparticle density after the phase transition can be calculated with the help of the Landau-Zener formula. It scales as a power-law with the quench time, where the exponent is given by the critical exponents and is consistent with the Kibble-Zurek prediction [188, 209]. For

more complex and non-integrable models, the Kibble-Zurek scaling was verified via adiabatic perturbation theory [122, 210]. In this method, the transition probabilities to the instantaneous eigenstates of the system are expanded in powers of $\dot{\epsilon}$ [122].

6.2 Experimental and Numerical Methods

After the theoretical introduction of quantum phase transitions and the Kibble-Zurek mechanism in general, I now turn to the investigation of the dynamics at the Mott to superfluid transition, which is the primary interest in this chapter. In this section, I describe the experimental sequence used to measure the emergence of coherence, both in 1D and in higher dimensions. To obtain the coherence length in the final system, we fit the resulting TOF images with calculated interference patterns. I show how we determine the *in situ* width of the clouds with a different method to reduce the number of free fitting parameters. I present the three numerical methods that our collaborators at FU Berlin used to simulate and explain our experimental results. These are density matrix renormalization group calculations [211], exact diagonalization and the doublon-holon fermionic model. Finally, I show how we extract the exponent of the power-law growth of coherence, both for experimental and numerical data.

6.2.1 Experimental Sequence for 1D

Initially, we created an essentially pure condensate of, depending on the data set, $(25 - 85) \cdot 10^3$ ^{39}K atoms in a dipole trap of oblate shape with trapping frequencies of $\omega = 2\pi \cdot (50, 50, 181)$ Hz along the (x, y, z) direction. The following sequence is shown in Fig. 6.2. Within 50 ms, we performed a linear ramp of a 3D optical lattice to a depth of $V_{\text{lat}} = V_i = 19 E_r$. Within 0.4 ms, we quickly increased the lattices along the y - and z -direction to $V_{\text{lat}}^y = V_{\text{lat}}^z = 30 E_r$ to reduce correlations along these directions even further. We performed the final ramp in a short time to prevent heating of the atoms via a resonance of amplitude noise of the Ti:Sa laser used for the optical lattice (Section 5.5.1). The scattering length during the loading procedure was set at $a = 148 a_0$, leading to a large $U/J = 350$ at the end of the lattice loading, deep in the Mott insulating regime and close to the atomic limit. To obtain a large $n = 1$ Mott insulating core in the center of the cloud, the trap frequencies in the horizontal plane were increased during the lattice loading to $\omega = 2\pi \cdot (91, 92, 158)$ Hz.

In the deep lattice, we ramped the scattering length to variable values by employing the Feshbach resonance at $B = 402.50(3)$ G [30], resulting in variable initial $(U/J)_i$ values. The ramp was not linear in the scattering length a as suggested by the schematic Fig. 6.2, but linear in the magnetic field B . Via an exact diagonalization calculation (Section 6.2.6), our theory colleagues verified that this Feshbach ramp is close to adiabatic, such that the final state can be well approximated by the ground state of the system (Fig. 6.3). For interactions $(U/J)_i \geq 40$, the ground state itself is close to a product state. We then linearly decreased the depth of the x -lattice to $V_{\text{lat}}^x = V_f = 6 E_r$ in a variable ramp time

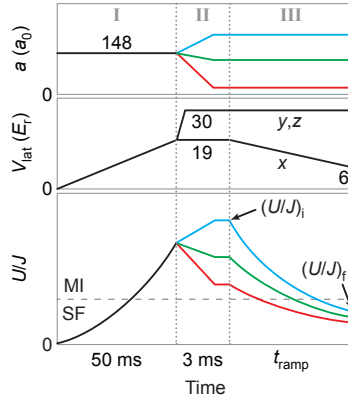


Figure 6.2: Experimental sequence for the emergence of coherence in 1D. Exemplary ramps of scattering length a , lattice depth V_{lat} and U/J . After loading the atoms into a 3D optical lattice (I), the lattice depth along the y - and z -direction is quickly increased to $V_{\text{lat}} = 30 E_r$ (cf. Section 5.5.1). In the deep lattice (II), the scattering length is quickly ramped to variable values. This leads to different initial $(U/J)_i$ and final $(U/J)_f$ values for the final lattice ramp (III) of the x -lattice in variable times t_{ramp} . The horizontal dashed line indicates the critical value $(U/J)_c$ that separates the superfluid (SF) from the Mott insulating regime (MI).

t_{ramp} ,

$$V_{\text{lat}}(t) = V_i + (V_f - V_i) \cdot t / t_{\text{ramp}}, \quad (6.13)$$

leading to a smaller final $(U/J)_f$ value. If the scattering length is not too large, this ramp leads to a crossing of the Mott to superfluid phase transition at $(U/J)_c \approx 3.3$ [102–104]. With this procedure, we can thus control the final interaction $(U/J)_f$ via the scattering length without changing the lattice ramp. The ratio of the initial to the final interaction is fixed at $(U/J)_i/(U/J)_f \approx 24$. The quench can be approximated well by an exponential function

$$(U/J)(t) = B \cdot a \cdot e^{-C(t/t_{\text{ramp}})^D}, \quad (6.14)$$

where $t \in [0, t_{\text{ramp}}]$. The parameters of this approximation, obtained from fits to the real ramps, are $B = 2.33/a_0$, $C = 3.04$, and $D = 1.10$. In the following, I parametrize the ramp time in dimensionless units by the quantity

$$\tau_{\text{ramp}} = t_{\text{ramp}} \cdot \frac{\bar{J}}{\hbar} \approx t_{\text{ramp}} \cdot 0.93/\text{ms}, \quad (6.15)$$

which equals the integral of the number of tunneling times (Eq. 3.19) during the ramp. Here, $\bar{J} = \int_{V_i}^{V_f} J(V) dV / (V_f - V_i)$ is the average tunneling rate during the ramp. This parametrization of the ramp time is directly proportional to the inverse of the quench rate at the critical point (Eq. 6.6), which is also frequently used as a parametrization [188]. Due to this proportionality, both parametrizations yield the same power-law exponents for the growth of the coherence length with ramp time, which is analyzed in detail in Section 6.2.8.

Subsequently, we switched off all trapping potentials and recorded absorption images along the z direction after a time-of-flight of $t_{\text{TOF}} = 7 \text{ ms}$ (Fig. 6.4). From these images,

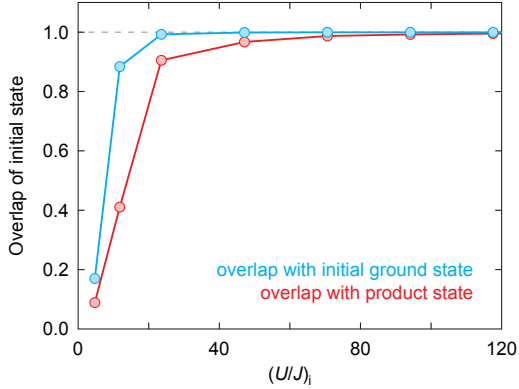


Figure 6.3: Exact diagonalization calculations of the overlap of the initial state with the ground state of the system and with a product state. These reveal that for not too small initial interactions $(U/J)_i \geq 20$, the initial state in the experiment is essentially the ground state of the system, i.e. excitations during the ramp of the scattering length in the deep lattice are negligible. For $(U/J)_i \geq 40$, the initial state is essentially a product state, the ground state deep in the Mott insulating regime.

we then determined the coherence length of the system. Alternatively, to obtain the width of the in situ distribution, we performed in situ imaging by freezing out the distribution in a very deep lattice and subsequently switching off the magnetic field (Section 3.4.1).

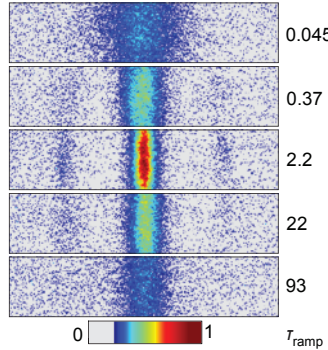


Figure 6.4: Time-of-flight images for $U(J)_i = 47$ and $(U/J)_f = 1.9$ in 1D for several τ_{ramp} . While for very short ramps, correlations cannot spread and no coherence is visible, for intermediate ramps, coherence has emerged in the system. For very long ramps, coherence is not observable either.

6.2.2 Experimental Sequence for Higher Dimensions and Attractive Interactions

The experimental sequence for the emergence of coherence in higher dimensions is very similar to the one in 1D and is shown in Fig. 6.5A,B for the 2D and 3D cases, respectively. Instead of ramping down the lattice power only along the x -direction, as in the 1D case, we simultaneously ramp down both horizontal lattices in 2D or all three lattices in 3D.

In contrast to the 1D case, in 2D we do not quickly ramp the z -lattice to a deeper depth of $V_{\text{latt}}^z = 30 E_r$, but stay at $V_{\text{latt}}^z = 19 E_r$, although this would also have been feasible in principle and would reduce correlations along the z -direction. The ratio of the initial to the final interaction is fixed at $(U/J)_i/(U/J)_f \approx 35$ in 2D and 50 in 3D. The parameters for the exponential approximation of the final lattice ramp (Section 6.14) are, for the 2D case, $B = 1.80/a_0$, $C = 3.32$, and $D = 1.11$. In the 3D case, they are $B = 1.79/a_0$, $C = 3.60$, and $D = 1.11$. Figure 6.6 shows TOF images for several ramp times τ_{ramp} in the 2D case

We realize the measurements for attractive interactions in both 1D and 2D, leading to negative temperature states in the case of thermalization, where the sequence for the 2D case is shown in Fig. 6.5C. Realizing stable negative temperatures in 3D in our experimental setup requires some technical improvements (Section 5.5.2) that could be implemented in future experiments. In contrast to the repulsive interactions case, the magnetic field is ramped over the Feshbach resonance at $B = 402.50(3)$ G to a magnetic field value that corresponds to a negative scattering length a . Thus, also the interaction parameter U is switched to negative values such that the ensemble realizes a Mott insulating state at large negative $(U/J)_i$, close to the highest excited state. Simultaneously to the Feshbach ramp, we also switch the external confinement from a trapping to an anti-trapping potential, and thereby realize a stable state at negative temperature in the case of thermalization (Chapter 5). The following lattice ramp decreases the absolute value $|U/J|$, crossing the critical value $(U/J)_c = -3.3$ [102–104] and finally reaching a small negative interaction strength $(U/J)_f$.

6.2.3 Extraction of Coherence Length

To extract the coherence length in all 1D, 2D and 3D cases, we integrated the TOF images over a small range of width $d_{\text{int}} \approx 0.2\hbar k_{\text{latt}} t_{\text{TOF}}/m$ along the y -direction which includes potential interference peaks (cf. Section 3.4.3). Thus, in the 2D and 3D case, we evaluated only a single row of interference peaks, discarding the others. We fitted the resulting 1D data with theoretically calculated curves, as detailed in Section 3.4.3. We determined the in situ width R externally (Section 6.2.4), instead of keeping it as a free fitting parameter in addition to the coherence length ξ . Figure 6.7 shows that the rather simple theoretical model of Eqs. 3.44–3.47 captures the experimental interference curves well.

6.2.4 Obtaining the In Situ Width

The fitting function given by Eqs. 3.44–3.47 contains two free parameters, the coherence length ξ and the in situ width R . For the fitting procedure, these are not entirely independent as both a larger ξ and a smaller R have similar effects on the interference pattern, namely decreasing peak widths (Fig. 6.8). Keeping both as free parameters in the fitting procedure leads to unstable fitting results. Therefore, we only kept ξ as a free parameter and determined R externally from in situ images.

In addition to the TOF images, we also recorded data sets with in situ images for each

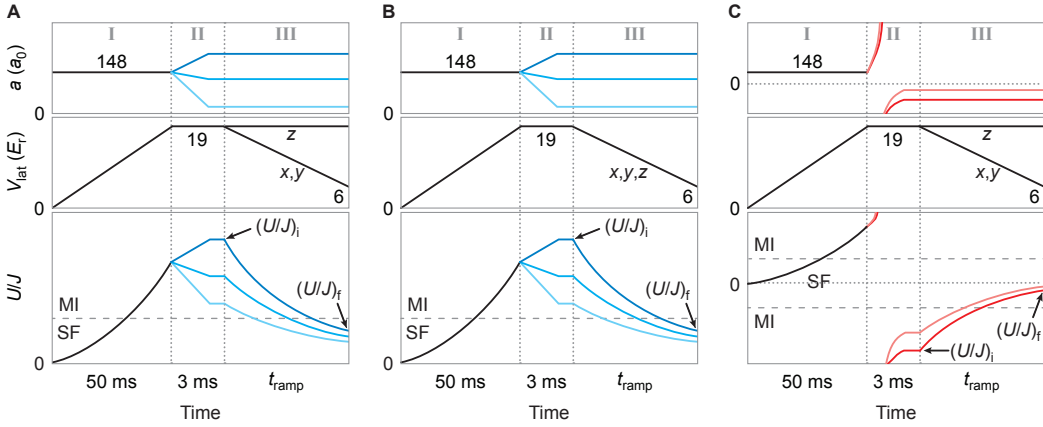


Figure 6.5: Experimental sequence for higher dimensions and attractive interactions. **A**, Sequence for the emergence of coherence in 2D. The sequence is similar to the 1D sequence (Fig. 6.2). In the 2D case, both x - and y -lattice depths are ramped down simultaneously. In contrast to the 1D sequence, the lattice depth along the z -direction stays at $V_{\text{lat}}^z = 19 E_r$ (see main text). **B**, In the 3D sequence, in contrast to the 2D sequence, we ramp down the depth of all three lattice axes simultaneously. **C**, Sequence for the emergence of coherence for attractive interactions in 2D. By crossing the Feshbach resonance with the magnetic field ramp in the deep lattice, the scattering length is rapidly switched to a negative value. This also leads to a large negative $(U/J)_i$ value that decreases (in absolute terms) to the negative final interaction $(U/J)_f$. During the Feshbach ramp, we rapidly switch the trapping to an anti-trapping potential (not shown), thereby creating a stable state at negative temperature (cf. Fig. 5.1).

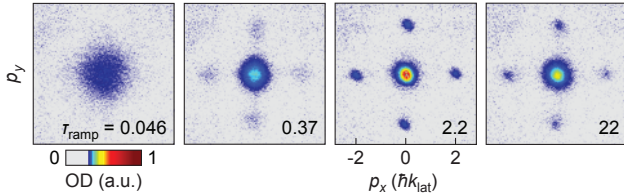


Figure 6.6: Time-of-flight images for the 2D case and repulsive interactions for $(U/J)_i = 110$ and $(U/J)_f = 3.2$. In contrast to the 1D case (Fig. 6.4), coherence is established along both horizontal directions. Again, there is an intermediate ramp time for which the final coherence is maximized.

ramp time of some $(U/J)_f$ values in 1D, 2D (both at repulsive and attractive interactions), and 3D. We fitted these distributions, which represent integrated 3D density distributions, with 2D Gaussian functions

$$n(x, y) = Ae^{-\frac{(x-x_0)^2}{2R_x^2} - \frac{(y-y_0)^2}{2R_y^2}}, \quad (6.16)$$

from which we obtained the free fit parameters A , x_0 , R_x , y_0 , and R_y . Cuts through some sample *in situ* images together with the fits are shown in Fig. 6.9. We obtained the *in situ* width as the root mean square

$$R = \sqrt{\frac{R_x^2 + R_y^2}{2}}. \quad (6.17)$$

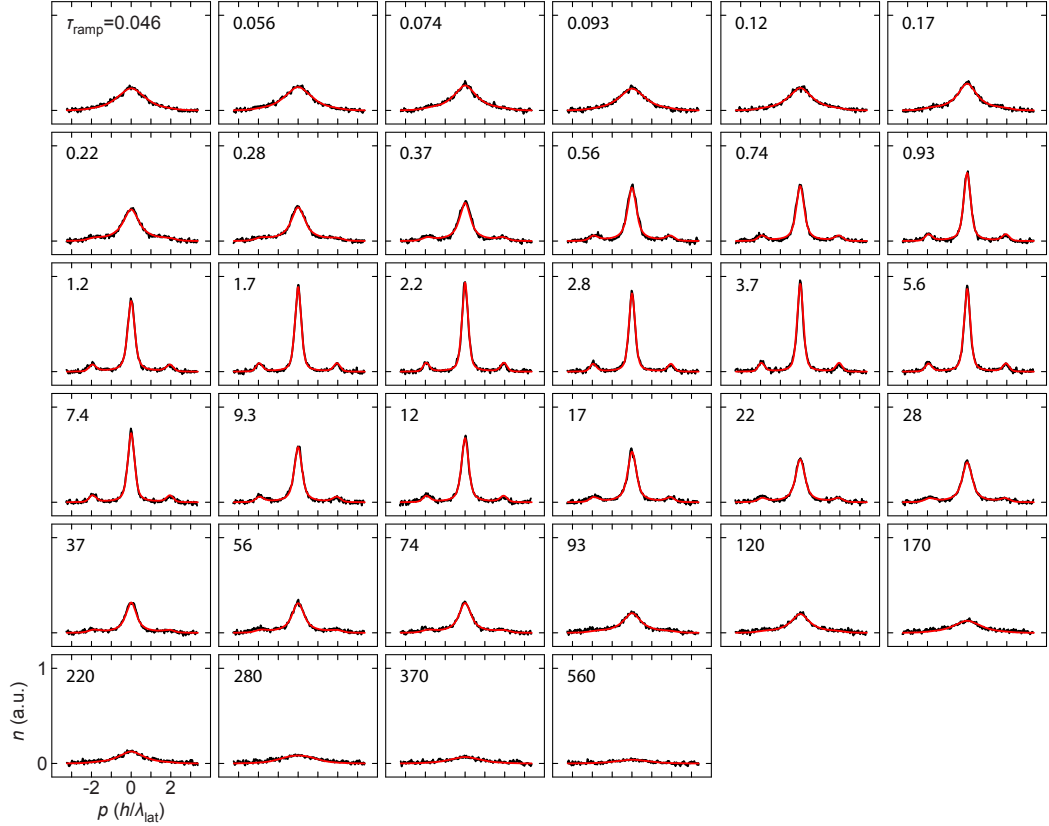


Figure 6.7: Extraction of coherence length. The experimental data (black) in a 1D measurement at $(U/J)_f = 2$ was integrated along y . The red curves are the fitted interference patterns for each ramp time τ_{ramp} with fixed in situ width $R = 31 d_{\text{lat}}$. For this figure, after fitting the normalized curves, both experimental and fitted curve were rescaled to the original amplitude of the experimental data.

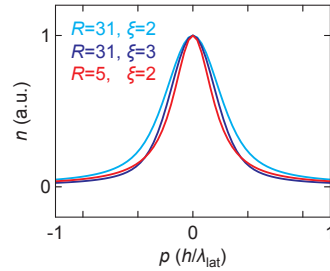


Figure 6.8: Dependence of width and coherence length. Compared to the calculated interference pattern for $R = 31 d_{\text{lat}}$, $\xi = 2 d_{\text{lat}}$ (light blue), both a larger coherence length ξ (dark blue) and a smaller width R lead to a decreasing peak width. These two parameters are therefore not completely independent in the fitting procedure.

The resulting widths R for the 1D case with repulsive interactions are plotted in Fig. 6.10 versus τ_{ramp} . For small and intermediate ramp times of $\tau_{\text{ramp}} \lesssim 10$, the width R

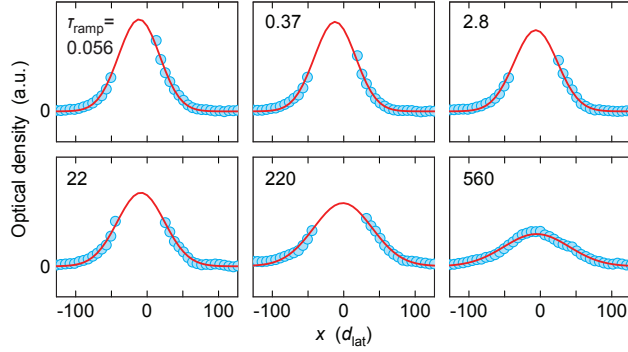


Figure 6.9: Fitting of in situ clouds. The blue curves are cuts through experimental in situ distributions for $(U/J)_f = 1.9$ in 1D for various ramp times. In some images, the high optical density of the cloud center exceeded the dynamical range of our imaging setup (cf. Section 3.4.1). We excluded the corresponding data points from the fits and also from this plot. The red curves are cuts through the 2D Gaussian fits.

is constant. Only for longer ramp times is global mass redistribution possible and the cloud expands during the lattice ramp. While in the 1D cases, the cloud expands along the x -direction where the lattice is lowered during ramp-down, in the 2D and 3D cases, the clouds expand along both the x - and y - directions that are visible in the images taken along the z -direction. As, in this project, we are mainly interested in short and intermediate timescales, we average all measured R up to a maximum ramp time $\tau_{\text{ramp}}^{\max} = 4$.

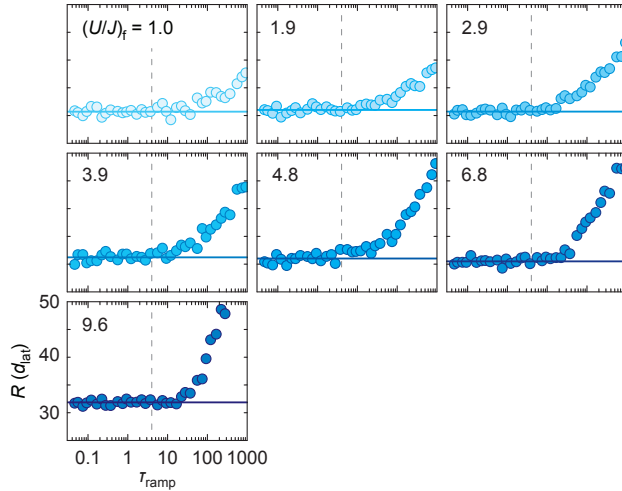


Figure 6.10: Fitted in situ widths R versus ramp time for various $(U/J)_f$ in 1D. The dashed line indicates the maximum ramp time $\tau_{\text{ramp}}^{\max} = 4$ up to which the widths are averaged. The solid horizontal lines indicate the resulting average.

We did not record in situ images for all data sets with $(U/J)_f$ for which we also recorded TOF images. We can, however, still estimate the width R for those data sets for which we only recorded TOF images. For this purpose, we determined the atom number from

the TOF images by performing a simple area sum and averaged all values for small and intermediate ramp times to obtain N . The atom number only decreases for large τ_{ramp} due to heating from technical noise and light scattering. As expected, when plotting the fitted width R versus $N^{1/3}$ for those data sets for which we recorded both TOF and in situ images, we observe a clear correlation (Fig. 6.11). In all 1D and 2D experiments, we used the same loading sequence for the optical lattice, leading to the same functional dependence $R = m \cdot N^{1/3}$, with a fitted slope $m_{1\text{D},2\text{D}} = 0.685(4) d_{\text{lat}}$. In the 3D case, the trap frequencies during lattice loading were different, leading to a different atomic distribution and a fitted slope $m_{3\text{D}} = 0.807(5) d_{\text{lat}}$. These fitted slopes allowed us to estimate the widths R also for those data sets for which we did not record in situ images. We rounded each R to an integer number of lattice constants d_{lat} and used the resulting value for the fitting of interference patterns to determine ξ . The resulting widths R of all data sets lie between 26 and $32 d_{\text{lat}}$.

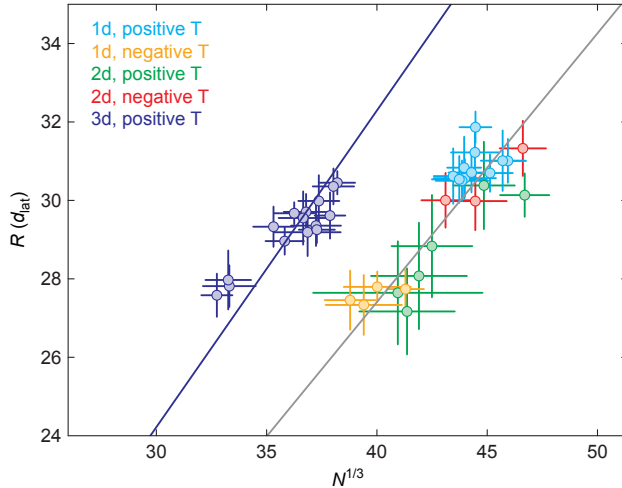


Figure 6.11: Fitted in situ widths R versus $N^{1/3}$, determined from area sums in TOF images. The two quantities show a strong correlation. The linear fit $R = m \cdot N^{1/3}$ (solid gray line) to both 1D and 2D data gives a slope of $m_{1\text{D},2\text{D}} = 0.685(4) d_{\text{lat}}$ and the fit to the 3D data (purple) $m_{3\text{D}} = 0.807(5) d_{\text{lat}}$.

6.2.5 DMRG Calculations

In the following three sections, I briefly describe the numerical calculation methods that were used by our colleagues at FU Berlin – Mathis Friesdorf, Jens Eisert, Arnau Riera, and Marco del Rey – to simulate our experimental measurements in 1D.

The key method in this project is a density matrix renormalization group (DMRG) simulation [211], based on the *Open Source TEBD* code [212]. It is performed for a homogeneous 1D system of variable system size between $N = 20$ and 55, and is based on matrix-product states. It was also extended to an inhomogeneous, trapped system (Section 6.3.3). The only input parameters for this calculation were the time-dependent parameters

$U(t)$ and $J(t)$ as they develop during the experimental sequence, and there was no fitting to experimental parameters. The code assumes open boundary conditions and truncates the occupation per lattice site at 6 particles. By varying technical DMRG parameters and monitoring the results of the simulation, the code was checked to be stable with respect to these parameters.

The calculations start in the ground state of the deep lattice, which turns out to be an excellent approximation for the experimental sequence (Section 6.2.1). The Feshbach ramp preparing the initial state at $(U/J)_i$ is performed deep in the Mott insulating regime with a large spectral gap and is very close to adiabatic. The simulation yields the correlator $\langle \hat{a}_\mu^\dagger \hat{a}_\nu \rangle$ and the coherence length is obtained by exponential fits of the correlations at the center of the system (Fig. 6.12). For large τ_{ramp} , the decay of correlations is expected to be exponential only for large distances, but to follow power-law characteristics over short distances [213]. However, we fit the overall decay with a single exponential function. This is supported by the good agreement of the resulting coherence lengths with the experimentally measured values (Section 6.3.1).

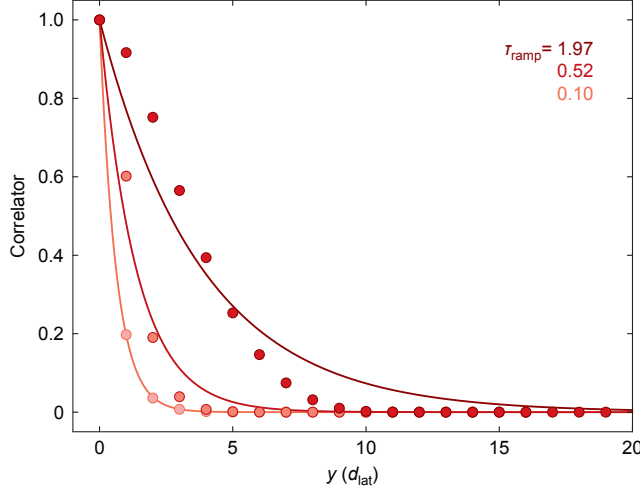


Figure 6.12: Non-equilibrium correlators obtained from DMRG calculations for $(U/J)_f = 1$ in 1D for various ramp times and corresponding exponential fits.

6.2.6 Exact Diagonalization Calculations

The exact diagonalization calculation consists of a numerical integration of the homogeneous 1D Bose-Hubbard model. It is restricted to 15 sites with unity filling, and restricts the on-site occupation to 9 bosons. Periodic boundary conditions were assumed and the computational complexity was reduced by taking into account all symmetries of the system.

The exact diagonalization simulation agrees with the DMRG calculations for short ramp times, despite its limitation to relatively small system sizes (Fig. 6.13): For short τ_{ramp} , the coherence length in the system is much smaller than the system size. For longer ramp

times, where the two methods deviate from each other, a finite size scaling was performed (Fig. 6.14). While the exact diagonalization calculation indeed shows limitations for long ramp times, the DMRG calculation for system sizes larger than a particular threshold yields essentially the same behavior as an infinite system. This is consistent with a light-cone picture, where correlations spread for longer ramps but cannot exceed a certain limit set by the maximum propagation velocity.

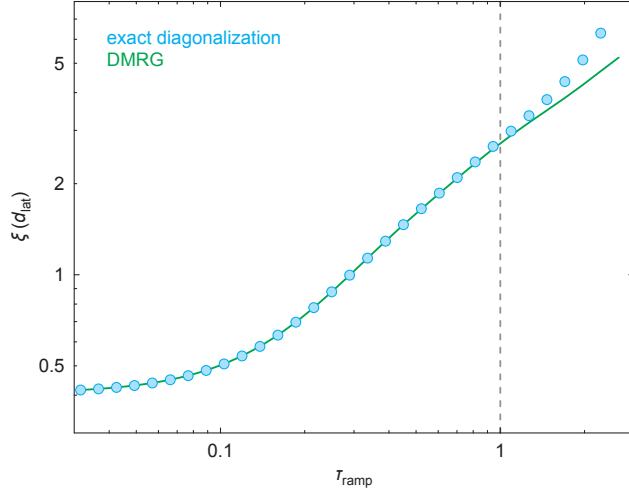


Figure 6.13: Comparison of the resulting coherence lengths between the DMRG and exact diagonalization calculations for $(U/J)_f = 2$ in 1D. The vertical dashed line indicates the ramp time at which deviations between the two methods become relevant.

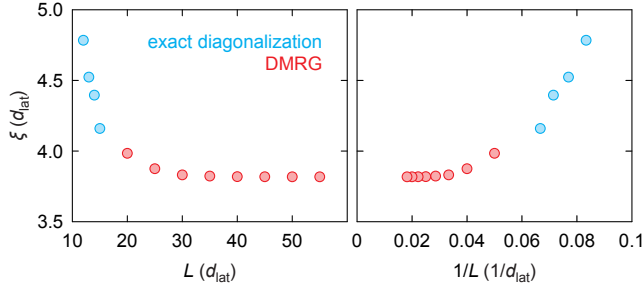


Figure 6.14: Finite size scaling of both DMRG and exact diagonalization calculations for a fixed ramp time $\tau_{\text{ramp}} = 2.0$ at $(U/J)_f = 1$ in 1D, plotted versus system size L (left). In the plot versus $1/L$ (right) one can extract the limit $L \rightarrow \infty$.

6.2.7 Doublon-Holon Fermionic Model

The doublon-holon fermionic model (DHFM) is a method that is based on the truncation of the Hilbert space in the quasiparticle picture of the Mott insulator with integer filling \bar{n} . It restricts the possible quasiparticle excitations to two kinds, holons and doublons,

corresponding to occupations $\bar{n} - 1$ and $\bar{n} + 1$, respectively. The model is a valid approximation for the 1D Bose-Hubbard model close to the Mott insulator ground state in the strong interaction regime ($U/J \gtrsim 8$ [214, 215]). Here, the density of quasiparticle excitations is low such that interactions between these are negligible. Applying this model to a lattice quench leads to the physical intuition that quasiparticle excitations are continuously created during the ramp. These excitations subsequently spread ballistically throughout the system with their corresponding quasiparticle velocity, which is ultimately limited by a Lieb-Robinson bound [216–222]. The model is exactly solvable and therefore allows the evolution of the system to be investigated for time-dependent parameters $U(t)$, $J(t)$ for very large system sizes up to several hundreds of bosons. Even though the model is not valid at the phase transition ($U/J_c \approx 3.3$ ($\bar{n} = 1$) [102–104]), which is crossed for the most relevant experimental ramps, it reproduces the results of the full Bose-Hubbard model for these ramps for sufficiently short ramp times. Further details about the model can be found in the supplementary material of [183].

The starting point of the model, following [214, 215], is the Bose-Hubbard Hamiltonian, where periodic boundary conditions and unity filling $\bar{n} = 1$ per lattice site are assumed. The local occupation was truncated at 2 bosons per site, and the quasiparticles are introduced as holons \hat{h} and doublons \hat{d} . New doublon and holon species were constructed via a double Jordan-Wigner transformation as fermionic excitations. As an additional approximation, the fermions in the model are unconstrained, i.e. can appear simultaneously on the same lattice site. As the density of excitations deep in the Mott insulating regime is low and the coincidence of two excitations at the same site is very unlikely, this approximation is justified. The model is solved in the Fourier basis, by exactly diagonalizing the Hamiltonian at a given time via a Bogoliubov transformation into modes $\gamma_{\hat{d},k}$, $\gamma_{\hat{h},-k}$ of quasiparticles with definite momenta k . From the dispersion relation of these modes, one obtains a maximum group velocity for the spread of correlations [215], i.e. a maximum relative velocity of a doublon-holon pair where both particles are created simultaneously during the quench at opposite momenta [214],

$$\mathcal{V} = \max_k \left| v_{\gamma_{\hat{h},-k}} - v_{\gamma_{\hat{d},k}} \right| = 6J - \frac{32}{3} \frac{J^3}{U^2} + O\left(\frac{J^4}{U^3}\right). \quad (6.18)$$

This maximum velocity is reminiscent of a Lieb-Robinson bound. To finally obtain the correlators $\langle \hat{a}_\mu^\dagger \hat{a}_\nu \rangle$ necessary for the comparison with the experiment, the initial state at the beginning of the quench is assumed to be a product state, i.e. without any doublons or holons.

In Fig. 6.15, the DHFM calculation is compared to the DMRG and exact diagonalization results. For short ramp times, the DHFM calculation agrees with the other two methods, even though the ramp crosses into the superfluid regime where the model loses validity. During these fast ramps, only few doublons and holons are created and, in particular, they also have only a short time to propagate. Therefore, in this regime, the limitations of the model (i.e. a maximum of 2 particles per site and unconstrained fermions) do not yet become relevant. In contrast, during longer ramp times, additional doublons and holons

as well as larger propagation distances both exceed the limitations of the model and lead to deviations from the exact calculations.

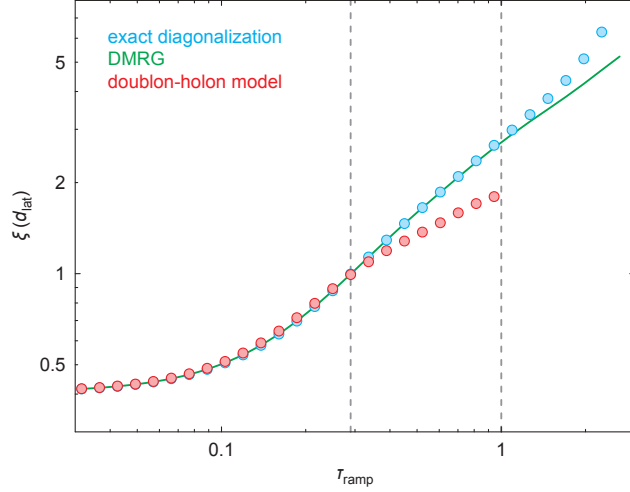


Figure 6.15: Comparison of the doublon-holon fermionic model (on 64 sites) with DMRG and exact diagonalization (on 15 sites) for $(U/J)_f = 2$ in 1D. The vertical dashed lines indicate the ramp times at which the methods start to deviate from each other. For other $(U/J)_f$ values, the behavior is qualitatively the same.

For Bose-Hubbard models, rigorous Lieb-Robinson bounds are not applicable in the case of unlimited local occupation, because Bose enhancement increases the tunnel coupling [214]. However, in the case of a truncated model such as the DHFM, we can estimate an upper limit for the emergence of coherence in the system via the time-dependent maximum velocity \mathcal{V} for the spreading of quasiparticles (Eq. 6.18). At the end of the lattice ramp, the spreading of quasiparticles is limited to $\int_0^{\tau_{\text{ramp}}} dt \mathcal{V}(t)$, corresponding to a crude upper bound for the emergence of coherence,

$$\xi(\tau) \leq \xi_0 + \int_0^{\tau_{\text{ramp}}} dt \mathcal{V}(t). \quad (6.19)$$

This limit takes into account the spreading of quasiparticles even close to the ground state deep in the Mott insulating regime where quasiparticles are absent, and therefore systematically overestimates the emergence of coherence. However, this intuitive estimate already leads to a functional behavior of the increasing coherence length that qualitatively resembles the exact calculation.

6.2.8 Determination of Power-Law Exponents

After the presentation of the three theoretical methods in the previous sections, in this section, I describe how we extracted the power-law exponents for both experimental and theoretical data. The experimentally measured coherence length is plotted in Fig. 6.17 for several final interaction strengths $(U/J)_f$. In this plot, one can distinguish several distinct

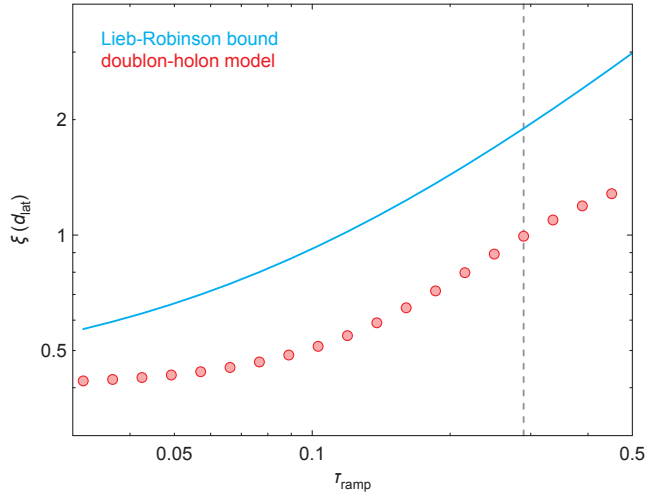


Figure 6.16: Emergence of coherence for the Lieb-Robinson bound provided by Eq. 6.19 and for the doublon-holon fermionic model for $(U/J)_f = 3$ in 1D. The vertical dashed line indicates the ramp time at which the DHFM deviates from the DMRG calculation (Fig. 6.15).

regimes. For very short ramp times, $\tau_{\text{ramp}} \lesssim 0.1$, the evolution can be approximated by the sudden approximation. The measured coherence length is therefore given by the initial coherence length ξ_i at the beginning of the lattice ramp. This coherence length is considerably below one lattice spacing, $\xi_i < d_{\text{lat}}$, and increases with decreasing $(U/J)_i$ closer to the superfluid regime (cf. Figs. 6.20 and 6.21). Thus, already during the Feshbach quench correlations build up between atoms, albeit only on a low level. For larger ramp times $0.1 \lesssim \tau_{\text{ramp}} \lesssim 1$, the coherence length quickly increases up to several lattice sites. In this project, we mainly focus on this regime, as it gives the major contribution to the emergence of coherence. Within almost one order of magnitude difference, the coherence length versus ramp time shows a power-law increase

$$\xi(\tau_{\text{ramp}}) = a \tau_{\text{ramp}}^b, \quad (6.20)$$

which I focus on in this section.

For larger ramp times $\tau_{\text{ramp}} \gtrsim 1$, the coherence length starts to deviate from the power-law increase and, at some point, decreases. The reason for this deviation is the external trapping potential present in the experiment which requires global mass and entropy redistributions when ramping from the Mott insulating into the superfluid regime. Details about the intricate effects of the external trapping potential are given in Section 6.3.3. For very long ramp times $\tau_{\text{ramp}} \gtrsim 100$, heating due to technical noise in the laser beams as well as by photon scattering decreases the coherence length even further: From hold time experiments in a shallow optical lattice potential, we know that phase coherence between lattice sites decreases on a timescale of several hundred ms (cf., e.g., Section 5.2.1), corresponding to ramp times τ_{ramp} of several hundred.

To obtain a reliable value for the exponent b of the power-law growth of the coherence

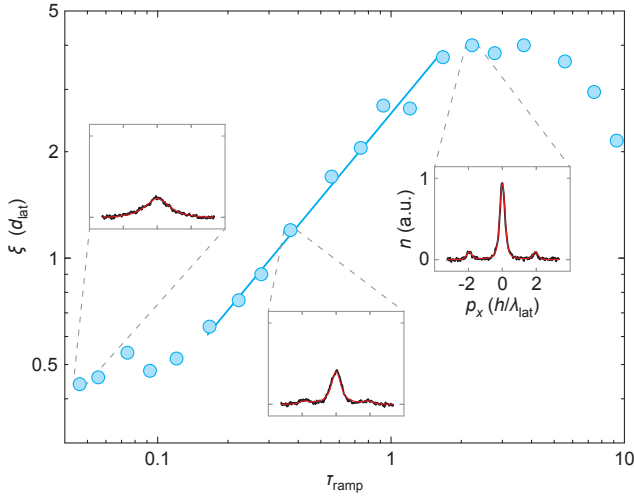


Figure 6.17: Emergence of coherence. Extracted coherence length ξ for the 1D system and $(U/J)_i = 47$, $(U/J)_f = 2$ versus ramp time τ_{ramp} in a double-logarithmic plot. For very short τ_{ramp} , the coherence length acquires a small, finite value ξ_i . The power-law increase for intermediate τ_{ramp} is qualitatively highlighted by the straight line. For large τ_{ramp} , the coherence length decreases due to the external trapping potential and heating (see main text). The insets show sample time-of-flight profiles (black) with the corresponding fitted calculated interference pattern (red).

length, it is desirable to include as many data points as possible into the fitting procedure. When fitting a pure power-law function $\xi(\tau_{\text{ramp}}) = a \tau_{\text{ramp}}^b$, however, the range of data points for the fit is limited by two effects: For small ramp times, the coherence length is given by the initial coherence length ξ_i , while for long ramp times $\tau_{\text{ramp}} \gtrsim 1$, the data deviates from a pure power-law increase due to the influence of the trap. To improve the stability of the fit, we include the initial coherence length ξ_i in the fitting procedure via an empirical function

$$\xi(\tau_{\text{ramp}}) = (\xi_i^q + (a \tau_{\text{ramp}}^b)^q)^{1/q}, \quad (6.21)$$

which approaches the pure power-law increase for large τ_{ramp} . Here, a , b , and ξ_i serve as free fit parameters; only for $(U/J)_f > (U/J)_c$, ξ_i is fixed to numerically calculated values (see below). With this fit function, we can include all data points for short and intermediate ramp times up to a maximum value $\tau_{\text{ramp}}^{\max}$. As in some data sets, clear deviations from the pure power-law behavior due to the trap appear for $\tau_{\text{ramp}} > 1$, we chose $\tau_{\text{ramp}}^{\max} = 1.0$, as it guarantees that for all data sets in any dimension and at both repulsive and attractive interactions the influence of the trap on the fitted exponent b is negligible.

To obtain a reasonable value for the parameter q , we perform sample fits on the data sets for $(U/J)_f = 1.0$ and 1.9 in 1D for varying q , for both experimental as well as exact diagonalization data (Section 6.2.6). As a measure of how close the fits are to the data, we determine the sum of squared residuals (SSR) of the fit and find that $q = 4$ is a good compromise (Fig. 6.18). Figure 6.19 indicates that the fitted exponents are robust with respect to the choice of q and Fig. 6.20 shows that the choice $q = 4$ indeed captures the

emergence of coherence well.

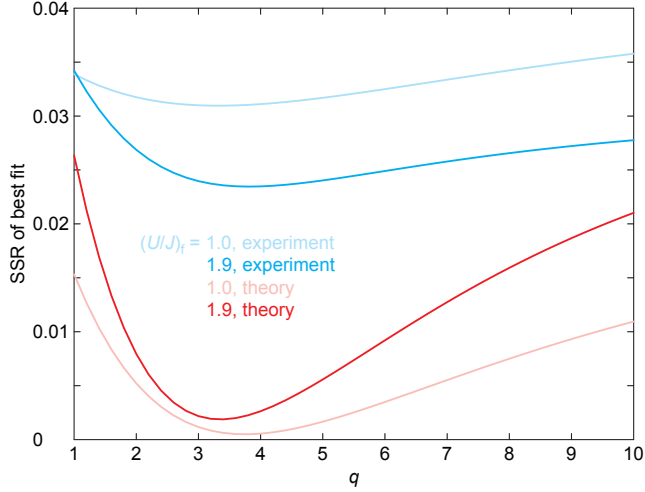


Figure 6.18: Sum of squared residuals (SSR) of the general power-law fit (Eq. 6.21) versus value of q for some 1D data. Light-blue and dark-blue are the results of fits to experimental data with $(U/J)_f = 1.0$ and 1.9 , respectively. Light-red and dark-red are the corresponding results for exact diagonalization data. A choice of $q = 4$ leads to close-to-minimum SSR values in all four cases.

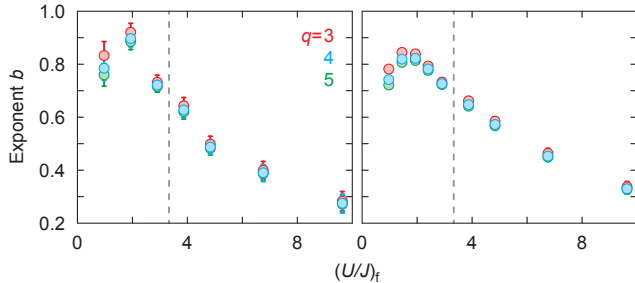


Figure 6.19: Fitted exponents in 1D for $\tau_{\text{ramp}}^{\max} = 1$ and variable $(U/J)_f$ for various q values. Left, experimental data, right, DMRG data. The error bars are fit uncertainties, and the vertical dashed line indicates $(U/J)_c$. For details of the fitting procedure, see Figs. 6.20 and 6.21.

In the 1D case, we also recorded data sets for which the system does not cross the phase transition during the lattice ramp, but where the final interaction strength is still larger than the critical value, at $(U/J)_f > (U/J)_c$. In these cases, the power-law increase of the coherence length is slow, such that it is difficult to distinguish the power-law regime from the regime that is dominated by the initial coherence length ξ_i , and the fit does not capture the behavior reliably anymore. Exact diagonalization calculations (Section 6.2.6) provide theory values for the initial coherence length ξ_i . In the case of the data sets with $(U/J)_f < (U/J)_c$ (Fig. 6.20), these agree well with the fitted ξ_i . For the data sets with $(U/J)_f > (U/J)_c$, we fix the initial coherence lengths to the calculated ones and thereby improve the stability of the fit. The resulting fits (Fig. 6.21) match the data well; only

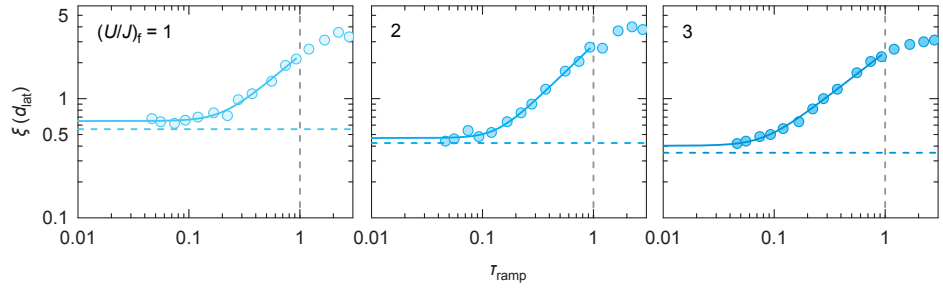


Figure 6.20: Power-law fits (solid lines) for $q = 4$ for experimental data in 1D with $(U/J)_f < (U/J)_c$ and the initial coherence length ξ_i as a free fit parameter. The vertical dashed lines indicate the upper end $\tau_{\text{ramp}}^{\max} = 1.0$ of the fitting range. The horizontal dashed lines denote ξ_i at the beginning of the lattice ramp obtained from exact diagonalization calculations that show good agreement with the extrapolated fitted values $\xi(\tau_{\text{ramp}} \rightarrow 0)$.

for very large interaction strengths $(U/J)_f \gg (U/J)_c$ do systematic deviations from the simple power-law behavior become relevant.

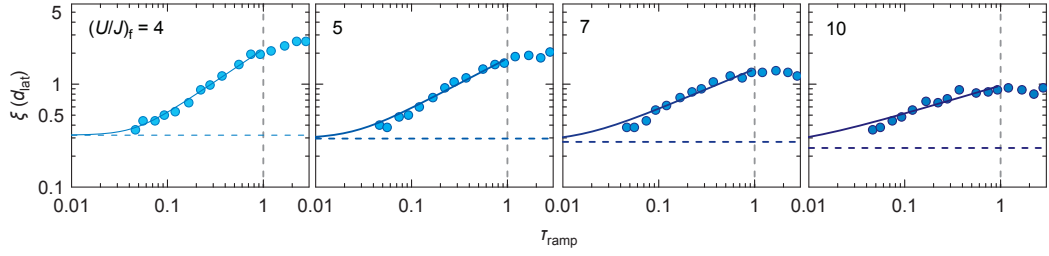


Figure 6.21: Power-law fits (solid lines) for $q = 4$ for experimental data in 1D with $(U/J)_f > (U/J)_c$. The initial coherence lengths ξ_i in the fit are fixed to the value obtained by exact diagonalization calculations, indicated by the horizontal dashed lines. The vertical dashed lines indicate the upper end $\tau_{\text{ramp}}^{\max} = 1.0$ of the fitting range. The fitting model captures the behavior well for not too large $(U/J)_f$. For very large $(U/J)_f$, systematic deviations of the model from the data appear.

With this procedure, we were able to reduce the problem of defining an appropriate fitting range. The upper limit $\tau_{\text{ramp}}^{\max}$, however, is still arbitrary. In the 1D case, where the phase transition at the multicritical point is of Kosterlitz-Thouless type [187], we expect the power-law exponent to depend slightly on the ramp time and therefore also on the upper limit for the fit (Section 6.3.1). As mentioned, we chose $\tau_{\text{ramp}}^{\max} = 1.0$, as it excludes data points that are considerably influenced by the trap, for all data sets in any dimension. To estimate the uncertainty of the resulting exponents b , we also performed fits for different values of $\tau_{\text{ramp}}^{\max} = 0.9$ and 0.7 . In Fig. 6.22, all resulting exponents in the 1D repulsive interactions case are plotted with the corresponding fit errors. As a measure for the uncertainty associated with the choice of $\tau_{\text{ramp}}^{\max}$, we determined the total amplitude of the fitting errors for the three different choices of $\tau_{\text{ramp}}^{\max}$.

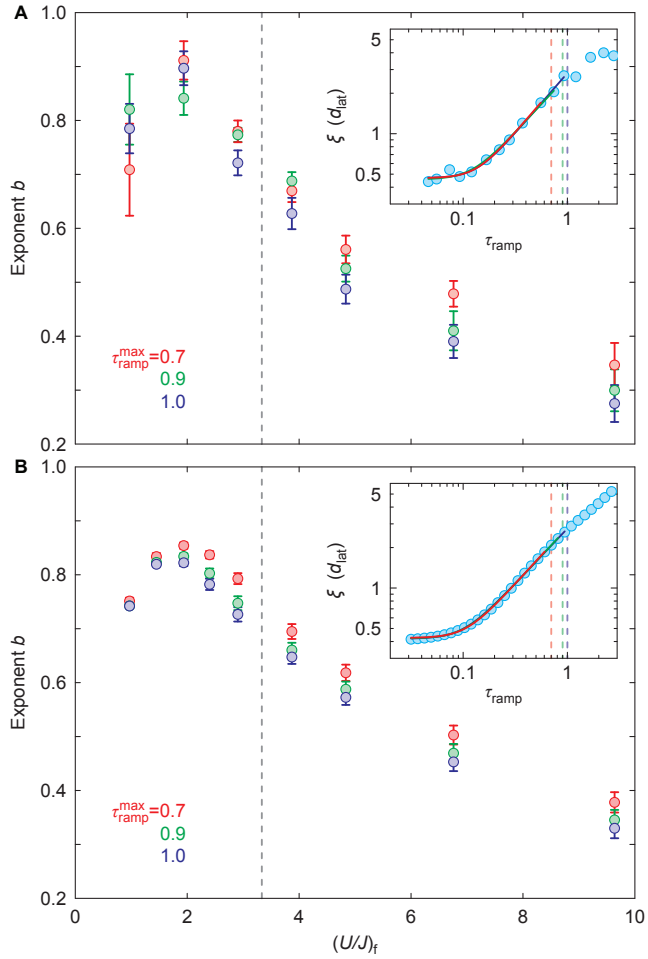


Figure 6.22: Fitted exponents for various upper limits of the fit range for **A**, experimental data, **B**, DMRG data. The error bars are the fit uncertainties and the vertical dashed line indicates $(U/J)_c$. The insets show sample fits for $(U/J)_f = 2$, with the vertical dashed lines indicating $\tau_{\text{ramp}}^{\text{max}}$.

6.3 Results in 1D

In this section, I present the results for the power-law emergence of coherence in 1D and compare them to the numerical simulations. After determining the predictions of the Kibble-Zurek mechanism for the 1D case, I compare them to our findings and analyze the applicability of this model to our particular situation. I give an analysis of the decrease of the coherence length in the experimental measurements for long ramp times, which is in some regime caused by the external trapping potential.

6.3.1 Power-Law Emergence of Coherence and the Kibble-Zurek Prediction

We find excellent agreement between the measured experimental data on the emergence of coherence in 1D and the results of DMRG calculations (Fig. 6.23). For both the initial coherence length ξ_i as well as the subsequent power-law increase of the coherence length up to ramp times of $\tau_{\text{ramp}} \lesssim 1 - 2$, the data of experiment and theory match very well. As the numerical calculations are performed on a homogeneous system, this agreement shows that for short and intermediate ramp times we effectively probe the homogeneous Bose-Hubbard model in the experiment: On short timescales of up to a few tunneling events, global mass redistribution in the system is negligible and thus the density is essentially constant during the ramp and given by that of the initial Mott insulator, i.e. a homogeneous distribution of one atom per site. In the homogeneous Bose-Hubbard model with integer filling the Mott insulator to superfluid phase transition crosses the multicritical point at the tip of the Mott lobe [32]. This experiment is the first investigation of the physics at a quantum critical point in an essentially homogeneous system. In contrast, an inhomogeneous system, where the dynamics is dominated by mass transport, crosses the phase transition at the side of the Mott lobe, corresponding to a change in density [195].

Inhomogeneities only become relevant for longer ramp times $\tau_{\text{ramp}} \gtrsim 2 - 5$: While the coherence length in the numerical data continues to increase, the experimental data deviates and starts to decrease. This effect is caused by the trap and is described in detail in Section 6.3.3. In this regime, the system does not cross the phase transition at the multicritical point anymore.

The doublon-holon fermionic model, which is consistent with the result of the DMRG calculations for ramp times $\tau_{\text{ramp}} \lesssim 0.3$, consequently also agrees with the experimental data in this regime. On these short timescales, the limitations of this analytic model are not yet relevant (Section 6.2.7). The dynamics in this regime can therefore be explained by quasiparticle excitations that are continuously created during the ramp and subsequently spread ballistically in the system. The velocity of the quasiparticles is ultimately limited by Lieb-Robinson bounds (Section 6.2.7). For intermediate ramp times $\tau_{\text{ramp}} \gtrsim 0.3$, however, interactions between the quasiparticles become relevant. These interactions, which are not captured by the doublon-holon fermionic model presented in this work, are expected to be one reason for the deviation of the model from the exact results.

For slow quenches, one can use the adiabatic theorem (Section 6.1.1) and the Kibble-Zurek mechanism (Section 6.1.2) to explain the dynamics. If the breakdown of adiabaticity happens close to the critical point, where the physics is governed by critical scaling, the KZM predicts a power-law increase of the coherence length, with exponents that are determined by the critical exponents of the corresponding universality class. The dynamical exponent of the Bose-Hubbard model for a phase transition at the multicritical point is $z = 1$, and the critical exponent ν depends on the dimensionality of the system. In 1D, the phase transition at the multicritical point is a Kosterlitz-Thouless transition [187]. A Kosterlitz-Thouless transition is characterized by an exponential, non-polynomial scaling

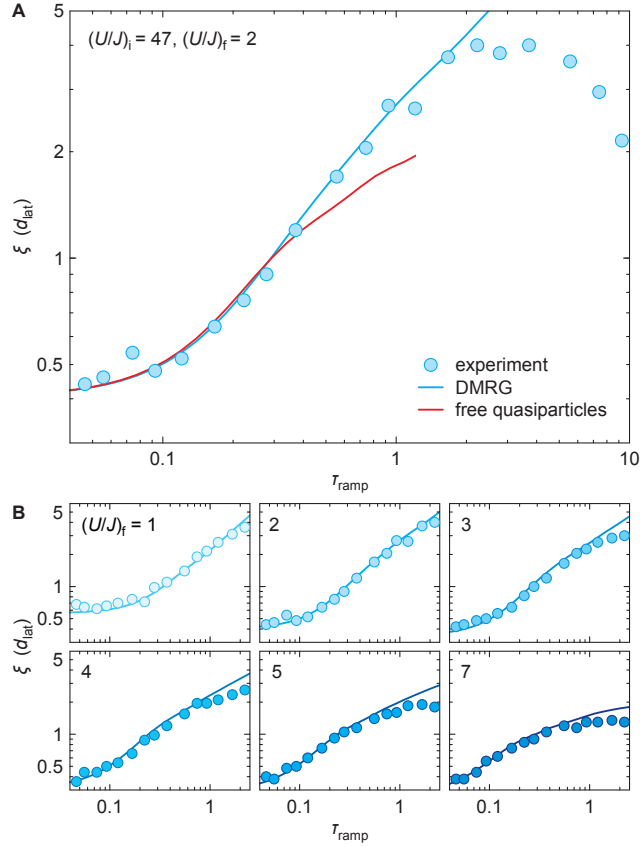


Figure 6.23: Emergence of coherence in 1D. The experimental data (points) is plotted together with DMRG calculations (blue curves). **A**, Comparison of $(U/J)_f = 2$ data with doublon-holon fermionic model (red curve). **B**, Data and DMRG calculations for various $(U/J)_f$.

of both the gap and the correlation length around the critical point, which can be described as $\nu \rightarrow \infty$ very close to the critical point. Following Eq. 6.11, the correlation length is expected to scale linearly with the quench time [223],

$$\hat{\xi} \propto \tau_Q^b = \tau_Q. \quad (6.22)$$

This scaling should, however, only be valid in the limit of very long quench times, as the exponential scaling of the gap in a Kosterlitz-Thouless transition implies that the coherence length follows a true power-law increase only for very long quench times [224]. For shorter quench times, the increase can, in a limited range of quench times, be approximated by a power-law behavior, with an exponent depending on the quench time [224]. Estimates from Ref. [224] yield an exponent $b < 0.1$, i.e. much smaller than the limiting case $b = 1$ of Eq. 6.22 for extremely long quench times.

In the case of the generic density-driven transition at the side of the Mott lobe, the critical exponents are $z = 2$ and $\nu = 0.5$ [187], leading to

$$\hat{\xi} \propto \tau_Q^{1/4}. \quad (6.23)$$

A classical phase transition with inhomogeneous Kibble-Zurek scaling has recently been investigated with ion chains [203, 204], and a thermal phase transition with ultracold atom systems [225, 226].

In both our experiment and in the numerical simulations, we observe a power-law increase for ramp times of about one order of magnitude (Section 6.2.8). This may be surprising, as rough estimates suggest that the breakdown of adiabaticity in the intermediate ramp time regime in the experiment happens outside of the critical regime, thus violating an applicability condition of the KZM (Section 6.3.2). The fitted power-law exponents (Section 6.2.8) in 1D are systematically below $b = 1$ expected from the above KZM scaling at the multicritical point for long quench times (Fig. 6.24). On the other hand, they are substantially larger than the estimate $b < 0.1$ for our ramp time regime. The KZM prediction for the generic transition at the side of the Mott lobe, $b = 1/4$, which we do not expect to be applicable in the intermediate ramp time regime, is also clearly lower than the experimental exponents.

More importantly than the deviation of the absolute value of the exponents from the KZM scaling, we observe a dependence of the experimental and numerical exponents on interaction $(U/J)_f$, even when neglecting those ramps that do not cross the phase transition. The Kibble-Zurek picture assumes a freezing of the state near the critical point and in a gapless phase, such that the coherence length should not depend on the final interaction $(U/J)_f$ of the ramp. While, therefore, the power-law is also expected to be independent of $(U/J)_f$, we clearly measure a dependence, both in the experiment as well as in the numerical simulations.

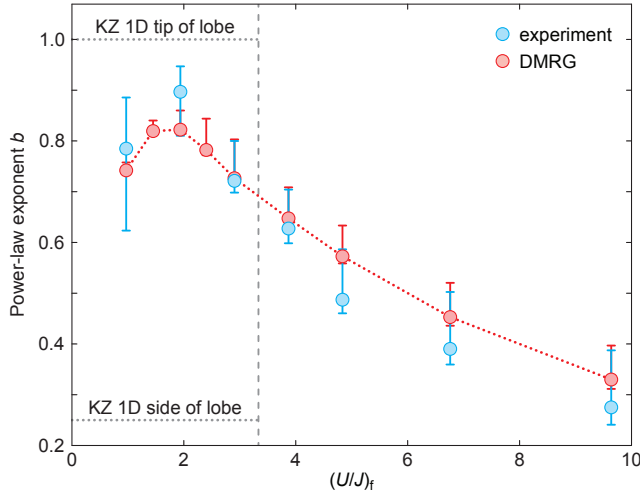


Figure 6.24: Fitted exponents for an upper limit of the fit range $\tau_{\text{ramp}}^{\max} = 1.0$ for experimental and DMRG data. The error bars are the total amplitude of fitting errors for $\tau_{\text{ramp}}^{\max} = 1.0, 0.9$, and 0.7 . The vertical dashed line indicates $(U/J)_c$. The horizontal dotted lines are the predictions $b = 1$ and $b = 1/4$ of a typical Kibble-Zurek model for the 1D case at the tip and the side of the Mott lobe, respectively.

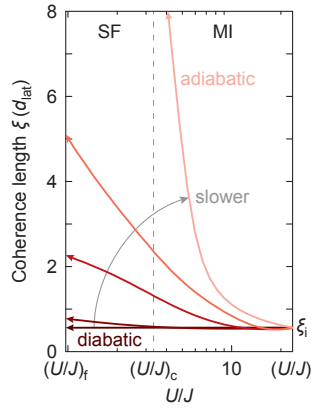


Figure 6.25: Exemplary exact diagonalization results of the development of ξ during the lattice ramp. The calculation is performed in 1D for $(U/J)_i = 24$ and $(U/J)_f = 1$ for total ramp times of $\tau_{\text{ramp}} = 0, 0.25, 1.1, 2.3$, and ∞ (from dark red to light red). While the coherence length diverges in an infinite system in the adiabatic limit ($\tau_{\text{ramp}} \rightarrow \infty$), it is restricted to finite values in the case of finite ramp times. The emergence of coherence mostly happens around the critical point $(U/J)_c$ (vertical dashed line), but barely during the initial part of the ramp at large (U/J) .

6.3.2 Applicability of the Kibble-Zurek Mechanism

The previous section showed that a simple Kibble-Zurek scaling is not sufficient to describe the complex dynamics at the Mott to superfluid phase transition in the regime of fast and intermediate quenches. Not only is the dependence of the exponent b not captured in the Kibble-Zurek framework, but also the dependence of the exponent on dimensionality is much weaker than suggested by Kibble-Zurek (Section 6.4). There are several reasons that could be responsible for these deviations, which I address in this section.

In the experiment, a different final interaction $(U/J)_f$ also entails a different value $(U/J)_i$ at the beginning of the quench. Exact diagonalization simulations (Section 6.2.6), however, show that the initial portion of the evolution is adiabatic and coherence emerges mainly around the critical point $(U/J)_c$ (Fig. 6.25). Thus, the influence of a different initial value $(U/J)_i$ – in contrast to the final value $(U/J)_f$ – on the final coherence length is negligible and cannot be responsible for the interaction dependence. Our collaborators have performed additional exact diagonalization calculations with analogous ramps starting in a deeper lattice $V_{\text{lat}} = 45 E_r$, in contrast to the usual $V_{\text{lat}} = 19 E_r$ (Fig. 6.26). The resulting power-law exponents do not change, except for the one quench that reaches deepest into the superfluid regime. The reason is that in the latter case, the initial state for the usual quench starting at $V_{\text{lat}} = 19 E_r$ is already excited by the Feshbach ramp (see below) such that the dynamics is not comparable to the dynamics of an initial ground state such as in the case of $V_{\text{lat}} = 45 E_r$. The overall dependence of the exponent on $(U/J)_f$ is still present. The influence of the initial and final values of the control parameter have also been investigated in [227, 228].

The calculations also prove that the deviation cannot be caused by the external trap, as

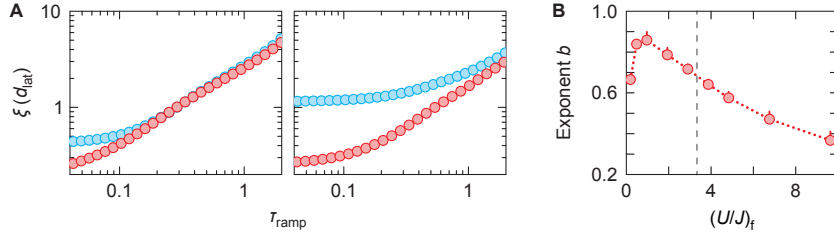


Figure 6.26: **A**, Comparison of exact diagonalization calculations of 15 particles for the experimental ramps starting at $V_{\text{lat}} = 19 E_r$ (blue) and ramps starting in a deeper lattice $V_{\text{lat}} = 45 E_r$ (red), for $(U/J)_f = 2$ (left) and $(U/J)_f = 0.5$ (right). **B**, Corresponding power-law exponents from the ramps starting in the deeper lattice. The dotted line is a guide to the eye, the vertical dashed line indicates $(U/J)_c$.

they are performed in a homogeneous system and agree very well with the experimental result. Furthermore, the influence of the trap becomes relevant in the experimental data only for large ramp times $\tau_{\text{ramp}} > 1$, which are excluded in the fitting of the power-law exponent (for details, see Section 6.3.3).

Also finite size effects [201, 229] cannot explain the deviation from the Kibble-Zurek prediction, as the maximum measured coherence lengths $\xi_{\text{max}} \approx 5 d_{\text{lat}}$ are much smaller than the system size $2R \approx 60 d_{\text{lat}}$. This is further supported by numerical calculations for various system sizes (Section 6.2.6), which converge for large systems and in which this limiting value agrees with the experimentally measured data.

The Kibble-Zurek mechanism assumes that the quench starts in the ground state of the system. The influence of the actual initial state has also been addressed in the literature [230]. Numerical simulations, however, show that the Feshbach ramp in the 1D system in general prepares the ground state of the system (Fig. 6.27A). Only for Feshbach ramps to very low interactions $(U/J)_i$ is the system excited. Additionally, our theory colleagues performed exact diagonalization calculations for initial states that include either a doublon or a hole, corresponding to defects or finite temperature (Fig. 6.27B). The power-law increase in both cases is slightly reduced compared to the zero temperature case, leading to marginally smaller exponents. This small effect, however, also indicates that finite temperature cannot be responsible for the deviation.

The ramp sequence may also have an influence on the resulting scaling [209, 231–233]. Our ramps of $(U/J)(t)$ are, for all dimensionalities, captured well by exponential functions (Eq. 6.14 and Section 6.2.2). In a large range around the critical point $(U/J)_c$, however, the quenches can be approximated by linear ramps, given by tangents to the experimental ramp at the critical point (cf. Eq. 6.6): Relative deviations of these linear approximations from the exponential ramps are below 10 % in a range $U/J \in [2.3, 5.6]$ in 1D, [12, 28] in 2D, and [20, 50] in 3D. Therefore, the influence of the precise ramp timing on the resultant scaling should be small. It is, however, not clear that the resulting power-laws only depend on the evolution of the ratio $(U/J)(t)$ rather than of each of the parameters $U(t)$ and $J(t)$ individually. In our ramps, which are performed by changing the lattice depth V_{lat} ,

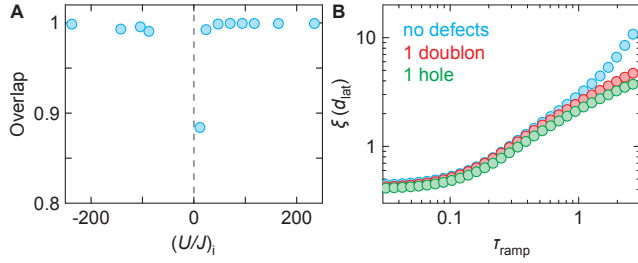


Figure 6.27: **A**, Adiabaticity of the Feshbach ramp. For positive $(U/J)_i$, the overlap with the ground state is indicated (cf. Fig. 6.3). For negative $(U/J)_i$, corresponding to negative temperatures in the case of thermalization, the overlap with the highest excited state is shown. **B**, Exact diagonalization calculation for 12 sites, showing the influence of a single defect. For details, see main text.

the interaction $U(t)$ is close to constant, whereas $J(t)$ increases almost exponentially and dominates the dynamics. This issue would be an interesting topic for future experiments or simulations.

An often stated assumption for the validity of the Kibble-Zurek mechanism is that adiabaticity is only broken close to the phase transition, where everything is dominated by critical scaling. Rough estimates suggest that the experimental ramps in the intermediate ramp time regime are so fast that adiabaticity is broken already outside of the critical regime and the Kibble-Zurek mechanism is not applicable. It is, however, difficult to give a precise value of the maximum quench rate for which the KZM is still applicable and so far, to our knowledge, no quantitative measure for this condition exists. It is therefore difficult to apply it to a particular, concrete experimental sequence. A complete formulation of the KZM should thus also include quantifiable limits of its applicability regime. Most likely, such limits would not only depend on the universality class of the transition, but on more details of the system such as the precise quench sequence. In addition, another uncertainty arises from the limited available data about the scaling of the gap away from the phase transition which sets the adiabaticity timescale (Section 6.1.1).

In general, the Kibble-Zurek mechanism does not seem to be applicable to the experimental situation at hand. Far away from the phase transition, the evolution is certainly adiabatic (Fig. 6.28). Adiabaticity breaks down close to the phase transition when the gap becomes comparable to the change of the Hamiltonian, consistent with the KZM. The dynamics around the phase transition, however, cannot be considered frozen in the current setting: Numerical simulations show that the major part of the dynamics happens close to the critical point (Fig. 6.28), in contrast to the Kibble-Zurek picture.

One may try to formulate potential intuitive explanations for the measured behavior of a $(U/J)_f$ dependence of the power-law exponents. For example, as coherence mainly emerges around the phase transition, the total time that the system spends at or near the phase transition may determine the resulting coherence length at the end of the ramp and thus also the power-law exponent. A different scattering length changes both $(U/J)_f$ and $(U/J)_i$ and indeed changes this time span. This rescaling, however, is identical for all ramp

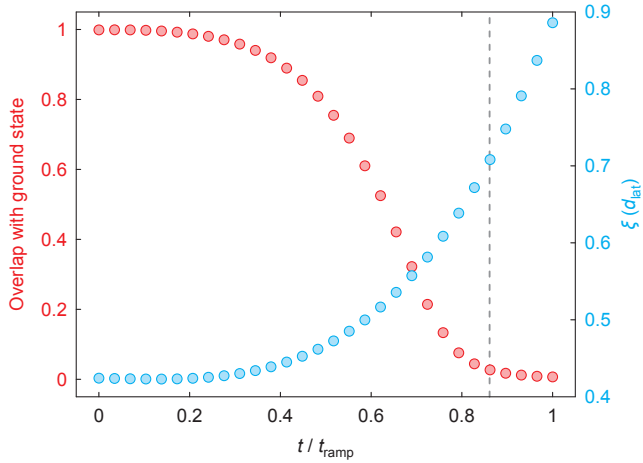


Figure 6.28: Numerical simulations showing the time evolution of the system during a ramp from $(U/J)_i = 47$ to $(U/J)_f = 2$ in 1D for a fixed ramp time $\tau_{\text{ramp}} = 0.25$. Red dots indicate the overlap with the ground state, and blue dots the instantaneous coherence length ξ . The vertical dashed line marks the phase transition.

times τ_{ramp} such that the prefactor of the power-law increase may be affected, but not the power-law exponent. An intuitive explanation for the observed behavior is still lacking, but hopefully this project encourages a scientific discussion.

6.3.3 Influence of the Trap

In a homogeneous system, both a Mott insulator as well as a superfluid are translation invariant. Therefore, when ramping from the Mott insulating into the superfluid regime, no mass redistribution is required. The same is also true for entropy transport. In contrast, in a trapped system, both mass and entropy distributions strongly depend on the phase of the atomic ensemble. While the mass distribution in the deep lattice is given by a flat distribution in the central Mott insulating core, surrounded by a superfluid or normal shell at lower filling, a weakly interacting superfluid in the shallow lattice at $T = 0$ is described by a parabolic Thomas-Fermi distribution. Entropy in the strongly interacting $(U/J) \gg (U/J)_c$ regime at $T = 0$ is only located in the shell around the central Mott insulating core, whereas in the superfluid regime, it is distributed more evenly throughout the system. Thus, when performing a quench from the Mott insulating into the superfluid regime, in addition to the establishment of phase coherence between lattice sites, mass and entropy have to be redistributed on a global scale, as illustrated in Fig. 6.29.

In the experiment, we employ a 50 ms ramp to load the atoms into the optical lattice, from $V_{\text{lat}} = 0 E_r$ to $19 E_r$. In previous experiments [234], this timescale turned out to produce large Mott insulating cores with only few double occupancies, thus allowing the major part of required mass and entropy redistribution. As the ramp is not perfectly adiabatic, the ensemble will still be heated and additional entropy will be created during the ramp. The state will therefore consist of a low-entropy Mott insulating core at unity

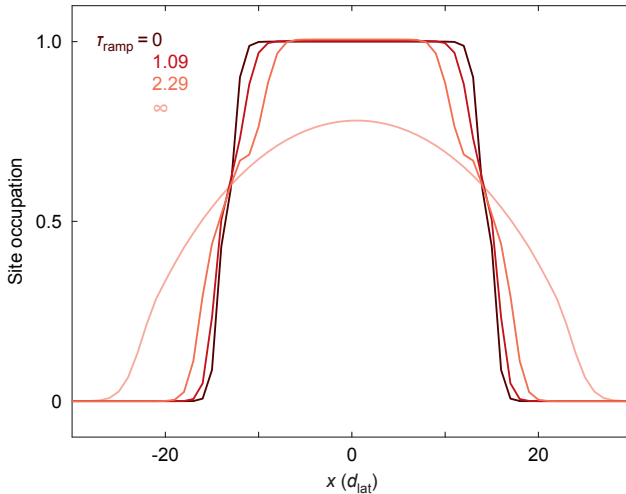


Figure 6.29: Density profiles for the ground state at the beginning (diabatic limit $\tau_{\text{ramp}} = 0$) and at the end of the ramp (adiabatic limit $\tau_{\text{ramp}} = \infty$), as well as for finite ramp times. The DMRG calculation was performed in 1D for $(U/J)_f = 3$ for 28 particles and a trap frequency of $\omega_x/2\pi = 66$ Hz by our colleagues at FU Berlin.

filling with a surrounding hot thermal gas at lower filling that accommodates most of the entropy. Some entropy will also be stored in the central core in the form of holes. Even if a large amount of mass and entropy is redistributed during the ramp, it remains unclear whether global thermal equilibrium is established during the ramp. This is particularly true for the employed blue-detuned optical lattice for which the resulting trap frequency of the external confinement decreases with increasing lattice depth (Section 3.1.2). In the case of a red-detuned lattice, the trap frequency during loading increases, thereby compressing the cloud during loading. The resulting wedding cake structure of the atomic distribution with higher occupancies in the center (Section 3.3.3) is closer to the distribution of the initial superfluid than the flat $n = 1$ Mott insulator which we prepare in this experiment. However, the very good agreement for short and intermediate ramp times between the experimental data and the numerical calculations, which assume a perfect initial Mott insulator, indicates that the observed experimental dynamics are indeed dominated by that of a low-entropy initial Mott insulator.

Analogously, mass and entropy transport are also required during lattice ramp-down from $V_{\text{lat}} = 19 E_r$ to $6 E_r$. The fitted in situ widths R (Fig. 6.10) indicate that mass transport on a global scale only happens for ramp times $\tau_{\text{ramp}} \gtrsim 10$, but is negligible for short lattice ramps. The fraction of the lattice loading from $V_{\text{lat}} = 6 E_r$ to $19 E_r$ is performed in $t_{\text{ramp}} \approx 34$ ms, corresponding to $\tau_{\text{ramp}} \approx 32$. This particular choice of ramp time for the loading ramp is therefore supported by the observed timescale for mass redistribution.

For short and intermediate ramps, the final density distribution cannot correspond to the equilibrium superfluid distribution at the particular parameters given. Thus, the chem-

ical potential is not constant across the system and leads to dephasing between atoms on different lattice sites. This phase difference can be seen in the complex two-point correlators in Fig. 6.32, and drives a particle current that tries to adapt the chemical potential throughout the system and thereby reach an equilibrium distribution. Dephasing already takes place during the lattice ramp, and competes with the emergence of phase coherence between lattice sites as soon as the latter starts to be established. The absolute amount of dephasing during the ramp is difficult to estimate due to the dynamics in the system. In general, the effect of dephasing increases with time; thus, for short ramp times $\tau_{\text{ramp}} \lesssim 1$, dephasing is negligible. For longer ramp times, dephasing becomes relevant and the measured coherence length ξ deviates from the pure power-law behavior of the homogeneous system. The dephasing rate is determined by the mismatch of the chemical potential across the system. Figure 6.30 shows that the choice of a different final horizontal trap frequency for the same interaction (U/J_f) leads to the same power-law exponent, but can increase the range of the pure power-law behavior and therefore reduces the mismatch of chemical potential. Figure 6.31 shows that there indeed exists an optimum trap frequency for which the effect of dephasing is minimized: For this particular trap frequency, the total amount of required mass redistribution is minimized such that also the chemical potential mismatch after a fixed ramp time is minimized.

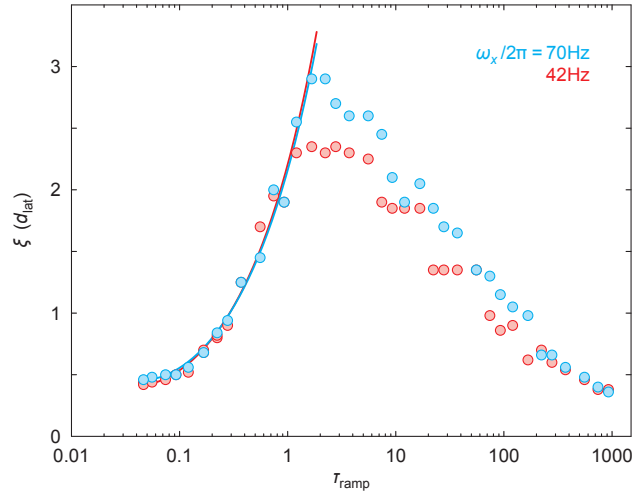


Figure 6.30: Coherence length versus ramp time for $(U/J)_f = 3.6$ in 1D on a semi-log plot, for two different trap frequencies. The solid curves are power-law fits up to $\tau_{\text{ramp}}^{\max} = 1.0$ that are plotted up to higher τ_{ramp} . In the larger trap frequency case, the power-law range is extended to higher ramp times. Thus, dephasing is reduced compared to the case with lower trap frequency (see main text).

For a ramp time $\tau_{\text{ramp}} \gtrsim 40$, the ramp should be close to adiabatic and most of the required mass redistribution should be achieved such that dephasing should not be relevant. Nonetheless, the measured coherence length after this ramp time is reduced by about a factor of 2 compared to the maximum measured coherence length. This reduction can

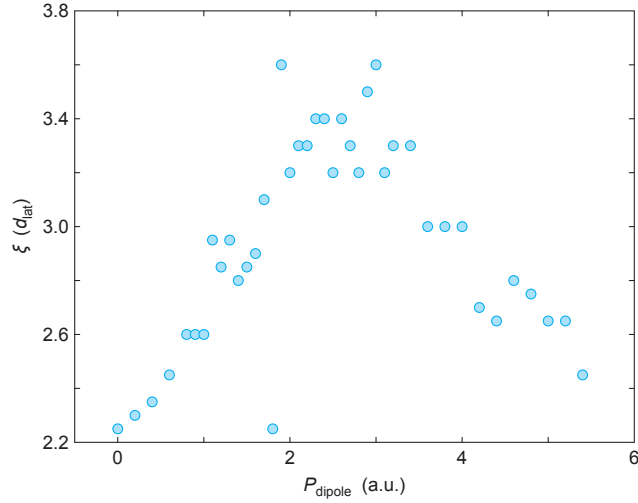


Figure 6.31: Coherence length for $(U/J)_f = 3.9$ in 1D for a fixed ramp time $\tau_{\text{ramp}} = 2.8$ versus power in the vertical dipole trap beam. The power at the maximum corresponds to a trap frequency $\omega_x/2\pi \approx 70$ Hz, consistent with Fig. 6.30. For this particular trap frequency, the effect of dephasing is minimized (see main text).

be attributed to entropy transport, which is expected to happen on a similar timescale as mass transport. After this ramp time, a global redistribution of entropy should have been achieved, and the entropy that was mainly concentrated in the shell around the Mott insulating core should have spread across the system. The increased entropy density on most lattice sites leads to a reduction of the phase coherence between lattice sites and therefore of the measured coherence length. For very long ramp times $\tau_{\text{ramp}} \gtrsim 100$, we expect heating due to light scattering and technical noise to reduce phase coherence even further (Section 6.2.3).

The above considerations show that it is difficult to model the initial in situ distribution precisely: The lattice loading is not perfectly adiabatic so that the initial state contains entropy in the surrounding shell, as well as in the central Mott insulating core in the form of holes. More importantly, the density distribution changes during lattice ramp down, and the total amount of mass redistribution depends on the ramp time. Therefore, technically, one would have to model the in situ distribution for each ramp time individually. In this project, however, we assume a simple Gaussian for the in situ distribution. The good agreement between the calculated interference patterns and the experimentally measured curves (Section 6.2.3) shows that this simple model captures the experimental situation very well. Also, the match of the experimentally extracted coherence lengths with the ones obtained from numerical calculations is further support for the model used in the experimental data evaluation.

Our collaborators have qualitatively modeled the effect of the trap by performing DMRG calculations of a 1D system with a harmonic confinement of $\omega_x/2\pi = 66$ Hz. The simulation was performed on tubes of variable length, i.e. where the initial state is a perfect $n = 1$ Mott

insulator with variable atom number. The experimentally measured data is an average over many such tubes of different lengths, where the length of each tube is determined by the ellipsoid created by the external harmonic confinement. For longer ramp times $\tau_{\text{ramp}} > 1$, the calculated two-point correlators obtain a significant imaginary contribution from dephasing due to the spatially varying chemical potential (Fig. 6.32).

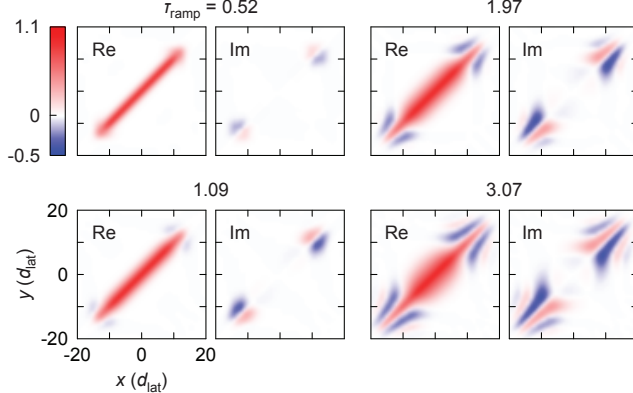


Figure 6.32: Real (Re) and imaginary (Im) part of the final two-point correlator for $(U/J)_f = 3$ in a trapped system with $N = 24$ particles for various ramp times.

To extract the coherence length, the two-point correlators were fitted under the assumption of exponentially decaying correlations (Eq. 3.47). The resulting coherence lengths demonstrate that the deviation of the coherence length from the power-law behavior is indeed caused by the trap and that this effect is dominated by the influence of the shorter tubes (Fig. 6.33). A more precise modeling of the trapped system is not feasible because of uncertainties regarding the initial state: Since the loading of the lattice is not perfectly adiabatic and the system is not guaranteed to be in thermal equilibrium in the deep lattice, a complete dynamical simulation of the 3D loading procedure would be necessary to precisely predict the *in situ* distribution of the system in the deep lattice.

6.4 Emergence of Coherence in Higher Dimensions and for Attractive Interactions

The very good agreement of the experimental measurements with the theoretical results of exact diagonalization and DMRG calculations provides confidence that both experiment and theory allow a reliable investigation of the actual quantum dynamics at the phase transition, i.e., it certifies our experiment as a quantum simulator. Whereas current numerical techniques are effectively limited to 1D systems, it is straightforward to extend the experimental setup to higher dimensions. In this section, I show results on the emergence of coherence in 2D and 3D, and compare them to the 1D case. I also present measurements and calculations about the emergence of coherence for attractive interactions that prove that the observed characteristic timescale is generic for the phase transition.

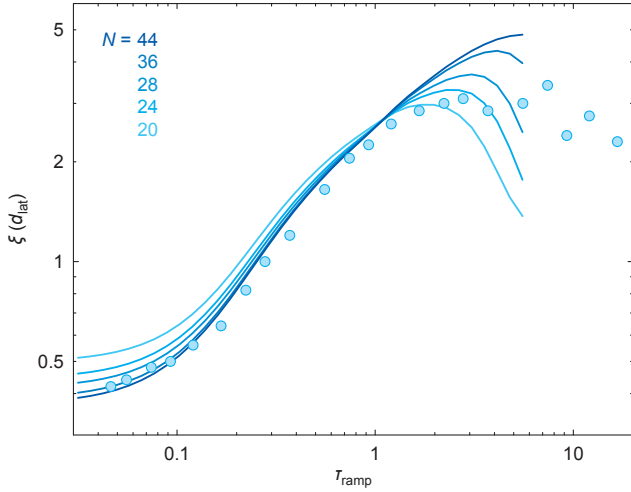


Figure 6.33: Emergence of coherence in a trapped system for $(U/J)_f = 3$ in 1D. The solid curves are DMRG calculations for various particle numbers N and the points are experimental data.

6.4.1 Emergence of Coherence in 2D and 3D

The experimental sequences for the 2D and 3D measurements are similar to the 1D case and are outlined in Section 6.2.2. The extraction of the coherence length from the individual images is performed in the same way as in the 1D case (Section 6.2.3). The resulting coherence lengths are shown in Fig. 6.34 as a function of ramp time. We found that, for short ramp times $\tau_{\text{ramp}} \lesssim 1$, the emergence of coherence is almost independent of dimensionality, showing similar curves for 1D, 2D and 3D up to the power-law regime. This is rather surprising, as the Kibble-Zurek mechanism predicts exponents that strongly depend on dimensionality (Section 6.1.2). Apparently, in the regime where the coherence length is not larger than a few lattice sites, dimensionality only has a minor effect on the spreading of correlations. For longer ramp times, the higher-dimensional systems continue the emergence of coherence to larger ξ than in lower dimensions. This difference might be explained by the different critical values $(U/J)_c \approx 3.3$ [102–104] in 1D, 16.7 [105] in 2D, and 29.3 [106] in 3D: A fixed $(U/J)_f$ in the 1D case is closer to or even deeper in the Mott insulating regime than for higher dimensions. Thereby, the maximum achievable coherence length, even for adiabatic ramps, is fundamentally limited by the final interaction $(U/J)_f$, in addition to potential dephasing effects.

Similarly to 1D, we find that the extracted power-law exponents in both 2D and 3D depend on the interaction $(U/J)_f$ (Fig. 6.35), in contrast to the prediction of the Kibble-Zurek mechanism. The precise dependence, however, looks different in the various dimensionalities. It may be interesting to perform a detailed analysis of the measured coherence lengths and exponents, also with the help of theoretical models. Due to the difficulty of simulations in higher dimensions, however, such a study is very challenging. The presented measurements already reveal complex dynamics in this regime where, currently, there are

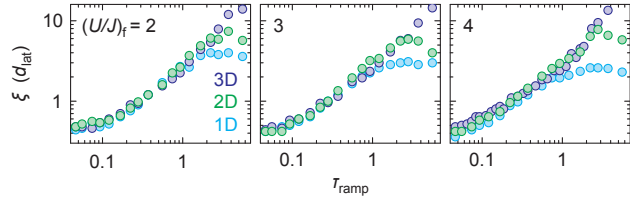


Figure 6.34: Experimentally measured coherence length in 1D, 2D, and 3D versus τ_{ramp} for various $(U/J)_f$. For short ramp times $\tau_{\text{ramp}} \lesssim 1$, the emergence of coherence is almost independent of dimensionality. For larger τ_{ramp} , the maximum achievable ξ is limited by the ratio $(U/J)_f/(U/J)_c$, which is different for the three dimensionalities (see main text).

no theoretical methods available. This may encourage future theoretical efforts. Detailed investigations have to include the precise ramp schedules employed in the experiment, the dimension-dependent critical values $(U/J)_c$, as well as the different nature of equilibrium correlations: Whereas quasi-long-range order is expected in 1D, true long-range order prevails in 2D in the case of $T = 0$ and in 3D.

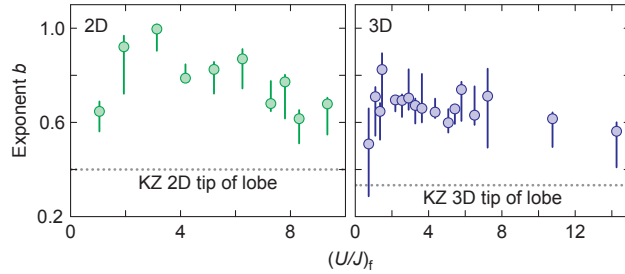


Figure 6.35: Power-law exponents b for the 2D (left) and 3D (right) cases. The fitting procedure to the experimental data, including error bars, is identical to the 1D case (Section 6.2.8). Also in higher dimensions, the exponent depends on the final interaction $(U/J)_f$, in contrast to a typical Kibble-Zurek type prediction (dotted lines).

6.4.2 Emergence of Coherence for Attractive Interactions

Qualitatively, the rather fast timescale for the emergence of coherence has already been observed in previous experiments [34]. In these experiments, similarly to the experiments presented above, the phase order of the initial superfluid at quasimomentum $\hbar\mathbf{q} = 0$ before loading into the deep lattice is identical to that of the final superfluid after ramping down the lattice again, namely with an identical phase factor $e^{i\mathbf{q}\mathbf{x}} = 1$ at each lattice site (cf. Fig. 3.3). Even in the deep optical lattice, if entropy is not too large, phase coherence is still present in the superfluid shell around the Mott insulating core, representing a remnant of the initial superfluid phase order. One might conjecture that the establishment of phase coherence in the final superfluid could be facilitated by this remnant: Instead of creating phase coherence out of completely scrambled local phases in a Mott insulating state, the surviving phase order in the superfluid shell could potentially *seed* phase order

across the system. With the help of negative temperatures, however, we can show that the timescale for the emergence of coherence is indeed generic for this particular phase transition, independent of the preparation procedure. The general idea is to choose different phase orders for the initial and the final superfluid such that the above speculation can be falsified.

The experimental sequence for the emergence of coherence measurements for attractive interactions is described in Section 6.2.2. With our experimental setup we were able to perform such measurements in 1D and 2D. The resulting emergence of coherence in 2D (Fig. 6.36) is almost identical to the repulsive interactions case, consistent with the symmetry of the Bose-Hubbard Hamiltonian for repulsive and attractive interactions (cf. Section 4.3.5). Only for strong interactions are deviations visible. These can qualitatively be explained by multi-band effects that lead to changes in the effective local Wannier functions [235]: Attractive and repulsive interactions lead to an effectively deeper or shallower lattice potential, respectively, that modifies the effective lattice ramp [236]. The corresponding exponents of the power-law increase (Fig. 6.37) agree within the error bars.

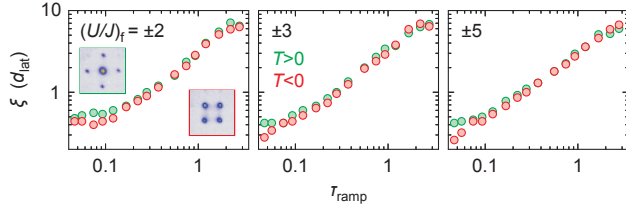


Figure 6.36: Experimental data of coherence length versus ramp time for repulsive and attractive interactions in 2D. For not too strong interactions $(U/J)_f$, the emergence of coherence for the two cases is very similar. The deviations for larger interactions can be attributed to self-trapping effects (see main text).

Also in 1D, we obtain very good agreement between the emergence of coherence for attractive and repulsive interactions, at least for large interactions (Fig. 6.38). We cannot reliably measure the emergence of coherence for small attractive interactions, as this requires ramping the Feshbach field over the range where the scattering length vanishes. This leads to a crossing from the Mott to the superfluid regime in the deep lattice. As the system cannot follow this quench due to the long timescales in the deep lattice, a lot of entropy is created and the system is heated.

Our theory collaborators performed exact diagonalization simulations of the 1D emergence of coherence for attractive interactions. These are identical to the calculations for repulsive interactions (Section 6.2.6). The simulated Feshbach ramp, in this case, crosses the Feshbach resonance such that the highest excited state in the lowest band is populated, consistent with a negative temperature state in the case of thermalization. The correlator contains an additional phase factor in comparison with the positive temperature state (Eq. 3.49). Just like in the repulsive interactions case, the resulting emergence of coherence signals show excellent agreement with the experimentally measured values (Fig. 6.39).

The quasimomentum distributions of negative and positive temperature states, as mea-

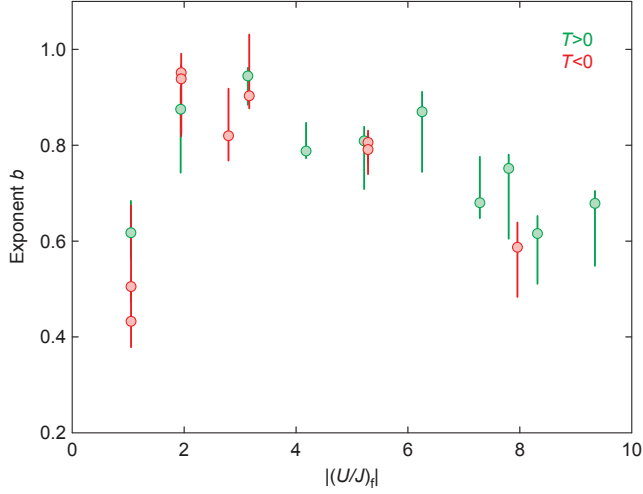


Figure 6.37: Power-law exponents for repulsive and attractive interactions in 2D, extracted from the data in Fig. 6.36. The fitting procedure is the same as described in Section 6.2.8. For not too strong interactions $|\langle U/J \rangle_f|$, the values for the two cases are consistent with each other.

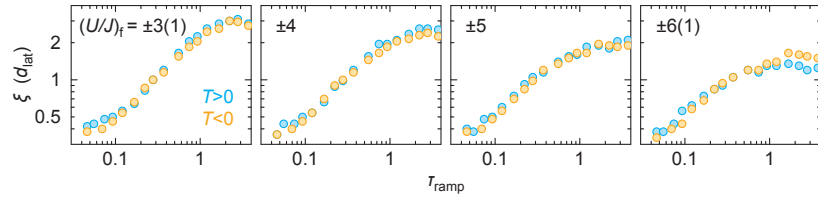


Figure 6.38: Experimental data of coherence length versus ramp time for repulsive and attractive interactions in 1D. For the available $(U/J)_f$ values, the emergence of coherence in the two cases is very similar.

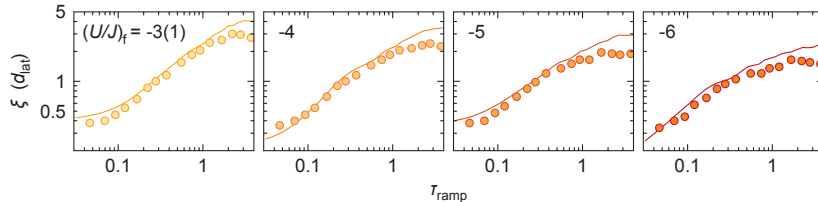


Figure 6.39: Emergence of coherence in 1D for attractive interactions for various $(U/J)_f$. The points are experimental data and the solid curves exact diagonalization calculations.

sured in time-of-flight images, are fundamentally different, corresponding to different phase factors at the lattice sites (Fig. 3.3). Nonetheless, we experimentally observe the same timescale for the emergence of coherence in these different superfluid states. The superfluid shell at the beginning of the lattice ramp, if any, still contains the phase order with identical phase factor at each lattice site: The switching of both interactions and external confinement cannot lead to the fast establishment, still in the deep lattice, of phase coherence with an alternating phase factor between lattice sites in the superfluid shell, as the

tunneling time of $\tau = 5.7 \text{ ms}$ is too large. Therefore, we conclude that the establishment of phase coherence in the final shallow lattice is independent of the preparation sequence and the timescale is generic for the Mott to superfluid phase transition.

6.5 Dynamics after and during the Quench

In this project, we have mostly evaluated the dynamics by varying the quench rate, i.e. the duration of the final lattice ramp and measuring the coherence length right at the end of the ramp. With our experimental setup, we can also extend the measurements to the dynamics in the system *after* the ramp, where the ramp time is fixed. In this section, I introduce several exemplary hold time measurements, for various dimensionalities, that are not presented in our corresponding publication. The sequence for the 2D case is shown in Fig. 6.40. In the following, I indicate the hold time, like the ramp time, in units of tunneling times, $\tau_{\text{hold}} = t_{\text{hold}} \cdot 2\pi J/h \approx t_{\text{hold}} \cdot 3.0/\text{ms}$. The dynamics of the in situ cloud size after the ramp reveals information on the adiabaticity of the preceding ramp. In this context, I also present measurements of how the in situ cloud size evolves during the ramp for a fixed ramp time.

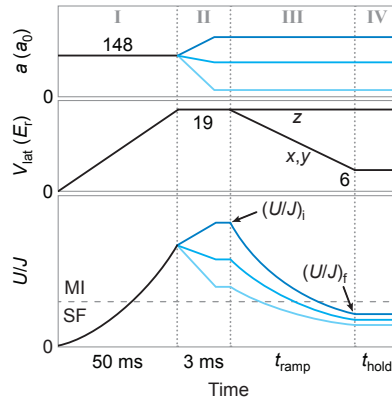


Figure 6.40: Experimental sequence for measuring the dynamics after the final ramp. In contrast to the previous ramps (Figs. 6.2 and 6.5), the ramp time t_{ramp} is fixed for this measurement. After a variable hold time t_{hold} , in situ or time-of-flight images are taken.

6.5.1 Dynamics of the Cloud Size after the Quench

I first present in situ data for long hold times that allows conclusions to be drawn about the timescale for global thermalization in the system. For this measurement in 3D, where we ramped down all three lattice axes simultaneously, we employed a fixed ramp time $\tau_{\text{ramp}} = 9.3$. This ramp time is outside the power-law regime and should already allow some mass redistribution in the system. We performed the measurement for various scattering lengths. The resulting in situ widths R (Fig. 6.41A) show dynamics for all interaction values, indicating that the state at the end of the ramp is not in global thermal equilibrium.

For very weak interactions (U/J_i), the system was already driven across the critical point ($U/J_c = 29.36$ [106] in the deep lattice by the Feshbach ramp. As the timescales in the deep lattice are very long, the short Feshbach ramp crossing the phase transition is strongly nonadiabatic and leads to excitations of the system. These excitations are reflected in strong oscillations after the lattice ramp. For stronger interactions, these oscillations become weaker until the cloud approaches its equilibrium value asymptotically for the strongest interactions. The dynamics happen on a timescale on the order of $\tau_{\text{hold}} = 40$, in addition to the dynamics that are achieved during the ramp. This timescale for equilibration is consistent with our choice of the lattice loading (Section 6.3.3). We also recorded a single measurement for a longer ramp time $\tau_{\text{ramp}} = 47$ (Fig. 6.41B). The cloud size is much more stable than in the case of the shorter ramp for the same interaction. This indicates that the bulk of the required mass distribution has already taken place during the lattice ramp.

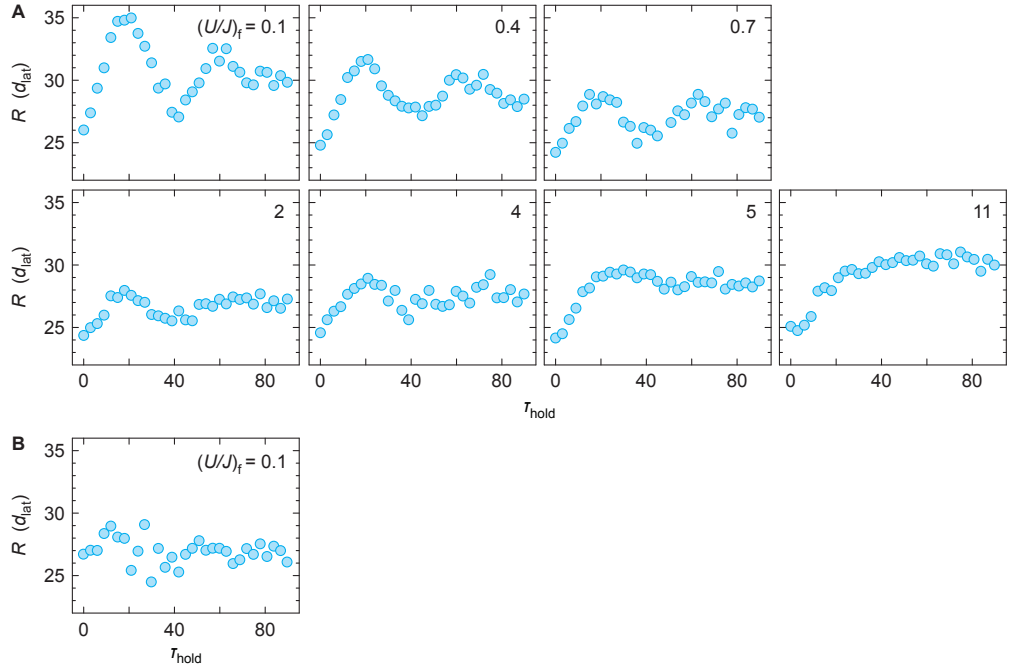


Figure 6.41: Fitted in situ widths R after variable hold time τ_{hold} . The ramp time of the 3D lattice ramp is fixed at **A**, $\tau_{\text{ramp}} = 9.3$, and **B**, $\tau_{\text{ramp}} = 47$. In contrast to most other measurements in this chapter, the time axis is linear. The two lowest interaction values $(U/J)_f = 0.1$ and 0.4 correspond to $(U/J)_i = 4$ and 18 , i.e. the final lattice ramp already started in the superfluid regime.

6.5.2 Dynamics of the Cloud Size during the Quench

We also performed measurements on the in situ cloud size during the final lattice ramp from $19 E_r$ to $6 E_r$ in the 3D case. We recorded data for several interactions, for the same

ramp times as above (Fig. 6.42). In both cases, the cloud size at the beginning of the ramp is approximately independent of interaction. During the initial part of the ramp, where the tunneling time is still large, there is not much dynamics. The bulk of the dynamics happens during the last part of the ramp in the shallow lattice, where the tunneling time is small. The dynamics are similar for all interactions. As expected, the cloud sizes reached at the end of the ramps approximately correspond to the initial cloud sizes in the hold time measurement above. The final cloud sizes in the case of $\tau_{\text{ramp}} = 9.3$, however, are smaller than for $\tau_{\text{ramp}} = 47$. This again supports the hypothesis that, during the short ramp, the total time for mass redistribution is insufficient to reach the large equilibrium value of R , whereas during the long ramp the cloud is able to converge closer to equilibrium.

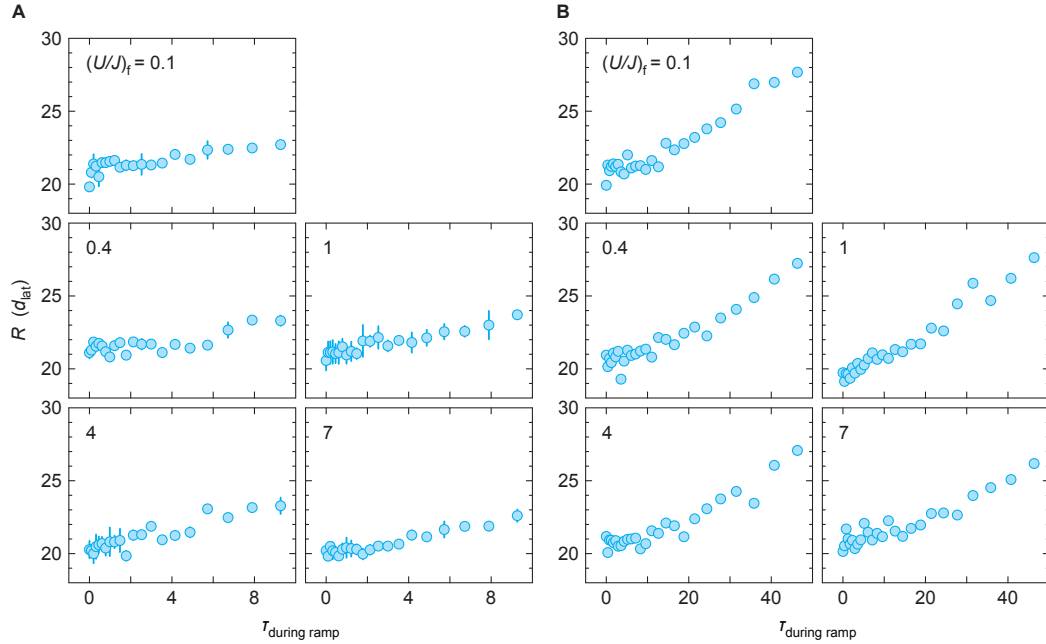


Figure 6.42: Fitted in situ widths R during the lattice ramp for various interactions in 3D for **A**, $\tau_{\text{ramp}} = 9.3$ and **B**, $\tau_{\text{ramp}} = 47$. The time during the ramp is indicated in units of integrated tunneling times. Error bars are the standard deviation of several averaged measurements.

6.5.3 Emergence of Coherence after the Quench

We also investigated how coherence emerges in the system while holding the atoms in the shallow optical lattice after the lattice ramp. The evaluation method is identical to the other measurements in this chapter where the ramp duration was varied. The chosen ramp times in this section are below $\tau_{\text{ramp}} = 0.5$ such that the global mass distribution is far from equilibrium. We perform sample measurements for all three dimensionalities.

1D

The dataset in 1D presented here was taken for a fixed ramp time $\tau_{\text{ramp}} = 0.09$. In the measurements for variable ramp times, the power-law behavior begins approximately at this ramp time, starting from the initial coherence length ξ_i (Section 6.3.1). We find that the coherence length indeed increases substantially during holding (Fig. 6.43A). The interactions $(U/J)_f = 1, 2, 3$ are the most relevant, as they are both initially close to the ground state (cf. Fig. 6.27) and cross the phase transition during the lattice ramp. In these cases, the coherence length after the ramp approximately doubles within a hold time of $\tau_{\text{hold}} \approx 1$. The maximum value $\xi_{\text{max}} \approx 1.3 d_{\text{lat}}$ is considerably below the maximum coherence length in the case of variable ramp times, where it reaches 3 to 4 lattice sites (cf. Fig. 6.23). The speed of the emergence increases with final interaction strength. This is also represented by the corresponding power-law exponents (Fig. 6.43B), even though the fit range is limited to a few data points only for which a power-law fit is not meaningful. However, in analogy to the measurements for variable ramp times, we fitted a power-law to obtain a qualitative measure. Whereas for very weak interactions, almost no coherence emerges during holding, the exponent approaches approximately a value of 0.5 for $(U/J)_f = (U/J)_c$.

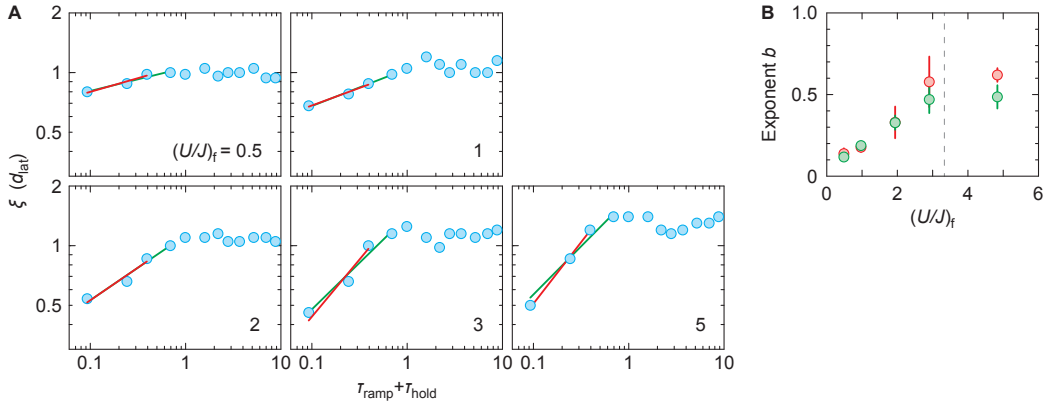


Figure 6.43: **A**, Coherence length ξ versus hold time τ_{hold} for various interactions in 1D, for a fixed ramp time $\tau_{\text{ramp}} = 0.093$. The straight lines are qualitative power-law fits to three or four data points. **B**, Extracted exponents from the power-law fits. The error bars are fit uncertainties. The vertical dashed line indicates $(U/J)_c$.

2D

In the case of 2D, I present data for a fixed ramp time $\tau_{\text{ramp}} = 0.47$. The initial coherence length is already above 1 lattice site (Fig. 6.44A), consistent with the measurement for variable ramp times (Fig. 6.34). Similarly to the 1D case above, for not too weak interactions, the coherence length approximately doubles within a hold time of $\tau_{\text{hold}} \approx 1$. The maximally achieved coherence lengths of $\xi_{\text{max}} \approx 3.5 d_{\text{lat}}$ are a factor of 2 smaller than in the case of variable ramp times. The speed of the emergence of coherence again increases with

interactions, where a power-law exponent $b \approx 0.5$ is reached at $(U/J)_f \approx 7$ (Fig. 6.44B).

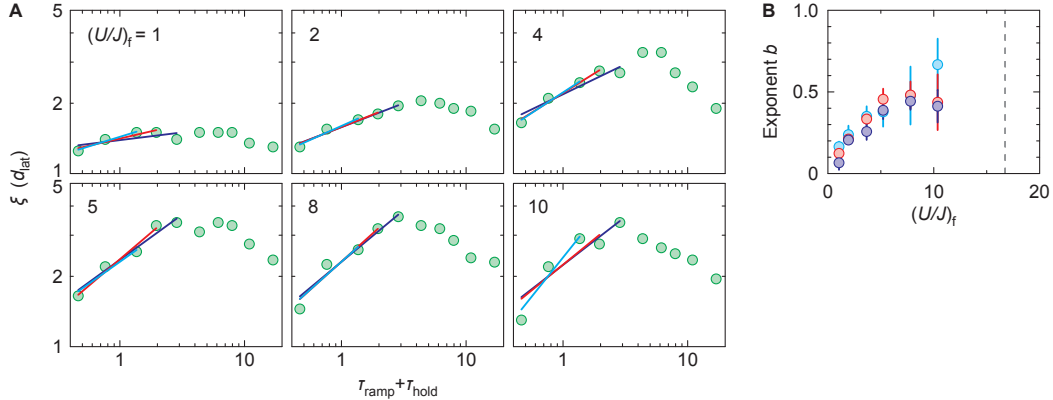


Figure 6.44: **A**, Coherence length ξ versus hold time τ_{hold} for various interactions in 2D, for a fixed ramp time $\tau_{\text{ramp}} = 0.47$. The straight lines are qualitative power-law fits for different fit ranges. **B**, Extracted exponents from the power-law fits. The error bars are fit uncertainties. The vertical dashed line indicates $(U/J)_c$.

3D

In the 3D case, we chose a ramp time $\tau_{\text{ramp}} = 0.23$. The observed dynamics are quite different to the 1D and 2D cases: Coherence emerges for much longer timescales, even for hold times $\tau_{\text{hold}} > 100$ for some interactions $(U/J)_f$ (Fig. 6.45A). The maximum achievable coherence length $\xi_{\text{max}} \approx 10 d_{\text{lat}}$ for some interactions is much higher than in the 1D and 2D cases. The speed of the emergence for $\tau_{\text{hold}} \lesssim 10$, on the other hand, is not higher than in the 1D and 2D cases (Fig. 6.45B). Also in this case, the power-law exponent increases with interaction. The accelerated spreading of correlations for $\tau_{\text{hold}} \gtrsim 50$ is a peculiarity of the 3D system and can already, to a smaller extent, be observed in the case of variable ramp times (Fig. 6.34). The corresponding power-law exponents are substantially larger than the ones for shorter hold times (Fig. 6.45B). In the case of $(U/J)_f = 2$ and 4 , they are compatible with $b = 1$ which corresponds to ballistic spreading of correlations. The underlying mechanism is an open question and could be worth investigating in future projects.

Summary

In all three dimensionalities, coherence also emerges after the quench. Compared to the case of variable ramp times, the maximum achievable coherence length is smaller (1D and 2D), or takes much longer to develop (3D). This can be explained by the fast quenches applied in the measurements of this section which excite the system strongly and thereby hinder the emergence of coherence after the quench. In general, the rate at which coherence emerges (i.e. the power-law exponent) during a hold time of up to a few tunneling times

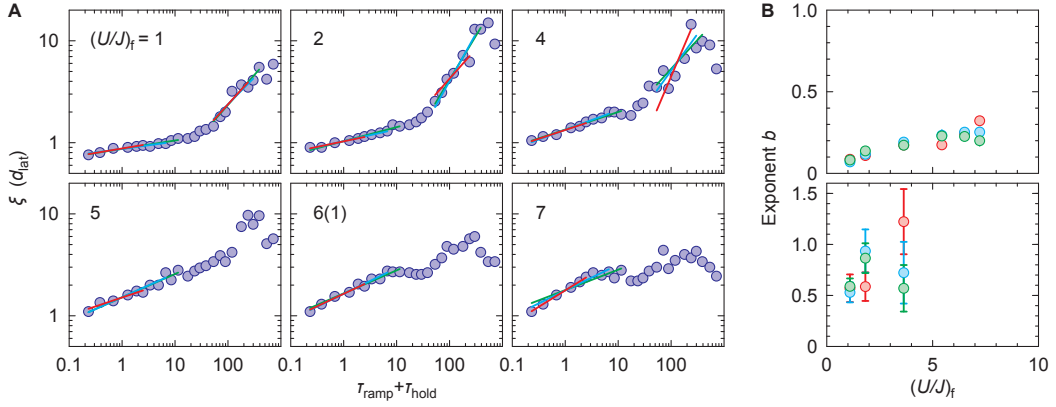


Figure 6.45: **A**, Coherence length ξ versus hold time τ_{hold} for various interactions in 3D, for a fixed ramp time $\tau_{\text{ramp}} = 0.23$. The straight lines are qualitative power-law fits for different fit ranges. **B**, Extracted exponents from the power-law fits for short ($\tau_{\text{hold}} \lesssim 10$, top) and long ($\tau_{\text{hold}} \gtrsim 50$, bottom) hold times. The error bars are fit uncertainties.

and in many cases also the maximum achievable coherence length increase with increasing interaction $(U/J)_f$. This behavior can also be explained by the excitations that are created during the fast lattice quench: For small interactions $(U/J)_f$, the fast quench reaches deep into the superfluid regime and thereby strongly excites the system. These excitations limit the maximum achievable coherence length after the quench and also the rate at which correlations can spread. In contrast, in the case of larger interactions $(U/J)_f$ the quench reaches less deep into the superfluid or even stays in the Mott insulating regime. It is therefore less violent and leads to less excitations in the system that allow coherence to emerge more efficiently and to higher values. In 3D, coherence emerges for much longer hold times and to much higher values than in lower dimensions. This may be related to the fact that, in contrast to 3D, real long-range order in 1D and, at finite temperature, in 2D does not exist [176, 177]. The observed behavior is certainly a very interesting topic for future investigations.

Comparing the timescale for the local emergence of coherence in this section to the long timescales required for mass redistribution (Sections 6.5.1 and 6.5.2) highlights the difference between local and global thermalization: While locally, thermal equilibrium and short-range phase coherence such as in the experiments on negative temperatures (Chapter 5) is achieved within a few tunneling times, global thermal equilibrium requires global mass and entropy flows and is much slower (cf. Section 4.2).

7 Conclusions and Outlook

In this thesis, I have presented the first realization of a negative temperature state for motional degrees of freedom. Ultracold atoms in optical lattices are particularly suitable for this exotic state of matter, as the band structure of the optical lattice potential creates an effective upper bound on the kinetic energy of the atoms. Using the combination of a red-detuned dipole trap and a blue-detuned optical lattice potential allowed full control of the external confinement, independent of the lattice depth. The use of bosonic potassium (^{39}K), which has a conveniently tunable Feshbach resonance, furthermore enabled us to control interactions, and therefore all three parameters of the Bose-Hubbard Hamiltonian independently. In addition to realizing negative temperatures, we used the flexibility of our experimental setup to carry out a detailed study of the complex and not yet fully understood dynamics at a quantum phase transition. We measured the emergence of coherence at the Mott insulator to superfluid transition for various interactions, dimensionalities and for repulsive and attractive interactions. Our results shed light on the intriguing question of how two vastly different quantum states are dynamically connected.

To create negative temperature states, we used the total control of the quantum system in our setup to create the required upper limit not only for the kinetic, but for the total energy of the system. We engineered an optimized sequence that results in a stable negative temperature state at low entropy. The negative temperature state manifested itself in time-of-flight images as four sharp peaks in the corners of the Brillouin zone, indicating a macroscopic occupation of the highest kinetic energy states. We found excellent agreement with a fitted Bose-Einstein distribution function that allowed us to extract an estimate for the (negative) temperature of the system. The negative temperature state turned out to be as stable as a corresponding low entropy state at positive temperatures, indicating thermal equilibrium of the final state and highlighting the symmetry between positive and negative temperatures. With some straightforward extensions, the laws of thermodynamics are fully consistent with negative temperatures. Seemingly counterintuitive consequences of negative temperatures such as Carnot efficiencies above unity are in full agreement with energy conservation and the second law of thermodynamics. Our published results have sparked a discussion on the very foundations of statistical mechanics that goes far beyond the direct implications of the experiments.

To investigate the dynamics of quantum phase transitions, we performed a quench from the Mott insulator into the superfluid regime. Measurements of the coherence length from

time-of-flight images revealed a power-law increase of the coherence length versus ramp time, as expected from critical behavior. However, the exponents show a dependence on the final interaction strength and indicate a complex behavior that reaches beyond any current analytical description, such as the Kibble-Zurek mechanism. Numerical simulations of the experimental sequence in 1D from our collaborators at FU Berlin show excellent agreement with our experimental data, proving the reliability of the experiment for the investigation of the quantum dynamics at the phase transition and thereby validating the experiment as a quantum simulator. On very short timescales, the dynamics can be captured in a free quasiparticle picture, which however fails to describe the observed power-law behavior. We found that short and intermediate timescales are consistent with dynamics in a homogeneous system, whereas the dynamics at large timescales are dominated by slow mass and entropy redistribution in the trap. The similarity of the emergence of coherence in higher dimensions on short timescales indicates a minor role of dimensionality in this process on these short timescales, in contrast to the strong dependence of the Kibble-Zurek description on dimensionality. The striking symmetry of the dynamics at repulsive and attractive interactions finally proves that the characteristic timescale does not depend on the preparation scheme, but is a generic feature of the Mott to superfluid transition.

The symmetry between positive and negative temperatures predicts the identical phase diagram for the attractive Bose-Hubbard model at negative temperatures as for the repulsive Bose-Hubbard model at positive temperatures, with only the quasimomenta shifted by half the Brillouin zone. A next step could therefore be to study this phase diagram by investigating the Feshbach-induced superfluid to Mott insulator transition at negative temperatures [154], similarly to the positive temperature case. The stability of the system in spite of the attractive interactions also allows future studies on the renormalization of Hubbard parameters by interactions, analogous to previous results for repulsive interactions [118, 154, 235, 237]. The tunability of the setup allows the upper bound on the kinetic energy to be removed by lowering the lattice depth. Thereby one could investigate the transition from a stable to an unstable system at attractive interactions in a controlled way and connect the negative temperature states to the collapse of BECs [27], which is even relevant for cosmology [238]. Furthermore, negative temperature states allow the study of new many-body systems that are only present close to the upper limit of kinetic energy. In kagome (i.e. trihexagonal) lattices, for example, the highest of three sub-bands is flat and therefore of particular interest [239]. The parameter space for quantum simulations can be extended with the use of negative temperatures, as these provide an elegant way to effectively change the sign of interactions when Feshbach resonances are not available or to stabilize a bosonic gas at attractive interactions against collapse [240]. For example, a simulation of the attractive, fermionic SU(3) model containing the quantum phase transition from color superfluidity to trion bound states is possible by using repulsively interacting ^{173}Yb , which features a low recombination loss rate [240].

A future improvement for the measurement of the dynamics of the Mott insulator to superfluid phase transition may utilize a box potential to remove the influence of the

trap on the experimental measurements. This would allow the observation of the power-law behavior of the emergence of coherence for longer ramp times and the detection of a possible dependence of the power-law exponent on ramp time in 1D [224]. In addition, driving the transition purely via the interaction $U(t)$, i.e. via the magnetic field close to the Feshbach resonance, would enable to decouple the influence of the simultaneous quenches in $U(t)$ and $J(t)$. Our findings on the dynamics at quantum phase transitions reach beyond currently available theoretical models such as the Kibble-Zurek mechanism or a quasiparticle picture. They raise the fundamental question of how well the dynamics at a quantum phase transition can be described in the context of simple scaling laws or, if the latter are not sufficient, how much knowledge about the system is in general required to characterize the evolution. The success of the Kibble-Zurek mechanism for various models suggests that much less information than a full knowledge of the quench, the energy levels and the eigenstates, may be sufficient. We hope that this work inspires scientific discussion in this direction. Our experimental measurements in 1D were confirmed by numerical simulations as a valid quantum simulation, i.e. the agreement between the two provides confidence that both approaches are free from systematic errors and reflect the true quantum dynamics faithfully. As the dynamical behavior in higher dimensions is out of reach of current numerical techniques, this work may also inspire an investigation on the general problem of how accurately quantum-mechanical experiments can really be certified as valid quantum simulators. Finally, also a general question concerning the computational power of analog quantum simulators may receive future attention: How do analog quantum simulations perform in relation to classical simulations in the context of computational complexity theory, e.g. which problems can be solved by analog quantum simulators in polynomial time that are exponentially hard on classical computers?

Bibliography

- [1] E. M. Purcell and R. V. Pound. *A nuclear spin system at negative temperature.* [Phys. Rev. **81**, 279 \(1951\)](#).
- [2] N. F. Ramsey. *Thermodynamics and statistical mechanics at negative absolute temperatures.* [Phys. Rev. **103**, 20 \(1956\)](#).
- [3] P. Hakonen and O. V. Lounasmaa. *Negative absolute temperatures: “Hot” spins in spontaneous magnetic order.* [Science **265**, 1821 \(1994\)](#).
- [4] A. S. Oja and O. V. Lounasmaa. *Nuclear magnetic ordering in simple metals at positive and negative nanokelvin temperatures.* [Rev. Mod. Phys. **69**, 1 \(1997\)](#).
- [5] P. Medley, D. M. Weld, H. Miyake, D. E. Pritchard, and W. Ketterle. *Spin gradient demagnetization cooling of ultracold atoms.* [Phys. Rev. Lett. **106**, 195301 \(2011\)](#).
- [6] A. P. Mosk. *Atomic gases at negative kinetic temperature.* [Phys. Rev. Lett. **95**, 040403 \(2005\)](#).
- [7] A. Rapp, S. Mandt, and A. Rosch. *Equilibration rates and negative absolute temperatures for ultracold atoms in optical lattices.* [Phys. Rev. Lett. **105**, 220405 \(2010\)](#).
- [8] M. H. Anderson, J. R. Ensher, M. R. Matthews, C. E. Wieman, and E. A. Cornell. *Observation of Bose-Einstein condensation in a dilute atomic vapor.* [Science **269**, 198 \(1995\)](#).
- [9] K. B. Davis, M. O. Mewes, M. R. Andrews, N. J. van Druten, D. S. Durfee, D. M. Kurn, and W. Ketterle. *Bose-Einstein condensation in a gas of sodium atoms.* [Phys. Rev. Lett. **75**, 3969 \(1995\)](#).
- [10] C. C. Bradley, C. A. Sackett, J. J. Tollett, and R. G. Hulet. *Evidence of Bose-Einstein condensation in an atomic gas with attractive interactions.* [Phys. Rev. Lett. **75**, 1687 \(1995\)](#).
- [11] M. R. Andrews, C. G. Townsend, H.-J. Miesner, D. S. Durfee, D. M. Kurn, and W. Ketterle. *Observation of interference between two Bose condensates.* [Science **275**, 637 \(1997\)](#).
- [12] I. Bloch, T. W. Hänsch, and T. Esslinger. *Measurement of the spatial coherence of a trapped Bose gas at the phase transition.* [Nature **403**, 166 \(2000\)](#).

- [13] M. R. Andrews, D. M. Kurn, H.-J. Miesner, D. S. Durfee, C. G. Townsend, S. Inouye, and W. Ketterle. *Propagation of sound in a Bose-Einstein condensate*. *Phys. Rev. Lett.* **79**, 553 (1997).
- [14] D. M. Stamper-Kurn, A. P. Chikkatur, A. Görlitz, S. Inouye, S. Gupta, D. E. Pritchard, and W. Ketterle. *Excitation of phonons in a Bose-Einstein condensate by light scattering*. *Phys. Rev. Lett.* **83**, 2876 (1999).
- [15] M. R. Matthews, B. P. Anderson, P. C. Haljan, D. S. Hall, C. E. Wieman, and E. A. Cornell. *Vortices in a Bose-Einstein condensate*. *Phys. Rev. Lett.* **83**, 2498 (1999).
- [16] K. W. Madison, F. Chevy, W. Wohlleben, and J. Dalibard. *Vortex formation in a stirred Bose-Einstein condensate*. *Phys. Rev. Lett.* **84**, 806 (2000).
- [17] J. R. Abo-Shaeer, C. Raman, J. M. Vogels, and W. Ketterle. *Observation of vortex lattices in Bose-Einstein condensates*. *Science* **292**, 476 (2001).
- [18] B. DeMarco and D. S. Jin. *Onset of Fermi degeneracy in a trapped atomic gas*. *Science* **285**, 1703 (1999).
- [19] S. Inouye, M. R. Andrews, J. Stenger, H.-J. Miesner, D. M. Stamper-Kurn, and W. Ketterle. *Observation of Feshbach resonances in a Bose-Einstein condensate*. *Nature* **392**, 151 (1998).
- [20] C. A. Regal, C. Ticknor, J. L. Bohn, and D. S. Jin. *Creation of ultracold molecules from a Fermi gas of atoms*. *Nature* **424**, 47 (2003).
- [21] M. Greiner, C. A. Regal, and D. S. Jin. *Emergence of a molecular Bose-Einstein condensate from a Fermi gas*. *Nature* **426**, 537 (2003).
- [22] S. Jochim et al. *Bose-Einstein condensation of molecules*. *Science* **302**, 2101 (2003).
- [23] M. W. Zwierlein, C. A. Stan, C. H. Schunck, S. M. F. Raupach, S. Gupta, Z. Hadzibabic, and W. Ketterle. *Observation of Bose-Einstein condensation of molecules*. *Phys. Rev. Lett.* **91**, 250401 (2003).
- [24] C. A. Regal, M. Greiner, and D. S. Jin. *Observation of resonance condensation of fermionic atom pairs*. *Phys. Rev. Lett.* **92**, 040403 (2004).
- [25] M. W. Zwierlein, C. A. Stan, C. H. Schunck, S. M. F. Raupach, A. J. Kerman, and W. Ketterle. *Condensation of pairs of fermionic atoms near a Feshbach resonance*. *Phys. Rev. Lett.* **92**, 120403 (2004).
- [26] M. W. Zwierlein, J. R. Abo-Shaeer, A. Schirotzek, C. H. Schunck, and W. Ketterle. *Vortices and superfluidity in a strongly interacting Fermi gas*. *Nature* **435**, 1047 (2005).
- [27] E. A. Donley, N. R. Claussen, S. L. Cornish, J. L. Roberts, E. A. Cornell, and C. E. Wieman. *Dynamics of collapsing and exploding Bose-Einstein condensates*. *Nature* **412**, 295 (2001).
- [28] T. Kraemer et al. *Evidence for Efimov quantum states in an ultracold gas of caesium atoms*. *Nature* **440**, 315 (2006).

- [29] S. Knoop, F. Ferlaino, M. Mark, M. Berninger, H. Schöbel, H.-C. Nägerl, and R. Grimm. *Observation of an Efimov-like trimer resonance in ultracold atom-dimer scattering.* *Nat. Phys.* **5**, 227 (2009).
- [30] M. Zaccanti et al. *Observation of an Efimov spectrum in an atomic system.* *Nat. Phys.* **5**, 586 (2009).
- [31] D. Jaksch, C. Bruder, J. I. Cirac, C. W. Gardiner, and P. Zoller. *Cold bosonic atoms in optical lattices.* *Phys. Rev. Lett.* **81**, 3108 (1998).
- [32] M. P. A. Fisher, P. B. Weichman, G. Grinstein, and D. S. Fisher. *Boson localization and the superfluid-insulator transition.* *Phys. Rev. B* **40**, 546 (1989).
- [33] I. Bloch, J. Dalibard, and W. Zwerger. *Many-body physics with ultracold gases.* *Rev. Mod. Phys.* **80**, 885 (2008).
- [34] M. Greiner, O. Mandel, T. Esslinger, T. W. Hänsch, and I. Bloch. *Quantum phase transition from a superfluid to a Mott insulator in a gas of ultracold atoms.* *Nature* **415**, 39 (2002).
- [35] T. Stöferle, H. Moritz, C. Schori, M. Köhl, and T. Esslinger. *Transition from a strongly interacting 1D superfluid to a Mott insulator.* *Phys. Rev. Lett.* **92**, 130403 (2004).
- [36] I. B. Spielman, W. D. Phillips, and J. V. Porto. *Mott-insulator transition in a two-dimensional atomic Bose gas.* *Phys. Rev. Lett.* **98**, 080404 (2007).
- [37] R. Jördens, N. Strohmaier, K. Günter, H. Moritz, and T. Esslinger. *A Mott insulator of fermionic atoms in an optical lattice.* *Nature* **455**, 204 (2008).
- [38] U. Schneider et al. *Metallic and insulating phases of repulsively interacting fermions in a 3D optical lattice.* *Science* **322**, 1520 (2008).
- [39] B. Paredes et al. *Tonks-Girardeau gas of ultracold atoms in an optical lattice.* *Nature* **429**, 277 (2004).
- [40] T. Kinoshita, T. Wenger, and D. S. Weiss. *Observation of a one-dimensional Tonks-Girardeau gas.* *Science* **305**, 1125 (2004).
- [41] M. Anderlini, P. J. Lee, B. L. Brown, J. Sebby-Strabley, W. D. Phillips, and J. V. Porto. *Controlled exchange interaction between pairs of neutral atoms in an optical lattice.* *Nature* **448**, 452 (2007).
- [42] S. Fölling et al. *Direct observation of second-order atom tunnelling.* *Nature* **448**, 1029 (2007).
- [43] S. Trotzky et al. *Time-resolved observation and control of superexchange interactions with ultracold atoms in optical lattices.* *Science* **319**, 295 (2008).
- [44] C. Becker, P. Soltan-Panahi, J. Kronjäger, S. Dörscher, K. Bongs, and K. Sengstock. *Ultracold quantum gases in triangular optical lattices.* *New J. Phys.* **12**, 065025 (2010).

- [45] P. Soltan-Panahi et al. *Multi-component quantum gases in spin-dependent hexagonal lattices*. *Nat. Phys.* **7**, 434 (2011).
- [46] W. S. Bakr, J. I. Gillen, A. Peng, S. Fölling, and M. Greiner. *A quantum gas microscope for detecting single atoms in a Hubbard-regime optical lattice*. *Nature* **462**, 74 (2009).
- [47] J. F. Sherson, C. Weitenberg, M. Endres, M. Cheneau, I. Bloch, and S. Kuhr. *Single-atom-resolved fluorescence imaging of an atomic Mott insulator*. *Nature* **467**, 68 (2010).
- [48] C. Weitenberg et al. *Single-spin addressing in an atomic Mott insulator*. *Nature* **471**, 319 (2011).
- [49] W. Ketterle, D. S. Durfee, and D. M. Stamper-Kurn. *Making, probing and understanding Bose-Einstein condensates*. *arXiv* 9904034 (1999).
- [50] S. Fölling, F. Gerbier, A. Widera, O. Mandel, T. Gericke, and I. Bloch. *Spatial quantum noise interferometry in expanding ultracold atom clouds*. *Nature* **434**, 481 (2005).
- [51] T. Rom, T. Best, D. van Oosten, U. Schneider, S. Fölling, B. Paredes, and I. Bloch. *Free fermion antibunching in a degenerate atomic Fermi gas released from an optical lattice*. *Nature* **444**, 733 (2006).
- [52] G. K. Campbell et al. *Imaging the Mott insulator shells by using atomic clock shifts*. *Science* **313**, 649 (2006).
- [53] P. T. Ernst, S. Götze, J. S. Krauser, K. Pyka, D.-S. Lühmann, D. Pfannkuche, and K. Sengstock. *Probing superfluids in optical lattices by momentum-resolved Bragg spectroscopy*. *Nat. Phys.* **6**, 56 (2010).
- [54] R. P. Feynman. *Simulating physics with computers*. *Int. J. Theor. Phys.* **21**, 467 (1982).
- [55] I. Buluta and F. Nori. *Quantum simulators*. *Science* **326**, 108 (2009).
- [56] I. Bloch, J. Dalibard, and S. Nascimbne. *Quantum simulations with ultracold quantum gases*. *Nat. Phys.* **8**, 267 (2012).
- [57] S. Sachdev. *Quantum phase transitions*, 2nd ed. Cambridge University Press (2011).
- [58] S. Bose. *Plancks Gesetz und Lichtquantenhypothese*. *Z. Phys.* **26**, 178 (1924).
- [59] A. Einstein. *Quantentheorie des einatomigen idealen Gases*. Zweite Abhandlung. *Sitzungsber. Preuss. Akad. Wiss.* 1, 3 (1925).
- [60] L. D. Landau and E. M. Lifshitz. *Statistical physics, Course of theoretical physics* 5, 3rd ed. Pergamon Press (1980).
- [61] O. Penrose and L. Onsager. *Bose-Einstein condensation and liquid helium*. *Phys. Rev.* **104**, 576 (1956).

- [62] C. Pethick and H. Smith. *Bose-Einstein condensation in dilute gases*. Cambridge University Press (2002).
- [63] J. Weiner, V. S. Bagnato, S. Zilio, and P. S. Julienne. *Experiments and theory in cold and ultracold collisions*. *Rev. Mod. Phys.* **71**, 1 (1999).
- [64] J. Dalibard. *Collisional dynamics of ultra-cold atomic gases*. In: *Proceedings of the international school of physics Enrico Fermi, CXL*. IOS Press (1999).
- [65] D. J. Heinzen. *Ultracold atomic interactions*. In: *Proceedings of the international school of physics Enrico Fermi, CXL*. IOS Press (1999).
- [66] N. N. Bogoliubov. *On the theory of superfluidity*. *J. Phys.* **11**, 23 (1947).
- [67] E. P. Gross. *Structure of a quantized vortex in boson systems*. *Nuovo Cim* **20**, 454 (1961).
- [68] L. Pitaevskii. *Vortex lines in an imperfect Bose gas*. *Sov. Phys. JETP* **13**, 451 (1961).
- [69] T. Köhler, K. Gral, and P. S. Julienne. *Production of cold molecules via magnetically tunable Feshbach resonances*. *Rev. Mod. Phys.* **78**, 1311 (2006).
- [70] H. Feshbach. *Unified theory of nuclear reactions*. *Ann. Phys.* **5**, 357 (1958).
- [71] U. Fano. *Effects of configuration interaction on intensities and phase shifts*. *Phys. Rev.* **124**, 1866 (1961).
- [72] W. C. Stwalley. *Stability of spin-aligned hydrogen at low temperatures and high magnetic fields: New field-dependent scattering resonances and predissociations*. *Phys. Rev. Lett.* **37**, 1628 (1976).
- [73] E. Tiesinga, B. J. Verhaar, and H. T. C. Stoof. *Threshold and resonance phenomena in ultracold ground-state collisions*. *Phys. Rev. A* **47**, 4114 (1993).
- [74] A. J. Moerdijk, B. J. Verhaar, and A. Axelsson. *Resonances in ultracold collisions of ^6Li , ^7Li , and ^{23}Na* . *Phys. Rev. A* **51**, 4852 (1995).
- [75] A. Simoni, M. Zaccanti, C. D'Errico, M. Fattori, G. Roati, M. Inguscio, and G. Modugno. *Near-threshold model for ultracold KRb dimers from interisotope Feshbach spectroscopy*. *Phys. Rev. A* **77**, 052705 (2008).
- [76] H. J. Metcalf and P. van der Straten. *Laser cooling and trapping*. Springer (1999).
- [77] R. Grimm, M. Weidemüller, and Y. B. Ovchinnikov. *Optical dipole traps for neutral atoms*. In: *Advances in atomic, molecular, and optical physics*, 42. Academic Press (2000).
- [78] T. G. Tiecke. *Properties of potassium*. PhD thesis, University of Amsterdam (2010).
- [79] T. Rom. *Bosonische und fermionische Quantengase in dreidimensionalen optischen Gittern*. PhD thesis, Ludwig-Maximilians-Universität München (2009).
- [80] T. Best. *Interacting Bose-Einstein mixtures in optical lattices*. Phd thesis, Johannes Gutenberg-Universität Mainz (2010).

- [81] U. Schneider. *Interacting fermionic atoms in optical lattices - A quantum simulator for condensed matter physics*. PhD thesis, Johannes Gutenberg-Universität Mainz (2010).
- [82] S. Will. *Interacting bosons and fermions in three-dimensional optical lattice potentials*. PhD thesis, Johannes Gutenberg-Universität Mainz (2011).
- [83] J. P. Ronzheimer. *Non-equilibrium dynamics of ultracold atoms in optical lattices*. Phd thesis, Ludwig-Maximilians-Universität München (2013).
- [84] M. Meucci, E. Mariotti, P. Bicchi, C. Marinelli, and L. Moi. *Light-induced atom desorption*. *Europhys. Lett.* **25**, 639 (1994).
- [85] D. A. Steck. *Rubidium 87 d line data*. Online (2001).
- [86] A. L. Migdall, J. V. Prodan, W. D. Phillips, T. H. Bergeman, and H. J. Metcalf. *First observation of magnetically trapped neutral atoms*. *Phys. Rev. Lett.* **54**, 2596 (1985).
- [87] M. Greiner, I. Bloch, T. W. Hänsch, and T. Esslinger. *Magnetic transport of trapped cold atoms over a large distance*. *Phys. Rev. A* **63**, 031401 (2001).
- [88] H. F. Hess. *Evaporative cooling of magnetically trapped and compressed spin-polarized hydrogen*. *Phys. Rev. B* **34**, 3476 (1986).
- [89] N. Masuhara, J. M. Doyle, J. C. Sandberg, D. Kleppner, T. J. Greytak, H. F. Hess, and G. P. Kochanski. *Evaporative cooling of spin-polarized atomic hydrogen*. *Phys. Rev. Lett.* **61**, 935 (1988).
- [90] K. B. Davis, M.-O. Mewes, M. A. Joffe, M. R. Andrews, and W. Ketterle. *Evaporative cooling of sodium atoms*. *Phys. Rev. Lett.* **74**, 5202 (1995).
- [91] L. De Sarlo, P. Maioli, G. Barontini, J. Catani, F. Minardi, and M. Inguscio. *Collisional properties of sympathetically cooled ^{39}K* . *Phys. Rev. A* **75**, 022715 (2007).
- [92] G. Roati et al. *^{39}K Bose-Einstein condensate with tunable interactions*. *Phys. Rev. Lett.* **99**, 010403 (2007).
- [93] O. Morsch and M. Oberthaler. *Dynamics of Bose-Einstein condensates in optical lattices*. *Rev. Mod. Phys.* **78**, 179 (2006).
- [94] M. Greiner. *Ultracold quantum gases in three-dimensional optical lattice potentials*. PhD thesis, Ludwig-Maximilians-Universität München (2003).
- [95] C. Kittel. *Introduction to solid state physics*. Wiley (2005).
- [96] R. Juregui, N. Poli, G. Roati, and G. Modugno. *Anharmonic parametric excitation in optical lattices*. *Phys. Rev. A* **64**, 033403 (2001).
- [97] W. Demtröder. *Atoms, molecules and photons: An introduction to atomic-, molecular- and quantum physics*. Springer (2010).
- [98] L. Cook. *Feshbach resonances and the three-body problem*. PhD thesis, University College London (2012).

- [99] K. M. Jones, E. Tiesinga, P. D. Lett, and P. S. Julienne. *Ultracold photoassociation spectroscopy: Long-range molecules and atomic scattering*. *Rev. Mod. Phys.* **78**, 483 (2006).
- [100] F. S. Cataliotti et al. *Josephson junction arrays with Bose-Einstein condensates*. *Science* **293**, 843 (2001).
- [101] R. J. Glauber. *Coherent and incoherent states of the radiation field*. *Phys. Rev.* **131**, 2766 (1963).
- [102] S. M. A. Rombouts, K. Van Houcke, and L. Pollet. *Loop updates for quantum Monte Carlo simulations in the canonical ensemble*. *Phys. Rev. Lett.* **96**, 180603 (2006).
- [103] S. Ejima, H. Fehske, and F. Gebhard. *Dynamic properties of the one-dimensional Bose-Hubbard model*. *Europhys. Lett.* **93**, 30002 (2011).
- [104] J. Carrasquilla, S. R. Manmana, and M. Rigol. *Scaling of the gap, fidelity susceptibility, and Bloch oscillations across the superfluid-to-Mott-insulator transition in the one-dimensional Bose-Hubbard model*. *Phys. Rev. A* **87**, 043606 (2013).
- [105] B. Capogrosso-Sansone, S. G. Söyler, N. Prokof'ev, and B. Svistunov. *Monte Carlo study of the two-dimensional Bose-Hubbard model*. *Phys. Rev. A* **77**, 015602 (2008).
- [106] B. Capogrosso-Sansone, N. V. Prokof'ev, and B. V. Svistunov. *Phase diagram and thermodynamics of the three-dimensional Bose-Hubbard model*. *Phys. Rev. B* **75**, 134302 (2007).
- [107] K. Sheshadri, H. R. Krishnamurthy, R. Pandit, and T. V. Ramakrishnan. *Superfluid and insulating phases in an interacting-boson model: Mean-field theory and the RPA*. *Europhys. Lett.* **22**, 257 (1993).
- [108] N. Elstner and H. Monien. *Dynamics and thermodynamics of the Bose-Hubbard model*. *Phys. Rev. B* **59**, 12184 (1999).
- [109] D. van Oosten, P. van der Straten, and H. T. C. Stoof. *Quantum phases in an optical lattice*. *Phys. Rev. A* **63**, 053601 (2001).
- [110] S. Fölling, A. Widera, T. Müller, F. Gerbier, and I. Bloch. *Formation of spatial shell structure in the superfluid to Mott insulator transition*. *Phys. Rev. Lett.* **97**, 060403 (2006).
- [111] W. S. Bakr et al. *Probing the superfluid-to-Mott insulator transition at the single-atom level*. *Science* **329**, 547 (2010).
- [112] M. Endres et al. *The ‘Higgs’ amplitude mode at the two-dimensional superfluid/Mott insulator transition*. *Nature* **487**, 454 (2012).
- [113] R. Darius. *The effects of saturation and optical pumping on the atom number calibration in absorption imaging*. Bachelor thesis, Ludwig-Maximilians-Universität München (2013).
- [114] F. Gerbier, A. Widera, S. Fölling, O. Mandel, T. Gericke, and I. Bloch. *Interference pattern and visibility of a Mott insulator*. *Phys. Rev. A* **72**, 053606 (2005).

- [115] F. Gerbier et al. *Expansion of a quantum gas released from an optical lattice*. *Phys. Rev. Lett.* **101**, 155303 (2008).
- [116] A. Kastberg, W. D. Phillips, S. L. Rolston, R. J. C. Spreeuw, and P. S. Jessen. *Adiabatic cooling of cesium to 700 nK in an optical lattice*. *Phys. Rev. Lett.* **74**, 1542 (1995).
- [117] M. Greiner, I. Bloch, O. Mandel, T. W. Hänsch, and T. Esslinger. *Exploring phase coherence in a 2D lattice of Bose-Einstein condensates*. *Phys. Rev. Lett.* **87**, 160405 (2001).
- [118] M. J. Mark, E. Haller, K. Lauber, J. G. Danzl, A. J. Daley, and H.-C. Nägerl. *Precision measurements on a tunable Mott insulator of ultracold atoms*. *Phys. Rev. Lett.* **107**, 175301 (2011).
- [119] S. Braun, J. P. Ronzheimer, M. Schreiber, S. S. Hodgman, T. Rom, I. Bloch, and U. Schneider. *Negative absolute temperature for motional degrees of freedom*. *Science* **339**, 52 (2013).
- [120] C. J. Adkins. *Equilibrium thermodynamics*. Cambridge University Press (1983).
- [121] S. Goldstein, J. L. Lebowitz, R. Tumulka, and N. Zangh. *Long-time behavior of macroscopic quantum systems*. *Eur. Phys. J. H* **35**, 173 (2010).
- [122] A. Polkovnikov, K. Sengupta, A. Silva, and M. Vengalattore. *Nonequilibrium dynamics of closed interacting quantum systems*. *Rev. Mod. Phys.* **83**, 863 (2011).
- [123] M. V. Berry. *Regular and irregular motion*. In: *AIP conference proceedings 46*, 1. AIP Publishing (1978).
- [124] E. Fermi, J. Pasta, and S. Ulam. *Studies of nonlinear problems*. Los Alamos Scientific Laboratory, LA-1940 (1955).
- [125] G. P. Berman and F. M. Izrailev. *The Fermi-Pasta-Ulam problem: Fifty years of progress*. *Chaos* **15**, 015104 (2005).
- [126] A. N. Kolmogorov. *On conservation of conditionally periodic motions under small perturbations of the Hamiltonian*. *Dokl. Akad. Nauk SSSR* **98**, 527 (1954).
- [127] J. Moser. *On invariant curves of area-preserving mappings of an annulus*. Vandenhoeck & Ruprecht (1962).
- [128] V. I. Arnol'd. *Proof of a theorem of A. N. Kolmogorov on the invariance of quasi-periodic motions under small perturbations of the Hamiltonian*. *Russ. Math. Surv.* **18**, 9 (1963).
- [129] A. Peres. *Ergodicity and mixing in quantum theory. I*. *Phys. Rev. A* **30**, 504 (1984).
- [130] M. Rigol, V. Dunjko, and M. Olshanii. *Thermalization and its mechanism for generic isolated quantum systems*. *Nature* **452**, 854 (2008).
- [131] J. M. Deutsch. *Quantum statistical mechanics in a closed system*. *Phys. Rev. A* **43**, 2046 (1991).

- [132] M. Srednicki. *Chaos and quantum thermalization*. *Phys. Rev. E* **50**, 888 (1994).
- [133] J.-S. Caux and J. Mossel. *Remarks on the notion of quantum integrability*. *J. Stat. Mech.* **2011**, P02023 (2011).
- [134] M. Girardeau. *Relationship between systems of impenetrable bosons and fermions in one dimension*. *J. Math. Phys.* **1**, 516 (1960).
- [135] P. Jordan and E. Wigner. *Über das Paulische Aequivalenzverbot*. *Z. Phys.* **47**, 631 (1928).
- [136] M. Rigol and A. Muramatsu. *Universal properties of hard-core bosons confined on one-dimensional lattices*. *Phys. Rev. A* **70**, 031603 (2004).
- [137] T. Kinoshita, T. Wenger, and D. S. Weiss. *A quantum Newton's cradle*. *Nature* **440**, 900 (2006).
- [138] S. Trotzky, Y.-A. Chen, A. Flesch, I. P. McCulloch, U. Schollwöck, J. Eisert, and I. Bloch. *Probing the relaxation towards equilibrium in an isolated strongly correlated one-dimensional Bose gas*. *Nat. Phys.* **8**, 325 (2012).
- [139] E. T. Jaynes. *Information theory and statistical mechanics*. *Phys. Rev.* **106**, 620 (1957).
- [140] M. Rigol, V. Dunjko, V. Yurovsky, and M. Olshanii. *Relaxation in a completely integrable many-body quantum system: An ab initio study of the dynamics of the highly excited states of 1D lattice hard-core bosons*. *Phys. Rev. Lett.* **98**, 050405 (2007).
- [141] S. Mandt, A. E. Feiguin, and S. R. Manmana. *Relaxation towards negative temperatures in bosonic systems: Generalized Gibbs ensembles and beyond integrability*. *Phys. Rev. A* **88**, 043643 (2013).
- [142] J. Berges, S. Borsányi, and C. Wetterich. *Prethermalization*. *Phys. Rev. Lett.* **93**, 142002 (2004).
- [143] C. Kollath, A. M. Läuchli, and E. Altman. *Quench dynamics and nonequilibrium phase diagram of the Bose-Hubbard model*. *Phys. Rev. Lett.* **98**, 180601 (2007).
- [144] M. Eckstein, M. Kollar, and P. Werner. *Thermalization after an interaction quench in the Hubbard model*. *Phys. Rev. Lett.* **103**, 056403 (2009).
- [145] M. Moeckel and S. Kehrein. *Crossover from adiabatic to sudden interaction quenches in the Hubbard model: prethermalization and non-equilibrium dynamics*. *New J. Phys.* **12**, 055016 (2010).
- [146] M. Gring et al. *Relaxation and prethermalization in an isolated quantum system*. *Science* **337**, 1318 (2012).
- [147] T. Langen, R. Geiger, M. Kuhnert, B. Rauer, and J. Schmiedmayer. *Local emergence of thermal correlations in an isolated quantum many-body system*. *Nat. Phys.* **9**, 640 (2013).

- [148] R. Nandkishore and D. A. Huse. *Many-body localization and thermalization in quantum statistical mechanics*. arXiv 1404.0686 (2014).
- [149] P. W. Anderson. *Absence of diffusion in certain random lattices*. Phys. Rev. **109**, 1492 (1958).
- [150] V. Romero-Rochín. *Nonexistence of equilibrium states at absolute negative temperatures*. Phys. Rev. E **88**, 022144 (2013).
- [151] E. M. Purcell, H. C. Torrey, and R. V. Pound. *Resonance absorption by nuclear magnetic moments in a solid*. Phys. Rev. **69**, 37 (1946).
- [152] R. V. Pound and W. D. Knight. *A radiofrequency spectrograph and simple magnetic-field meter*. Rev. Sci. Instrum. **21**, 219 (1950).
- [153] D. M. Weld, P. Medley, H. Miyake, D. Hucul, D. E. Pritchard, and W. Ketterle. *Spin gradient thermometry for ultracold atoms in optical lattices*. Phys. Rev. Lett. **103**, 245301 (2009).
- [154] M. J. Mark et al. *Preparation and spectroscopy of a metastable Mott-insulator state with attractive interactions*. Phys. Rev. Lett. **108**, 215302 (2012).
- [155] N. Tsuji, T. Oka, P. Werner, and H. Aoki. *Dynamical band flipping in fermionic lattice systems: An ac-field-driven change of the interaction from repulsive to attractive*. Phys. Rev. Lett. **106**, 236401 (2011).
- [156] U. Schneider et al. *Fermionic transport and out-of-equilibrium dynamics in a homogeneous Hubbard model with ultracold atoms*. Nat. Phys. **8**, 213 (2012).
- [157] A.-M. Tremblay. *Comment on “Negative Kelvin temperatures: Some anomalies and a speculation”*. Am. J. Phys **44**, 994 (1975).
- [158] S. Gupta, A. E. Leanhardt, A. D. Cronin, and D. E. Pritchard. *Coherent manipulation of atoms with standing light waves*. CR Acad. Sci. IV Phys. **2**, 479 (2001).
- [159] A. G. Riess et al. *Observational evidence from supernovae for an accelerating universe and a cosmological constant*. Astron. J. **116**, 1009 (1998).
- [160] S. Perlmutter et al. *Measurements of Ω and Λ from 42 high-redshift supernovae*. Astrophys. J. **517**, 565 (1999).
- [161] A. Friedman. *Über die Krümmung des Raumes*. Z. Phys. **10**, 377 (1922).
- [162] Planck-Collaboration. *Planck 2013 results. XVI. Cosmological parameters*. arXiv 1303.5076 (2013).
- [163] K. Huang. *Statistical mechanics, 2nd ed.* Wiley (1987).
- [164] J. Dunkel and S. Hilbert. *Consistent thermostatistics forbids negative absolute temperatures*. Nat. Phys. **10**, 67 (2014).
- [165] H. Touchette. *Ensemble equivalence for general many-body systems*. Europhys. Lett. **96**, 50010 (2011).

- [166] J. W. Gibbs. *Elementary principles in statistical physics*. Yale University Press (1902).
- [167] P. Hertz. *Über die mechanischen Grundlagen der Thermodynamik*. *Ann. Phys.* **338**, 225274 (1910).
- [168] I. M. Sokolov. *Thermodynamics: Not hotter than hot*. *Nat. Phys.* **10**, 7 (2014).
- [169] D. Frenkel and P. B. Warren. *Gibbs, Boltzmann, and negative temperatures*. *arXiv* 1403.4299 (2014).
- [170] U. Schneider, S. Mandt, A. Rapp, S. Braun, H. Weimer, I. Bloch, and A. Rosch. *Comment on “Consistent thermostatistics forbids negative absolute temperatures”*. *arXiv* 1407.4127 (2014).
- [171] J. Dunkel and S. Hilbert. *Reply to Frenkel and Warren [arXiv:1403.4299v1]*. *arXiv* 1403.6058 (2014).
- [172] J. Dunkel and S. Hilbert. *Reply to Schneider et al. [arXiv:1407.4127v1]*. *arXiv* 1408.5392 (2014).
- [173] T. Busch, B.-G. Englert, K. Rzazewski, and M. Wilkens. *Two cold atoms in a harmonic trap*. *Found. Phys.* **28**, 549 (1998).
- [174] K. Xu, Y. Liu, D. E. Miller, J. K. Chin, W. Setiawan, and W. Ketterle. *Observation of strong quantum depletion in a gaseous Bose-Einstein condensate*. *Phys. Rev. Lett.* **96**, 180405 (2006).
- [175] A. Rapp. *Mean-field dynamics to negative absolute temperatures in the Bose-Hubbard model*. *Phys. Rev. A* **87**, 043611 (2013).
- [176] N. D. Mermin and H. Wagner. *Absence of ferromagnetism or antiferromagnetism in one- or two-dimensional isotropic Heisenberg models*. *Phys. Rev. Lett.* **17**, 1133 (1966).
- [177] P. C. Hohenberg. *Existence of long-range order in one and two dimensions*. *Phys. Rev.* **158**, 383 (1967).
- [178] V. Bagnato and D. Kleppner. *Bose-Einstein condensation in low-dimensional traps*. *Phys. Rev. A* **44**, 7439 (1991).
- [179] W. J. Mullin. *Bose-Einstein condensation in a harmonic potential*. *J. Low Temp. Phys.* **106**, 615 (1997).
- [180] D. S. Petrov, M. Holzmann, and G. V. Shlyapnikov. *Bose-Einstein condensation in quasi-2D trapped gases*. *Phys. Rev. Lett.* **84**, 2551 (2000).
- [181] Z. Hadzibabic, P. Krüger, M. Cheneau, B. Battelier, and J. Dalibard. *Berezinskii-Kosterlitz-Thouless crossover in a trapped atomic gas*. *Nature* **441**, 1118 (2006).
- [182] Y. Kagan, V. A. Kashurnikov, A. V. Krasavin, N. V. Prokof'ev, and B. Svistunov. *Quasicondensation in a two-dimensional interacting Bose gas*. *Phys. Rev. A* **61**, 043608 (2000).

- [183] S. Braun et al. *Emergence of coherence and the dynamics of quantum phase transitions*. arXiv 1403.7199 (2014).
- [184] J. P. Sethna. *Statistical mechanics: Entropy, order parameters and complexity*. Oxford University Press (2006).
- [185] P. Papon, J. Leblond, and P. H. E. Meijer. *The physics of phase transitions: concepts and applications*. Springer (2006).
- [186] K. Binder. *Theory of first-order phase transitions*. Rep. Prog. Phys. **50**, 783 (1987).
- [187] G. G. Batrouni, R. T. Scalettar, and G. T. Zimanyi. *Quantum critical phenomena in one-dimensional Bose systems*. Phys. Rev. Lett. **65**, 1765 (1990).
- [188] J. Dziarmaga. *Dynamics of a quantum phase transition and relaxation to a steady state*. Adv. Phys. **59**, 1063 (2010).
- [189] H. E. Stanley. *Introduction to phase transitions and critical phenomena, rev. ed.* Oxford University Press (1971).
- [190] M. A. Anisimov. *Critical phenomena in liquids and liquid crystals*. CRC Press (1991).
- [191] L. D. Carr. *Understanding quantum phase transitions*. Taylor & Francis (2010).
- [192] S. Sachdev. *Quantum magnetism and criticality*. Nat. Phys. **4**, 173 (2008).
- [193] C. Pfleiderer. *Why first order quantum phase transitions are interesting*. J. Phys.-Condens. Mat. **17**, S987 (2005).
- [194] A. Kinross, M. Fu, T. Munsie, H. Dabkowska, G. Luke, S. Sachdev, and T. Imai. *Evolution of quantum fluctuations near the quantum critical point of the transverse field Ising chain system CoNb₂O₆*. Phys. Rev. X **4**, 031008 (2014).
- [195] D. Chen, M. White, C. Borries, and B. DeMarco. *Quantum quench of an atomic Mott insulator*. Phys. Rev. Lett. **106**, 235304 (2011).
- [196] X. Zhang, C.-L. Hung, S.-K. Tung, N. Gemelke, and C. Chin. *Exploring quantum criticality based on ultracold atoms in optical lattices*. New J. Phys. **13**, 045011 (2011).
- [197] L. E. Sadler, J. M. Higbie, S. R. Leslie, M. Vengalattore, and D. M. Stamper-Kurn. *Spontaneous symmetry breaking in a quenched ferromagnetic spinor Bose-Einstein condensate*. Nature **443**, 312 (2006).
- [198] A. Messiah. *Quantum mechanics 2*. North-Holland Publishing Company (1975).
- [199] T. W. B. Kibble. *Some implications of a cosmological phase transition*. Phys. Rep. **67**, 183 (1980).
- [200] W. H. Zurek. *Cosmological experiments in superfluid helium?* Nature **317**, 505 (1985).
- [201] W. H. Zurek, U. Dorner, and P. Zoller. *Dynamics of a quantum phase transition*. Phys. Rev. Lett. **95**, 105701 (2005).

- [202] A. del Campo and W. H. Zurek. *Universality of phase transition dynamics: Topological defects from symmetry breaking*. arXiv 1310.1600 (2013).
- [203] S. Ulm et al. *Observation of the Kibble-Zurek scaling law for defect formation in ion crystals*. *Nature Commun.* **4**, 2290 (2013).
- [204] K. Pyka et al. *Topological defect formation and spontaneous symmetry breaking in ion Coulomb crystals*. *Nature Commun.* **4**, 2291 (2013).
- [205] R. W. Cherng and L. S. Levitov. *Entropy and correlation functions of a driven quantum spin chain*. *Phys. Rev. A* **73**, 043614 (2006).
- [206] D. Pekker, B. Wunsch, T. Kitagawa, E. Manousakis, A. S. Sørensen, and E. Demler. *Signatures of the superfluid to Mott insulator transition in equilibrium and in dynamical ramps*. *Phys. Rev. B* **86**, 144527 (2012).
- [207] J. Dziarmaga, M. Tylutki, and W. H. Zurek. *Quench from Mott insulator to superfluid*. *Phys. Rev. B* **86**, 144521 (2012).
- [208] W. H. Zurek. *Cosmological experiments in condensed matter systems*. *Phys. Rep.* **276**, 177 (1996).
- [209] S. Mondal, D. Sen, and K. Sengupta. *Non-equilibrium dynamics of quantum systems: Order parameter evolution, defect generation, and qubit transfer*. In: *Quantum quenching, annealing and computation*. Springer (2010).
- [210] V. Gritsev and A. Polkovnikov. *Universal dynamics near quantum critical points*. In: *Understanding quantum phase transitions*. Taylor & Francis (2010).
- [211] U. Schollwöck. *The density-matrix renormalization group*. *Rev. Mod. Phys.* **77**, 259 (2005).
- [212] M. L. Wall and L. D. Carr. *Open Source TEBD*. Online (2013).
- [213] J.-S. Bernier, R. Citro, C. Kollath, and E. Orignac. *Correlation dynamics during a slow interaction quench in a one-dimensional Bose gas*. *Phys. Rev. Lett.* **112**, 065301 (2014).
- [214] M. Cheneau et al. *Light-cone-like spreading of correlations in a quantum many-body system*. *Nature* **481**, 484 (2012).
- [215] P. Barmettler, D. Poletti, M. Cheneau, and C. Kollath. *Propagation front of correlations in an interacting Bose gas*. *Phys. Rev. A* **85**, 053625 (2012).
- [216] E. H. Lieb and D. W. Robinson. *The finite group velocity of quantum spin systems*. *Commun. Math. Phys.* **28**, 251 (1972).
- [217] P. Calabrese and J. Cardy. *Time dependence of correlation functions following a quantum quench*. *Phys. Rev. Lett.* **96**, 136801 (2006).
- [218] M. Cramer, C. M. Dawson, J. Eisert, and T. J. Osborne. *Exact relaxation in a class of nonequilibrium quantum lattice systems*. *Phys. Rev. Lett.* **100**, 030602 (2008).

- [219] J. Eisert and T. J. Osborne. *General entanglement scaling laws from time evolution*. *Phys. Rev. Lett.* **97**, 150404 (2006).
- [220] S. Bravyi, M. B. Hastings, and F. Verstraete. *Lieb-robinson bounds and the generation of correlations and topological quantum order*. *Phys. Rev. Lett.* **97**, 050401 (2006).
- [221] A. Flesch, M. Cramer, I. P. McCulloch, U. Schollwöck, and J. Eisert. *Probing local relaxation of cold atoms in optical superlattices*. *Phys. Rev. A* **78**, 033608 (2008).
- [222] J.-S. Bernier, D. Poletti, P. Barmettler, G. Roux, and C. Kollath. *Slow quench dynamics of Mott-insulating regions in a trapped Bose gas*. *Phys. Rev. A* **85**, 033641 (2012).
- [223] F. M. Cucchietti, B. Damski, J. Dziarmaga, and W. H. Zurek. *Dynamics of the Bose-Hubbard model: Transition from a Mott insulator to a superfluid*. *Phys. Rev. A* **75**, 023603 (2007).
- [224] J. Dziarmaga and W. H. Zurek. *Quench in the 1d Bose-Hubbard model: Topological defects and excitations from Kosterlitz-Thouless phase transition dynamics*. [arXiv 1312.5139](https://arxiv.org/abs/1312.5139) (2013).
- [225] D. R. Scherer, C. N. Weiler, T. W. Neely, and B. P. Anderson. *Vortex formation by merging of multiple trapped Bose-Einstein condensates*. *Phys. Rev. Lett.* **98**, 110402 (2007).
- [226] G. Lamporesi, S. Donadello, S. Serafini, F. Dalfovo, and G. Ferrari. *Spontaneous creation of Kibble-Zurek solitons in a Bose-Einstein condensate*. *Nat. Phys.* **9**, 656 (2013).
- [227] A. Chandran, A. Erez, S. S. Gubser, and S. L. Sondhi. *Kibble-Zurek problem: Universality and the scaling limit*. *Phys. Rev. B* **86**, 064304 (2012).
- [228] G. Biroli, L. F. Cugliandolo, and A. Sicilia. *Kibble-Zurek mechanism and infinitely slow annealing through critical points*. *Phys. Rev. E* **81**, 050101 (2010).
- [229] E. Canovi, D. Rossini, R. Fazio, and G. E. Santoro. *Adiabatic dynamics in a spin-1 chain with uniaxial single-spin anisotropy*. *J. Stat. Mech.* **2009**, P03038 (2009).
- [230] S. Deng, G. Ortiz, and L. Viola. *Dynamical non-ergodic scaling in continuous finite-order quantum phase transitions*. *EPL* **84**, 67008 (2008).
- [231] D. Sen, K. Sengupta, and S. Mondal. *Defect production in nonlinear quench across a quantum critical point*. *Phys. Rev. Lett.* **101**, 016806 (2008).
- [232] M. Haque and F. E. Zimmer. *Slow interaction ramps in trapped many-particle systems: Universal deviations from adiabaticity*. *Phys. Rev. A* **87**, 033613 (2013).
- [233] H. T. Quan and W. H. Zurek. *Testing quantum adiabaticity with quench echo*. *New J. Phys.* **12**, 093025 (2010).
- [234] J. P. Ronzheimer et al. *Expansion dynamics of interacting bosons in homogeneous lattices in one and two dimensions*. *Phys. Rev. Lett.* **110**, 205301 (2013).

- [235] S. Will, T. Best, U. Schneider, L. Hackermüller, D.-S. Lühmann, and I. Bloch. *Time-resolved observation of coherent multi-body interactions in quantum phase revivals*. *Nature* **465**, 197 (2010).
- [236] D.-S. Lühmann, K. Bongs, K. Sengstock, and D. Pfannkuche. *Self-trapping of bosons and fermions in optical lattices*. *Phys. Rev. Lett.* **101**, 050402 (2008).
- [237] J. Heinze et al. *Multiband spectroscopy of ultracold fermions: Observation of reduced tunneling in attractive Bose-Einstein mixtures*. *Phys. Rev. Lett.* **107**, 135303 (2011).
- [238] T. Fukuyama, M. Morikawa, and T. Tatekawa. *Cosmic structures via Bose-Einstein condensation and its collapse*. *J. Cosmol. Astropart. Phys.* **2008**, 033 (2008).
- [239] G.-B. Jo, J. Guzman, C. K. Thomas, P. Hosur, A. Vishwanath, and D. M. Stamper-Kurn. *Ultracold atoms in a tunable optical kagome lattice*. *Phys. Rev. Lett.* **108**, 045305 (2012).
- [240] A. Rapp. *Quantum simulators at negative absolute temperatures*. *Phys. Rev. A* **85**, 043612 (2012).